

Dark Matter Halo Properties from Galaxy-Galaxy Lensing



Fabrice Brimiouille

Dark Matter Halo Properties from Galaxy-Galaxy Lensing

Dissertation

der
Fakultät für Physik
der
Ludwig-Maximilians-Universität (LMU) München

Ph.D. Thesis

of the
Faculty of Physics
of the
Ludwig-Maximilians University (LMU) Munich

vorgelegt von

Fabrice Brimiouille

geboren am 9. Januar 1979 in Namur

München, 16. April 2013

1. Gutachter: Prof. Dr. Ralf Bender
2. Gutachter: Prof. Dr. Joseph Mohr

Tag der mündlichen Prüfung: 19. Juli 2013

Zusammenfassung

Die Forschungsergebnisse der letzten Jahre haben gezeigt, dass das Universum bei weitem nicht nur aus baryonischer Materie besteht. Tatsächlich scheinen 72% aus sogenannter Dunkler Energie zu bestehen, während selbst vom verbleibenden Teil nur etwa ein Fünftel baryonischer Materie zugeordnet werden kann. Der Rest besteht aus Dunkler Materie, deren Beschaffenheit bis heute nicht mit Sicherheit geklärt ist. Ursprünglich in den Rotationskurven von Spiralgalaxien beobachtet, wurde die Notwendigkeit ihrer Existenz inzwischen auch in elliptischen Galaxien und Galaxienhaufen nachgewiesen. Tatsächlich scheint Dunkle Materie eine entscheidende Rolle in der Strukturbildung im Universum gespielt zu haben. In der Frühzeit des Universums, als die Materieverteilung im Weltraum noch äußerst gleichmäßig war und nur sehr geringe Inhomogenitäten aufwies, bildeten sie die Kondensationskeime für den gravitativen Kollaps der Materie. Numerische Simulationen haben gezeigt, dass der heute beobachtbare Entwicklungszustand des Universums erst durch die zusätzliche Masse Dunkler Materie ermöglicht wurde, die den strukturellen Kollaps erheblich beschleunigte und nur dadurch zur heute beobachtbaren Komplexität der Strukturen führen konnte. Da Dunkle Materie nicht elektromagnetisch wechselwirkt, sondern sich nur durch ihre Schwerkraft bemerkbar macht, stellt der Gravitationslinseneffekt eine ausgezeichnete Methode dar, die Existenz und Menge an Dunkler Materie nachzuweisen. Der schwache Gravitationslinseneffekt macht sich zu Nutzen, dass die intrinsischen Orientierungen der Galaxien im Weltraum keine Vorzugsrichtung haben, gleichbedeutend mit ihrer statistischen Gleichverteilung. Die gravitationsbedingte kohärente Verzerrung der Hintergrundobjekte führt zu einer Abweichung von dieser Gleichverteilung, die von den Eigenschaften der Gravitationslinsen abhängt und daher zu deren Analyse genutzt werden kann.

Diese Dissertation beschreibt die Galaxy-Galaxy-Lensing-Analyse von insgesamt 89 deg^2 optischer Daten, die im Rahmen des CFHTLS-WIDE-Surveys beobachtet wurden und aus denen im Rahmen dieser Arbeit photometrische Rotverschiebungs- und Elliptizitätskataloge erzeugt wurden. Das Galaxiensample besteht aus insgesamt 5×10^6 Linsen mit Rotverschiebungen von $0.05 < z_{\text{phot}} \leq 1$ und einem zugehörigen Hintergrund von insgesamt 1.7×10^6 Quellen mit erfolgreich gemessenen Elliptizitäten in einem Rotverschiebungsintervall von $0.05 < z_{\text{phot}} \leq 2$. Unter Annahme analytischer Galaxienhaloprofile wurden für die Galaxien die Masse, das Masse-zu-Leuchtkraft-Verhältnis und die entsprechenden Halomodellprofilparameter sowie ihre Skalenrelationen bezüglich der absoluten Leuchtkraft untersucht. Dies geschah sowohl für das gesamte Linsensample als auch für Linsensamples in Abhängigkeit des SED-Typs und der Umgebungsdichte. Die ermittelten Skalenrelationen wurden genutzt, um die durchschnittlichen Werte für die Galaxienhaloparameter und eine mittlere Masse für die Galaxien in Abhängigkeit ihres SED-Typs zu bestimmen. Es ergibt sich eine Gesamtmasse von $M_{\text{total}} = 23.2_{-2.5}^{+2.8} \times 10^{11} h^{-1} M_{\odot}$ für eine durchschnittliche Galaxie mit einer Referenzleuchtkraft von $L^* = 1.6 \times 10^{10} h^{-2} L_{\odot}$. Die Gesamtmasse roter Galaxien bei gleicher Leuchtkraft überschreitet diejenige des entsprechenden gemischten Samples um ca. 130%, während die mittlere Masse einer blauen Galaxie ca. 65% unterhalb des Durchschnitts liegt. Die Gesamtmasse der Galaxien steigt stark mit der Umgebungsdichte an, betrachtet man die Geschwindigkeitsdispersion ist dies jedoch nicht der Fall. Dies bedeutet, dass die zentrale Galaxienmateriedichte kaum von der Umgebung sondern fast nur von der Leuchtkraft abhängt. Die Belastbarkeit der Ergebnisse wurde von zu diesem Zweck erzeugten Simulationen bestätigt. Es hat sich dabei gezeigt, dass der Effekt mehrfacher gravitativer Ablenkung an verschiedenen Galaxien angemessen berücksichtigt werden muss, um systematische Abweichungen zu vermeiden.

Abstract

The scientific results over the past years have shown that the Universe is by far not only composed of baryonic matter. In fact the major energy content of 72% of the Universe appears to be represented by so-called dark energy, while even from the remaining components only about one fifth is of baryonic origin, whereas 80% have to be attributed to dark matter. Originally appearing in observations of spiral galaxy rotation curves, the need for dark matter has also been verified investigating elliptical galaxies and galaxy clusters. In fact, it appears that dark matter played a major role during structure formation in the early Universe. Shortly after the Big Bang, when the matter distribution was almost homogeneous, initially very small inhomogeneities in the matter distribution formed the seeds for the gravitational collapse of the matter structures. Numerical n-body simulations, for instance, clearly indicate that the presently observable evolutionary state and complexity of the matter structure in the Universe would not have been possible without dark matter, which significantly accelerated the structure collapse due to its gravitational interaction. As dark matter does not interact electromagnetically and therefore is non-luminous but only interacts gravitationally, the gravitational lens effect provides an excellent opportunity for its detection and estimation of its amount. Weak gravitational lensing is a technique that makes use of the random orientation of the intrinsic galaxy ellipticities and thus their uniform distribution. Gravitational tidal forces introduce a coherent distortion of the background object shapes, leading to a deviation from the uniform distribution which depends on the lens galaxy properties and therefore can be used to study them.

This thesis describes the galaxy-galaxy lensing analysis of 89 deg² of optical data, observed within the CFHTLS-WIDE survey. In the framework of this thesis the data were used in order to create photometric redshift and galaxy shape catalogs. The complete galaxy sample consists of a total number of 5×10^6 lens galaxies within a redshift range of $0.05 < z_{\text{phot}} \leq 1$ and 1.7×10^6 corresponding source galaxies with redshifts of $0.05 < z_{\text{phot}} \leq 2$ and successfully extracted shapes. Assuming that the galaxy halos can be described by analytic profiles, the scaling relations with absolute luminosity for the galaxy masses, their mass-to-light ratios and the corresponding halo parameters have been extracted. Based on the obtained scaling relations, the average values for the corresponding halo parameters and the mean galaxy masses for a given luminosity were derived as a function of considered halo model, the galaxy SED and the local environment density. We obtain a total mass of $M_{\text{total}} = 23.2^{+2.8}_{-2.5} \times 10^{11} h^{-1} M_{\odot}$ for an average galaxy with chosen reference luminosity of $L^* = 1.6 \times 10^{10} h^{-2} L_{\odot}$. In contrast, the mean total masses for red galaxies of same luminosity exceed the value of the average galaxy about 130%, while the mass of a blue galaxy is about 65% below the value of an average fiducial galaxy. Investigating the influence of the environmental density on the galaxy properties we observe a significant increase of the total integrated masses with galaxy density, however the velocity dispersions are not affected. This indicates that the central galaxy matter density mostly depends on the galaxy luminosity but not on the environment. Simulations based on the extracted scientific results were built, verifying the robustness of the scientific results. They give a clear hint that multiple deflections on different lens galaxies have to be properly accounted for in order to avoid systematically biased results.

Contents

Zusammenfassung	vii
Abstract	ix
Contents	xi
List of Figures	xv
List of Tables	xix
1 Introduction	1
2 Cosmological Framework	5
2.1 The Homogeneous Universe	5
2.1.1 Newtonian Ansatz	5
2.1.2 Relativistic Extension	7
2.1.3 Cosmological Redshift	10
2.1.4 Distances	10
Comoving Distance	11
Angular Diameter Distance	11
Luminosity distance	11
Distance Modulus	12
2.2 The Inhomogeneous Universe	13
2.2.1 Linear Structure Formation	13
2.2.2 Correlation Function and Power Spectrum	15
The Correlation Function	15
The Power Spectrum	15
Dark Matter	15
2.2.3 Non-Linear Structure Growth	16
The Spherical Collapse Model	16
Press-Schechter Model	17
3 Lensing Theory	19
3.1 Gravity	19
3.2 The Lens Equation	20
3.3 Weak Lensing	22

3.3.1	Shape Measurement	23
3.3.2	Statistical Ansatz	23
3.3.3	Estimation of Object Shapes with the KSB Pipeline	25
3.4	Theory of Galaxy-Galaxy Lensing	26
3.4.1	Lens Profiles	26
	Singular Isothermal Sphere	26
	Truncated Isothermal Sphere (BBS)	27
	Universal Density Profile (NFW)	29
3.4.2	Scaling Relations for the Galaxy Halo Models	30
3.4.3	Maximum Likelihood Analysis	33
3.4.4	3D-LOS-Projected Lensing Signal Simulations	34
4	Photometric Redshifts	35
4.1	Techniques	35
4.2	The Template-Fitting Method	36
4.2.1	Principle	36
4.2.2	Subtleties	36
4.2.3	Galaxy Types	37
	Early Type Galaxies	38
	Late Type Galaxies	39
4.2.4	PhotoZ	40
5	Data	43
5.1	Imaging Data	43
5.2	Spectroscopic Data	46
5.3	Photometric Catalogs	46
5.3.1	Creation of Multicolor Catalogs	46
5.3.2	Calibration of Photometric Zeropoints	49
	Calibration on Stellar Sequences	54
	Calibration on Spectroscopic Redshifts	54
5.3.3	Star/Galaxy Separation	57
5.3.4	Calculation of Photometric Redshifts	60
5.4	Estimation of Object Shapes and Shears	64
5.5	Properties of the Galaxies in the Photometric and in the Shape Catalogs	70
5.5.1	Definition of Lens and Source Galaxy Samples	72
5.5.2	Definition of Lens Subsamples	73
5.6	Lens Mass Errors from Photometric Redshifts and Shape Measurement Errors	75
5.7	Systematic Errors from Intrinsic Alignment	80
6	Weak Lensing Analysis	83
6.1	Measurement of the Tangential Shear	83
6.2	Measurement of the Excess Surface Mass Density	95
6.2.1	Measurement of $\Delta\Sigma$ for Several Luminosity Intervals	95
6.2.2	Investigation of Halo Parameter Scaling Relations	100
	L- σ -Scaling Based on Fits to $\Delta\Sigma$	100

	L- r_{200} - and L- M_{200} -Scaling Based on Fits to $\Delta\Sigma$	103
6.3	Checks for Systematic Errors from γ_t and $\Delta\Sigma$ Measurements	108
6.3.1	Shear Estimates Relative to Stars and Random Points	108
6.3.2	Signal Dilution from Contamination of the Background Sample	110
6.3.3	Signal Contribution of Undetected Low Mass Nearby Galaxies	111
6.3.4	Systematic Checks by Analyzing the Shear Signal on Subsamples	112
6.4	Maximum Likelihood Analysis	116
6.4.1	Truncated Isothermal Sphere (BBS)	117
6.4.2	Universal Density Profile (NFW)	121
6.4.3	Extraction of Scaling Relations from Maximum Likelihood Analyses	123
	Mass-to-Light-Ratio	123
	Concentration-Mass-Relation	129
6.4.4	Comparison of the Results	133
6.4.5	Consistency of Maximum Likelihood and $\Delta\Sigma$ -Fit Results	133
6.5	Comparison of Observed $\Delta\Sigma$ -Profiles to Expectations from Lensing Simulations	135
6.5.1	Combined, Red and Blue Lens Samples in Average Environment	135
6.5.2	Combined Lens Sample in Over- and Underdense Environments	143
7	Summary and Conclusions	145
	Bibliography	151
A	Zeropoint Corrections	163
	Acknowledgments / Danksagung	167

List of Figures

2.1	Cosmic evolution since Big Bang	6
2.2	Evolution of $H(z)$	10
2.3	Evolution and comparison of cosmological distances	12
3.1	Sketch of gravitational lensing	21
3.2	Illustration of ellipticity components	24
4.1	Hubble sequence	37
4.2	PhotoZ template set	41
4.3	PhotoZ priors	42
5.1	Layout of the CFHTLS-Wide	44
5.2	CFHT filter curves	45
5.3	PSF variation, i' -band, CFHTLS-Wide W1p2p3	47
5.4	Stellar colors in different apertures, convolved, CFHTLS-Wide W1p2p3	48
5.5	Number counts and magnitude errors, CFHTLS-Wide W1p2p3	50
5.6	z_{spec} vs. z_{phot} , uncalibrated, $17.0 \leq i' \leq 22.5$, CFHTLS-Wide	51
5.7	Stellar sequence, color-color-diagram, CFHTLS-Wide W1p2p3	52
5.8	z_{spec} vs. z_{phot} , calibrated on stars, $17.0 \leq i' \leq 22.5$, CFHTLS-Wide	53
5.9	Photoz distribution with optical filters	57
5.10	Photoz distribution with and without NIR filters	58
5.11	z_{spec} vs. z_{phot} , calibrated on spectra, $17.0 \leq i' \leq 22.5$, CFHTLS-Wide	59
5.12	z_{spec} vs. z_{phot} , calibrated on spectra, $22.5 \leq i' \leq 24.0$, CFHTLS-Wide W1 and W3	60
5.13	z_{spec} vs. z_{phot} , calibrated on spectra, CFHTLS-D D1 and D3	61
5.14	z_{spec} vs. z_{phot} , comparison with SDSS spectroscopic sample	62
5.15	FWHM_IMAGE vs. CLASS_STAR	63
5.16	Photometric redshift distribution, CFHTLS-Wide	63
5.17	Object distributions, star selection for KSB	65
5.18	PSF anisotropy patten, pre-lensflip	66
5.19	PSF anisotropy pattern, post-lensflip	67
5.20	Ellipticity component histogram, source sample	69
5.21	Absolute ellipticity histogram, source sample	69
5.22	Flux radius and S/N histogram, source sample	70
5.23	Magnitude histogram (i')	71
5.24	Photo-z histogram, lens sample	71

5.25	Flowchart for our lens and background definition.	73
5.26	(B-V)-histogram for SDSS-LRGs	74
5.27	Density contours, M_r vs. $g - r$, separation of red and blue galaxies	76
5.28	Density contours, $g - r$ vs. $r - i$, separation of red and blue galaxies	77
5.29	Fractional systematic and statistical error $\delta D_d/D_d$	79
5.30	Fractional systematic and statistical error $\delta \Sigma_c/\Sigma_c$	81
6.1	γ_t for $-24 \leq i' \leq -20$	86
6.2	Simulated γ_t for $-24 \leq i' \leq -20$	87
6.3	γ_t for all lenses, individual luminosity bins for $-24 \leq i' \leq -20$	88
6.4	Simulated γ_t for all lenses, individual luminosity bins for $-24 \leq i' \leq -20$	89
6.5	Tangential shear γ_t for red lenses, individual luminosity bins for $-24 \leq i' \leq -20$	90
6.6	Simulated γ_t for red lenses, individual luminosity bins for $-24 \leq i' \leq -20$	91
6.7	Tangential shear γ_t for blue lenses, individual luminosity bins for $-24 \leq i' \leq -20$	92
6.8	Simulated γ_t for blue lenses, individual luminosity bins for $-24 \leq i' \leq -20$	93
6.9	γ_t for different environment lens samples	94
6.10	$\Delta \Sigma$ for $-24 \leq i' \leq -17$	96
6.11	$\Delta \Sigma$, individual luminosity bins for $-24 \leq i' \leq -17$	97
6.12	$\Delta \Sigma$, individual luminosity bins for $-24 \leq i' \leq -17$ and $z \leq 0.3$	99
6.13	σ -luminosity, scaling relation, environment dependency	101
6.14	L- σ	102
6.15	L- σ for red galaxies	103
6.16	L- r_{200}	105
6.17	L- v_{200} for blue galaxies	106
6.18	L- M_{200}	107
6.19	M_{star} vs. M_{200}/M_{star} for red galaxies	107
6.20	Tangential shear γ_t relative to stars	109
6.21	Tangential shear for random samples	110
6.22	Relative background density around the foreground galaxies	111
6.23	Contamination of $\Delta \Sigma$ by unresolved satellite galaxies	112
6.24	Redshift scaling GGL	113
6.25	Systematic check for different source luminosities	114
6.26	Systematic check for different source signal-to-noise ratios	114
6.27	Systematic check for different source sizes	116
6.28	Maximum likelihood result for the scaling relation of σ , red and blue galaxies	118
6.29	Maximum likelihood analysis for the BBS profile.	120
6.30	Maximum likelihood analysis for the NFW profile.	122
6.31	Maximum likelihood result for the scaling relation of s , red and blue galaxies	125
6.32	Maximum likelihood for s , bright and faint galaxies	126
6.33	Maximum likelihood for s , bright and faint galaxies, low density environment	127
6.34	Truncation radius s and M/L -ratio as function of L_r	128
6.35	Maximum likelihood result for c-L-relation, red and blue galaxies	130
6.36	c-L-relation for bright and faint galaxies	131
6.37	$c - M_{200}$ -relation, single- and double power law fit	132
6.38	Influence of multiple deflections on simulated BBS and NFW profiles	134

6.39	$\Delta\Sigma$, combined lens sample, observation and simulation	136
6.40	$\Delta\Sigma$, red lens sample, observation and simulation	137
6.41	$\Delta\Sigma$, blue lens sample, observation and simulation	138
6.42	$\Delta\Sigma$, combined lens sample, high density environment, observation and simulation . .	139
6.43	$\Delta\Sigma$, combined lens sample, very high density environment, observation and simulation	140
6.44	$\Delta\Sigma$, combined lens sample, low density environment, observation and simulation . .	141
6.45	$\Delta\Sigma$, combined lens sample, very low density environment, observation and simulation	142

List of Tables

5.1	Photo-z statistics in comparison with spectro-z	56
6.1	σ -fits from χ , data and simulations	85
6.2	Scaling relation indices derived from $\Delta\Sigma$ profiles	108
6.3	Results, systematic check	115
6.4	Best-fitting values from the maximum likelihood analyses	124
A.1	Zeropoint corrections	163

Chapter 1

Introduction

In the past few years we came to learn that the Universe is not as simple as we thought it to be. We had to discover that the luminous baryonic matter, the matter component we ourselves are built of, only represents a very small fraction of the energy content of the Universe. First, a few decades ago the rotation curves of spiral galaxies gave a hint to an additional invisible mass component, the so-called dark matter, which only interacts by its gravity, leading to the significantly higher rotation velocity values on large scales than expected. Then, only 15 years ago, the distance and luminosity measurements of distant supernovae type Ia taught us, that the main ingredient with a fraction of about 72% is neither baryonic nor dark matter, but that our Universe is dominated by a mysterious phenomenon called dark energy.

Dark energy makes itself noticeable by causing an accelerated expansion of the Universe instead of a decelerated expansion due to gravitational interaction of the matter in the Universe. Although representing by far the largest fraction of the energy content in the Universe, the existence of dark energy only became obvious in the recent past, when the expansion of the Universe reached a certain level. But even looking at the remaining fraction of the cosmological energy content, the baryonic matter fraction only makes about a fifth of the total matter content. Both, the nature of dark energy and the nature of dark matter are not really understood, leaving us with the knowledge that our world is dominated by phenomena we do neither see nor fully understand. Although dark energy and thus the cosmic acceleration could be seen as the consequence of a non-zero vacuum energy ground state, a concept for a direct detection does not exist yet. The only way to trace it are large-scale-structure and cosmological studies which are trying to determine constraints on cosmological parameters in order to infer implications for dark energy. The situation for dark matter is significantly better as there are several concepts to unravel its mystery. Several candidates for these hypothetical dark matter particles have been suggested, from axions to weakly interacting massive particles (WIMPs) as supersymmetric particles. In the latter case the most probable candidate is the neutralino, as the dark matter particle is required to be uncharged in order to not interact electromagnetically and to be optically invisible. This led to the development of several concepts to measure dark matter, from detectors on Earth trying to directly trace them, to astrophysical observations measuring the dark matter content via its gravitational interaction. Dark matter does not only appear in spiral galaxies, its necessity has also been detected investigating early type galaxies, galaxy clusters and large scale structure. As a matter of fact, dark matter even appears to have played a key role during structure formation in the early Universe. Looking back to the time of recombination ($z \sim 1100$), measurements of the CMB power spectrum tell us that the matter distribution was almost homogeneous, showing

only very small inhomogeneities of the order of $\Delta T/T \sim 10^{-5}$ (see Smoot *et al.* 1992). Nonetheless, as small as they might have originally been, it is exactly these initially tiny inhomogeneities that represent the seeds from which all presently visible structure, galaxies, galaxy clusters and the presently forming galaxy superclusters arose. Regions with slightly higher local density, thus having higher gravity, attracted additional matter, which led to an enhancement of the density contrast and a further increase of the gravitational attraction. Above a certain threshold these inhomogeneities could continuously grow and eventually form the known extended structures, while the regions of underdensity bled out, becoming the large, almost empty regions in the Universe called voids. However, numerical simulations have shown that the amount of baryonic matter is not sufficient in order to explain the presently observable advanced complexity and inhomogeneity of matter structure in space. It appears that originally structure formation was driven by larger amounts of neutral dark matter, which had decoupled from the photon plasma on an earlier timescale. This significantly accelerated the collapse of the matter structures and led to the creation of dark matter halos whose centers eventually were populated by those baryonic cores representing the well-known luminous galaxies. We see that in order to understand structure formation, galaxy formation and evolution, one cannot avoid to learn about the origin, the properties and the distribution of dark matter in the Universe.

As dark matter only interacts via its gravitational attraction, the gravitational lens effect is predestined for detection and quantification of the dark matter content. The gravitational deflection of the light of a background source on a foreground lens leads, due to tidal effects, to a coherent distortion of the original source image shape called gravitational shear, which carries the imprint of the lens matter distribution. However, measurements of gravitational shears are complicated by the fact that in weak gravitational lensing these distortions are quite small and galaxies in general are not intrinsically round but elliptical. As the distortion of the source galaxy image on average is only of the order of a few per cent of the intrinsic galaxy ellipticity, it is impossible to disentangle the induced gravitational shear from the intrinsic ellipticity for an individual galaxy. Yet in this case statistics is a helpful tool. The basic cosmological assumption is that we live in an homogeneous and isotropic Universe, which also means that the orientation of the major axes of the galaxy ellipticities are not supposed to show a preferred direction but should be randomly distributed (at least on average over a large enough volume). This means, considering a sufficiently large number of source galaxies and averaging their measured apparent ellipticities, the ellipticity contributions should cancel out, leaving a zero-signal if there is no gravitational imprint from lens galaxies. This implies that values deviating from zero in theory are to be caused by gravitational lensing. The comparison of the statistical properties of the gravitational lensing distortions with predictions of theoretical models then gives us information about the amount and distribution of the dark matter. In principle weak lensing is capable of tracing any matter foreground distribution as long as there is a sufficient number of background galaxies carrying the gravitational lens imprint. Galaxy clusters, due to their high masses, provide the strongest observational weak lensing signals, making it quite easy to analyze, as the number of background galaxies does not need to be particularly high. Anyhow, background galaxies with too small projected separations from the cluster centers have to be omitted, as above a certain signal strength the basic weak lensing assumptions start to break down and a proper strong lensing analysis needs to be done. The weakest signal is introduced by lensing of the large scale structure, the so-called cosmic shear, significantly raising the requirements in galaxy number and precision of the ellipticity extraction from imaging data. In a cosmic shear analysis no specific lens

sample is considered, but the auto-correlation of the lensed galaxy shapes is analyzed in order to infer foreground properties and cosmological parameters. The galaxy lensing signal magnitude finally lies in between, raising the requirements on the background galaxy number, but still high enough to not be too excruciatingly sensitive to small systematic errors in the ellipticity estimation. While in the more central parts of galaxies mass measurements still can be derived with dynamical methods, weak gravitational lensing is an important mass estimator when observing larger scales, considering the lack of other mass tracers, besides the rare case of dynamical tracing of satellite galaxies. However, when investigating very large scales, multiple deflections on neighboring lenses need to be properly taken into account, as they additionally influence the lensing signal on those scales, leading to a bias in the measurements if ignored.

Due to the small magnitude of the lensing signal the weak lensing analysis of a single lens galaxy is hardly possible. Therefore it is necessary to analyze a larger sample of galaxies in order to extract their properties. Galaxy-galaxy lensing (GGL) is the application of the weak gravitational lens formalism on lens galaxies, analyzing larger samples of galaxies in order to obtain the mean properties of the investigated galaxy sample or to estimate the galaxy properties for a fiducial galaxy, assuming basic scaling relations of the halo parameters with galaxy mass or luminosity. The selection of specific galaxy samples provides the opportunity to derive the halo properties as a function of luminosity, galaxy SED or the environment the galaxies populate. The first attempt to detect GGL was already made in the 1980s by Tyson *et al.* (1984), who used scans of photographic plates and searched for an excess of background galaxy images tangentially aligned to brighter candidate lens galaxies. However, it took more than ten years until the first actual detection could be reported. Since then several GGL analyses have been performed on ground-based (e.g., Brainerd *et al.* 1996 or Hoekstra *et al.* 2002, 2004), but also on space-based observations (e.g., dell'Antonio & Tyson 1996, Griffiths *et al.* 1996 or Hudson *et al.* 1998), giving some first constraints on velocity dispersions, galaxy sizes and thus masses. The Sloan Digital Sky Survey (SDSS) finally provided the first large dataset applicable for GGL studies, covering a large area of more than 8000 deg^2 , that forms the basis of the analyses of, e.g., McKay *et al.* (2001), Sheldon *et al.* (2004) or Mandelbaum *et al.* (2006a,c). However, the distance estimates for the source galaxies contained large uncertainties, being dived according to statistical principles, as either there was no multi-band photometry available, or, as in the case of SDSS, the depth of the observations was not sufficient to obtain reliable photometric redshifts. Precise photometric redshift knowledge is crucial in order to properly select foreground and background objects without mismatch and to disentangle intrinsic alignments between galaxies due to physical associations as for nearby galaxies from actual gravitational lensing. Further it allows to translate angular separations into physical lengths without a mixing of scales. In addition, photometric redshifts significantly facilitate the investigation of galaxy evolution with redshift and thus time, as the lens samples can be explicitly selected for their redshifts. The CFHT Legacy Wide Survey (CFHTLS-Wide) is the first survey to provide a reasonable depth in order to estimate precise photometric redshifts on a larger area (over 190 deg^2), allowing a detailed GGL study for several specific galaxy samples.

The aim of this thesis is to measure the galaxy halo properties as a function of luminosity, galaxy SED, and galaxy environment. Further we want to derive scaling relations for the basic halo parameters with luminosity for a general galaxy sample, but also discriminating early and late type galaxies. We analyze the galaxy properties for the cumulative halos, composed by individual

neighboring galaxy halos, but also for the individual galaxy halos themselves, applying maximum likelihood analyses.

The structure of this thesis is as follows. In Chapter 2 we give a basic introduction to the cosmological framework, including the definition of cosmological distances, as they are required in the gravitational lensing analyses. Chapter 3 gives an overview over the weak lensing theory, including GGL and the theoretical and technical estimation of galaxy ellipticities from imaging data. A theoretical and technical introduction to the estimation of photometric redshifts, representing the basis for the galaxy distance estimation in our lensing analysis, and a short overview about galaxies in general is given in Chapter 4. Chapter 5 contains the description of our CFHTLS-Wide dataset, including object extraction, catalog creation, photometric redshift estimation and galaxy shape extraction and the characterization of our galaxy samples. In Chapter 6 we then present our GGL analyses, comprising of measurements of the dark matter halo properties and their scaling behavior with luminosity or mass, respectively, also as a function of galaxy SED. Finally we conclude this thesis in Chapter 7.

Throughout this work we adopt a cosmology with $\Omega_M = 0.27$, $\Omega_\Lambda = 0.73$ and a dimensionless Hubble parameter $h = 0.72$, unless explicitly stated otherwise. All referred apparent magnitudes and colors are given in AB, all rest-frame magnitudes are calculated in Vega system, assuming a Hubble constant of $H_0 = 72 \text{ km s}^{-1} \text{ Mpc}^{-1}$.

Chapter 2

Cosmological Framework

This chapter gives a small overview over the cosmological framework and widely follows Schneider (2006a) and Bartelmann & Schneider (2001). An extended review can be found there or also in Schneider (2006b).

According to the Big Bang theory our Universe arose from a dense and very hot state. The Big Bang, occurring about 13.7 billion years ago, builds the starting point for the cosmic expansion history which is still observed at present time. During the expansion, the temperature cooled from values over 10^{30} K down to below 2.73 K, passing through an inflationary phase that stretched all scales to cosmic dimensions, the recombination neutralizing the Universe when atoms formed, the formation of the first stars, inducing the reionization, before larger structures like galaxies, galaxy clusters and presently super-clusters started forming.

2.1 The Homogeneous Universe

The basic assumption of cosmology is that our Universe is homogeneous and isotropic at every point without any preferred location. Considering large scales (> 200 Mpc), observations do justify this assumption. For the appropriate description of gravity in a curved space-time, General Relativity (Einstein 1914) is needed. On the other hand in a homogeneous Universe, as no section can be distinguished from another, any considered section is a valid representation of the Universe. We therefore start the description from a Newtonian vantage point and then later account for relativistic corrections (see Schneider 2006a).

2.1.1 Newtonian Ansatz

Firstly we introduce comoving coordinates

$$\mathbf{x} = \frac{\mathbf{r}(t)}{a(t)}, \quad (2.1)$$

canceling out the dependence on the scale radius $a(t)$ and hence on the cosmological expansion. The scale radius is normalized to the value of $a(t_0) = 1$ for the present time. The velocity of a particle in

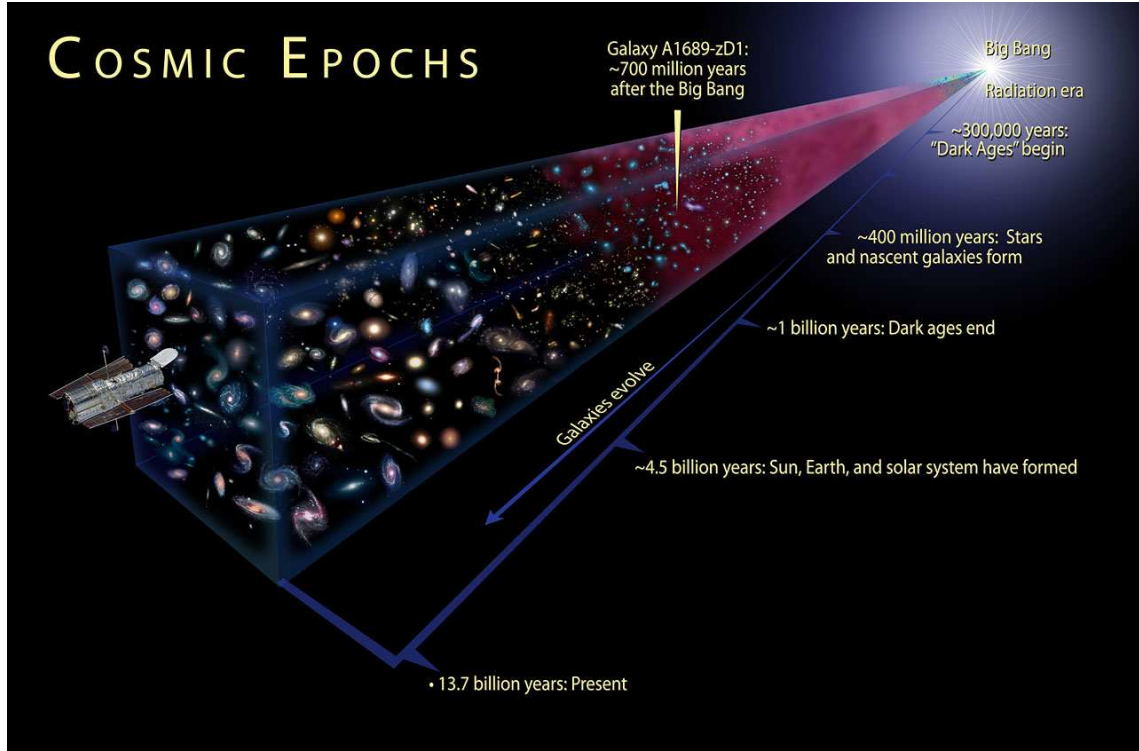


Fig. 2.1: Illustration of the cosmic evolution in the Universe since the Big Bang. (Credits for the image: http://3.bp.blogspot.com/_Rx3psh1zpCY/THe27LIxjjI/AAAAAAAAARo/uQwodUCgzag/s1600/Evolution+of+universe.jpg)

the expanding Universe is then given by

$$\mathbf{v}(t) = \frac{d\mathbf{r}(t)}{dt} = \frac{da(t)}{dt} \mathbf{x} = \dot{a} \mathbf{x} = \frac{\dot{a}}{a} \mathbf{r} = H(t) \mathbf{r}, \quad (2.2)$$

where the expansion rate of the Universe is defined as

$$H(t) := \frac{\dot{a}}{a}. \quad (2.3)$$

This leads to a relative velocity of two particles between \mathbf{r} and $\mathbf{r} + \Delta\mathbf{r}$ of

$$\Delta\mathbf{v} = \mathbf{v}(\mathbf{r} + \Delta\mathbf{r}, t) - \mathbf{v}(\mathbf{r}, t) = H(t)(\mathbf{r} + \Delta\mathbf{r}) - H(t)\mathbf{r} = H(t)\Delta\mathbf{r}. \quad (2.4)$$

We now address the dynamics of the expansion and consider for that purpose a spherical shell with comoving radius x for time t_0 and radius $r(t) = a(t)x$ for any arbitrary time. The mass within the shell is then given by

$$M(x) = \frac{4\pi}{3} \rho_0 x^3 = \frac{4\pi}{3} \rho(t) a^3 r^3(t). \quad (2.5)$$

Due to the conservation of mass, the mass density $\rho(t)$ then decreases with

$$\rho(t) = \rho_0 a^{-3}. \quad (2.6)$$

Calculating the gravitational acceleration of a particle on this spherical shell we obtain

$$\ddot{r}(t) = \frac{d^2 r(t)}{dt^2} = -\frac{GM(x)}{r^2} = -\frac{4\pi G \rho_0 x^3}{3 r^2} . \quad (2.7)$$

If we replace \dot{r} with $\dot{a}x$:

$$\ddot{a}(t) = -\frac{4\pi G \rho_0}{3} \frac{\rho_0}{a^2(t)} = -\frac{4\pi G}{3} \rho(t) a(t) , \quad (2.8)$$

multiply both sides of the equation with $2\dot{a}$

$$2\dot{a}(t)\ddot{a}(t) = -\frac{8\pi G}{3} \rho_0 \frac{\dot{a}(t)}{a^2(t)} ,$$

and integrate the whole equation over time using

$$\frac{d}{dt} \dot{a}^2(t) = 2\dot{a}(t)\ddot{a}(t) \quad \text{and} \quad \frac{d}{dt} \frac{1}{a(t)} = -\frac{\dot{a}(t)}{a^2(t)} ,$$

we receive

$$\dot{a}^2(t) = \frac{8\pi G}{3} \rho_0 \frac{1}{a(t)} - Kc^2 = \frac{8\pi G}{3} \rho(t) a^2 t - Kc^2 , \quad (2.9)$$

with Kc^2 being a constant of integration. We will see later that the constant of integration can be interpreted as the curvature of the space in General Relativity. We rewrite equation (2.9) by multiplying with $x^2/2$. With

$$v(t) = \dot{r}(t) = \dot{a}(t)x$$

we obtain

$$\frac{v^2(t)}{2} - \frac{GM}{r} = -Kc^2 . \quad (2.10)$$

The left side of this equation is the sum of kinetic and potential energy of a particle and is therefore conserved. We see that the future behavior of the Universe concerning expansion depends on the value of K . For negative K the right side of equation (2.9) is always positive, which means that the derivative of the scale factor $a(t)$ with respect to time is positive at all times and the expansion of the Universe will never stop. The same conclusion follows for $K = 0$. If K is positive the right side of equation (2.9) vanishes for $a = a_{\max} = (8\pi G \rho_0)/(3Kc^2)$, for larger values of K the Universe will eventually recollapse. In the special case of $K = 0$, the present value of the density of the Universe is called the critical density

$$\rho_c := \frac{3H_0}{8\pi G} . \quad (2.11)$$

2.1.2 Relativistic Extension

General Relativity modifies the Newtonian theory in several aspects. Matter with pressure changes the equations of motions. Further Einstein's field equations (2.12) (see Einstein 1915) introduce the cosmological constant Λ . Finally, the interpretation of expansion of the Universe is changed as it is not the particles in space which move apart, but it is the space itself which is expanding. The Universe is now described, as already mentioned, by Einstein's field equations

$$G_{\mu\nu} = -\frac{8\pi G}{c^4} T_{\mu\nu} - \Lambda g_{\mu\nu} , \quad (2.12)$$

with $G_{\mu\nu}$ being the Einstein Tensor that represents the geometry of space-time, $T_{\mu\nu}$ the energy-momentum tensor which describes the energy content, the cosmological constant Λ and the metric tensor $g_{\mu\nu}$. The space-time in a homogeneous and isotropic Universe is described by the Robertson-Walker metric

$$ds^2 = c^2 dt^2 - a^2(t) [d\chi^2 + f_K^2(\chi) (d\theta^2 + \sin^2\theta d\phi^2)], \quad (2.13)$$

which solves the field equations as has been shown independently by Robertson (1935) and Walker (1937). The coordinate system is given by the spherical coordinates (χ, θ, ϕ) with χ being the comoving radial coordinate and θ and ϕ being the angular ones. The factor $f_K(\chi)$ is called the comoving angular diameter distance and depends on the curvature K :

$$f_K(\chi) = \begin{cases} K^{-1/2} \sin(K^{1/2}\chi) & K > 0 \\ \chi & K = 0 \\ (-K)^{-1/2} \sinh[(-K)^{1/2}\chi] & K < 0, \end{cases} \quad (2.14)$$

where $1/\sqrt{K}$ can be interpreted as the curvature radius of the space. For vanishing curvature $K = 0$, the Robertson-Walker metric (see equation 2.13) describes the metric of a plane, for positive curvature $K > 0$ it describes the metric of a sphere and for negative curvature $K < 0$ it describes the metric of a pseudosphere with negative curvature which can locally be approximated by a hyperboloid. Inserting the Robertson-Walker metric (equation 2.13) into the field equations of General Relativity the energy-momentum tensor is restricted to the form of a perfect fluid with density $\rho(t)$ and pressure $p(t)$. The solution of the equation then leads to the generalization of the previously derived equations (2.9) and (2.8) to

$$\left(\frac{\dot{a}}{a}\right)^2 = \frac{8\pi G}{3}\rho - \frac{Kc^2}{a^2} + \frac{\Lambda}{3} \quad (2.15)$$

and

$$\frac{\ddot{a}}{a} = -\frac{4\pi G}{3}\left(\rho + \frac{3p}{c^2}\right) + \frac{\Lambda}{3}. \quad (2.16)$$

Equations (2.15) and (2.16) are called the *Friedmann equations* (see Friedmann 1924). These two equations can be combined to obtain the *adiabatic equation*:

$$\frac{d}{dt} [a^3(t)\rho(t)c^2] + p(t) \frac{da^3(t)}{dt} = 0. \quad (2.17)$$

What does this equation tell us about the characteristic behavior of the matter content? For pressureless matter (dust), the derivative of the product of density and scale radius to the third power vanishes, implying the conservation of mass. This confirms the decrease of mass density with

$$\rho_m = \rho_{m0} a^{-3} \quad (2.18)$$

as already derived in equation (2.6) in the Newtonian ansatz. For matter with pressure the adiabatic equation (2.17) implies that the variation of energy is equal to the product of pressure and variation of volume

$$\frac{d}{dt}(c^2 \rho a^3) = -p \frac{da^3}{dt}. \quad (2.19)$$

In the limiting case of relativistic particles with velocities close to or equal c (radiation), the pressure is given by

$$p = \frac{\rho c^2}{3}. \quad (2.20)$$

If we insert this relation into the adiabatic equation (2.17), we see that the energy density for radiation evolves with

$$\rho_r = \rho_{r0} a^{-4}. \quad (2.21)$$

Since the photon number density decreases with a^{-3} but the energy density decreases with a^{-4} , it is obvious that the individual photon energy must decrease with a^{-1} . This accommodates the fact that the photon is redshifted due to the expansion of space.

If we now consider a component which can be interpreted as vacuum energy and whose density is independent of time, the adiabatic equation gives us

$$p_v = -\rho_v c^2. \quad (2.22)$$

This means that the matter density and pressure in the Universe are composed by the sum of these three components

$$\rho = \rho_m + \rho_r + \rho_v = \rho_{m0} a^{-3} + \rho_{r0} a^{-4} + \rho_v \quad \text{and} \quad p = \frac{\rho_r c^2}{3} - \rho_v c^2 = \frac{\rho_{r0} c^2}{3a^4} - \rho_v c^2. \quad (2.23)$$

If we insert this result into the Friedmann equations (2.15) and (2.16), we see that the form of the ρ_v -term corresponds to the Λ -term, therefore Λ can be interpreted as a vacuum energy density with

$$c^2 \rho_v = \frac{c^2 \Lambda}{8\pi G}. \quad (2.24)$$

Based on the derived densities we define the density parameters

$$\Omega_m = \frac{\rho_{m0}}{\rho_c}, \quad \Omega_r = \frac{\rho_{r0}}{\rho_c} \quad \text{and} \quad \Omega_\Lambda = \frac{\rho_v}{\rho_c} = \frac{\Lambda}{3H_0^2}. \quad (2.25)$$

Using these definitions we can rewrite the expansion equation (2.15) as

$$H^2(t) = H_0^2 \left(a^{-4} \Omega_r + a^{-3} \Omega_m - a^{-2} \frac{Kc^2}{H_0^2} + \Omega_\Lambda \right). \quad (2.26)$$

As for the present time, $\Omega_r \ll \Omega_m$, we obtain for the curvature

$$K = \left(\frac{H_0}{c} \right)^2 (\Omega_m + \Omega_\Lambda - 1). \quad (2.27)$$

If we reinsert this result back to the expansion equation (2.26) we derive following expansion equation:

$$H^2(t) = H_0^2 [a^{-4} \Omega_r + a^{-3} \Omega_m + a^{-2} (1 - \Omega_m - \Omega_\Lambda) + \Omega_\Lambda]. \quad (2.28)$$

We see that for small scale radii a the first term is dominating, which means that the Universe is radiation-dominated. For larger values, the second term is eventually dominating, the Universe is then matter-dominated. For a not vanishing curvature and even larger values of a the third term, the curvature term is dominating and for very large values of the scale radius the cosmological constant becomes dominant. The evolution of the expansion rate $H(z)$ starting at redshift $z = 9$ is shown in Fig. 2.2.

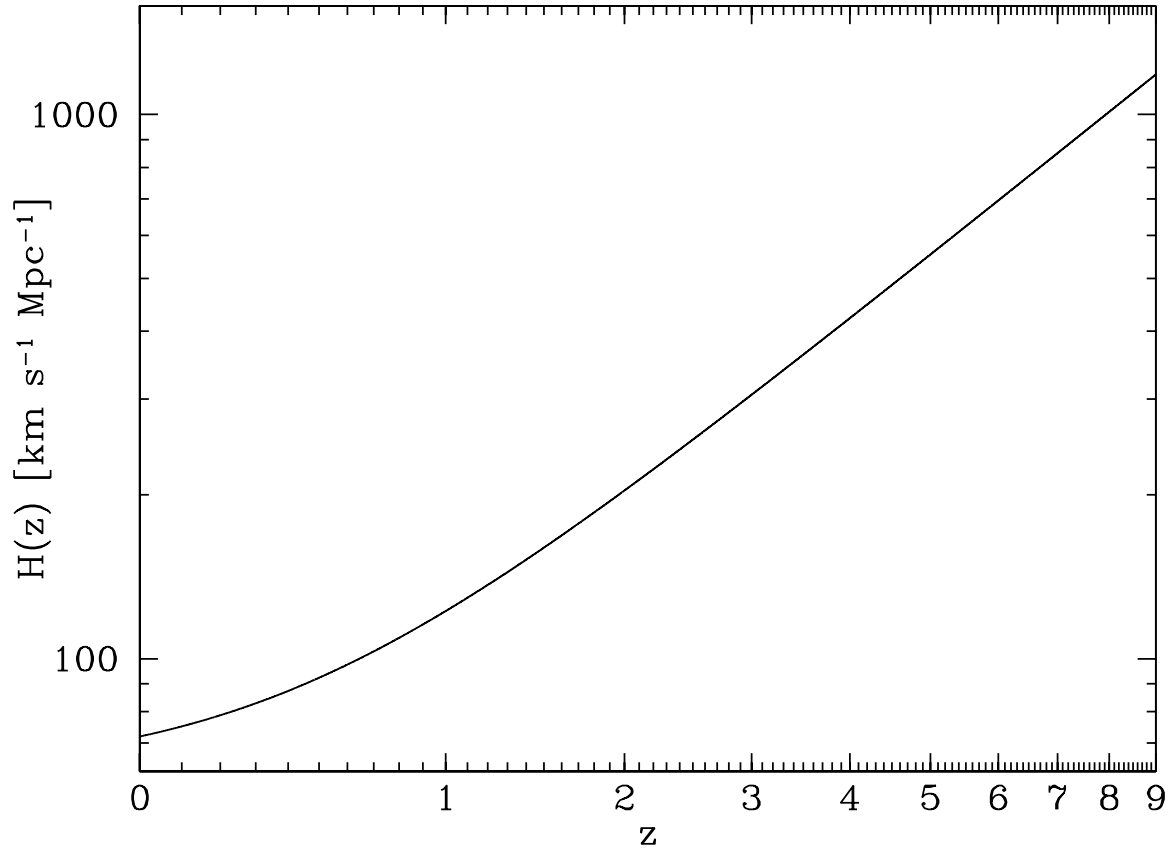


Fig. 2.2: Evolution of the expansion rate $H(z)$ with redshift up to $z = 9$. The chosen cosmological parameters are $H_0 = 72 \text{ km s}^{-1} \text{ Mpc}^{-1}$, $\Omega_m = 0.27$ and $\Omega_\Lambda = 0.73$.

2.1.3 Cosmological Redshift

The expansion of the Universe leads to a redshift of the light emitted by distant sources. The redshift z is defined as

$$z := \frac{\lambda_a - \lambda_e}{\lambda_e} = \frac{a(t_a)}{a(t_e)} - 1, \quad (2.29)$$

with λ_e being the wavelength at the emission time t_e and λ_a being the wavelength at the absorption time t_a or

$$z = a^{-1} - 1 \quad (2.30)$$

for present time $t = t_0$. This energy loss for the individual photon has already been predicted in equation (2.21).

2.1.4 Distances

In the following we have to define a concept of distances. Given the fact that our Universe in general might be curved and that the light speed is finite, which can lead to a remarkable time shift between

the two final points of the distance measurement, the term *distance* is not unambiguous anymore but depends on our definition.

Comoving Distance

The comoving distance describes the distance of two points on the spatial hypersurface of the Universe at present time $t = t_0$. The underlying grid follows the expansion of the Universe, therefore the comoving distance between two events is fixed and does not depend on time, i.e., the expansion of the Universe. The comoving distance is defined in the following way:

$$c dt = -a\chi \quad \text{or} \quad \chi = \int_{t_2}^{t_1} \frac{c}{a} dt, \quad (2.31)$$

with t_2 being the emission time and t_1 the absorption time. This leads to

$$\chi(z_1, z_2) = \frac{c}{H_0} \int_{z_1}^{z_2} dz' \left[\Omega_r (1+z')^4 + \Omega_m (1+z')^3 + (1 - \Omega_m - \Omega_\Lambda) (1+z')^2 + \Omega_\Lambda \right]^{-1}. \quad (2.32)$$

A special case is given by the proper distance, which is only mentioned for reasons of completeness. The proper distance gives the distance observers at a certain redshift would measure themselves using, e.g., rulers. It is given by

$$D_{\text{prop}}(z_1, z_2) = a(z_1) [\chi(z_1, z_2)]. \quad (2.33)$$

At present time the proper distance is identical to the comoving distance.

Angular Diameter Distance

A further very important concept of distance is given by the angular diameter distance. It gives us the relation between the physical size of an object ($2R$) and the angle δ under which it is observable on the sky:

$$D_{\text{ang}} = \frac{2R}{\delta} = a(z) f_K(\chi). \quad (2.34)$$

The angular diameter distance between two redshifted objects is given by

$$D_{\text{ang}}(z_1, z_2) = a(z_2) f_K[\chi(z_1, z_2)]. \quad (2.35)$$

An interesting aspect about the angular diameter distance is that it does not increase infinitely with redshift but reaches a maximum beyond which it starts decreasing again. For a cosmology with $\Omega_m = 0.27$, $\Omega_\Lambda = 0.73$ and $H_0 = 72 \text{ km s}^{-1} \text{ Mpc}^{-1}$ this maximum is at a redshift of $z \approx 1.6$. This can be seen in Fig. 2.3.

Luminosity distance

Finally the luminosity distance gives the decrease of flux with increasing distance. While in Euclidean space the flux decreases with the inverse square of the distance, in a curved or expanding space this is not the case in general for the comoving or the angular diameter distance. The luminosity distance is given by

$$D_{\text{lum}}(z) = \sqrt{\frac{L}{4\pi S}}, \quad (2.36)$$

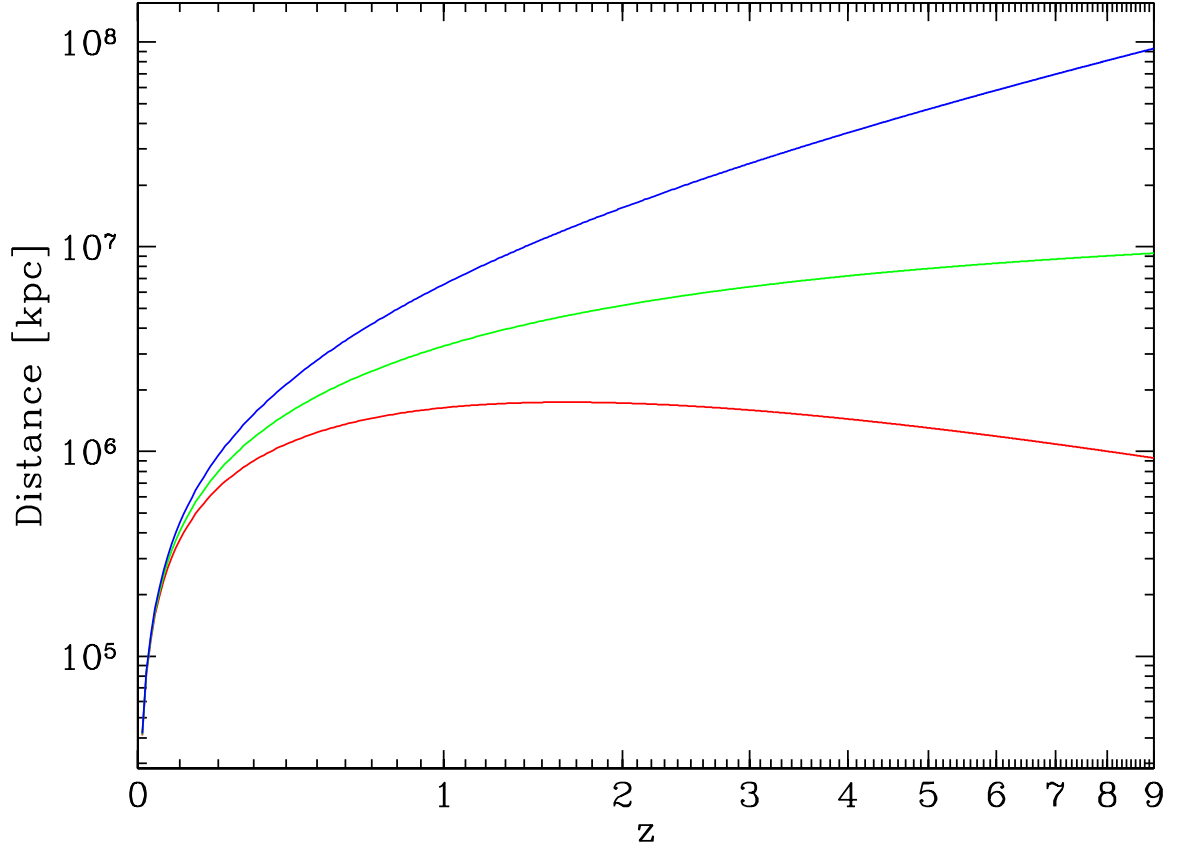


Fig. 2.3: Different distances as a function of the redshift for a cosmology with $\Omega_m = 0.27$, $\Omega_\Lambda = 0.73$ and $H_0 = 72 \text{ km s}^{-1} \text{ Mpc}^{-1}$. The red line shows the angular diameter distance with maximum value at $z \approx 1.6$, whereas the green line shows the comoving distance and the blue line shows the luminosity distance.

with L being the luminosity and S the Flux. Etherington (1933) showed that in general the luminosity distance is related to the comoving and the angular diameter distance in the following way:

$$D_{\text{lum}}(z) = (1+z)^2 D_{\text{ang}}(z) = (1+z) f_K(\chi). \quad (2.37)$$

This relation is only correct for bolometric quantities. If fluxes at specific wavelength ranges are considered, a K-correction depending the spectrum of the sources needs to be applied to account for the cosmological redshift.

Distance Modulus

Another important quantity is represented by the distance modulus which describes the difference between absolute magnitude (defined as the magnitude in a distance of 10 pc) and apparent magnitude, representing the application of the luminosity distance if magnitudes are used instead of fluxes. The distance modulus is given by

$$\text{DM} = 5 \log \left(\frac{D_{\text{lum}}}{10 \text{ pc}} \right). \quad (2.38)$$

2.2 The Inhomogeneous Universe

The previous section described the homogeneous characteristics in the Universe present on large scales. But as we observe, the Universe is far from being homogeneous on shorter scales. Otherwise there would be no galaxies, stars and other structures. The question is now how the matter could collapse and structure, transforming the initially almost homogeneous Universe into the cosmos we observe today. A possible answer is given by the inflation theory. It gives an explanation to flatness and homogeneity over large distances and the correlation of fluctuations on causally disconnected scales on the sky and further provides a source for the primordial density fluctuations. According to inflation theory the visible Universe was initially small with causal contact between the presently visible regions before an exponential expansion set in, enlarging the Universe by many orders of magnitude. The homogeneity of the Universe is therefore explained by the circumstance that the observable Universe initially was only of small size in causal contact. The origin of the inhomogeneities eventually rising to the structure we observe today is then given by quantum fluctuations which have been stretched to cosmic scales during the inflationary expansion. The smallness of the cosmic microwave background (CMB) anisotropy ($\Delta T/T \sim 10^{-5}$, see Smoot *et al.* 1992) suggests that the density inhomogeneities were still very small at the time of recombination ($z \sim 1100$). The density contrast is defined as

$$\delta(\mathbf{r}, t) = \frac{\rho(\mathbf{r}, t) - \bar{\rho}(t)}{\bar{\rho}(t)}, \quad (2.39)$$

with $\bar{\rho}(t)$ being the mean density of the Universe. In underdense regions the density contrast is $-1 \leq \delta < 0$, in overdense regions the density contrast is $\delta > 0$. In overdense regions the gravitational self-attraction will lead to a slower expansion than in the average regions. This causes the density contrast to increase even further. On the other hand, the lower self-gravity in underdense regions results in faster expansion and hence in a decreasing density contrast in these regions. This gravitational instability builds the starting point for structure formation.

2.2.1 Linear Structure Formation

As we have seen in Section 2.1 the matter in the Universe can be described as a perfect fluid. It is characterized by the density $\rho(\mathbf{r}, t)$ and the velocity field $\mathbf{v}(\mathbf{r}, t)$ and is described by the following equations. The continuity equation

$$\frac{\partial \rho}{\partial t} + \nabla \cdot (\rho \mathbf{v}) = 0 \quad (2.40)$$

indicates that mass is conserved. If the fluid has a divergent velocity field, meaning that particles are streaming out, the density decreases. On the other hand, if the fluid has a convergent velocity field with particles streaming in, the density has to increase. Further the fluid follows the Euler equation

$$\frac{\partial \mathbf{v}}{\partial t} + (\mathbf{v} \cdot \nabla) \mathbf{v} = -\frac{\nabla p}{\rho} - \nabla \Phi. \quad (2.41)$$

The left side is the derivative of the velocity with respect to time as it is perceived by an observer flowing with the current. It is influenced by the pressure gradient and the gravitational potential Φ which is described by the Poisson equation

$$\nabla^2 \Phi = 4\pi G \rho. \quad (2.42)$$

As we only consider non-radiative matter the pressure vanishes $p \equiv 0$. In general these three equations cannot be solved, but it can be shown that the homogeneous expanding Universe represents a solution to this system of equations for a homogeneous density distribution ρ decreasing with a^{-3} (see equation 2.18) and a velocity field $\mathbf{v}(\mathbf{r}, t) = H(t) \mathbf{r}$. We now apply the ansatz of linear perturbation theory, adding a small perturbation $\delta\rho$, $\delta\mathbf{v}$ and $\delta\Phi$ to the unperturbed quantities in order to obtain the perturbed equation system. If we now subtract the unperturbed equations from the perturbed ones, neglecting all terms of higher than first order, we get the following system of equations:

$$\left(\frac{\partial}{\partial t} + \mathbf{v}_0 \nabla \right) \delta + \nabla \cdot \delta\mathbf{v} = 0, \quad (2.43)$$

with $\delta \equiv \delta\rho/\rho_0$. The Euler equation then becomes

$$\left(\frac{\partial}{\partial t} + \mathbf{v}_0 \nabla \right) \delta\mathbf{v} + \frac{\nabla \delta p}{\rho_0} + \nabla \delta\Phi + H \delta\mathbf{v} = 0, \quad (2.44)$$

and the Poisson equation becomes

$$\nabla^2 \delta\Phi = 4\pi G \rho_0 \delta. \quad (2.45)$$

It is now convenient to continue in comoving coordinates. The coordinates are then described by

$$\mathbf{x} = \frac{\mathbf{r}}{a(t)}$$

and

$$\mathbf{v}(t) = \frac{\dot{a}}{a} \mathbf{r} + \mathbf{u} \left(\frac{\mathbf{r}}{a}, t \right),$$

with \mathbf{u} being the peculiar velocity. The subsequently transformed equations can be used to eliminate the peculiar velocity \mathbf{u} and the gravitational potential Φ . We then obtain a differential equation of second-order in δ :

$$\frac{\partial^2 \delta}{\partial t^2} + \frac{2\dot{a}}{a} \frac{\partial \delta}{\partial t} = 4\pi G \rho_0 \delta. \quad (2.46)$$

As equation (2.46) does not contain spatial derivatives, the solutions can be factorized in the following way:

$$\delta(\mathbf{x}, t) = D(t) \tilde{\delta}(\mathbf{x}). \quad (2.47)$$

We then get a solution of the form

$$\delta(\mathbf{x}, t) = D_+(t) \delta_+(\mathbf{x}) + D_-(t) \delta_-(\mathbf{x}), \quad (2.48)$$

with D_+ representing a growing and D_- representing a decaying mode. As the decaying mode D_- is decreasing with time, eventually the growing mode will be dominating and the decaying mode can be neglected. Therefore we only consider the growing mode, following

$$\delta(\mathbf{x}, t) = D_+ \delta_0(\mathbf{x}), \quad (2.49)$$

where D_+ , also called the growth factor, has been normalized to $D_+(t_0) = 1$. The actual form of the growth factor depends on the cosmological density parameters. It can be explicitly calculated for different cosmologies. In an Einstein-de Sitter (EdS) universe ($\Omega_m = 1$ and $\Omega_\Lambda = 0$), for instance, the growth factor is identical to the scale factor $a(t)$.

2.2.2 Correlation Function and Power Spectrum

As the Universe is not homogeneous on shorter scales anymore, the probability of finding galaxies at certain points is not uniform, as due to matter collapse and structure formation the matter in the Universe started to cluster. The clustering properties and the probability of finding objects like galaxies in the neighborhood of other galaxies can be described by the two-point-correlation function or equivalently by the power spectrum.

The Correlation Function

The correlation function describes the distribution of matter in the Universe. For instance, let the probability to find a galaxy in the volume dV at position \mathbf{x} be given by P_1 . As the Universe is statistically homogeneous this probability does not depend on position. Consequently the probability to find this galaxy and another galaxy in the volume dV at position \mathbf{y} simultaneously would be P_1^2 if the probabilities were independent. Due to structural collapse matter started to cluster and therefore its distribution is correlated. To account for this increased probability a (two-point-)correlation function has to be introduced, correcting the probability P_1^2 to $P_1^2[1 + \xi_g(\mathbf{x}, \mathbf{y})]$. The correlation function $\xi(\mathbf{x}, \mathbf{y})$ can be defined for the complete matter distribution by the following equation:

$$\langle \rho(\mathbf{x})\rho(\mathbf{y}) \rangle = \bar{\rho}^2 \langle [1 + \delta(\mathbf{x})][1 + \delta(\mathbf{y})] \rangle = \bar{\rho} [1 + \langle \delta(\mathbf{x})\delta(\mathbf{y}) \rangle] =: \bar{\rho} [1 + \xi(\mathbf{x}, \mathbf{y})] , \quad (2.50)$$

with $\xi(\mathbf{x}, \mathbf{y})$ being the correlation function. Because of homogeneity and isotropy of the Universe the correlation function does not depend on the explicit values of \mathbf{x} and \mathbf{y} but only on their spatial separation $r = |\mathbf{x} - \mathbf{y}|$.

The Power Spectrum

The power spectrum provides a description of structure in the Universe which is equivalent to the two-point-correlation function. It can be calculated from the two-point-correlation-function by Fourier transformation:

$$P(k) = 2\pi \int_0^\infty dr r^2 \frac{\sin kr}{kr} \xi(r) . \quad (2.51)$$

Having a look at the primordial power spectrum originally there was no natural characteristic length scale given in the Universe. This suggests that the primordial power spectrum can be written in the form of a power law $P_k \propto k^n$ as this is the only mathematical function which does not depend on a characteristic scale.

Dark Matter

As already mentioned, CMB shows an anisotropy of only about $\Delta T/T \sim 10^{-5}$ (Smoot *et al.* 1992), displaying the conditions at the time of recombination ($z \sim 1100$). Having a look at the inhomogeneity which is observable at present time and assuming only baryonic matter one would expect a much higher anisotropy of $\Delta T/T \sim 10^{-3}$. A solution to this discrepancy is provided by the introduction of dark matter. CMB only mirrors the anisotropies present in radiative matter and matter coupling to it (this means photons and electromagnetically interacting particles). Uncharged dark matter particles could have decoupled from the photon plasma at earlier times and already started to cluster before recombination. After recombination the baryonic matter then fell into the potential well already formed by the dark matter.

2.2.3 Non-Linear Structure Growth

The linear structure formation theory is based on perturbation theory and is only valid for small perturbations. If the density contrast exceeds a value of $|\delta| \sim 1$ the linear structure formation theory breaks down and the neglected terms of higher order cannot be ignored anymore. In general the problem can no longer be treated analytically and needs to be addressed by numerical simulations.

The Spherical Collapse Model

We consider a spherical region in the Universe with increased matter density

$$\rho(t) = [1 + \delta(t)] \bar{\rho}(t), \quad (2.52)$$

with respect to the mean density of the Universe and with $\delta(t)$ as defined in equation (2.39). For small times t the perturbation is still small so we can treat its growth linearly. We consider an early point in time t_i where

$$\delta(t_i) \ll 1 \quad \text{and} \quad \delta(t_i) = \delta_0 D_+(t_i), \quad (2.53)$$

with δ_0 being the extrapolated linear value for δ at present time (actually $\delta_0 \neq \delta(t_0)$ because non-linear effects will change the evolution of the structure!). The initial comoving radius R_{com} of the overdense region will remain nearly unchanged as long the perturbation is still small ($\delta \ll 1$). The mass within this sphere is then given by

$$M = \frac{4\pi}{3} R_{\text{com}}^3 \rho_0 (1 + \delta_i) \approx \frac{4\pi}{3} R_{\text{com}}^3 \rho_0, \quad (2.54)$$

with physical radius $R = aR_{\text{com}}$ and $\rho_0 = a^{-3}\bar{\rho}$. The sphere will expand slower than the average Universe due to its own gravity, enhancing the density contrast δ and therefore further decelerating the expansion. Due to symmetry reasons the expansion of the sphere can be described equivalently to the cosmic expansion using the Friedmann equations (2.15) and (2.16) but with different density parameters. Depending on δ_i , the critical density can be exceeded, eventually leading to a halt of the expansion of the sphere and resulting in its recollapse. In an ideal theory the sphere would recollapse into a single point but in practice the particles inside the sphere do not follow purely radial trajectories due to small scale fluctuations in density and gravity. The collapse will therefore lead to an overdense virialized structure with characteristic radius r_{vir} and a mean density of

$$\langle \rho \rangle = (1 + \delta_{\text{vir}}) \quad \text{with} \quad (1 + \delta_{\text{vir}}) \simeq 178 \Omega_{\text{m}}^{-0.6}. \quad (2.55)$$

For this reason the r_{200} , defined as the radius of a structure with mean density $\bar{\rho} = 200\rho_c$ is used as an approximate value for the virial radius r_{vir} . In the special case of an Einstein-de Sitter universe every sphere with $\delta_0 > 0$ represents a ‘closed Universe’ that will eventually recollapse. Nonetheless a threshold has to be exceeded to make the collapse happen before a given time t_1 . This threshold is given by

$$\delta_0 \geq \delta_c (1 + z) = \frac{3}{20} (12\pi)^{2/3} (1 + z) \simeq 1.69 (1 + z) \quad (2.56)$$

for the collapse to occur before redshift z .

Press-Schechter Model

The spherical collapse model (see Press & Schechter 1974) provides the opportunity to estimate the number density of dark matter halos. The starting point is a density fluctuation field $\delta(\mathbf{x})$ with fluctuations on all scales corresponding to the power spectrum $P_0(k)$. We now smooth this density fluctuation field by convolving it with a filter function with a comoving filter scale of R . Linearly extrapolated to present time we receive the smoothed density fluctuation field $\delta_R(\mathbf{x})$ without fluctuations on scales $\lesssim R$. Therefore any maximum of the density fluctuation field goes along with a characteristic scale of $\gtrsim R$ and a corresponding mass peak $M \sim (4\pi r^3/3)\rho_0$ according to equation (2.54). For sufficient amplitude δ_R a sphere with comoving radius R around the peak will decouple from linear structure growth and start growing non-linearly. The following growth and subsequent recollapse can be approximated by the spherical collapse model. For Gaussian characteristic properties of the density fluctuation field its attributes are described by the power spectrum $P(k)$ and the number density of density maxima with $\delta_R \geq \delta_{\min}$ and therefore the number density $n(M, z)$ of relaxed dark matter haloes with respect to mass M and redshift z can be calculated. The number density depends on several variables. Firstly, it depends on the amplitude of the density fluctuations, i.e., it depends on the normalization of the power spectrum $P_0(k)$ which can be determined by comparison of the Press-Schechter prediction with the observed number density of galaxy clusters. This is called ‘cluster-normalized power spectrum’. Further the number density $n(M, z)$ decreases exponentially with increasing mass M , as larger masses correspond to higher smoothing lengths and the number of maxima with fixed amplitude δ_{\min} decreases with increasing smoothing length. The number density of massive galaxy clusters with $M \geq 10^{15} M_\odot$ is therefore quite low (10^{-7} Mpc^{-3}) corresponding to a mean distance of 100 Mpc between two clusters. The redshift dependence of the number density $n(M, z)$ depends on the considered cosmology. The general minimal density contrast is given by $\delta_{\min} = \delta_c/D_+(z)$ (see Einstein-de Sitter universe in equation 2.56) with δ_c and D_+ depending on the cosmology. As D_+ is larger for lower Ω_m at fixed z with $z > 0$, the ratio in number density $n(M, z)/n(M, 0)$ increases with decreasing Ω_m . We now consider the case where the power spectrum can be described with a power law $P_0 \propto k^n$. In this case the mass function can be written in a closed form:

$$n(M, z) = \frac{\rho_c \Omega_m}{\sqrt{\pi}} \frac{\gamma}{M^2} \left(\frac{M}{M^*(z)} \right)^{\gamma/2} \cdot \exp \left[- \left(\frac{M}{M^*(z)} \right)^\gamma \right], \quad (2.57)$$

with the redshift-dependent mass scale

$$M^*(z) = M_0^* [D_+(z)]^{2/\gamma} \left(= M_0^* (1+z)^{-2/\gamma} \text{ for an Einstein-de Sitter universe} \right) \quad (2.58)$$

and $\gamma = 1 + n/3$. The characteristic mass scale is increasing, describing the mass scale where a mass distribution starts to grow non-linearly. The mass spectrum well below $M^*(z)$ is basically a power law while masses above the characteristic mass scale are cut off exponentially. Although being a rather simple model the Press-Schechter model agrees surprisingly well with the prediction of numerical simulations. More sophisticated Press-Schechter models based on elliptical collapse models are even able to compete against the latest numerical simulations.

Chapter 3

Lensing Theory

This chapter gives a short overview over the lensing and weak lensing theory and widely follows Schneider (2006b) and Bartelmann & Schneider (2001). An extended review can be found there or, e.g., in Schneider *et al.* (1992).

3.1 Gravity

Gravity is the most noticeable of the four fundamental interactions in daily life, it explains why the apple falls to the ground, why we are bound to Earth, why Earth orbits sun and why stellar systems form galaxies or even larger structures. But does it not only affect matter, also light rays are deflected by gravitational attraction. In 1914/15 Albert Einstein introduced General Relativity (see Einstein 1914, 1915) replacing the theory developed by Isaac Newton and correcting the deflection by a factor of 2. For a spherically symmetric mass distribution, General relativity in the weak field limit predicts the deflection angle $\hat{\alpha}$ to be

$$\hat{\alpha} = \frac{4GM}{c^2\xi}, \quad (3.1)$$

where G is the gravitational constant, M is the total mass of the mass distribution and ξ is the impact parameter. As long as the impact parameter ξ is much larger than the Schwarzschild radius $R_S \equiv 2GM/c^2$, leading to a small value for the deflection angle $\hat{\alpha} \ll 1$, the gravitational field strength is small and the field equations of general relativity can be linearized. This means that the deflection angle of an ensemble of mass points can be described by the vectorial sum of the deflection angles caused by the individual mass points. The deflection angle $\hat{\alpha}$ of a light ray described by the spatial trajectory $(\xi_1(\lambda), \xi_2(\lambda), r_3(\lambda))$, propagating along r_3 , caused by a mass distribution

$$M = \sum dm = \sum \rho(r) dV \quad (3.2)$$

is therefore described by

$$\hat{\alpha}(\xi) = \frac{4G}{c^2} \sum dm(\xi'_1, \xi'_2, r'_3) \frac{\xi - \xi'}{|\xi - \xi'|^2} = \frac{4G}{c^2} \int d^2 \xi' \int dr'_3 \rho(\xi'_1, \xi'_2, r'_3) \frac{\xi - \xi'}{|\xi - \xi'|^2}. \quad (3.3)$$

Using the definition of the surface mass density

$$\Sigma(\xi) \equiv \int dr_3 \rho(\xi_1, \xi_2, r_3) \quad (3.4)$$

and the independence of the last factor from r'_3 , we carry out the r'_3 -integration and obtain

$$\hat{\alpha}(\xi) = \frac{4G}{c^2} \int d^2 \xi' \Sigma(\xi) \frac{\xi - \xi'}{|\xi - \xi'|^2}. \quad (3.5)$$

3.2 The Lens Equation

A typical situation for a (single) gravitational deflection is shown in Fig. 3.1. An object at distance D_s and redshift z_s (source plane) emits light rays. The light rays traveling in direction of the observer pass close to a mass distribution at distance D_d and redshift z_d (lens plane) and are deflected. Source and lens plane are defined to be perpendicular to the line of sight. Assuming that the extent of the deflecting mass is much smaller than the distances D_d and D_{ds} , the trajectory of the light rays can be replaced by two straight lines with a sharp bend in the lens plane. In this figure η stands for the two-dimensional position of the source in the source plane. The corresponding angle would be β . Due to the gravitational deflection the image appears under an angle θ which corresponds to the impact vector ξ in the lens plane. $\hat{\alpha}$ is the deflection angle in the lens plane. Making use of the smallness of the deflection angle $\hat{\alpha}$ we derive from geometrical considerations (intercept theorem)

$$\frac{\eta + D_{ds} \hat{\alpha}(\xi)}{\xi} = \frac{D_s}{D_d}$$

or

$$\eta = \frac{D_s}{D_d} \xi - D_{ds} \hat{\alpha}(\xi).$$

If we translate this equation into an angular coordinate system using

$$\xi = D_d \theta \quad \text{and} \quad \eta = D_s \beta$$

we obtain

$$\beta = \theta - \frac{D_{ds}}{D_s} \hat{\alpha}(D_d \theta) \equiv \theta - \alpha(\theta), \quad (3.6)$$

defining $\alpha(\theta)$ as the scaled deflection angle.

Introducing the dimensionless surface mass density or convergence

$$\kappa(\theta) := \frac{\Sigma(D_d \theta)}{\Sigma_c} \quad (3.7)$$

with the critical surface mass density

$$\Sigma_c = \frac{c^2}{4\pi G} \frac{D_s}{D_d D_{ds}} \quad (3.8)$$

we can transform equation (3.5) into

$$\alpha(\theta) = \frac{1}{\pi} \int_{\mathbb{R}^2} d^2 \theta' \kappa(\theta') \frac{\theta - \theta'}{|\theta - \theta'|^2} \quad (3.9)$$

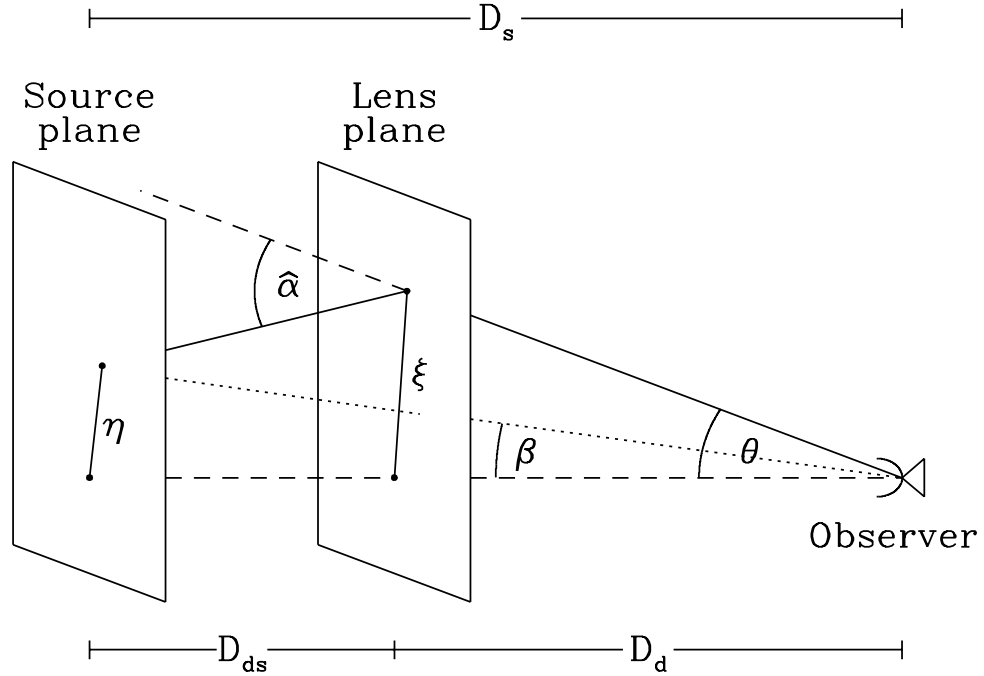


Fig. 3.1: Typical situation for a gravitational lens system. An object in the source plane emits lights rays and would be visible under an angle of β . On their way to the observer the light bundles are deflected by a mass distribution in the lens plane by an angle of $\hat{\alpha}$ and finally appear under an angle of θ .

in order to express the scaled deflection angle in terms of the surface mass density.

Now we can make use of the identity $\nabla \ln |\boldsymbol{\theta}| = \boldsymbol{\theta}/|\boldsymbol{\theta}|^2$, which is valid for any two-dimensional vector $\boldsymbol{\theta}$. Consequently the scaled deflection angle can be written as the gradient of a deflection potential ψ :

$$\boldsymbol{\alpha}(\boldsymbol{\theta}) = \nabla \psi(\boldsymbol{\theta}) \quad (3.10)$$

with

$$\psi(\boldsymbol{\theta}) = \frac{1}{\pi} \int_{\mathbb{R}^2} d^2\theta' \kappa(\boldsymbol{\theta}') \ln |\boldsymbol{\theta} - \boldsymbol{\theta}'|. \quad (3.11)$$

Furthermore if we use the identity

$$\nabla^2 \ln |\boldsymbol{\theta}| = 2\delta(\boldsymbol{\theta}), \quad (3.12)$$

with $\delta(\boldsymbol{\theta})$ being the Dirac delta function, we obtain

$$\nabla^2 \psi(\boldsymbol{\theta}) = 2\kappa(\boldsymbol{\theta}), \quad (3.13)$$

the Poisson equation in two dimensions.

As the light bundles are deflected differentially, in general the shapes of source and image will differ. If the source is much smaller than the scale where the lens properties change, the mapping from source to image plane can be locally linearized. The distortions are then described by the Jacobian Matrix (Schneider 2006b, Seitz *et al.* 1994)

$$\mathcal{A}(\boldsymbol{\theta}) = \frac{\partial \boldsymbol{\beta}}{\partial \boldsymbol{\theta}} = \left(\delta_{ij} - \frac{\partial^2 \psi(\boldsymbol{\theta})}{\partial \theta_i \partial \theta_j} \right) = \begin{pmatrix} 1 - \kappa - \gamma_1 & -\gamma_2 \\ -\gamma_2 & 1 - \kappa + \gamma_1 \end{pmatrix}, \quad (3.14)$$

introducing the shear $\gamma \equiv \gamma_1 + i\gamma_2 = |\gamma|e^{i2\phi}$ with the components

$$\gamma_1 = \frac{1}{2} \left(\frac{\partial \psi}{\partial \theta_1^2} - \frac{\partial \psi}{\partial \theta_2^2} \right), \quad \gamma_2 = \frac{\partial \psi}{\partial \theta_1 \partial \theta_2}. \quad (3.15)$$

Defining the reduced shear

$$g \equiv \frac{\gamma}{1 - \kappa} = \frac{|\gamma|}{1 - \kappa} e^{i2\phi}, \quad (3.16)$$

we can rewrite the Jacobian Matrix as

$$\mathcal{A}(\boldsymbol{\theta}) = (1 - \kappa) \begin{pmatrix} 1 - g_1 & -g_2 \\ -g_2 & 1 + g_1 \end{pmatrix}. \quad (3.17)$$

We see from equations (3.13) and (3.15) that the convergence κ and the gravitational shear γ are directly related to each other via the gravitational deflection potential ϕ . Kaiser (1995) showed that

$$\nabla \kappa = \begin{pmatrix} \frac{\partial \gamma_1}{\partial \theta_1} + \frac{\partial \gamma_2}{\partial \theta_2} \\ \frac{\partial \gamma_2}{\partial \theta_1} - \frac{\partial \gamma_1}{\partial \theta_2} \end{pmatrix}. \quad (3.18)$$

This means that $\nabla \kappa$ can be derived from shape measurements in the weak lensing limit $\kappa \ll 1$. For the more general case relations can be found in Kaiser (1995), Schneider & Seitz (1995) and Seitz & Schneider (1995). These relations were used, e.g., in Kaiser *et al.* (1995), Seitz & Schneider (1996) and Seitz & Schneider (2001) to obtain κ -maps from local shape estimates.

Kaiser (1995) showed that the mean tangential shear $\langle \gamma \rangle$ can be written as the difference between the mean convergence $\bar{\kappa}$ within a circle of radius θ and the convergence κ on the edge of this circle

$$\langle \gamma \rangle(\theta) = \bar{\kappa}(\theta) - \langle \kappa \rangle(\theta). \quad (3.19)$$

Multiplying this equation with the critical surface mass density Σ_c , we then obtain the excess surface mass density

$$\Sigma_c \langle \gamma \rangle(R) = \bar{\Sigma}(R) - \langle \Sigma \rangle(R) \equiv \Delta \Sigma(R). \quad (3.20)$$

3.3 Weak Lensing

In general the shear caused by mass distributions can be quite large. Close to the Einstein radius, sources can be distorted into giant arcs or, under almost symmetrical conditions, into a ring. In this thesis we do not deal with such large distortions. We only consider the weak lensing regime where the Jacobian matrix is close to the unity matrix, leading to small distortions and therefore small shears.

3.3.1 Shape Measurement

In order to apply the theoretical formalism we still need to connect it to the observational data. Therefore we need to derive how observable quantities of the surface brightness distribution change under shear. For a brightness distribution $I(\boldsymbol{\theta})$ we define

$$\bar{\boldsymbol{\theta}} \equiv \frac{\int d^2\boldsymbol{\theta} I(\boldsymbol{\theta}) q_I[I(\boldsymbol{\theta})] \boldsymbol{\theta}}{\int d^2\boldsymbol{\theta} I(\boldsymbol{\theta}) q_I[I(\boldsymbol{\theta})]} \quad (3.21)$$

as the center of the light distribution with $q_I(I)$ being a suitably chosen weight function. From the second brightness moments

$$Q_{ij} = \frac{\int d^2\boldsymbol{\theta} I(\boldsymbol{\theta}) q_I[I(\boldsymbol{\theta})] (\theta_i - \bar{\theta}_i)(\theta_j - \bar{\theta}_j)}{\int d^2\boldsymbol{\theta} I(\boldsymbol{\theta}) q_I[I(\boldsymbol{\theta})]} \quad (3.22)$$

two different complex ellipticities can be defined:

$$\boldsymbol{\chi} = \frac{Q_{11} - Q_{22} + 2iQ_{12}}{Q_{11} + Q_{22}} = \chi_1 + i \chi_2 \quad (3.23)$$

and

$$\boldsymbol{\varepsilon} = \frac{Q_{11} - Q_{22} + 2iQ_{12}}{Q_{11} + Q_{22} + 2(Q_{11}Q_{22} - Q_{12}^2)^{\frac{1}{2}}} = \varepsilon_1 + i \varepsilon_2 . \quad (3.24)$$

For r being the axis ratio of the elliptical isophotes of an object we obtain

$$|\boldsymbol{\chi}| = \frac{1 - r^2}{1 + r^2} \text{ and } |\boldsymbol{\varepsilon}| = \frac{1 - r}{1 + r} . \quad (3.25)$$

The ellipticities in the source and in the lens plane are related via

$$\boldsymbol{\chi}^{(s)} = \frac{\boldsymbol{\chi} - 2\mathbf{g} + \mathbf{g}^2 \boldsymbol{\chi}^*}{1 + |\mathbf{g}|^2 - 2\Re(\mathbf{g} \boldsymbol{\chi}^*)} , \quad (3.26)$$

which was derived by Schneider & Seitz (1995). The transformation in terms of $\boldsymbol{\varepsilon}$ is given by

$$\boldsymbol{\varepsilon}^{(s)} = \begin{cases} \frac{\boldsymbol{\varepsilon} - \mathbf{g}}{1 - \mathbf{g}^* \boldsymbol{\varepsilon}} & |\mathbf{g}| \leq 1 \\ \frac{1 - \mathbf{g} \boldsymbol{\varepsilon}^*}{\boldsymbol{\varepsilon}^* - \mathbf{g}^*} & |\mathbf{g}| > 1 , \end{cases} \quad (3.27)$$

derived by Seitz & Schneider (1997). To obtain the inverse relations $\boldsymbol{\chi}$ and $\boldsymbol{\chi}^{(s)}$ ($\boldsymbol{\varepsilon}$ and $\boldsymbol{\varepsilon}^{(s)}$) need to be interchanged and \mathbf{g} needs to be replaced by $-\mathbf{g}$ in equations (3.26) and (3.27).

3.3.2 Statistical Ansatz

The major problem of weak lensing is the smallness of the distortion, since the measured ellipticities do not represent only the gravitational signature. In general galaxies are not intrinsically round but elliptical, so the observed ellipticity is composed of both intrinsic ellipticity and gravitational shear. It is not possible to disentangle these two quantities for an individual source, but looking at an ensemble of galaxies, it is possible to extract a gravitational signal. The basic assumption in weak lensing is the random orientation of the intrinsic ellipticities. Therefore without gravitational influence the mean

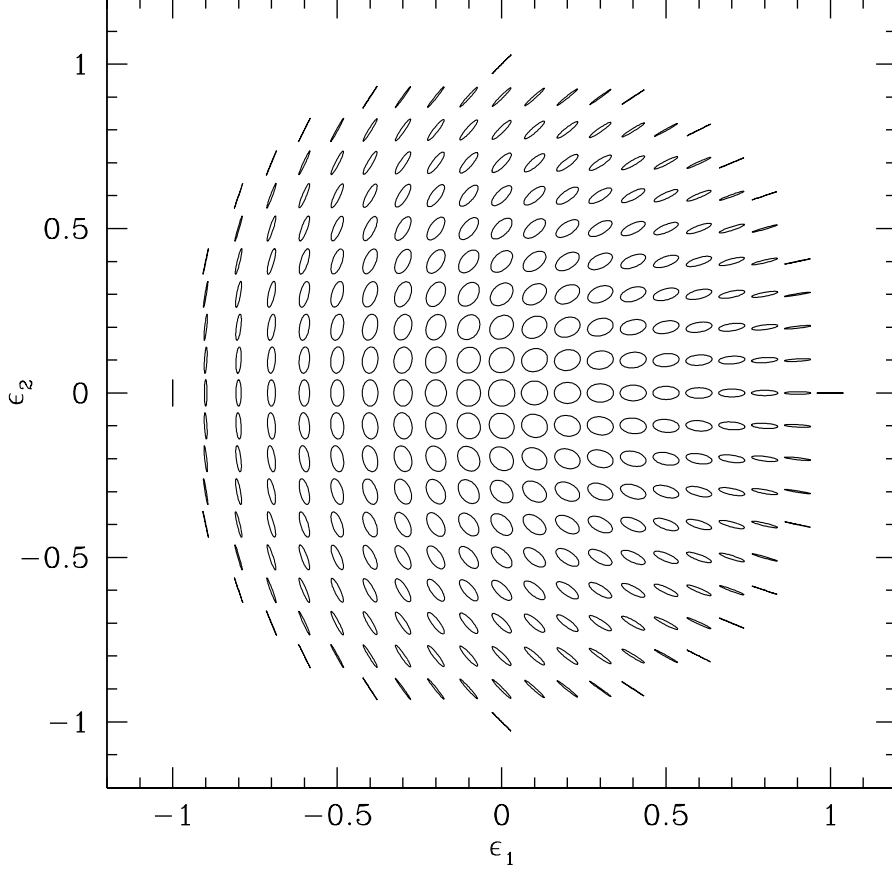


Fig. 3.2: The shapes of images with corresponding ellipticities ϵ_1 and ϵ_2 . Objects with $\epsilon_1 = \epsilon_2 = 0$ are circular, objects with $\epsilon_1 = \pm 1$ are aligned along the x- respectively the y-axis while objects with $\epsilon_2 = \pm 1$ are rotated by 45° .

ellipticity of an ensemble of background sources should vanish. Applying the averaging on a sheared source sample then provides an estimate for the gravitational shear

$$\langle \boldsymbol{\epsilon} \rangle = \langle \boldsymbol{\epsilon}^{(s)} \rangle + \langle \boldsymbol{\gamma} \rangle = \langle \boldsymbol{\gamma} \rangle. \quad (3.28)$$

The shear components γ_1 and γ_2 are defined in Cartesian coordinates but as gravity is a conservative force and does not produce curls, the induced signal should only show imprints tangentially to the lens. This projected shear is called the tangential shear γ_t . Its counterpart is called cross-shear γ_c and is measured by rotating the ellipticities of the source sample by 45° . These quantities are calculated from the shear γ in following way:

$$\gamma_t = -\Re[\gamma e^{-2i\Phi}], \gamma_c = -\Im[\gamma e^{-2i\Phi}]. \quad (3.29)$$

The cross-shear provides an excellent estimator for systematics as gravity cannot contribute. Analogously to electrodynamics tangential and cross-shear are called E- and B-modes. Any signal showing

up in the B-mode indicates a contamination of the lensing signal, possibly by distortions introduced by the telescope optics or atmospheric turbulences (PSF). Vanishing B-modes do not guarantee that the observed sample is systematic-free, but their presence is a strong indicator for systematic errors.

3.3.3 Estimation of Object Shapes with the KSB Pipeline

Measuring image ellipticities in practice is not as easy as it looks in theory. Unfortunately the ellipticities which are extracted from observational data in general cannot serve as unbiased estimators, since they suffer from different contaminations such as atmospheric, telescope optics and camera distortions. Kaiser *et al.* (1995) (extended by Hoekstra *et al.* 1998) developed a formalism to estimate the reduced gravitational shear

$$\mathbf{g} = g_1 + ig_2 = \frac{\gamma}{1 - \kappa} \quad (3.30)$$

and correct for the contamination distortions introduced by PSF and instrument. The KSB+ pipeline used in this thesis, which was kindly provided by Thomas Erben and Tim Schrabback, is well described in Erben *et al.* (2001) and Schrabback *et al.* (2007). The ellipticities in this formalism are defined by

$$\boldsymbol{\varepsilon} = \varepsilon_1 + i\varepsilon_2 = \frac{Q_{11} - Q_{22} + 2iQ_{12}}{Q_{11} + Q_{22}} \quad (3.31)$$

where

$$Q_{ij} = \int d^2\theta W_{r_g}(|\boldsymbol{\theta}|) \theta_i \theta_j I(\boldsymbol{\theta}) \quad (3.32)$$

are the quadrupole moments of the light distribution, with $W_{r_g}(|\boldsymbol{\theta}|)$ being a circular Gaussian weight function with filter scale r_g . The principle of KSB+ is based on the assumption that the PSF P can be decomposed into an isotropic part P^{iso} (the ‘smearing’ which makes the galaxies larger) and a small anisotropic part described by the anisotropy kernel q^* (which distorts the galaxies). The observed ellipticities are described by

$$\varepsilon_\alpha = \varepsilon_\alpha^s + P_{\alpha\beta}^g g_\beta + P_{\alpha\beta}^{\text{sm}} q_\beta^*, \quad (3.33)$$

with the intrinsic source ellipticity ε^s and the reduced shear g . The ‘pre-seeing’ polarizability introduced by Luppino & Kaiser (1997)

$$P_{\alpha\beta}^g = P_{\alpha\beta}^{\text{sh}} - P_{\alpha\gamma}^{\text{sm}} \left[(P^{\text{sm}*})_{\gamma\delta}^{-1} P_{\delta\beta}^{\text{sh}*} \right] \quad (3.34)$$

describes how the image ellipticity responds to shear in the presence of the PSF smearing. P^{sm} , the smear polarizability tensor, describing how the image ellipticity responds to the presence of PSF anisotropy and P^{sh} , the shear polarizability tensor, are calculated from higher-order brightness moments as described in detail in Hoekstra *et al.* (1998). As the trace-free part of the tensor is much smaller than the trace (Erben *et al.* 2001), the calculations of the ‘pre-seeing’ polarizability and its inversion are approximated by

$$\left[(P^{\text{sm}*})_{\gamma\delta}^{-1} P_{\delta\beta}^{\text{sh}*} \right] \approx \frac{\text{Tr} [P^{\text{sh}*}]}{\text{Tr} [P^{\text{sm}*}]} \delta_{\gamma\beta}, \quad (P^g)_{\alpha\beta}^{-1} \approx \frac{2}{\text{Tr} [P^g]} \delta_{\alpha\beta}. \quad (3.35)$$

The anisotropy kernel can be extracted from stellar objects. As stars have no intrinsic ellipticity and are not gravitationally sheared, we obtain

$$\varepsilon^s = 0 \text{ and } \gamma = 0. \quad (3.36)$$

This leads to

$$\varepsilon_\alpha = P_{\alpha\beta}^{\text{sm}} q_\beta^* \quad (3.37)$$

or

$$q_\beta^* = (P^{\text{sm}*})_{\alpha\beta}^{-1} \varepsilon_\alpha. \quad (3.38)$$

The anisotropy corrected ellipticity is defined as

$$\varepsilon_\alpha^{\text{ani}} = \varepsilon_\alpha - P_{\alpha\beta}^{\text{sm}} q_\beta^*, \quad (3.39)$$

the fully corrected ellipticity as

$$\varepsilon_\alpha^{\text{iso}} = (P^{\text{g}})_{\alpha\beta}^{-1} \varepsilon_\beta^{\text{ani}}. \quad (3.40)$$

Under the assumption of randomly oriented intrinsic source ellipticities ε^{s} , the so obtained ellipticity can serve as unbiased shear estimator. For weak gravitational distortions, the convergence is very small ($\kappa \ll 1$) and therefore

$$\langle e^{\text{iso}} \rangle = g \simeq \gamma. \quad (3.41)$$

As the STEP simulation has shown (see Heymans *et al.* 2006) a significant bias remained after the correction. Therefore a shear calibration factor was introduced and applied:

$$\langle \gamma_\alpha \rangle = c_{\text{cal}} \langle e_\alpha^{\text{iso}} \rangle \quad (3.42)$$

with $c_{\text{cal}} = 1/0.91$.

3.4 Theory of Galaxy-Galaxy Lensing

3.4.1 Lens Profiles

In the following we give a short introduction to several analytic galaxy halo profiles.

Singular Isothermal Sphere

A very simple lens profile is represented by the singular isothermal sphere (SIS). This mass distribution is very famous as it yields flat rotation curves as observed in spiral galaxies. The spherically symmetric spatial mass density distribution is described by

$$\rho_{\text{SIS}}(R) = \frac{\sigma^2}{2\pi GR^2}, \quad (3.43)$$

with σ being the velocity dispersion. To obtain the surface mass density, we integrate the 3D-mass density distribution along the line of sight:

$$\begin{aligned} \Sigma_{\text{SIS}}(\xi) &= \int_{-\infty}^{\infty} dz \rho(\xi, z) = \int_{-\infty}^{\infty} dz \frac{\sigma^2}{2\pi G} \cdot \frac{1}{z^2 + \xi^2} = \\ &= \frac{\sigma^2}{2\pi G \xi} \int_{-\infty}^{\infty} dz' \frac{1}{1 + z'^2} = \frac{\sigma^2}{2\pi G \xi} \cdot [\arctan(z')]_{-\frac{\pi}{2}}^{+\frac{\pi}{2}} = \\ &= \frac{\sigma^2}{2G\xi}. \end{aligned} \quad (3.44)$$

As defined in equation (3.7), the convergence κ is the ratio between surface mass density Σ and critical surface mass density Σ_c :

$$\kappa_{\text{SIS}}(\theta) = \frac{\Sigma}{\Sigma_c} = 4\pi \left(\frac{\sigma}{c}\right)^2 \frac{D_{\text{ds}}}{D_s} \cdot \frac{1}{2\theta} = \frac{\theta_E}{2\theta} \quad (3.45)$$

with θ_E being the Einstein angle:

$$\theta_E = 4\pi \left(\frac{\sigma}{c}\right)^2 \frac{D_{\text{ds}}}{D_s}. \quad (3.46)$$

By integrating the Poisson equation (3.13) we derive the scaled the deflection angle

$$\alpha_{\text{SIS}}(\boldsymbol{\theta}) = \theta_E \frac{\boldsymbol{\theta}}{|\boldsymbol{\theta}|} \quad (3.47)$$

and the deflection potential

$$\Psi_{\text{SIS}}(\boldsymbol{\theta}) = \theta_E |\boldsymbol{\theta}|. \quad (3.48)$$

If we calculate the derivatives of the deflection potential according to equation (3.15) we obtain

$$\gamma_{\text{SIS}}(\theta) = \frac{\theta_E}{2\theta} \quad (3.49)$$

for the shear of a singular isothermal sphere. By multiplying the tangential shear γ_t with the critical surface mass density Σ_c and applying the definition of the Einstein angle θ_E with $\theta = R/D_d$, we receive the excess surface mass density

$$\Delta \Sigma_{\text{SIS}}(R) = \Sigma_c \gamma_{t,\text{SIS}} = \frac{c^2}{4\pi G} \frac{D_s}{D_d D_{\text{ds}}} \cdot 4\pi \left(\frac{\sigma}{c}\right)^2 \frac{D_{\text{ds}}}{D_s} \frac{D_d}{2R} = \frac{\sigma^2}{2GR}. \quad (3.50)$$

The line-of-sight projected mass within a sphere of radius R is given by

$$M_{\text{SIS}}(< R) = \frac{2\sigma^2}{G} R, \quad (3.51)$$

which means that the total SIS mass diverges.

Truncated Isothermal Sphere (BBS)

Being a very simple and easily calculable profile the singular isothermal sphere, as mentioned, unfortunately also has a big disadvantage: the total mass does not converge but is infinite. Therefore a more sophisticated and physical profile was suggested by Brainerd *et al.* (1996), the truncated isothermal sphere (BBS profile), introducing the truncation radius s . The spatial mass density distribution is described by

$$\rho_{\text{BBS}}(R) = \frac{\sigma^2}{2\pi GR^2} \cdot \frac{s^2}{R^2 + s^2} = \frac{\sigma^2}{2\pi G} \cdot \left(\frac{1}{R^2} - \frac{1}{R^2 + s^2} \right). \quad (3.52)$$

In the inner part the profile corresponds almost to that of an SIS, but in the outer part the density decreases much faster (at the truncation radius the mass density is only half the value of an SIS). For a diverging truncation radius ($s \rightarrow \infty$) the BBS profile asymptotically transforms back into an SIS. Integrating along the line of sight we find for surface mass density Σ of a BBS profile

$$\Sigma_{\text{BBS}}(\xi) = \int_0^\infty dz \rho(\xi, z) = \int_0^\infty dz \frac{\sigma^2}{2\pi G} \cdot \left(\frac{1}{z^2 + \xi^2} - \frac{1}{z^2 + \xi^2 + s^2} \right) =$$

$$\begin{aligned}
&= \frac{\sigma^2}{2\pi G} \left(\frac{1}{\xi} \cdot \int_0^\infty dz' \frac{1}{1+z'^2} - \frac{1}{\sqrt{\xi^2+s^2}} \cdot \int_0^\infty dz'' \frac{1}{1+z''^2} \right) = \\
&= \frac{\sigma^2}{2\pi G} \cdot \left(\frac{1}{\xi} - \frac{1}{\sqrt{\xi^2+s^2}} \right) \cdot [\arctan(z')]_{-\frac{\pi}{2}}^{+\frac{\pi}{2}} = \\
&\quad \frac{\sigma^2}{2G} \cdot \left(\frac{1}{\xi} - \frac{1}{\sqrt{\xi^2+s^2}} \right)
\end{aligned} \tag{3.53}$$

and subsequently for the convergence

$$\kappa_{\text{BBS}}(\theta) = \frac{\Sigma}{\Sigma_c} = 4\pi \left(\frac{\sigma}{c} \right)^2 \frac{D_{\text{ds}}}{D_s} \cdot \frac{1}{2\theta} \cdot \left(\frac{1}{\theta} - \frac{1}{\sqrt{\theta^2 + \theta_s^2}} \right) = \frac{\theta_E}{2\theta} \cdot \left(\frac{1}{\theta} - \frac{1}{\sqrt{\theta^2 + \theta_s^2}} \right) \tag{3.54}$$

with

$$\theta_s = \frac{s}{D_d}.$$

Integrating the Poisson equation (3.13) for the BBS profile we receive for the scaled deflection angle

$$\alpha_{\text{BBS}}(\theta) = \theta_E \cdot \left(1 - \frac{\sqrt{\theta^2 + \theta_s^2} - \theta_s}{\theta} \right) \tag{3.55}$$

and the deflection potential

$$\Psi_{\text{BBS}}(\theta) = \theta_E \cdot \left[\theta - \sqrt{\theta^2 + \theta_s^2} + \theta_s \cdot \ln \left(\frac{1}{\theta_s} \sqrt{\theta^2 + \theta_s^2} + 1 \right) \right]. \tag{3.56}$$

Applying equation (3.15) we derive

$$\gamma_{\text{BBS}}(\theta) = \frac{\theta_E}{2\theta} \left(1 + \frac{2\theta_s}{\theta} - \frac{\theta^2 + 2\theta_s^2}{\theta \sqrt{\theta^2 + \theta_s^2}} \right) \tag{3.57}$$

for the shear γ of a truncated isothermal sphere. Analogously to equation (3.50), we obtain the excess surface mass density for the BBS profile

$$\Delta \Sigma_{\text{BBS}}(R) = \frac{\sigma^2}{2GR} \left(\frac{R+2s}{R} - \frac{R^2+2s^2}{R\sqrt{R^2+s^2}} \right). \tag{3.58}$$

By integrating the BBS mass density distribution (see equation 3.52) we obtain

$$M_{\text{BBS}}(< R) = \frac{2\sigma^2 s}{G} \arctan \left(\frac{R}{s} \right) \tag{3.59}$$

for the mass within a radius R and

$$\begin{aligned}
M_{\text{total,BBS}} &= \frac{\pi\sigma^2 s}{G} = \\
&7.3 \times 10^{12} h^{-1} M_\odot \left(\frac{\sigma}{1000 \text{ km s}^{-1}} \right)^2 \left(\frac{s}{1 \text{ Mpc}} \right)
\end{aligned} \tag{3.60}$$

for the total mass.

Universal Density Profile (NFW)

Another more sophisticated profile with two free halo parameters was motivated by the results of dark matter simulations. The so-called universal density profile or NFW profile was introduced by Navarro *et al.* (1996, 1997). The spatial mass density distribution is described by

$$\rho_{\text{NFW}}(R) = \frac{\delta_c \rho_c}{R/r_s + (1 + R/r_s)^2} \quad (3.61)$$

with the scale radius r_s , the critical density of the Universe at redshift z

$$\rho_c = \frac{3H(z)^2}{8\pi G} \quad (3.62)$$

and the density contrast

$$\delta_c = \frac{200}{3} \frac{c^3}{\ln(1+c) - c/(1+c)}. \quad (3.63)$$

The density contrast itself is a function of the concentration parameter

$$c = \frac{r_{200}}{r_s}, \quad (3.64)$$

the ratio between the ‘virial radius’ r_{200} and scale radius r_s , describing the distribution of matter inside and outside the scale radius, literally describing the matter concentration. The physical meaning of the radii is the following. The r_{200} is defined via the spherical region with mean density being 200 times the critical density of the Universe while the scale radius r_s marks the transition point of the density from declining with first to third order with distance. Subsequently the virial mass M_{200} is defined as the mass contained within a radius of r_{200} :

$$M_{200} = \frac{800\pi}{3} \rho_c r_{200}^3. \quad (3.65)$$

In order to calculate the mass enclosed by an arbitrary radius we integrate the spatial NFW mass density distribution (see equation 3.61):

$$\begin{aligned} M_{\text{NFW}}(< R) &= \\ &= \int_0^R dr' 4\pi r'^2 \rho_{\text{NFW}}(r') = 4\pi \rho_c \delta_c \int_0^R dr' \frac{r'^2}{r'/r_s + (1 + r'/r_s)^2} = \\ &= 4\pi \rho_c \delta_c r_s \int_0^R dr' \frac{r'}{(1 + r'/r_s)^2} = 4\pi \rho_c \delta_c r_s \left[r_s^2 \ln \left(1 + \frac{r'}{r_s} \right) + r_s^2 \cdot \frac{1}{1 + r'/r_s} \right]_0^R = \\ &= 4\pi \rho_c \delta_c r_s^3 \left[\ln \left(1 + \frac{r'}{r_s} \right) + \frac{1}{1 + r'/r_s} \right]_0^R. \end{aligned} \quad (3.66)$$

Thus the enclosed mass at an infinite radius does not converge but is also infinite. Although the NFW- M_{200} -mass only gives the part of the mass which is already virtualized and does not specify the the mass associated with this structure outside this radius, it therefore does not make sense to integrate this profile for much larger radii. A modification which is NFW-like inside r_{200} and

describes a cutoff relative to the original NFW profile for larger radii similar to the BBS cutoff was presented by Baltz *et al.* (2009). In this case the total mass of the truncated NFW halo then is similar in interpretation as the total BBS mass, i.e., it equals the total mass associated with this halo.

The corresponding rotation velocity at the virial radius (also called circular velocity) is given by

$$v_{200} = \sqrt{\frac{GM_{200}}{r_{200}}} = \sqrt{\frac{800\pi\rho_c G}{3}} r_{200}. \quad (3.67)$$

The following formulae for the surface mass densities and shears of the universal density profile are taken from Wright & Brainerd (2000) and were derived by Bartelmann (1996). For convenience, a dimensionless radius $x = R/s$ is adopted. It has been shown, that by integrating equation (3.61) along the line of sight the surface mass density can be expressed by

$$\Sigma_{\text{NFW}}(x) = \begin{cases} \frac{2r_s\rho_c\delta_c}{(x^2-1)} \left[1 - \frac{2}{\sqrt{1-x^2}} \operatorname{artanh}\sqrt{\frac{1-x}{1+x}} \right] & x < 1 \\ \frac{2r_s\rho_c\delta_c}{3} & x = 1 \\ \frac{2r_s\rho_c\delta_c}{(x^2-1)} \left[1 - \frac{2}{\sqrt{x^2-2}} \arctan\sqrt{\frac{x-1}{x+1}} \right] & x > 1 \end{cases}. \quad (3.68)$$

The shear of the universal density profile is described by

$$\gamma_{\text{NFW}} = \begin{cases} \frac{r_s\delta_c\rho_c}{\Sigma_c} g_{<}(x) & x < 1 \\ \frac{r_s\delta_c\rho_c}{\Sigma_c} \frac{10}{3} + 4 \ln\frac{1}{2} & x = 0 \\ \frac{r_s\delta_c\rho_c}{\Sigma_c} g_{>}(x) & x > 1 \end{cases} \quad (3.69)$$

with

$$g_{<}(x) = \frac{8 \operatorname{artanh}\sqrt{(1-x)/(1+x)}}{x^2\sqrt{1-x^2}} + 4 \ln\left(\frac{x}{2}\right) - \frac{2}{(x^2-1)} + \frac{4 \operatorname{artanh}\sqrt{(1-x)/(1+x)}}{(x^2-1)(1-x^2)^{1/2}} \quad (3.70)$$

and

$$g_{>}(x) = \frac{8 \arctan\sqrt{(x-1)/(x+1)}}{x^2\sqrt{x-1^2}} + 4 \ln\left(\frac{x}{2}\right) - \frac{2}{(x^2-1)} + \frac{4 \arctan\sqrt{(x-1)/(x+1)}}{(x^2-1)^{3/2}} \quad (3.71)$$

being functions independent from cosmology and only depending on the dimensionless radial distance x . Analogously to equations (3.50) and (3.58), the excess surface mass density for an NFW profile is given by

$$\Delta\Sigma_{\text{NFW}} = \begin{cases} r_s\delta_c\rho_c g_{<}(x) & x < 1 \\ r_s\delta_c\rho_c \left(\frac{10}{3} + 4 \ln\frac{1}{2}\right) & x = 0 \\ r_s\delta_c\rho_c g_{>}(x) & x > 1 \end{cases}. \quad (3.72)$$

3.4.2 Scaling Relations for the Galaxy Halo Models

In general considering galaxies over a wider range of luminosities, the question about the dependence of the halo parameters on the galaxy luminosity is raised. We therefore have a look on the scaling

relations for the free parameters of the previously described halo profiles. Firstly we consider a very basic parameter, the halo mass M , where M can be the total halo mass of the BBS profile or the virial mass M_{200} of the NFW profile:

$$\left(\frac{M}{M^*}\right) = \left(\frac{L}{L^*}\right)^{\eta_M}, \quad (3.73)$$

with η_M being the characteristic the slope of this scaling relation in logarithmic space. Dividing the total mass by the luminosity L , this directly leads to

$$\left(\frac{M/L}{(M/L)^*}\right) = \left(\frac{L}{L^*}\right)^{\eta_{M/L}}, \quad (3.74)$$

with

$$\eta_{M/L} = \eta_M - 1. \quad (3.75)$$

In principle the scaling indices for M_{BBS} and M_{200} do not necessarily need to be the same but can be different. Further the luminosities in these equations do not describe the bolometric ones but the fluxes in a specific filter, in the following to be chosen the r' -band.

These relations build the starting point for the estimation of the following scaling relations. Considering the SIS and the BBS profile, we notice that the SIS can be described as a special case of the BBS profile, consisting of an infinite truncation radius. Therefore the scaling relations for the velocity dispersion in both profiles are identical. Faber & Jackson (1976) and Tully & Fisher (1977) found that the scaling relation for σ is described by a power law

$$\left(\frac{\sigma}{\sigma^*}\right) = \left(\frac{L}{L^*}\right)^{\eta_\sigma}. \quad (3.76)$$

In order to derive the scaling relation of the second free parameter of the BBS profile, the truncation radius s , we can combine equations (3.73) and (3.76) to obtain

$$\left(\frac{s}{s^*}\right) = \left(\frac{L}{L^*}\right)^{\eta_s} \quad (3.77)$$

with

$$\eta_{M_{\text{BBS}}} = 2 \cdot \eta_\sigma + \eta_s. \quad (3.78)$$

We now discuss the values for the scaling indices of the corresponding scaling relations. Considering the mass, Guzik & Seljak (2002) found, analyzing the GGL signal in g' -band SDSS data, a scaling index of $\eta_M = 1.2 \pm 0.2$ for the mass-luminosity relation, being the same scaling behavior which has already been found for the dynamical mass-to-light ratio for the centers of elliptical galaxies, the so-called fundamental plane (see, e.g., Bender *et al.* 1992 or Saglia *et al.* 2010). Considering the velocity dispersion, the exact value for η_σ is still under debate. The original measurements of the Faber-Jackson (Faber & Jackson 1976) and the Tully-Fisher relation (Tully & Fisher 1977) suggested a value of $\eta_\sigma = 0.25$, but various measurements applying data from different filters and different galaxy samples (see, e.g., Davies *et al.* 1983 analyzing faint early type galaxies and Matkovic & Guzmán 2007 analyzing dwarf early type galaxies, both in B -band, or Nigoche-Netro *et al.* 2010 analyzing SDSS early type galaxies in g - and r -band for the Faber-Jackson relation and analyzing the

Tully-Fisher relation for disk galaxies, e.g., Bamford *et al.* 2006, Miller *et al.* 2011 in B -band and Pizagno *et al.* 2005, Fernández Lorenzo *et al.* 2009 or Reyes *et al.* 2011 in I -band) showed possible variations in dependence of wavelength range and galaxy morphology, also including Cappellari *et al.* (2012) separately investigating the properties of fast and slow rotating early type galaxies (S0s and Es) or Williams *et al.* (2010) for early type spiral and S0 galaxies. In the past when assuming or attempting to measure the scaling behavior of the velocity dispersion in GGL analyses, different assumptions were made and different results were obtained. Measuring the B -band slope of the Tully-Fisher relation, e.g., Verheijen (2001) found a value of $\eta_\sigma = 0.3$. Further Seljak (2002) applied a classical Faber-Jackson relation for his sample while Hoekstra *et al.* (2004) assumed a scaling behavior of $\sigma \propto L^{0.3}$ for his mixed SED sample. On the other hand Kleinheinrich *et al.* (2006) obtained values for η_σ between 0.3 and 0.4, depending on the considered maximum separation between foreground and background objects. We will see in our later analysis, that the scaling relation indeed strongly depends on the properties of the examined galaxy sample, as galaxy SED, in particular on whether a pure or mixed SED galaxy sample is considered.

Assuming $\eta_M = 1.2$ and $\eta_\sigma = 0.3$ (which corresponds best to the measured value of a mixed SED sample, as we will see in Sections 6.2 and 6.4.1) this leads to value of $\eta_s = 0.6$ for the truncation radius. From these three values a generic model can be built to analyze a combined galaxy sample and obtain the velocity dispersion and galaxy halo size for a fiducial galaxy with luminosity L^* .

The last discussed halo profile, the NFW profile, also consists of two free parameters, the virial radius r_{200} and the concentration parameter c . The virial radius is directly linked to the virial mass M_{200} via equation (3.65). If the virial radius scales with

$$\left(\frac{r_{200}}{r_{200}^*}\right) = \left(\frac{L}{L^*}\right)^{\eta_{r_{200}}}, \quad (3.79)$$

we directly obtain

$$\eta_{M_{200}} = 3\eta_{r_{200}}, \quad (3.80)$$

leading to a scaling parameter of $\eta_{r_{200}} = 0.4$ for $\eta_{M_{200}} = 1.2$. However, with virial radius and thus virial mass being a function of the critical density ρ_c (see equation 3.62), the zeropoint of this equation changes with redshift.

Finally we have a look at the last remaining parameter, the concentration parameter c . As the previous equations do not provide a direct estimate for a scaling relation, we therefore consider the results of Duffy *et al.* (2008), who found the following relation between concentration parameter and halo mass:

$$c \propto M^{-0.084 \pm 0.006} (1+z)^{-0.47 \pm 0.04}. \quad (3.81)$$

Already previous measurements of the concentration-mass relation showed a slight decrease of the concentration parameter with increasing mass (see, e.g., Bullock *et al.* 2001 or Shaw *et al.* 2006). Further concentration-mass relations also have been discussed by, e.g., Bhattacharya *et al.* (2013), finding a scaling relation very similar to Duffy *et al.* (2008), but with slightly higher amplitude or Klypin *et al.* (2011), reporting an even higher amplitude and shallower decrease of the concentration with increasing mass. Recently Prada *et al.* (2012) presented a new concentration-mass relation, introducing a novel feature looking at virial masses higher than $10^{15} h^{-1} M_\odot$, not showing a further decrease but an increase of concentration with increasing mass.

The concentration-mass relation can be translated into a concentration-luminosity relation using the scaling relation between mass and luminosity. Applying equation (3.73) we obtain the following dependence of concentration on the direct observable L :

$$c \propto L^{\eta_c}, \quad (3.82)$$

with

$$\eta_c = \frac{-0.084 \pm 0.006}{\eta_M} \quad (3.83)$$

being the scaling parameter for the halo concentration.

Most mentioned values for the scaling parameters assume a mixed galaxy sample, showing a transition from red SED dominated for bright massive galaxies to blue SED dominated for fainter and thus less massive galaxies. The later sections will show that this transition introduces a modification in the parameters for the scaling relations, accounting for the different mass of red and blue galaxies for given luminosity, thus leading to deviating values for pure and mixed galaxy SED samples. In particular we will further investigate the halo parameter scaling relations in Sections 6.2.2, 6.4.1 and 6.4.3.

3.4.3 Maximum Likelihood Analysis

The analyses of the tangential shear signal γ_t and the excess surface mass density $\Delta\Sigma$ draw a picture of the cumulative halo profile, presenting a composition of many halos, including central halos, but also neighboring halos and therefore the contribution of the nearby galaxies or galaxy group or cluster halo. In order to investigate and quantify the properties of the individual galaxy halos we further perform a maximum likelihood analysis as introduced by Schneider & Rix (1997). This method derives the best-fitting parameters for the individual galaxy for given luminosity, by comparing the prediction for specific profiles as the BBS profile or the NFW profile with observed values of the galaxy shapes. The log-likelihood is given by the equation

$$\log \mathcal{L} = - \sum_{i,j} \left(\frac{e_{i,j} - P_j^\gamma g_{i,j}^{model}}{\sigma_{e_j}} \right)^2, \quad (3.84)$$

with $e_{i,j}$ being the PSF corrected polarizations for the j -th galaxy, P_j^γ the shear polarizability and $g_{i,j}$ the analytic shear values for the investigated halo profile. The values for σ_{e_j} are given by the scatter of source ellipticities, quantifying the shape noise and the shape measurement errors. The best-fitting profile parameters are those, which best reproduce the observed galaxy polarizations, thus leading to a maximal log-likelihood value. In order to properly treat a sample of lenses distributed over a certain range of luminosities it is necessary to define a fiducial point and to scale the lenses to this fiducial point. As fiducial luminosity we choose $L_{r'}^* = 1.6 \times 10^{10} h^{-2} L_{r',\odot}$ (corresponding to an absolute magnitude of $M_{r'} \sim -21.7$). The applied scaling relations for the maximum likelihood analyses and the performed analyses themselves will be discussed in the Sections 6.2.2 and 6.4.

3.4.4 3D-LOS-Projected Lensing Signal Simulations

The proper interpretation of GGL results requires a well understood system and knowledge to which limitations this system is valid. We therefore create two 3D-line-of-sight(LOS)-projected lensing signal simulations without shape noise, one assuming a truncated isothermal sphere (BBS) and the other assuming a universal density profile (NFW) for the galaxy halos. For the simulation we keep positions, luminosities and redshifts of all lenses and sources but analytically calculate and assign the theoretical shear values as ‘measured’ polarizations to the simulated source sample. As profile parameters for the fiducial luminosity we adopt the best-fitting values from our maximum likelihood analyses, explicitly distinguishing between red and blue lens halos and therefore for the different halo mass at given same luminosity. Firstly considering the BBS profile, we adopt a velocity dispersion of $\sigma_{\text{red}}^* = 149 \text{ km s}^{-1}$ and a truncation radius of $s_{\text{red}}^* = 337 h^{-1} \text{ kpc}$ for red lens galaxies and for the blue lens galaxies we adopt a velocity dispersion of $\sigma_{\text{blue}}^* = 118 \text{ km s}^{-1}$ and a truncation radius of $s_{\text{blue}}^* = 84 h^{-1} \text{ kpc}$. Secondly considering the NFW profile we adopt a concentration parameter of $c_{\text{red}}^* = 6.4$ and a virial radius of $r_{200,\text{red}}^* = 160 h^{-1} \text{ kpc}$ for the red lenses and a concentration parameter $c_{\text{blue}}^* = 7.0$ and a virial radius of $r_{200,\text{blue}}^* = 115 h^{-1} \text{ kpc}$ for the blue lens galaxies. We further apply the scaling relations obtained in the maximum likelihood analyses. The in this way created lens-source samples, consisting of observed lenses and simulated sources, are then used to calculate the expectable tangential shear profiles γ and excess surface mass densities $\Delta\Sigma$ and to compare them to the observational results in the Sections 6.1 and 6.2.

Chapter 4

Photometric Redshifts

The cosmic expansion of the Universe provides an excellent opportunity to estimate distances on a cosmic scale. As we already have seen in Section 2.1.3, the expansion does not only result in an elongation of space but also leads to a redshift of emitted photons by stretching the spectrum with the same factor as the space. The most accurate method to determine the redshift of an object is to observe its spectrum, to analyze the spectral energy distribution (SED) and further to identify features in it as well known absorption or emission lines and to compare their wavelength with the wavelength in the rest-frame. Unfortunately, the observation and analysis of spectra is very time-consuming and not feasible for faint and distant objects, which is why especially in wide-field surveys it is impossible to take spectra of all objects. Therefore already Baum (1962) suggested the photometric redshift technique, observing objects in several filters and consider the observed fluxes as a kind of low resolution spectra.

4.1 Techniques

In principal there are two different approaches for determining photometric redshifts: the template-fitting method and empirical methods. Empirical fitting methods derive a relation between observational fluxes and redshift, for instance via polynomial fitting or by application of machine learning. The application of artificial neural networks (e.g., ANNz, see Collister & Lahav 2004) can lead to very accurate results. For these empirical methods a training sample with known redshifts is required to estimate the photometric redshifts. In general this represents the major problem. In order to be perfectly applicable, the properties of the training set should precisely correspond to the properties of the complete investigated sample, which is difficult to realize, especially for deep surveys. Furthermore, spectroscopic surveys require higher photometric signal-to-noise ratios than photometric surveys, leading to a lower limiting magnitude. Objects observed in photometric surveys beyond the spectroscopic limiting magnitude might populate regions in color-space which are not spectroscopically covered. Further, deeper observations are able to trace higher redshifts, possibly introducing an SED-variety which is not present in the spectroscopic sample. These effects can lead to significant systematic errors when not taking them into account. Therefore it is indispensable to ensure the proper applicability of the training sample to the complete sample.

4.2 The Template-Fitting Method

4.2.1 Principle

The template-fitting method follows a different philosophy (see, e.g., Bender *et al.* 2001, Benítez 2000 or Bolzonella *et al.* 2000). The basic idea of template-fitting methods is that all galaxy SEDs shifted to their rest-frame can be described by a certain variety of SED templates. These template sets comprise artificial spectra which are derived from stellar population models, from empirical templates extracted from spectroscopic observations or from combinations of both. Most template-fitting methods operate on a discrete redshift grid onto which the templates are redshifted. For a given filter set the photometric throughput of the model is calculated in every redshift grid point. The calculated model fluxes are then compared to the observational data to derive the best-fitting parameter set. The best-fitting models and redshifts are determined by maximum likelihood calculation

$$\chi^2(z, \text{Model}) = \sum_i^{N_{\text{filter}}} \left[\frac{F_{\text{obs},i} - a \cdot F_{\text{temp},i}(z)}{\sigma_i} \right]^2, \quad (4.1)$$

with N_{filter} being the number of considered filters, $F_{\text{obs},i}$ the observed object fluxes, $F_{\text{temp},i}(z)$ the model fluxes as a function of redshift, a a scaling parameter to scale the model fluxes and σ_i the uncertainty in the flux measurement. A two-dimensional matrix with redshift- and template axes is created from which the pair with the lowest χ^2 -value is selected. Template-fitting codes can be run either with fluxes or magnitudes. However, the flux being the basic physical quantity, the usage of magnitudes can have some significant disadvantages. Very low fluxes in one filter (e.g., in case of a drop-out) below the detection limit can lead to an extracted magnitude value of 99. Therefore, in general, this filter will be ignored for the photometric redshift estimation, losing the information in this filter. In contrast when fluxes are used instead, even negative values still can be considered (which in general is only reasonable as long as the flux is consistent with low positive or zero values within the uncertainties), being of tremendous advantage when dealing with, e.g., drop-outs, as already mentioned.

4.2.2 Subtleties

A well determined magnitude zeropoint is necessary to minimize systematical shifts in color-space. Inaccurate zeropoint determination can easily increase the bias in redshift estimation so that $\langle z_{\text{phot}} - z_{\text{spec}} \rangle \neq 0$. Also a further photometric calibration might be necessary, in order to match the used template set to the used filter set. This calibration can be done by comparison of the photometric redshift output to the spectroscopic redshift predictions and iterative zeropoint corrections in order to minimize the difference between photometric and spectroscopic redshifts. A further major problem of photometric redshifts is that the investigated wavelength range is quite limited. As no spectral features like absorption or emission lines can be resolved, the shape of continuum of the SED-template has to serve as estimator. Especially if only optical data are considered, this can easily lead to degeneracies between different templates or redshifts, for example a mismatch between Lyman break and Balmer break or 4000 Å break (D4000), respectively, leading to an increased value of catastrophic outliers. These degeneracies can in general only be broken by extending the wavelength range, for instance by including near-infrared (NIR) information. Another approach to break these degeneracies is the application of a priori knowledge in form of priors. Possible choices for the prior are the SED-prior restricting the redshift space for specific models. Other choices would be the limitation of absolute

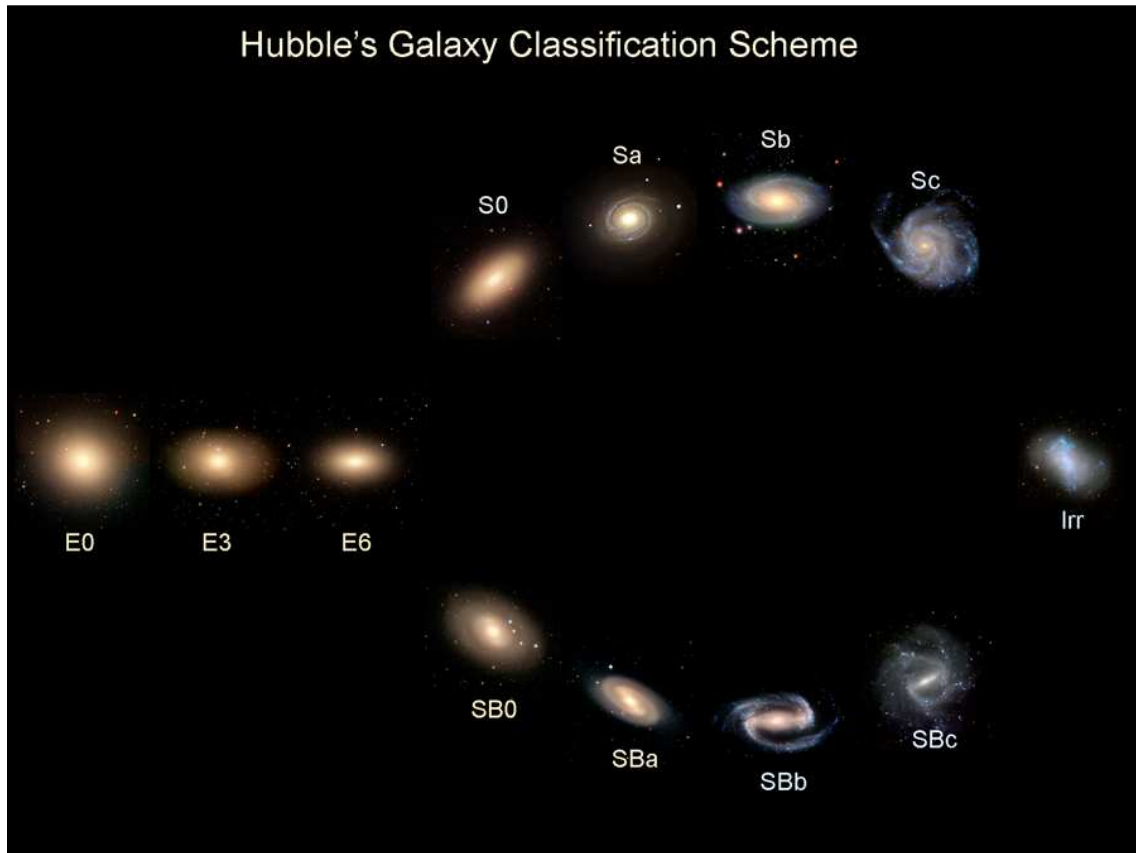


Fig. 4.1: Classification scheme of galaxies as introduced by Edwin Hubble. On the left side we see the elliptical galaxies classified according to their projected ellipticity from E0 to E7, in the middle the lenticular galaxies (S0/SB0), consisting of a more or less structureless disk but showing a spectrum typical for elliptical galaxies, while on the right side we see the two branches of spiral galaxies, normal and barred spirals. Spiral galaxies are classified from Sa to Sc and SBa to SBc for barred ones, depending on how pronounced their bulge is. The classification scheme is completed by irregular galaxies (Irr I and II), which in general show hardly or no structure (credits for the image: <http://www.galaxyzoo.org>).

magnitude to physical values which are observed in nature or applying a probability distribution for templates with respect to apparent magnitudes.

4.2.3 Galaxy Types

The best-known example for a galaxy classification is the so-called Hubble sequence (see Fig. 4.1), based on optical imaging. The basic scheme distinguishes between so-called early type galaxies, represented by elliptical (E0-E7) and lenticular galaxies (S0, SB0), and late type galaxies, represented by spiral (Sa-Sd) and barred spiral galaxies (SBa-SBd). The term early and late type is of pure historical origin and does not mirror the evolutionary state of the described galaxy. Further there are galaxies which do not show strong regularities in structure. Thus, these galaxies are called irregular galaxies (Irr I and Irr II).

Early Type Galaxies

Early type galaxies, comprising elliptical (E) and lenticular galaxies (S0 and SB0), do not show strong signs of structure. Until the late 1970s elliptical galaxies were believed to be rather simple systems. It was assumed that they are disk-free rotationally flattened systems. Being dominated by very old red stellar populations and showing a lack of recent star formation, they were further assumed to be gas-free. Most of these assumptions emerged to be crude approximations and had to be adjusted. Elliptical galaxies are in fact not gas-free but contain extremely hot gas with temperatures about 10^{10} K, preventing significant star formation. The lack of young and massive blue stars also leads to a pronounced 4000 Å break (D4000), which is a dominant feature in the elliptical's spectrum. Only low mass elliptical galaxies seem to contain intermediate age stellar populations. Massive elliptical galaxies are further not flattened by rotation but by an anisotropic velocity distribution. Elliptical galaxies are characterized by their projected ellipticity and classified as E0 ... E7 where the number stands for $10 \cdot (1 - \frac{b}{a})$, with $\frac{b}{a}$ being the axis ratio of the galaxy (see also Fig. 4.1). In general elliptical galaxies are triaxial ellipsoids. The apparent ellipticities do in general not trace exactly the ellipticity of the ellipsoid as they depend on the orientation and the inclination of the galactic ellipsoid towards the observer. The surface brightness is described by the de Vaucouleurs profile (see de Vaucouleurs 1948, 1953)

$$I(r) = I_e \exp \left[-7.667 \left((r/r_e)^{1/4} - 1 \right) \right], \quad (4.2)$$

where the effective radius r_e contains half of the projected light and I_e is the surface brightness at the effective radius. Faber & Jackson (1976) found a relation between the total blue luminosity of elliptical galaxies and their velocity dispersion

$$L_B \propto \sigma^4, \quad (4.3)$$

the so-called Faber-Jackson relation, connecting the mass via velocity dispersion with the absolute luminosity. Elliptical galaxies show signs of a violent evolution history, as several ones with a counter-rotating core have been observed, indicating an elapsed galaxy merger.

As the term *elliptical* galaxy already indicates, the isophotes of elliptical galaxies are described by almost perfect ellipses. The deviation from the elliptical shape is described by the boxiness parameter a_4 (see Carter 1978) which is obtained by expanding the distance $R(\theta)$ of the isophote from the galactical center,

$$R(\theta) = a_0 + a_2 \cos(2\theta) + a_4 \cos(4\theta) + \dots, \quad (4.4)$$

thereby assuming an orientation of the major axis along the x-axis for $\theta = 0$ and $a_2 \geq 0$. For $a_2 = a_4 = 0$ the isophote is described by a circle, with the radius depending on the distance of the isophote. For $a_2 \neq 0$ and $a_4 = 0$ the isophote is described by a perfect ellipse with axis ratio a_2/a_0 . The parameter a_4 describes the deviation of the isophote from a perfect ellipse. For $a_4 > 0$ the isophote appears diskly, for $a_4 < 0$ the isophote appears boxy. The typical deviations of the isophotes of an elliptical galaxy are rather small, being of the order of $a_4/a_0 \sim 0.01$. Surprisingly, a correlation between the boxiness and the kinematical properties of elliptical galaxies have been observed. While the flattening of boxy galaxies originates in the anisotropic velocity distribution, the ratio of circular velocities and velocity dispersions in diskly galaxies indicate that diskly galaxies are at least partially flattened by rotation (see Bender 1988).

Showing a similar SED as classical elliptical galaxies the so-called lenticular galaxies (S0 and SB0) are also counted to early type galaxies and form a transition type between classical ellipticals and the

early spiral type galaxies (Sa and SBa). It is assumed that lenticular galaxies are former spirals with quenched star formation rate and thus relatively old stellar populations, leading to the spectral early-type-like characteristics. This is also confirmed by the observation that lenticular galaxies in general show stronger rotation than classical elliptical galaxies.

Late Type Galaxies

Spiral galaxies apparently consist of two major components, a central bulge and an extended flat disk with more or less pronounced spiral arms. Spiral galaxies are discriminated from early type spirals (Sa) to late type spirals (Sd) (see Fig. 4.1), based on their bulge-to-disk ratio $L_{\text{bulge}}/L_{\text{disk}}$ and the opening angles and brightness structure of the spiral arms. However, this classification is of pure historical origin and does not describe an evolutionary path. The typical bulge-to-disk ratios span a range of $L_{\text{bulge}}/L_{\text{disk}} = 0.3$ for Sa galaxies to $L_{\text{bulge}}/L_{\text{disk}} = 0.05$ for Sd galaxies, the opening angles of the spiral arms increase from $\sim 6^\circ$ to $\sim 18^\circ$ from Sa to Sc and the stellar distribution along the spiral arms becomes less smooth but clumpier for later spiral types (see the lecture books of Carroll & Ostlie 1996 and Schneider 2006a). The properties of the bulge are very similar to those of an elliptical galaxy. In general it is dominated by old stellar populations and the surface brightness profile follows the de Vaucouleurs law (see equation 4.2). Further, the amplitude of rotation velocity and velocity dispersion are of about the same order. The disk consists of metal-rich stars, HI and H₂ gas, molecular clouds, dust and hot gas and shows a much higher rotation velocity than velocity dispersion. Due to the ongoing star formation it is also populated by young stars and therefore shows a much bluer spectrum than the bulge or elliptical galaxies. The surface brightness profile of the disk is in general exponential (see de Vaucouleurs 1958; Freeman 1970),

$$I(r) = I_0 \exp\left(-\frac{r}{r_0}\right), \quad (4.5)$$

with r being the cylindrical radius, r_0 the scale length of the disk and I_0 the central surface brightness. The disk is usually dominated by extended spiral arms, populated by young blue stars and HII-regions. This is also the reason for the increasing brightness contrast when observing the spiral structure in bluer filters. It is highly unlikely that the spiral arms are actual ‘solid’ structures rotating around the galactic center as the rest of the disk, as the differential rotation would have led to a much stronger wind-up of the spiral arms than observed. It is assumed that spiral arms are created by density waves, mildly compressing the local gas to a slightly higher density by about 10-20%, thus inducing a higher star formation rate and leading to an enhanced formation of young blue stars. This also explains the bluish color of spiral arms, dominated by those young blue stars which are born and also die as supernovae in exactly these spiral arms.

The baryonic halo consists of very metal-poor stars with metallicities of a factor 10-1000 lower than solar metallicity.

A similar relationship to the Faber-Jackson relation for ellipticals has been found by Tully & Fisher (1977) for spiral galaxies

$$L \sim v_c^3 \dots^4, \quad (4.6)$$

connecting the absolute luminosity with the circular velocity. The Tully-Fisher relation represents an important tool for distance determination of spiral galaxies. By measuring the circular velocity, the rest-frame luminosity can be calculated and compared to the observed apparent luminosity. The magnitude difference directly relates to the luminosity distance (see equation 2.36) or distance

modulus (see equation 2.38) of the considered galaxy. Considering the rotation curve of spiral galaxies it becomes obvious that the kinematics do not only trace the luminous matter. On large scales the rotation velocity does not decrease but remains almost constant along all kinematically traceable scales, implying an increase of galaxy mass directly proportional to the enclosed radius. As this cannot be easily explained only with baryonic matter the observed rotation curves were one of the first hints to non-luminous and non-baryonic matter, so-called dark matter.

Beside the ordinary spiral galaxy types there is a further type where the spiral arms do not arise from the galaxy centers but from the ends of a central bar, which goes through the galactic center. These galaxies are called barred spiral galaxies, classified in an analogous way as the normal spiral galaxies from SBa to SBd.

Finally, when extending the Hubble sequence at the late type end there are low mass galaxies which do show hardly (Irr I) or do not show (Irr II) show regular structures. These galaxies appear in much bluer colors and consist of a higher fraction of massive young blue stars and molecular clouds.

4.2.4 PhotoZ

To estimate photometric redshifts we use the PhotoZ code of Bender *et al.* (2001). The PhotoZ code was successfully applied in a variety of contexts, e.g., in Gabasch *et al.* (2004a, 2006, 2008), Feulner *et al.* (2005, 2006), Drory *et al.* (2001), Brimiouille *et al.* (2008), Lerchster *et al.* (2011), Spinelli *et al.* (2012) and recently Gruen *et al.* (2013). The template set was developed by Bender *et al.* (2001) and was composed from Mannucci *et al.* (2001), Kinney *et al.* (1996) and semi-empirical templates constructed by fitting combinations of theoretical SEDs from Maraston (1998) and Bruzual A. & Charlot (1993) with variable reddening (Kinney *et al.* 1994), as described in Gabasch *et al.* (2004a,b). Some of these SEDs actually were made to match galaxies at redshifts between 3 and 4, and between 4 and 5, respectively, which are a minority in the CFHTLS-Wide data. We therefore replace some of these SED templates and complete the sample by templates taken from the LePhare code (Ilbert *et al.* 2006), based on models from Coleman *et al.* (1980) to better match the colors of local, star-forming blue galaxies.

We run the PhotoZ code, assuming a Λ CDM-universe with values of $\Omega_m = 0.27$, $\Omega_\Lambda = 0.73$ and a Hubble constant of $H_0 = 72 \text{ km s}^{-1} \text{ Mpc}^{-1}$. We fit a redshift range of $0 \leq z \leq 9$ with a step size of $\Delta z = 0.01$. The code accepts both magnitudes and fluxes as input. We use fluxes in units of nJy (f_ν). The χ^2 -value for a given model at a certain redshift is calculated according to equation (4.1). However, in order to avoid unphysical solutions as early type galaxies at unreasonably high redshifts or galaxies with unphysical high or low rest-frame luminosities, the PhotoZ code has implemented a redshift prior and an absolute luminosity prior. The redshift prior is defined as

$$P_z(z) = \exp \left[-0.693 \cdot \left(\frac{z}{a} \right)^b \right]. \quad (4.7)$$

The value of a indicates the redshift where the redshift prior drops down to a value of 50%. This means, the lower the value of a , the sooner the considered SED-template ‘dies out’. Therefore the value of a is smaller for early type galaxies ($0.5 \leq a \leq 1$) than for late type galaxies ($2 \leq a \leq 5$). The value of b gives the steepness of the prior profile, the larger b , the steeper the profile becomes. For models with prior values of $a \leq 2$ we use values of $b = 4$, for models with $a > 2$ we use $b = 2$. The redshift prior is also illustrated in the upper panels of Fig. 4.3 for different values of a and b .

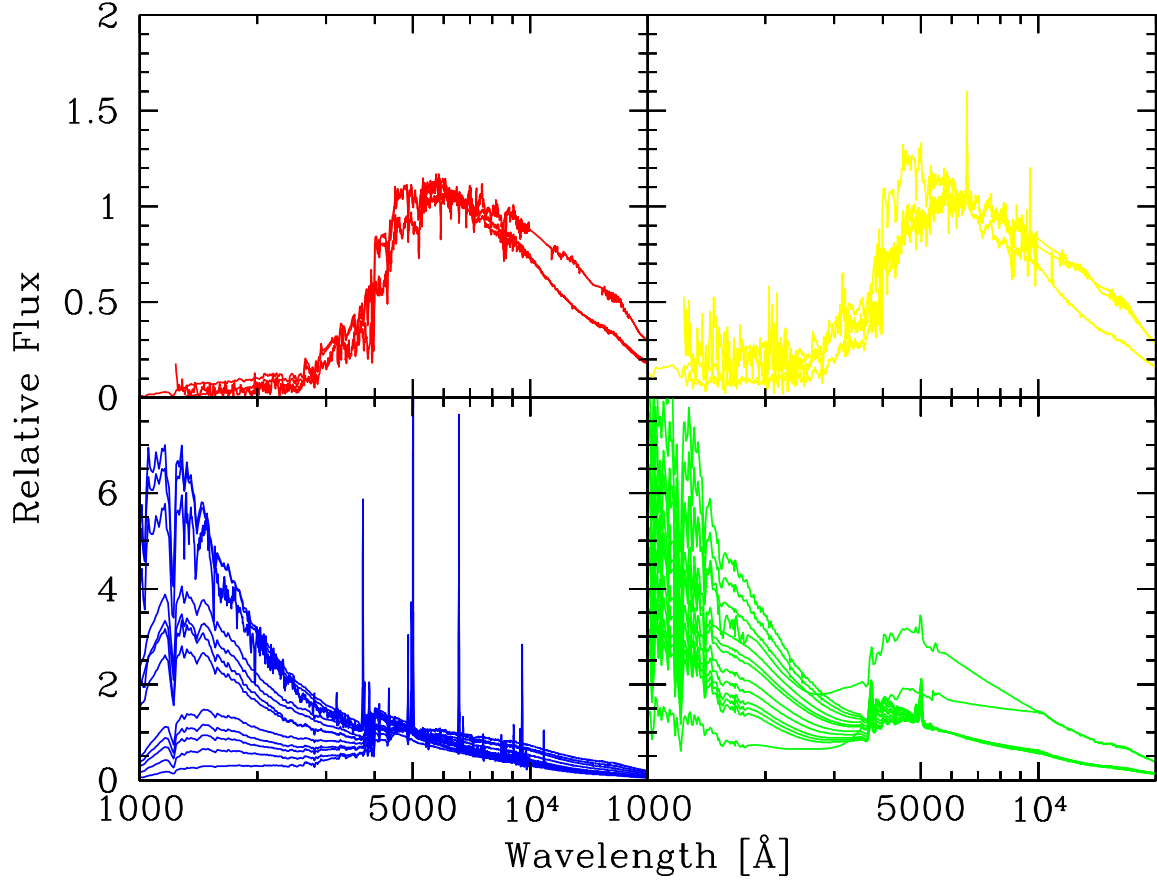


Fig. 4.2: Applied template set. The upper panel on the left side shows the early type templates set. The upper right panel shows the transition galaxies between the early type sample and the strongly starforming galaxy sample derived from semi-analytic models (lower left panel). The lower right panel shows the templates chosen from Ilbert *et al.* 2006.

The second prior, the luminosity prior, suppresses solutions with unphysical absolute luminosity values and is defined as

$$P_L(M) = \exp \left[-0.693 \cdot \left(\frac{M - M^*}{\sigma^*} \right)^p \right]. \quad (4.8)$$

M^* indicates the magnitude, the luminosity prior is centered on. We choose as central value a magnitude of $M_B = -19$ in the B -band. The value of σ^* defines the width of the luminosity prior, i.e., the larger σ^* , the larger the window of allowed absolute luminosities around the central value M^* . Finally, the value of p determines the steepness of the luminosity prior. The larger the value of p , the steeper the profile becomes. For low values of p , the luminosity prior resembles the shape of a Mexican Hat, while for infinitely large σ^* the luminosity prior becomes a top hat function. This is also illustrated in the lower panels of Fig. 4.3 for different values of σ^* and p . For the luminosity prior we use values of $M^* = -19$, $\sigma^* = 6$ and $p = 6$ in B -band.

Thus, including both priors, the total probability of an SED-template for a certain redshift is given by

$$P(z, \text{Model}) = P_z \cdot P_L \cdot \exp(-\chi^2/2). \quad (4.9)$$

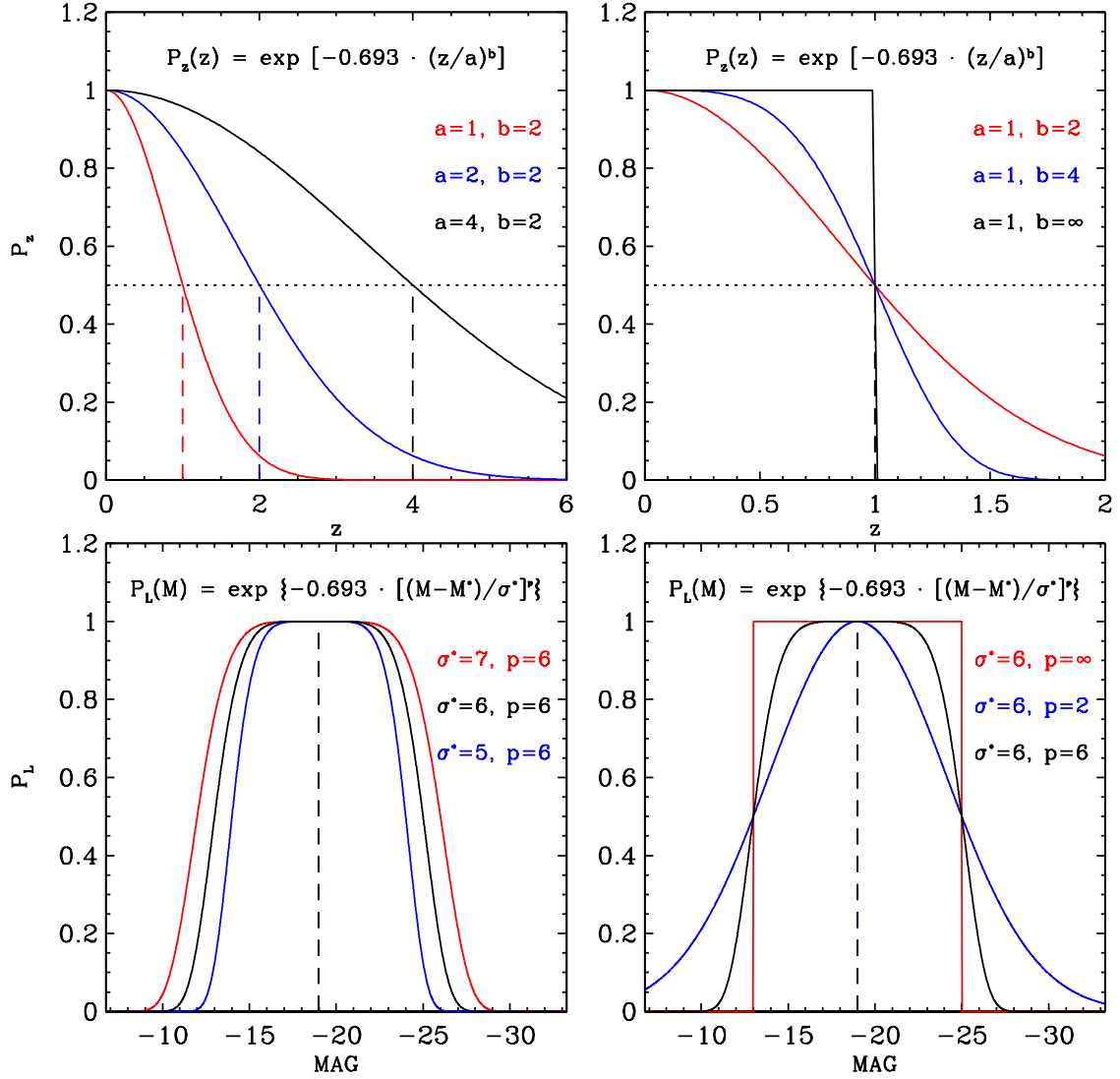


Fig. 4.3: Priors used in the PhotoZ code. The upper panels show the redshift prior, the lower panels the luminosity prior. Parameter a indicates the redshift, where the redshift prior for the considered redshift drops down to 50%. The upper left panel shows the redshift prior for values of $a = 1$ (red), $a = 2$ (blue) and $a = 4$ (black). Parameter b gives the steepness of the redshift prior. The upper right panel shows the redshift prior for values of $b = 2$ (red), $b = 4$ (blue) and $b = \infty$ (black), for identical parameter $a = 1$. We see, the higher the value of b , the steeper the profile.

Regarding the luminosity prior, the value of M^* gives the center of the luminosity prior, the value of σ^* gives its width. The lower left panel shows the luminosity prior for values of $\sigma^* = 7$ (red), $\sigma^* = 6$ (black) and $\sigma^* = 5$. The value of p indicates the steepness of the luminosity prior. The lower right panel shows luminosity prior for values of $p = \infty$ (red), $p = 2$ (blue) and $p = 6$ (black). The higher the value of p , the steeper the profile. The luminosity priors in the lower panels are centered at a magnitude of $M^* = -19$.

Chapter 5

Data

This chapter describes analyses and results which have been submitted (Brimioulle *et al.* 2008 and Brimioulle *et al.* 2013).

Data acquisition and data reduction (imaging and spectroscopic data) described in the following sections have been performed by Mike Lerchster.

5.1 Imaging Data

This work uses public CFHT Legacy Survey¹ Wide (CFHTLS-Wide) and Deep (CFHTLS-Deep) data. The CFHTLS maps over 190 deg² in Wide and 4 deg² in Deep, covering the fields in $u^*g'r'i'z'$ -band observations with the MegaPrime camera. MegaPrime (see Boulade *et al.* 2003) is an optical multi-chip instrument, consisting of a 9×4 CCD array with 2048×4096 pixels in each CCD, a pixel scale of 0.186 arcsec/pixel and a total field of view of $\sim 1^\circ \times 1^\circ$. The CFHTLS-Wide comprises four large tiles W1 (72 deg²), W2 (49 deg²), W3 (49 deg²) and W4 (25 deg²).² The survey is described in various publications (e.g., Hoekstra *et al.* 2006; Semboloni *et al.* 2006; Coupon *et al.* 2009; Astier *et al.* 2006). Our photometric analyses are restricted to an area of 124 deg² (W1: 49 deg², W2: 25 deg², W3: 30 deg² and W4: 20 deg²), representing the publicly available imaging data in February 2009 with completed five-band-photometry. Additionally we include the significantly deeper (~ 70 hours exposure time in i' for the Deep fields in comparison to 1-2 hours exposure time in i' for the Wide fields) CFHTLS-Deep fields D1 and D3 for comparison, as they overlap with W1 and W3. The layout of the analyzed CFHTLS pointings is shown in Fig. 5.1. An overview of the observed filters is given in Fig. 5.2.

The *Elixir* (see Magnier & Cuillandre 2004) preprocessed single-frame imaging data are downloaded from the Canadian Astronomical Data Centre (CADC)³. The *Elixir* preprocessing includes bias and dark subtraction, flatfielding, fringe correction in the i' - and z' -band data, as well as photometric calibration and a preliminary astrometric solution. We then use the *THELI* -pipeline⁴ (see also Erben *et al.* 2005 and Erben *et al.* 2009) to improve the astrometric solution, remap and finally stack the single exposures. The reduction procedure is described in detail in Erben *et al.* (2009). The

¹ <http://www.cfht.hawaii.edu/Science/CFHTLS>

² <http://terapix.iap.fr/cplt/oldSite/Descart/summarycfhtlswide.html>

³ <http://www1.cadc-ccda.hia-ihp.nrc-cnrc.gc.ca/cadc/>

⁴ <http://www.astro.uni-bonn.de/~mischa/theli.html>

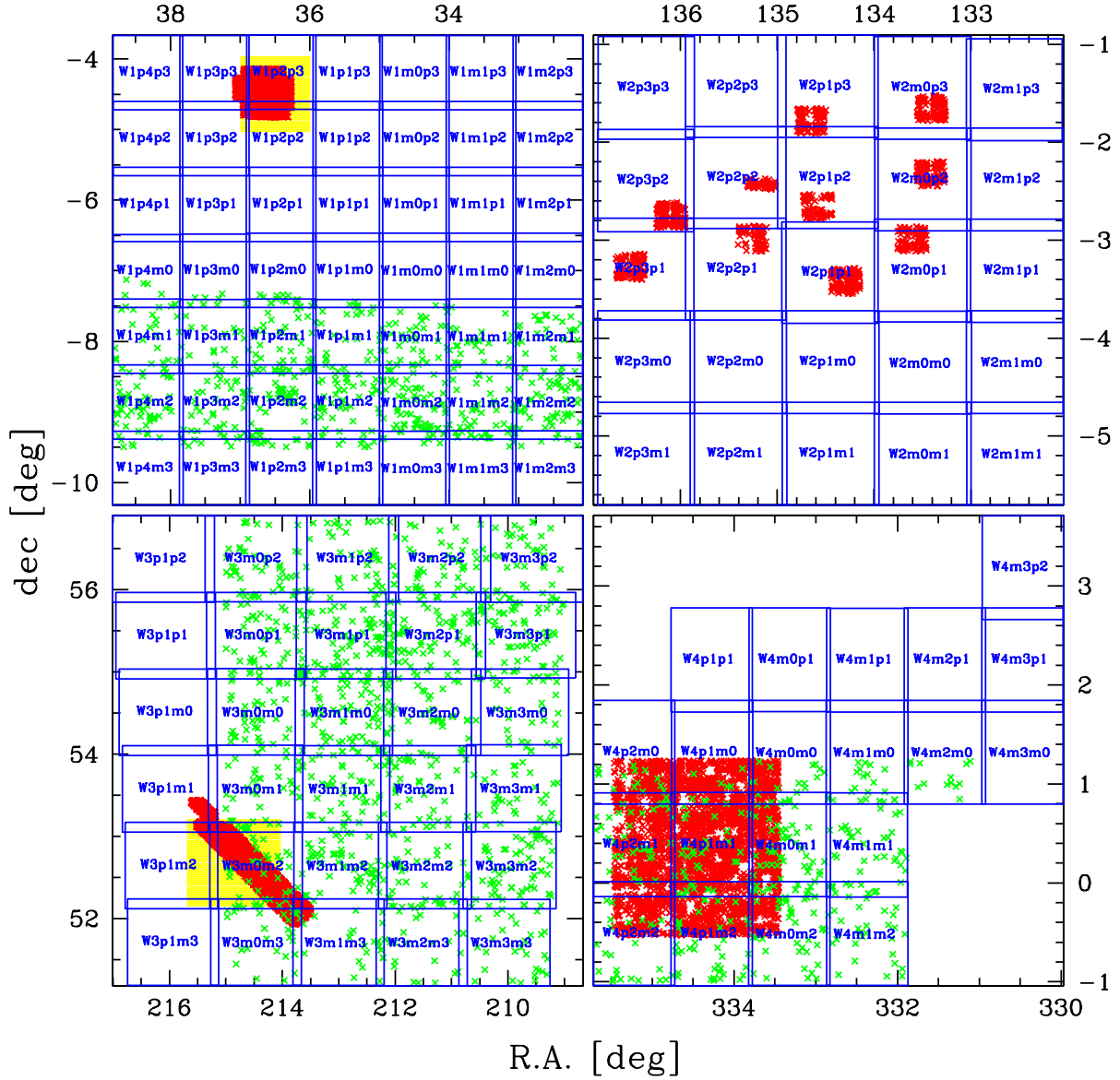


Fig. 5.1: Layout of the CFHTLS-Wide, W1 (upper left panel), W2 (upper right panel), W3 (lower left panel) and W4 (lower right panel). The individual field names and boundaries are marked in blue, the spectroscopic data used for photometric redshift calibration are shown in red and the green symbols show the overlap with spectroscopic SDSS data. The yellow areas in W1 and W3 indicate the locations of the CFHTLS-Deep fields D1 and D3.

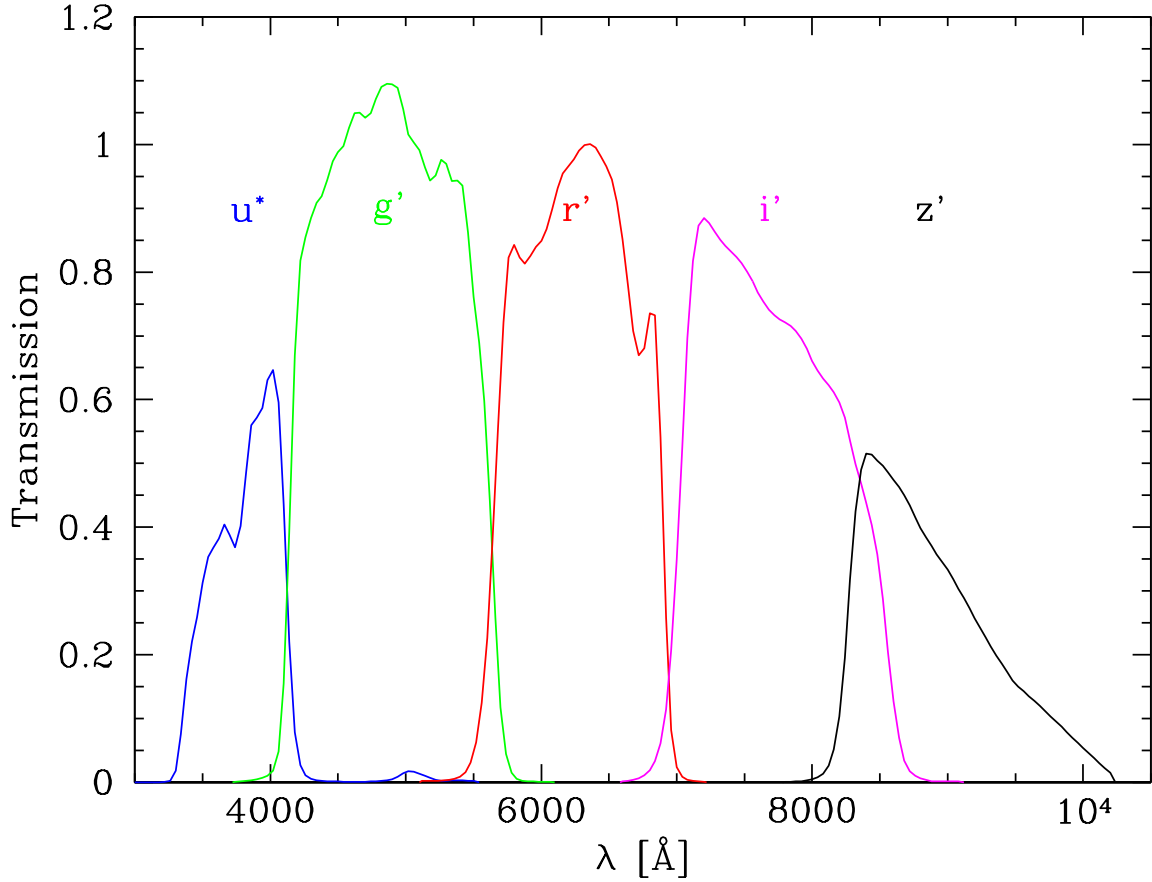


Fig. 5.2: Filter transmission curves for the CFHTLS u^* , g' , r' , i' and z' . The filter transmission curves have been corrected with respect to atmospheric extinction.

original approach for astrometric calibration uses reference catalogs from the United States Naval Observatory (USNO) (see also Erben *et al.* 2009). A better astrometric solution can be fitted if reference catalogs from the Sloan Digital Survey Data Release 6 (SDSS-DR6, Adelman-McCarthy & et al. 2007) or, where not available, from the Two Micron All-Sky Survey (2MASS, Jarrett *et al.* 2000) are used instead. This reduces shape artefacts in the remapping to the astrometric solution, which is relevant in the anisotropy correction of the point spread function (PSF) of the objects used in the lensing analysis later on, but only plays a minor role for photometric issues. We therefore use stacked i' -band images with SDSS- and 2MASS-based astrometry for the shape determination and analysis and USNO-based astrometry $u^*g'r'i'z'$ -band images for the photometric extraction. The mean limiting magnitudes of the CFHTLS-Wide images are 25.3, 25.6, 24.5, 24.6 and 23.6 (5σ detection within a 2 arcsec diameter aperture for a point source) for u^* , g' , r' , i' and z' . The PSF full width at half maximum (FWHM) of the i' -bands is close to 0.8 arcsec for all fields. The reduced imaging data consists of coadded science frames and the corresponding error frames (weight files) and image masks. The subsequent analyses are carried out strictly on a one square degree base, not coadding or mixing data from neighboring pointings. The investigations for the individual CFHTLS-Wide fields are then combined to a global conclusion.

5.2 Spectroscopic Data

The dataset is extended by several spectroscopic samples which overlap with our photometric data. These are the VIMOS VLT Deep Survey (VVDS)-Deep (Le Fèvre *et al.* 2005) on W1 and VVDS-F22 (Le Fèvre *et al.* 2004, 2005; Garilli *et al.* 2008) on W4, the Deep Extragalactic Evolutionary Probe (DEEP) 2 survey (Davis *et al.* 2003, 2007; Vogt *et al.* 2005; Weiner *et al.* 2005) on the W3 and VIisible Multi Object Spectrograph (VIMOS) spectra from the ESO Program ID 082.A-0922(B) (PI: Mike Lerchster) on the W2. The data reduction of the W2-spectra follows the description on the zCOSMOS release webpage⁵ and Lilly *et al.* (2007). While the VVDS-Deep and DEEP2 contain spectroscopic redshifts down to $i' \sim 24$, the spectroscopic redshifts from VVDS-F22 and ESO Program ID 082.A-0922(B) are limited to $i' \sim 22.5$. Additionally several pointings in the W1, W3 and W4 have overlap with spectroscopic objects from the Sloan Digital Sky Survey (SDSS). In total we obtain 3 562, 960, 7 986 and 3 746 high quality spectroscopic redshifts in the W1, W2, W3 and W4, summing up to a total number of 16 254 spectroscopic redshifts (not including SDSS spectra), of which 10 025 are for objects brighter than $i' = 22.5$.

5.3 Photometric Catalogs

5.3.1 Creation of Multicolor Catalogs

The calculation of colors appears to be a quite simple task at first look, as it just means the measurement of fluxes of an object in different filters and the calculation of their ratio. In practice there are some complications. In order to obtain meaningful colors it is necessary to consider the light fraction from the same galaxy area. To ensure this we use aperture photometry to measure the fluxes. Unfortunately this approach is not sufficient, as the photometric conditions as PSF, i.e., mainly the seeing in the observations in different filters, are in general not identical. The light of objects in an image with worse PSF is distributed over a larger area than the light in an image with better seeing. Therefore for the creation of the multicolor catalogs we need to adjust the PSF of the different filter images to the same value, i.e., the value of the worst filter. This is in most cases the u^* -band with seeing values spanning a range between 0.63 and 1.22 arcsec with a median of 0.9 arcsec. For this we perform a convolution with a Gaussian kernel on each one square degree pointing. The simplest approach is a global convolution with a constant convolution kernel. Under ideal circumstances this kernel can be calculated with the formula

$$FWHM_{\text{kernel}} = \sqrt{FWHM_{\text{bad}}^2 - FWHM_{\text{good}}^2}, \quad (5.1)$$

$FWHM_{\text{good}}$ indicating the original seeing and $FWHM_{\text{bad}}$ the seeing which is to be accomplished. We cross-check the accuracy of this method by considering the colors of stellar objects in circular apertures of different diameters from 8 to 18 pixels (i.e., 1.5 to 3.3 arcsec). Stars appear as point-like sources on the sky, being smeared out by the PSF of atmosphere and telescope optics. Therefore we should observe identical colors in the different apertures if the PSF profiles in all filters are the same. Unfortunately this is not the case. As the PSF profile in general is not an analytic Gaussian and due to anisotropy of the PSF pattern, variation over the field of view and differing PSF profiles in the different filters, this approach turns out not to be sufficient. Especially the PSF turns out not to be

⁵ http://irsa.ipac.caltech.edu/data/COSMOS/spectra/z-cosmos/Z-COSMOS_INFO.html

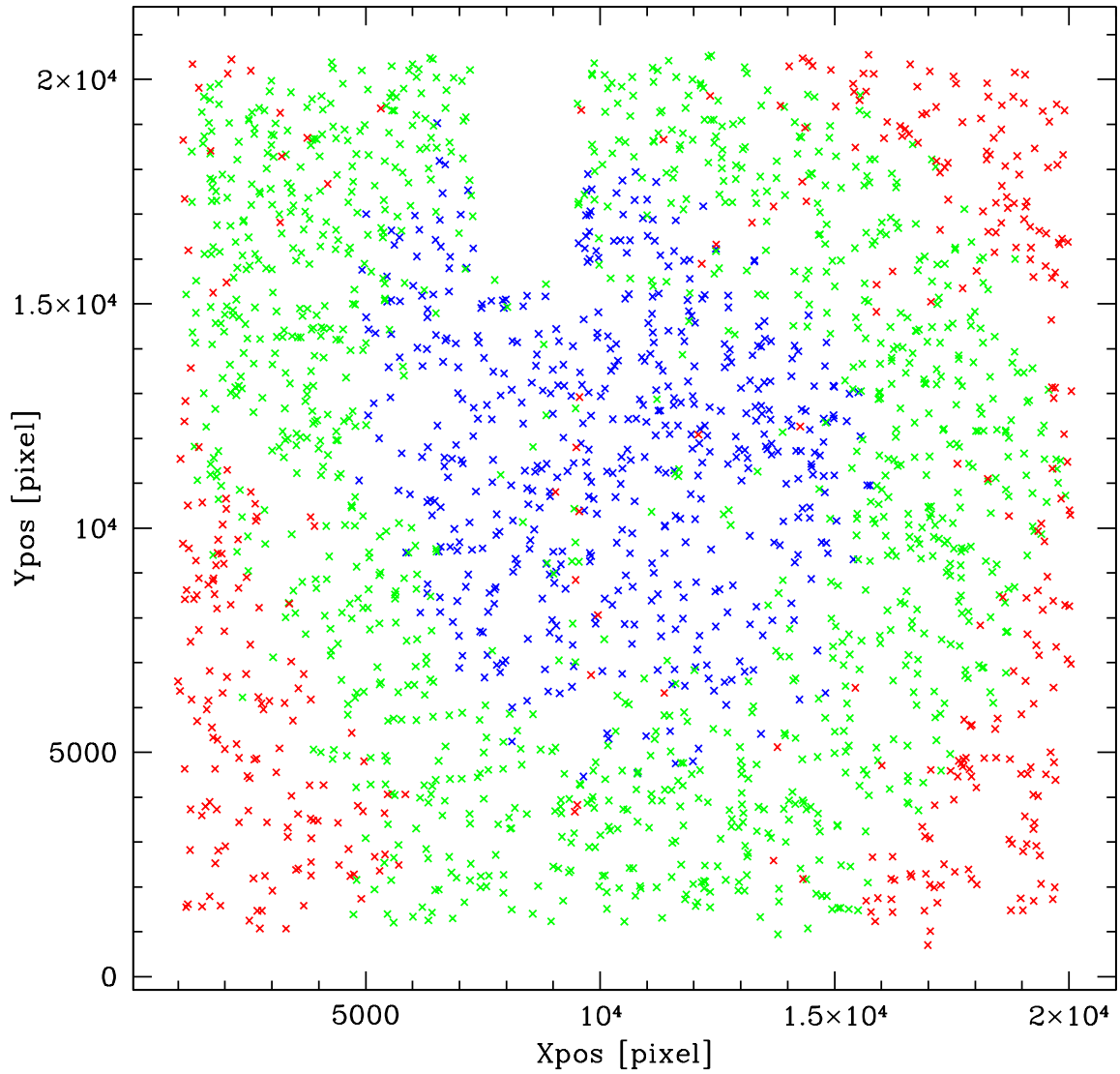


Fig. 5.3: Example of the PSF behavior shown on the i' -band observation of the W1p2p3. The blue symbols show the region with $FWHM < 0.7$, the green symbols the region with $0.7 \leq FWHM \leq 0.8$ and the red symbols the region with $FWHM > 0.8$. The empty region in upper middle has been masked due to a broken chip of the CCD during the observation time of this specific pointing.

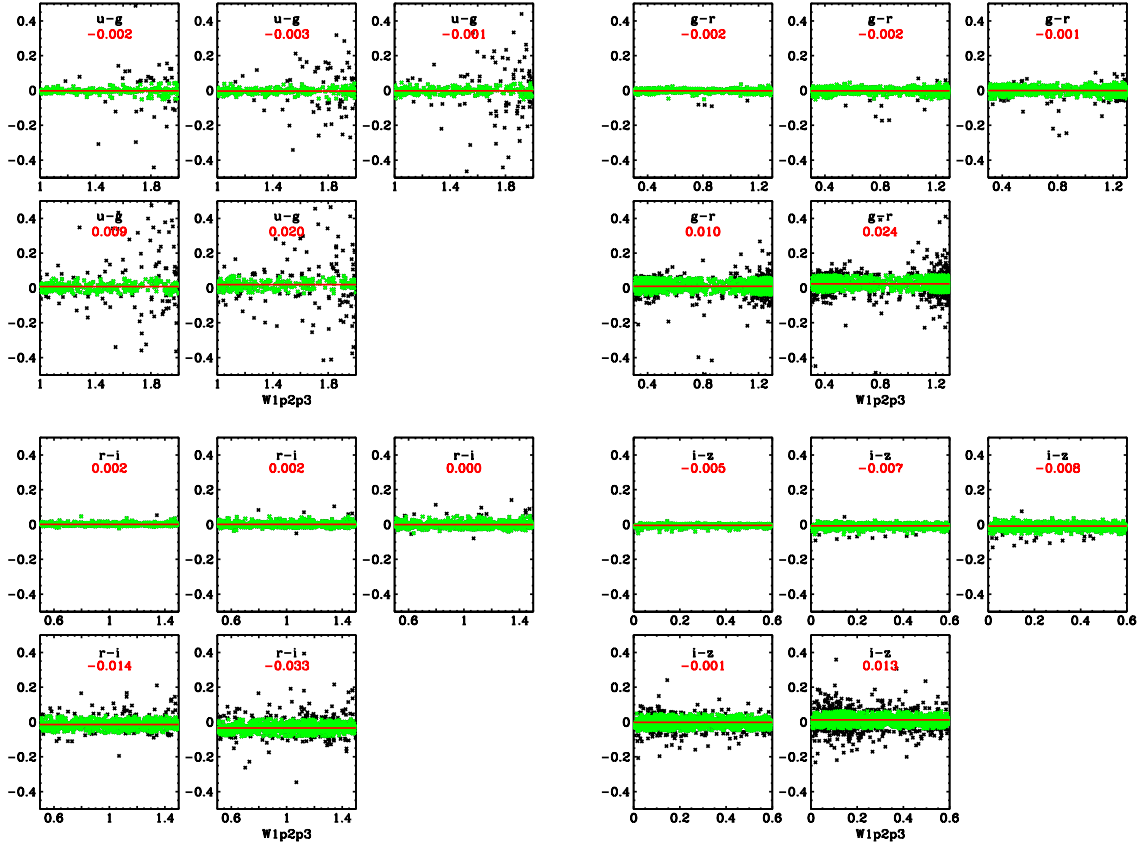


Fig. 5.4: Stellar colors after convolving to equal PSF. The five minor panels within each of the four major panels show the stellar colors in aperture 1 (8 pixels diameter) against the color difference to aperture 2, 3, 4 and 5. The major upper left panel shows the $u - g$ -color, the major upper right $g - r$, the major lower left one shows $r - i$ and the major lower right one shows $i - z$. The green symbols show the stars which have been used to estimate the deviation in color (added in red to every single panel).

constant over the whole field, simply speaking, the seeing deteriorates with increasing distance from the image center. The convolution to exactly matching PSF patterns is a difficult and delicate task (see for example Darnell *et al.* 2009 or Hildebrandt *et al.* 2012), but fortunately the PSF variations from image center to image border in most filters happen to be almost self-similar, so that convolution with an adjusted constant Gaussian kernel delivers satisfactory results. An example for the PSF behavior on the field of view of one pointing is shown in Fig. 5.3. As the analytic approach does not properly apply, we derive the best-fitting convolution by empirical investigation. We run a series of test-convolutions with iteratively adjusted convolution kernels and compare after each step the stellar colors in apertures for all available filters. This process converges very well and quickly leads to stable and meaningful colors for stars and should also provide reasonable colors for the galaxies. Fig. 5.4 shows the remaining color deviations on the example of the W1p2p3 pointing.

After convolution of all images to matching PSF patterns the multicolor catalogs can be cre-

ated. For this we run the `SExtractor` software⁶ (see Bertin & Arnouts 1996) in dual-image mode. Being the deepest exposure we choose the unconvolved i' -band as our detection band and extract the fluxes and flux errors from the convolved $u^*g'r'i'z'$ -bands. We detect objects with a threshold of 2σ above the background on at least four contiguous pixels. We make use of the `SExtractor` option of convolving the data with a FWHM of 0.4 arcsec before detection on the unconvolved i' -band to suppress correlated noise on scales shorter than the PSF. After detection and flux extraction we need to adjust the flux errors. The flux error in `SExtractor` is estimated by

$$\Delta F = \sqrt{A\sigma^2 + \frac{F}{g}}, \quad (5.2)$$

with A being the area over which the flux is summed, σ the standard background deviation estimated from the image background, F the object flux and g the effective detector gain (see Bertin & Arnouts 1996). Therefore the flux error estimates strongly depend on the background root mean square (rms). The convolution of the frames smooths the background, seriously reducing the rms and leading to a significant underestimation of the photometric errors. In order to correct for this we rerun `SExtractor` measuring the rms on the unconvolved $u^*g'r'i'z'$ -bands, set them into relation with the values of the convolved images and recalculate the flux errors. The morphological information as FWHM and `SExtractor` stellar classification are extracted from the unconvolved i' -band. As the final step we paste the individual filter catalogs for each field and assign the image masks to identify regions with doubtful photometry, creating color catalogs for all pointings, comprising all fluxes, magnitudes, bad area masks and photometric flags. In Fig. 5.5 we show the number counts and magnitude errors of the W1p2p3 as example for our CFHTLS Wide catalogs.

5.3.2 Calibration of Photometric Zeropoints

In order to evaluate the quality of the photometric redshifts we introduce three quantities:

- i) the outlier rate η , defined as the fraction of objects exceeding a rest-frame error of 0.15, i.e.,

$$\eta = \text{fraction with } \left\{ \frac{|z_{\text{spec}} - z_{\text{phot}}|}{1 + z_{\text{spec}}} \geq 0.15 \right\}, \quad (5.3)$$

- ii) the photometric redshift scatter, calculated from the width of the central part of the error distribution

$$\sigma_{\Delta z/(1+z)} = 1.48 \times \text{median of } \left\{ \frac{|z_{\text{spec}} - z_{\text{phot}}|}{1 + z_{\text{spec}}} \right\}_{\text{Non-outliers}}, \quad (5.4)$$

which is insensitive to outliers, and

- iii) the mean photometric redshift error

$$\Delta z/(1+z) = \frac{1}{N_{\text{spec}}} \sum_i^{N_{\text{spec}}} \frac{|z_{\text{phot},i} - z_{\text{spec},i}|}{1 + z_{\text{spec},i}}. \quad (5.5)$$

⁶ <http://www.astromatic.net/software/sextractor>

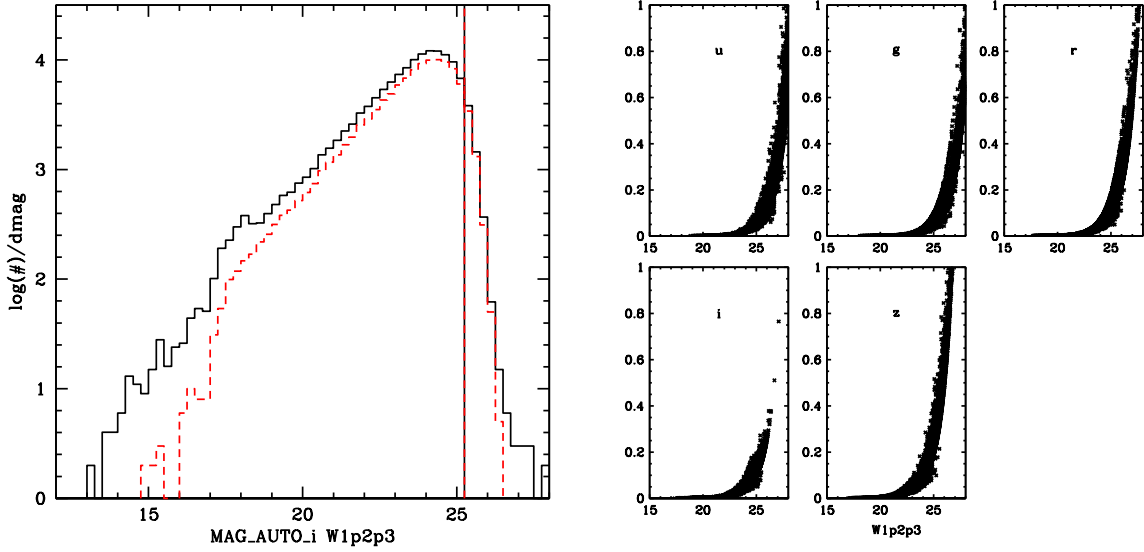


Fig. 5.5: The left panel shows the number counts of the W1p2p3 i' -band magnitude, the black line shows all objects, the red line shows all objects in unmasked areas. On the bright end the number counts of the unmasked objects rapidly drop down, as all stellar objects are masked and further bright objects are easily discarded due to saturation effects. The right panel show the magnitude errors in all five filters as a function of magnitude.

In these equations N_{spec} stands for the number of spectroscopic redshifts, z_{spec} and z_{phot} are the spectroscopic and photometric redshifts, respectively.

The accurate estimation of photometric redshifts requires precise color estimates. Matching the PSF in the different filters is only the first step to achieve this. The next step is a proper absolute and relative calibration of the photometric magnitude zeropoints of the images. Possible error sources are inaccurate zeropoint determination during the data reduction and furthermore galactic extinction, leading to a reddening of the colors as shorter wavelengths are absorbed more strongly by the galactic dust. Discarding the following steps of zeropoint calibration can lead to increased catastrophic outlier rates and significantly larger systematic and statistical redshift errors. This is shown very well in Fig. 5.6, presenting the photometric redshift results without further zeropoint calibration. The results of the photometric redshift estimates are very inhomogeneous due to differing zeropoint accuracy in the four major patches. While the photometric redshift estimates for objects with $17.0 \leq i' \leq 22.5$ in W1 still look rather descent with an outlier rate of $\eta \sim 5\%$ and a photometric redshift scatter of $\Delta z/(1+z) \sim 0.06(1+z)$ and $\Delta_{\Delta z/(1+z)} \sim 0.06(1+z)$, especially in W4 the photometric redshift quality is completely unsatisfactory, showing an outlier rate of more than 17% and a high mean redshift error of $\Delta z/(1+z) \sim 0.11(1+z)$ and $\Delta_{\Delta z/(1+z)} \sim 0.07(1+z)$ with a dramatic scatter for $z_{\text{phot}} \leq 0.5$. As we see in the Appendix in Table A.1, for this effect the insufficient zeropoint determination in the u^* -band is most likely to blame. The results are summarized in Table 5.1.

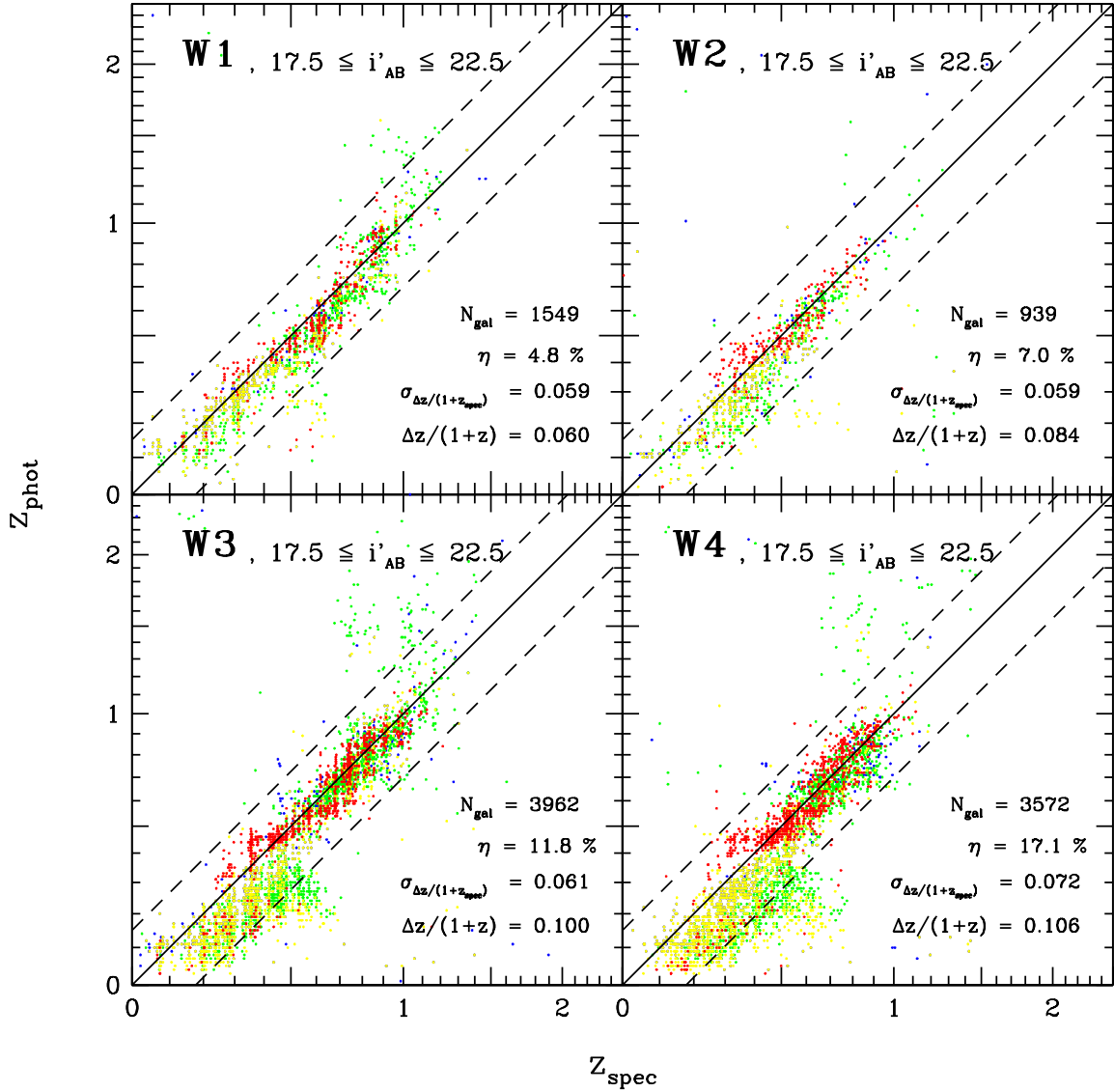


Fig. 5.6: Comparison between photometric redshifts estimated without any zeropoint correction (y-axis) and spectroscopic redshifts (x-axis) for all galaxies with $17.0 \leq i' \leq 22.5$ in the four large CFHTLS-Wide pointings. The mean photometric redshift error $\Delta z/(1+z)$ and photometric redshift scatter $\sigma_{\Delta z/(1+z)}$, respectively, are large and the catastrophic outlier rate is very unsatisfactory. Further the large variations between the four major fields show a certain inhomogeneity in zeropoint estimation. The symbol colors indicate the SED type of the galaxies, going from red (early type galaxies) over yellow and green to blue (very strongly star-forming late type galaxies). The results are summarized in Table 5.1.

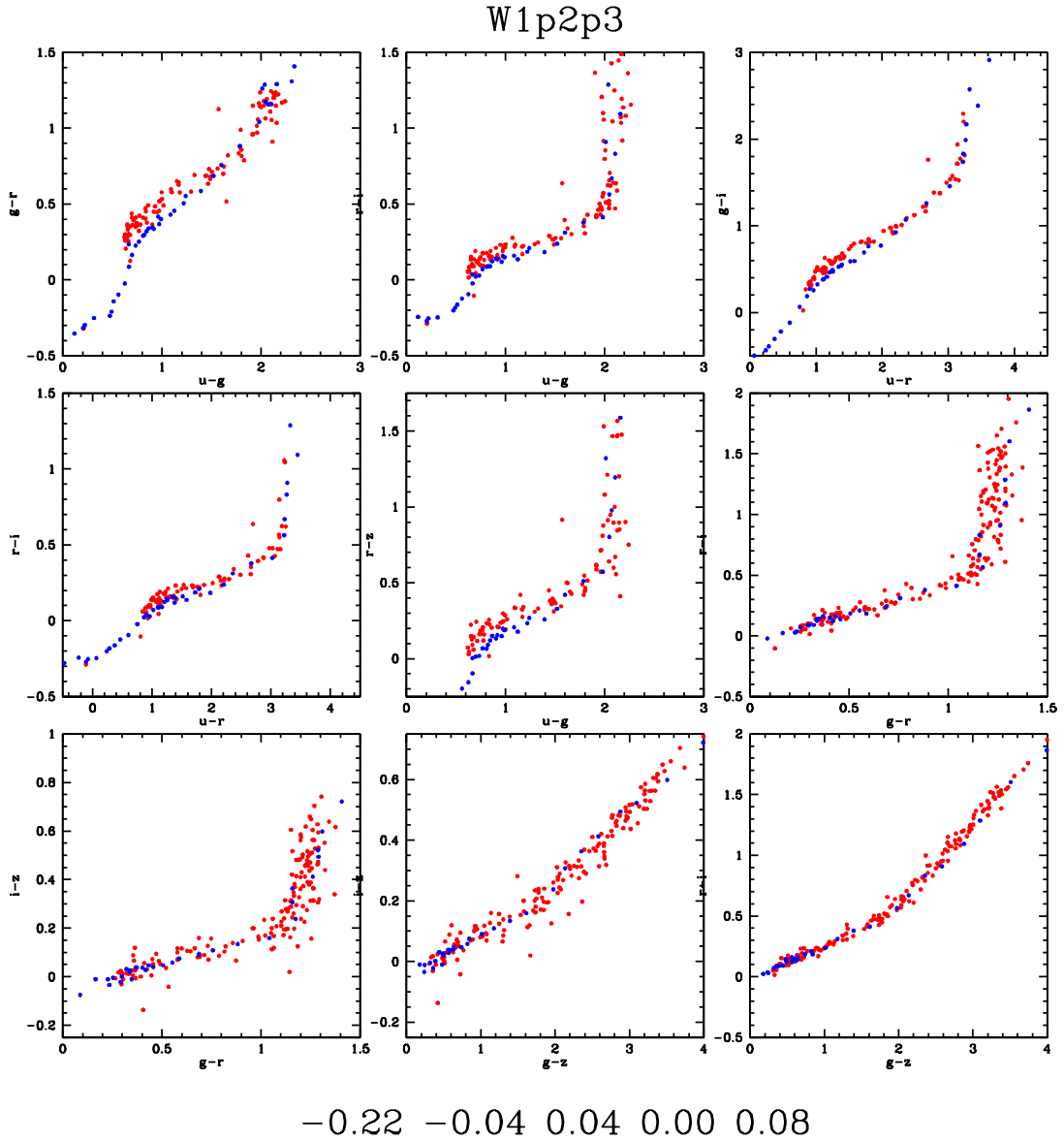


Fig. 5.7: Color-color plots of the observed stellar sequence in W1p2p3 (red symbols) in comparison to the Pickles star library (Pickles 1998) (blue symbols). The theoretical and observational stellar colors match well after the zeropoint correction. The only exception is the u^* -band, where we fit the red end of the stellar sequence to provide a homogeneous base for the complete CFHTLS-Wide. Below the x-axis the applied zeropoint offsets are shown.

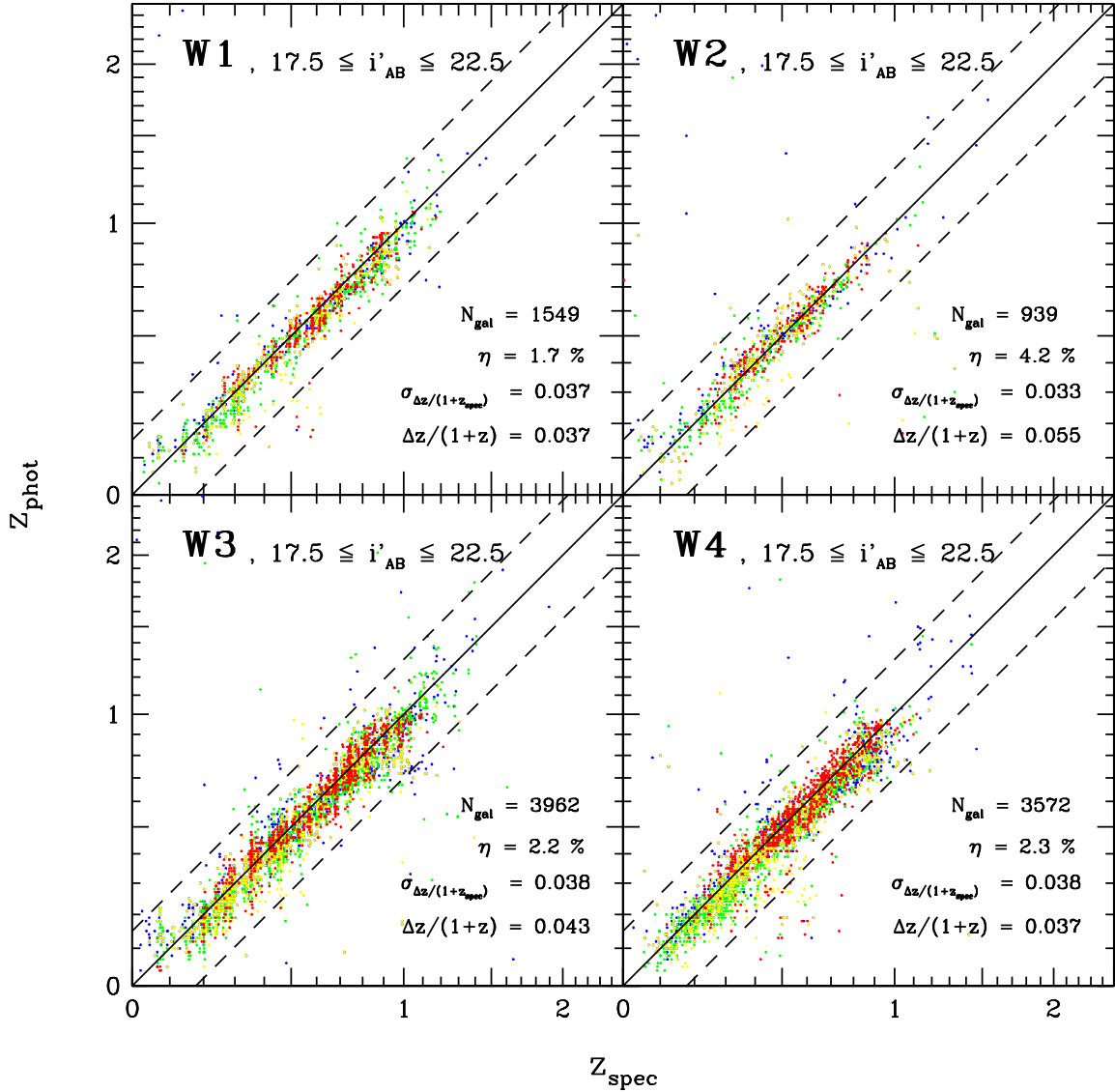


Fig. 5.8: Same as Fig. 5.6 for photometric redshifts after zeropoint calibration on the stellar sequence using the Pickles star library (Pickles 1998). Both, photometric redshift scatter and catastrophic outlier rate decrease significantly, further leading to a much larger homogeneity between the different CFHTLS-Wide fields. The symbol colors indicate the SED type of the galaxies, going from red (early type galaxies) over yellow and green to blue (very strongly star-forming late type galaxies). The results are summarized in Table 5.1.

Calibration on Stellar Sequences

Being the deepest exposure we assume the zeropoint determination of the i' -band to be the most accurate and choose it as absolute calibration reference. We assume the galactic extinction to be approximately constant over the field of view of one pointing (one square degree). We look up the values for the galactic extinction⁷ for each pointing and correct the fluxes and magnitudes of the i' -band. For the zeropoint calibration of the remaining filters we make use of the Pickles star library (Pickles 1998) and consider the stellar sequences in color-color-diagrams. We compare the sequences of the stars from the star library with the sequence of stars extracted from the data, thus applying a relative zeropoint calibration, using the calibrated i' -band zeropoint as reference. For this correction we select all objects with a `SExtractor` stellar classification of better than 0.97 and an extraction flag of 0. We then apply zeropoint shifts in that way, that theoretical and measured stellar sequences match in color-space. An example for the W1p2p3 is shown in Fig. 5.7. This method corrects the observed stellar colors very well, with exception of the u^* -band, where the photometric throughput is not entirely understood. We choose to fit the red end of the stellar sequences for all individual pointings in order to receive a homogeneously calibrated base for the complete CFHTLS-Wide.

The zeropoint calibration on the stellar sequences from the color-color-diagrams significantly improves the quality and the homogeneity of the photometric redshift estimates (see Fig. 5.8). For objects with $17.0 \leq i \leq 22.5'$ the outlier rate η only varies now between 1.7 and 4.2%, the photometric redshift scatter only varies between 0.037 and 0.055 ($1+z$) for $\Delta z/(1+z)$ and 0.033 and 0.038 ($1+z$) for $\sigma_{\Delta z/(1+z)}$. The results are summarized in Table 5.1. The applied stellar calibration offsets for all investigated CFHTLS-Wide pointings are summarized in the Appendix in Table A.1.

Calibration on Spectroscopic Redshifts

In theory we can start to calculate photometric redshifts from this point, but practice teaches us that the results without further calibration in most cases are not entirely satisfactory. Firstly we do not know the photometric throughput to ultimate precision (this especially concerns the u^* -band, see the stellar sequences in Fig. 5.7). Further we do not optimize our template set to match the colors of the CFHTLS-Wide. Therefore a further calibration step is recommendable. The PhotoZ code does not only calculate photometric redshift estimates but is also able to be run with a given true redshift (obtained from spectroscopic observation), delivering the best-fitting SED model and the corresponding apparent flux. We can make use of this by calculating the ratio between optimized and observed apparent flux and apply it as a zeropoint correction to the dataset. In order to estimate the required zeropoint correction we split our spectroscopic sample and use one half of it for calibration and the second half for validation. This method can be iterated and converges quite fast. We derive the correction for all individual fields where spectroscopic data are available. For these specific pointings we directly apply the determined zeropoint offsets. For fields without spectroscopic validation we apply a correction calculated from the median of all zeropoint corrections from the corresponding major CHFTLS-Wide tile (i.e., for all W1-fields the median of all spectroscopically covered fields in W1). The photometric redshift probability distribution is shown in Fig. 5.9. The results for this final zeropoint calibration step are shown in Figs. 5.11 and 5.12. The outlier rate drops further down to $\eta = 1.2$ to 3.5% and the photometric redshift scatter reduces to $\Delta z/(1+z) = 0.032$ to 0.045 ($1+z$) and $\sigma_{\Delta z/(1+z)} = 0.028$ to 0.034 ($1+z$). The results are

⁷ <http://ned.ipac.caltech.edu/forms/calculator.html>

summarized in Table 5.1. The applied spectroscopic redshift calibration offsets for all investigated CFHTLS-Wide pointings are summarized in the Appendix in Table A.1. Given the greater depth of the spectroscopic surveys VVDS-Deep and DEEP2 we can further inspect our photometric redshifts for objects with $22.5 \leq i' \leq 24.0$. Due to the lower signal-to-noise in the photometry for these fainter objects the accuracy suffers. The outlier rate increases to $\eta = 4.8\%$ for W1 and 5.5% for W3, the redshift scatter increases to $\Delta z/(1+z) = 0.039 (1+z)$ and $\sigma_{\Delta z/(1+z)} = 0.053 (1+z)$ for W1 and $\Delta z/(1+z) = 0.047 (1+z)$ and $\sigma_{\Delta z/(1+z)} = 0.054 (1+z)$ for W3. The results are summarized in Table 5.1. For the deterioration of the photometric redshift accuracy there are two major possible explanations, the increasing photometric noise in flux measurement for faint objects and the increasing variety of SEDs due to increasing redshift for decreasing apparent fluxes, which might be no longer fully covered by our template set. We will address this problem in the following, investigating significant deeper observations. In principal there are two ways to reduce the probability of catastrophic outliers. The first way is to increase the total integration time in order to reduce the photometric noise. The second possibility is to extend the investigated wavelength range, e.g., by including flux information from NIR filters. The influence of NIR filter information is illustrated in Fig. 5.10.

The main uncertainty source for systematic photometric errors as catastrophic outliers is the mismatch between prominent features as the Lyman break at 1216 \AA and the Balmer break at 3648 \AA or the D4000 at roughly 4000 \AA . As we want to evaluate the reason for the decreasing redshift accuracy in our sample we have a look on significantly deeper images. For this we consider the CFHTLS-Deep D1 and D3 fields with exposure times of 60-70 hours instead of 1-2 hours. The significantly lower photometric noise substantially reduces the photometric redshift scatter. Considering objects with luminosities $i' \leq 22.5$ we find a catastrophic outlier rate of $\eta = 1.4\%$, a photometric redshift scatter of $\sigma_{\Delta z/(1+z)} = 0.029$ and a mean photometric redshift error of $\Delta z/(1+z) = 0.031$ for the D1 and a catastrophic outlier rate of $\eta = 1.5\%$, a photometric redshift scatter of $\sigma_{\Delta z/(1+z)} = 0.029$ and a mean photometric redshift error of $\Delta z/(1+z) = 0.031$ for the D3. The improvement in photometric redshift accuracy is more obvious when considering fainter objects with magnitudes of $22.5 \leq i' \leq 24.0$. For these objects we obtain a catastrophic outlier rate of $\eta = 4.1\%$, a photometric redshift scatter of $\sigma_{\Delta z/(1+z)} = 0.023$ and a mean photometric redshift error of $\Delta z/(1+z) = 0.041$ for the D1 and a catastrophic outlier rate of $\eta = 1.9\%$, a photometric redshift scatter of $\sigma_{\Delta z/(1+z)} = 0.026$ and a mean photometric redshift error of $\Delta z/(1+z) = 0.032$ for the D3. Looking at the low level of deterioration of the photometric redshift accuracy for fainter apparent luminosities, our photometric template set appears to still fit the variety of SEDs at higher redshifts well enough, suggesting that the main source of decreasing photometric redshift accuracy is given by the accuracy of the investigated photometry. The results are summarized in Table 5.1. The photometric redshift results for the CFHTLS-Deep fields are also shown in Fig. 5.13.

We cross-check our photometric redshifts with a further spectroscopic validation set which was not used for calibration, spectroscopic redshifts from the SDSS (Strauss *et al.* 2002), partially overlapping with W1, W3 and W4. The spectroscopic sample is limited to a maximal redshift of $z \sim 0.5$, dominated by red SEDs. We obtain an outlier rate of $\eta = 4.6\%$, a photometric redshift scatter of $\sigma_{\Delta z/(1+z)} = 0.052$ and a mean photometric redshift error of $\Delta z/(1+z) = 0.058$ for the W1, an outlier rate of $\eta = 1.5\%$, a photometric redshift scatter of $\sigma_{\Delta z/(1+z)} = 0.058$ and a mean photometric redshift error of $\Delta z/(1+z) = 0.048$ for the W3 and an outlier rate of $\eta = 0.8\%$, a photometric redshift scatter of $\sigma_{\Delta z/(1+z)} = 0.051$ and a mean photometric redshift error of $\Delta z/(1+z) = 0.047$ for the W4. These values are worse than for the spectroscopic training set, but given the circumstance, that this

field	N_{gal}	η_{uncalib}	$\sigma_{\Delta z/(1+z)\text{uncalib}}$	$\Delta z/(1+z)\text{uncalib}$	η_{stars}	$\sigma_{\Delta z/(1+z)\text{stars}}$	$\Delta z/(1+z)\text{stars}$	η_{spectra}	$\sigma_{\Delta z/(1+z)\text{spec}}$	$\Delta z/(1+z)\text{spec}$
W1 _{bright}	1 549	4.8 %	0.059	0.060	1.7 %	0.037	0.037	1.2 %	0.032	0.032
W2 _{bright}	939	7.0 %	0.059	0.084	4.2 %	0.033	0.055	3.5 %	0.028	0.046
W3 _{bright}	3 962	11.8 %	0.061	0.100	2.2 %	0.038	0.043	1.8 %	0.034	0.037
W4 _{bright}	3 572	17.1 %	0.072	0.106	2.3 %	0.038	0.037	2.2 %	0.033	0.035
W1 _{faint}	2 014	-	-	-	-	-	-	4.8 %	0.039	0.053
W3 _{faint}	4 026	-	-	-	-	-	-	5.5 %	0.047	0.054
D1 _{bright}	1 577	-	-	-	-	-	-	1.5 %	0.029	0.031
D3 _{bright}	2 760	-	-	-	-	-	-	1.4 %	0.029	0.031
D1 _{faint}	1 929	-	-	-	-	-	-	4.1 %	0.023	0.041
D3 _{faint}	2 530	-	-	-	-	-	-	1.9 %	0.026	0.032

Table 5.1: Photo-z statistics in comparison with spectro-z. For each field the object number, the outlier rate and the photometric redshift scatter ($\sigma_{\Delta z/(1+z)}$ and $\Delta z/(1+z)$) are given for calculation without any zeropoint calibration (uncalib), calibration on the Pickles star library (stars) and calibration on spectroscopic redshifts (spec). Field names without index consider spectra with $i' \leq 22.5$, fields with index ‘faint’ consider spectra with $22.5 < i' \leq 24.0$.

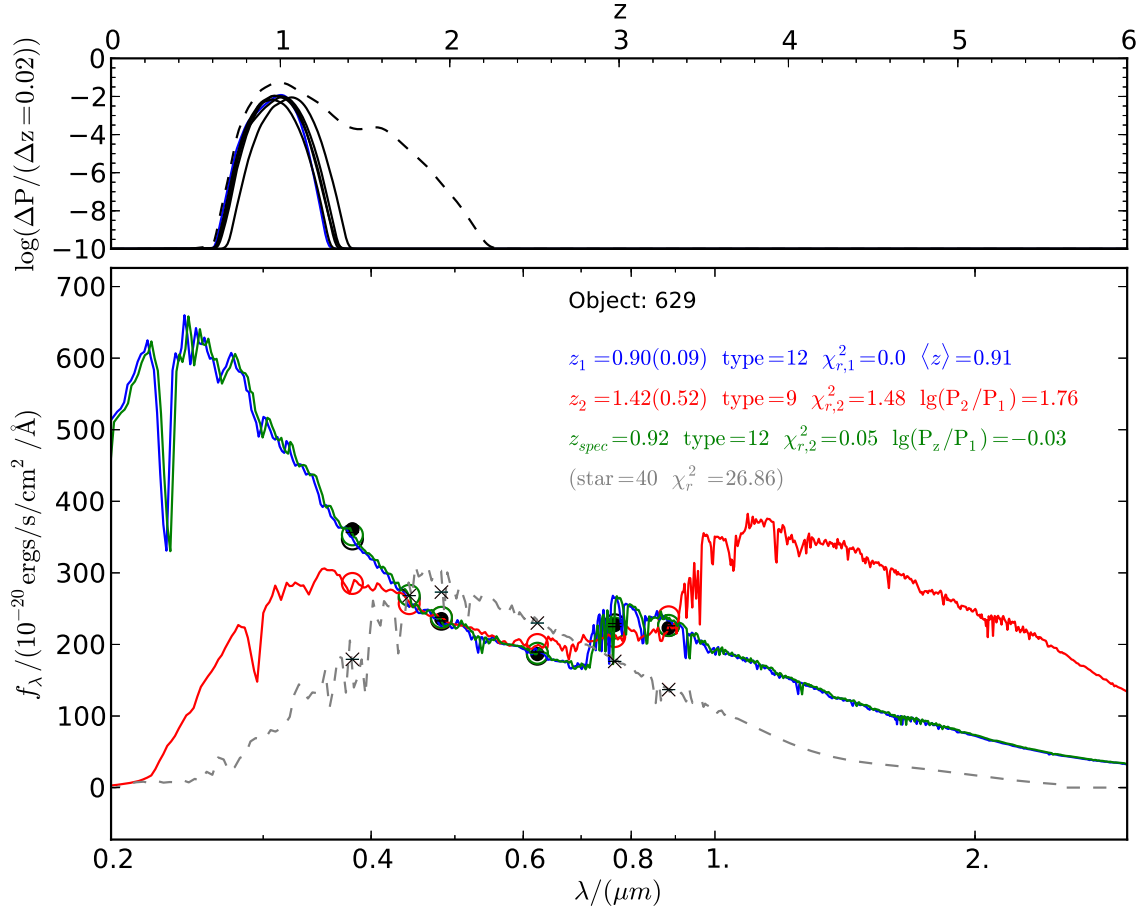


Fig. 5.9: The upper panel shows the photometric redshift probability distribution for an object in the CFHTLS-Wide with available flux information in u^* , g' , r' , i' , z' . The solid lines show the distribution for the best-fitting galaxy templates, the dashed line shows the cumulative distribution. The lower panel shows the SED for the best-fitting template in blue, the second-best-fitting template in red and the best-fitting template for the fixed spectroscopic redshift in green. As can be seen the photometric redshift agrees very well with the spectroscopic one.

is a cross-check for a blind validation set with very low redshifts (i.e., $(1+z) \sim 1$) the results are acceptable. The results also are shown in Fig. 5.14.

5.3.3 Star/Galaxy Separation

We use two approaches to separate stars and galaxies, a morphological and a SED-based one. The morphological approach bases on the `SExtractor` star classification using an artificial neural network, requiring an accurate measurement of the seeing (FWHM). We extract this value from `SExtractor` `FWHM_IMAGE` parameter, measuring the image size of the objects located in the stellar sequence in the magnitude-FWHM_IMAGE diagram. We classify all objects with a star classifier of higher than 0.96 as a star. Further the PhotoZ redshift code does not only fit galaxy SEDs

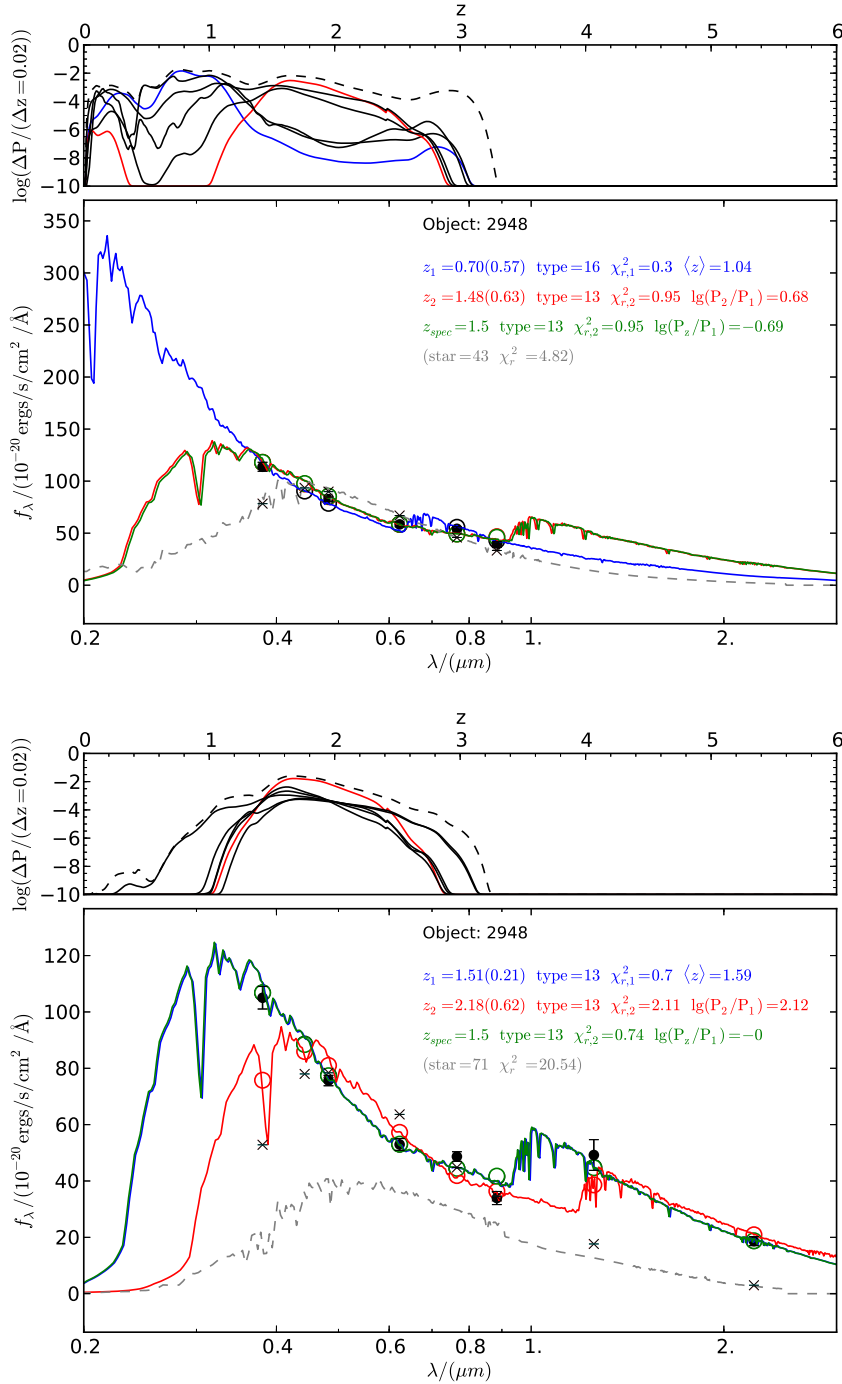


Fig. 5.10: Impact of NIR filters on the photometric redshifts. The upper panel shows the result without NIR information, the lower panel shows the result for the same object including J and Ks filter information. As can be seen without NIR flux information the proper redshift only provides the second-best fit. However, the additional information helps to break the degeneracy and leads to a proper redshift estimate.

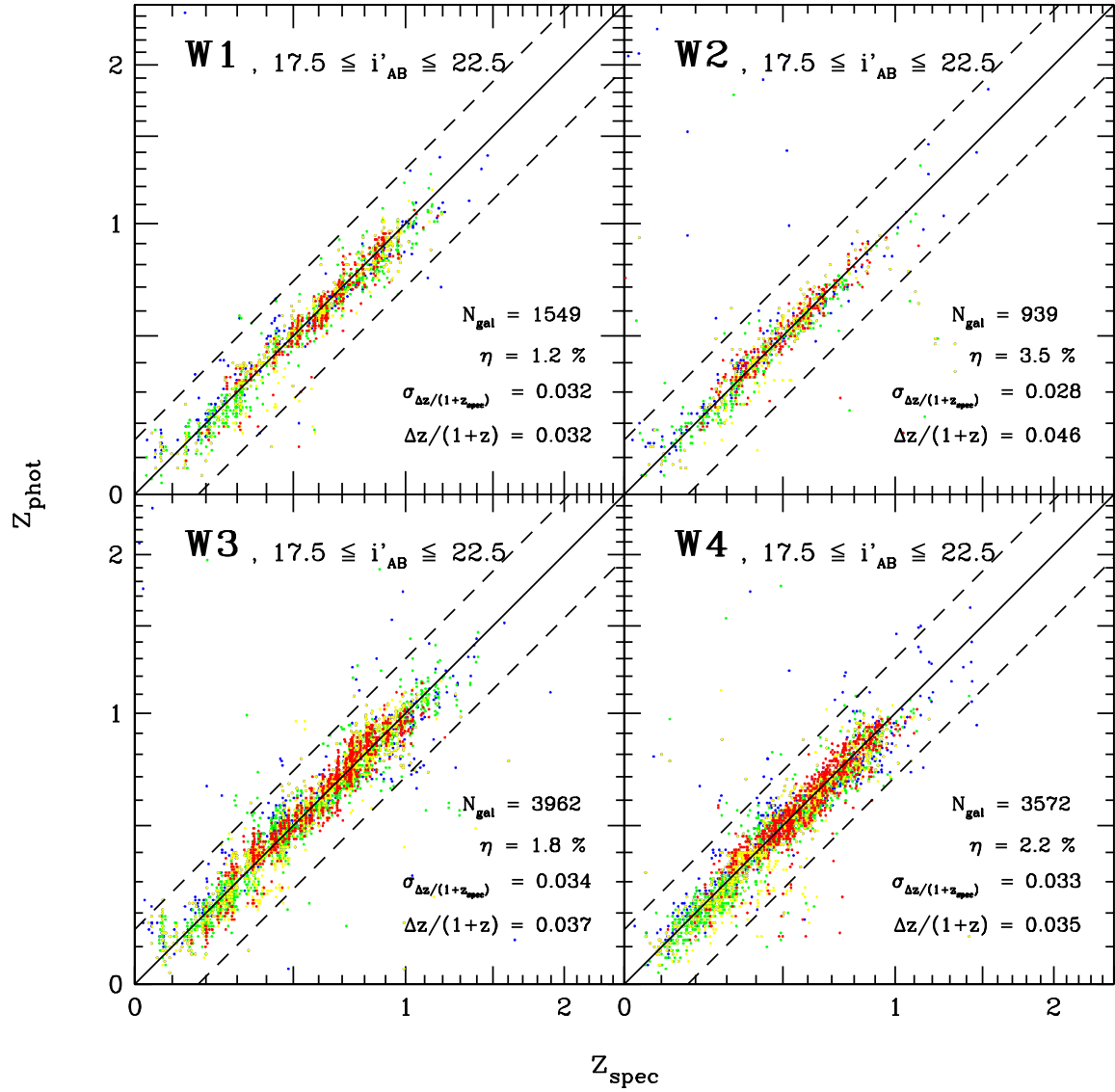


Fig. 5.11: Comparison between photometric (y-axis) and spectroscopic redshifts (x-axis) after calibration on spectroscopic redshifts. The accuracy further improves in regards of redshift scatter $\Delta z/(1+z)/\sigma_{\Delta z/(1+z)}$ and catastrophic outlier rate η . The symbol colors indicate the SED type of the galaxies, going from red (early type galaxies) over yellow and green to blue (very strongly star-forming late type galaxies). The results are summarized in Table 5.1.

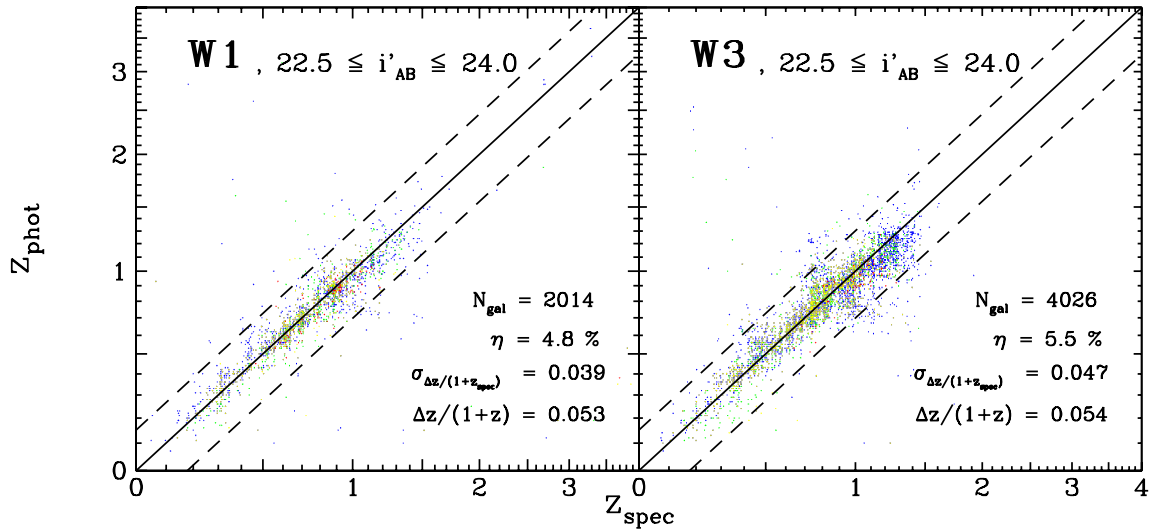


Fig. 5.12: Photometric redshifts (y-axis) vs. spectroscopic redshifts (x-axis) for $22.5 \leq i' \leq 24.0$ due to higher limiting magnitude of the corresponding spectroscopic surveys overlapping with W1 and W3. The larger noise leads to an increase of both redshift scatter and outlier rate. The symbol colors indicate the SED type of the galaxies, going from red (early type galaxies) over yellow and green to blue (very strongly star-forming late type galaxies). The results are summarized in Table 5.1.

but also runs a set of stellar templates based on the Pickles star library (Pickles 1998). We require for objects to be classified as galaxy a best-fitting χ^2 -value which is better than the corresponding best-fitting stellar value. This might be a rather strict criterion, but for the later performed gravitational lensing analysis we prefer to discard a small number of possible galaxies to contaminating our galaxy sample with a small number of possible stars.

5.3.4 Calculation of Photometric Redshifts

After the final zeropoint calibration step the photometric redshift estimation can be done straightforwardly. We obtain the best-fitting photometric redshifts z_{phot} , the photometric redshift uncertainty $d_{z_{\text{phot}}}$, the χ^2 -value, indicating the quality of the template fit to the observational data, the corresponding best-fitting templates and absolute rest-frame magnitudes. We denote the photometric redshifts with several flag values in order to quantify their reliability. The first flag value is assigned to objects smaller than the PSF FWHM. For that we have a look at all objects in FWHM-CLASS_STAR-diagram and connect the smallest objects with a star classifier of 1 with the smallest objects with a star classifier of 0 (see Fig. 5.15). All objects smaller than objects on this line receive a flag value of 1. This especially concerns objects with SExtractor star classification of ~ 0.5 , as for this class of objects, due to low signal-to-noise ratio, a reliable analysis of the light profile is very difficult. This further could have influence on the photometric flux and flux error measurements, which might be underestimated due to the small object size, thus affecting the photometric redshift accuracy. A more direct criterion is used for the next flag value. A flag value of 2 is assigned to objects with relatively large redshift uncertainty $\Delta z_{\text{phot}} > 0.25 (1 + z_{\text{phot}})$ in the template-fitting procedure. Further objects which are saturated on at least one pixel in the extraction with SExtractor (extraction flag 4, see

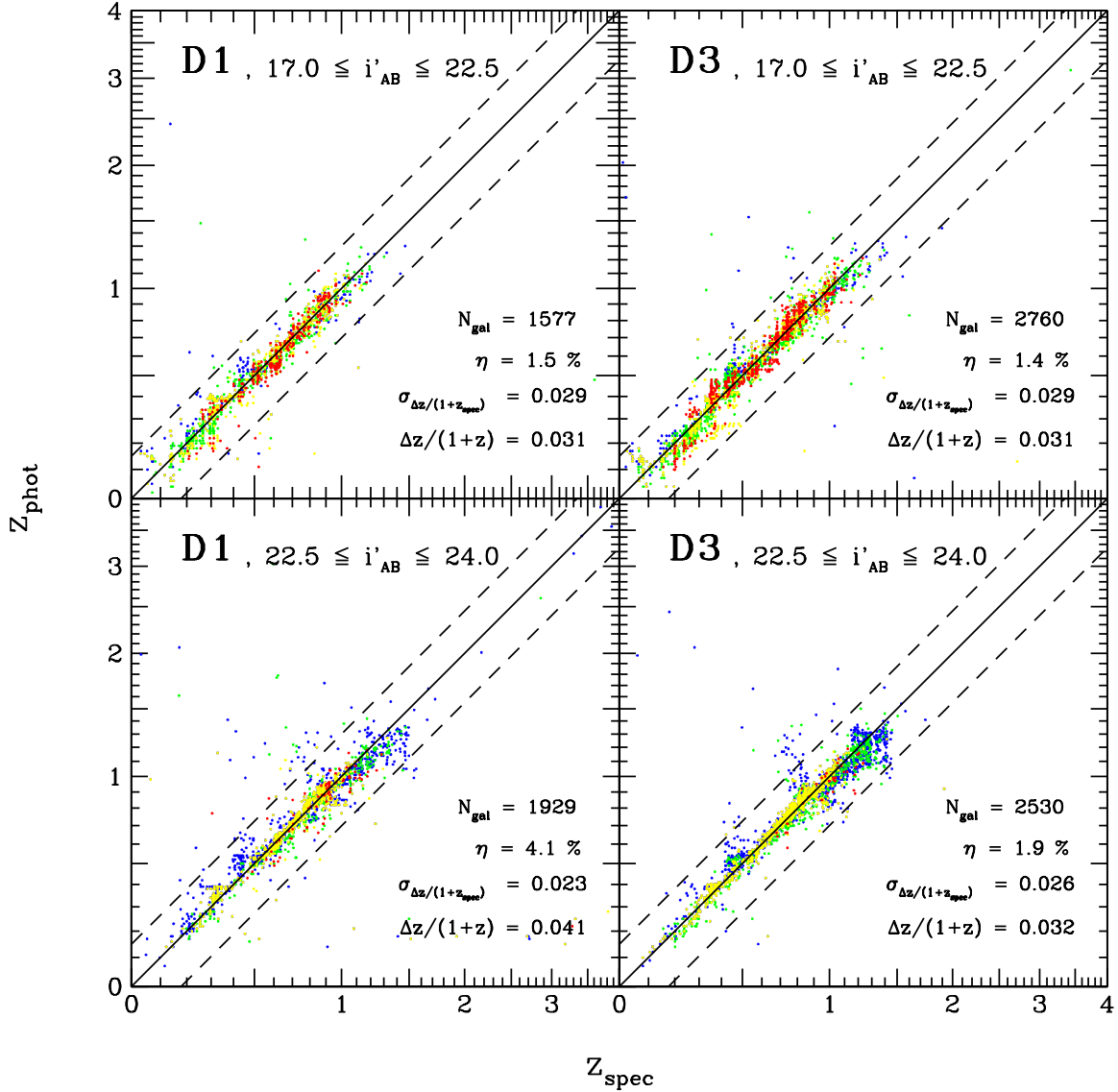


Fig. 5.13: Photometric redshifts (y-axis) vs. spectroscopic redshifts (x-axis) for the CFHTLS-D D1 and D3, which are overlapping with W1 and W3. The upper panels show high signal-to-noise objects ($17.0 \leq i' \leq 22.5$) the lower panel low signal-to-noise objects ($22.5 \leq i' \leq 24.0$). The greater depth of the Deep fields leads to improved photometric redshift scatter and outlier rates especially for faint objects. The symbol colors indicate the SED type of the galaxies, going from red (early type galaxies) over yellow and green to blue (very strongly star-forming late type galaxies). The results are summarized in Table 5.1.

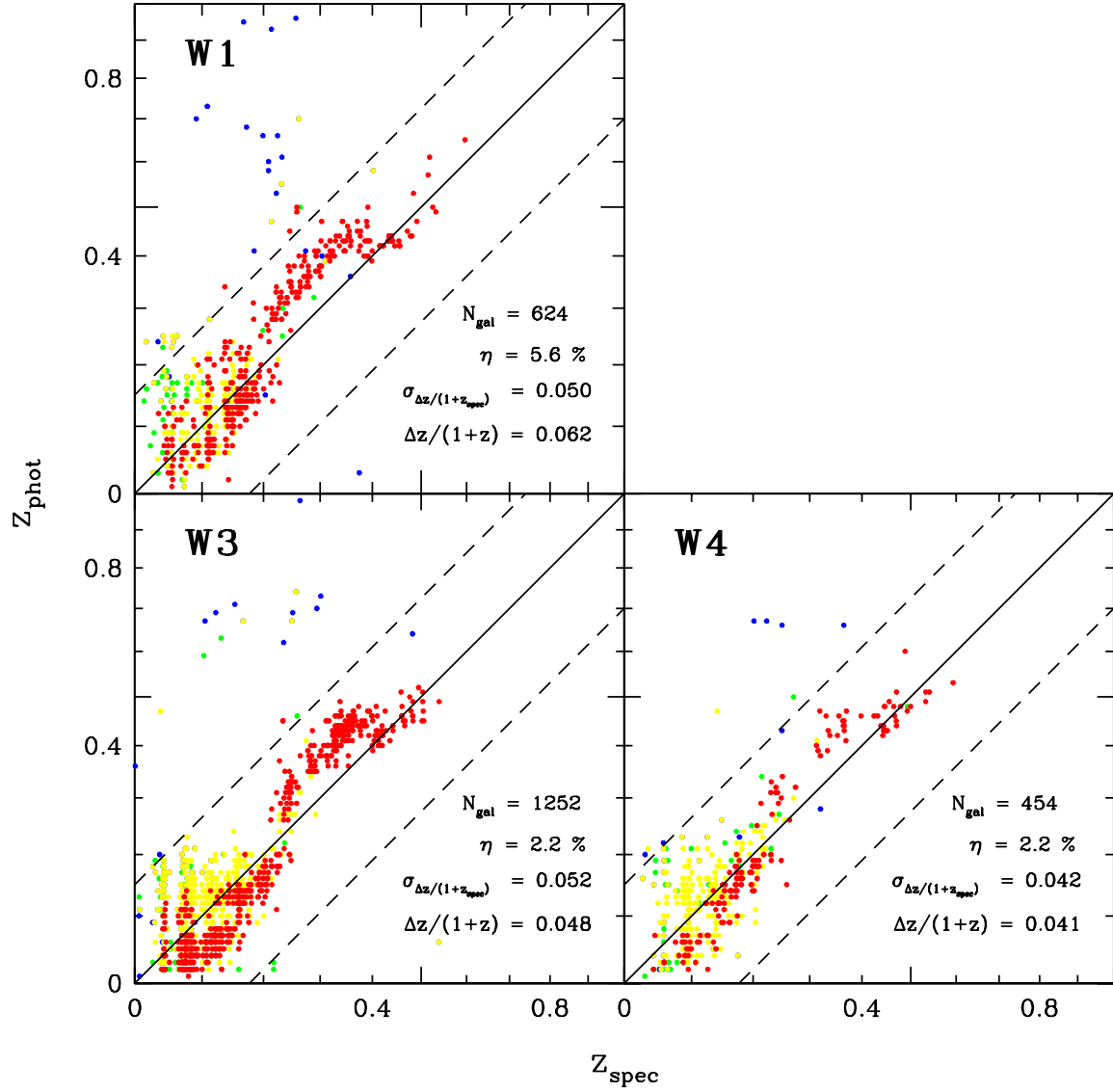


Fig. 5.14: Comparison of our photometric redshifts with spectroscopic redshifts from the SDSS (Strauss *et al.* 2002). We only consider spectroscopic redshifts with a confidence ≥ 0.99 . The colors indicate the best-fitting SED types. Red denotes early type galaxies, yellow, green and blue symbols denote star-forming galaxies, increasing in star-formation rate from yellow to blue. The outlier rate is in general low. Being a pure validation set which was used at no point for zeropoint calibration, the photometric redshift scatter is higher than in for the spectroscopic training sets. Especially considering objects with $z_{\text{spec}} > 0.3$ we observe a slight tendency to overestimate the actual redshift.

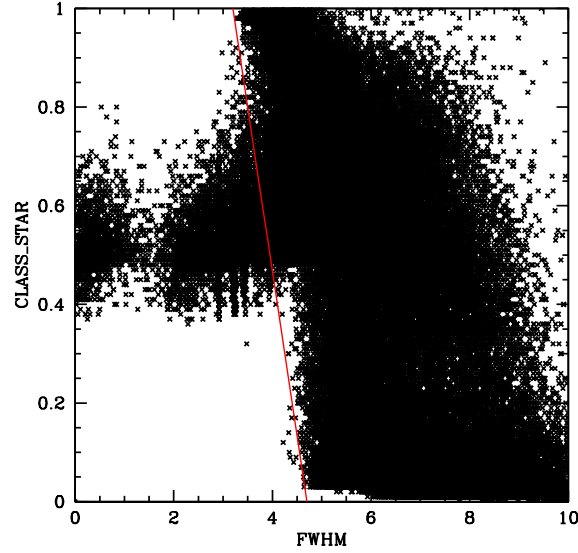


Fig. 5.15: SE extractor FWHM_IMAGE parameter vs. SE extractor star classifier. This diagram is used to define the first photometric redshift flag value. We draw a red line, linking the smallest high signal-to-noise stars (CLASS_STAR=1) with the smallest high signal-to-noise galaxies (CLASS_STAR=0), and assign to all objects left from this line a photometric redshift flag value of 1.

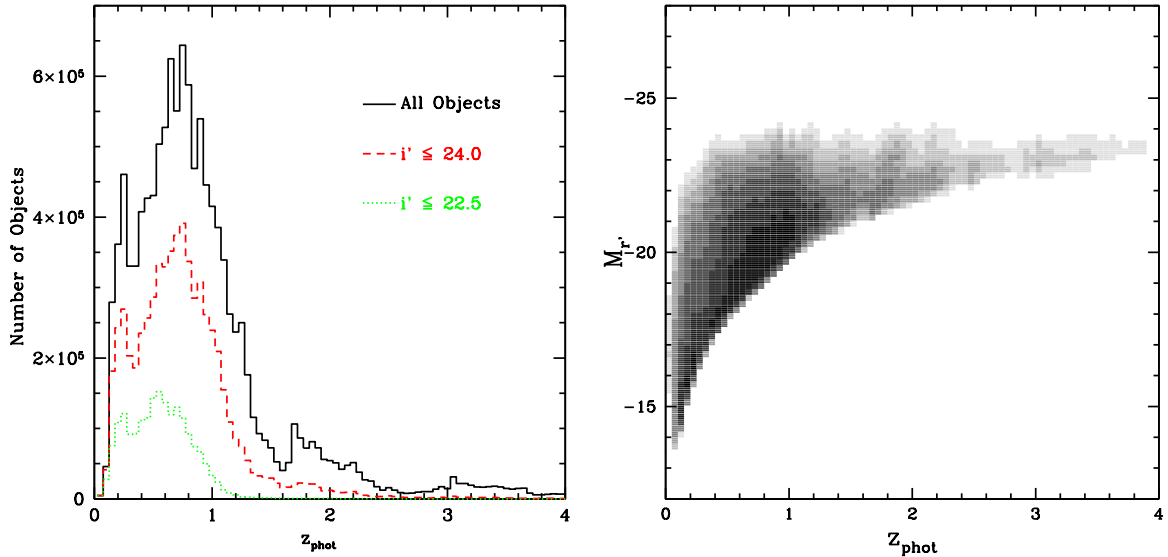


Fig. 5.16: Photometric redshift distribution for the CFHTLS-Wide. The left panel shows the total photometric redshift histogram for all fields, the black solid line shows all objects, the red dashed line shows all objects with $i' \leq 24.0$ and the green dotted line all objects with $i' \leq 22.5$. The right panel the distribution of objects in photometric redshift and absolute magnitude space.

Bertin & Arnouts 1996) receive a photometric redshift flag of **4**. Even larger flags are assigned to objects which are classified as stars or do not return a photometric redshift, but for our analyses these objects do not play a role. All individual flags are summed up. Objects with flags larger than **3** are discarded for any further investigation, for shape analyses all objects with flags larger than **0** are rejected. The distribution of our complete high quality photometric redshift sample is shown in Fig. 5.16.

5.4 Estimation of Object Shapes and Shears

This subsection describes the practical proceeding in the estimation of the object shapes. The method is discussed in Section 3.3.3. We use the KSB+-implementation (see Kaiser *et al.* 1995 and Hoekstra *et al.* 1998), adapted from the TS-pipeline (Schrabback *et al.* 2007), which was kindly provided by Thomas Erben and Tim Schrabback, mostly based on code from Erben *et al.* (2001), itself using code from Kaiser's original IMCAT tools.⁸ The first step in measuring the object ellipticities is the detection of the objects themselves. For this purpose we run `SEXTRACTOR` with a threshold of 3σ on at least four contiguous pixels, using an error frame (weighted map). As saturated objects are not valid shape tracers, we discard objects with at least one saturated pixel. For this we make use of a flag image created during the data reduction, indicating saturated pixels and additionally apply a saturation level of 90. We suppress correlated noise smaller than the PSF making use of the `SEXTRACTOR` option to convolve the data with a Gaussian before detection (see also in Section 5.3.1). The PSF patterns vary over the whole field of view, showing discontinuities at the chip borders. We therefore mask and ignore regions on all fields with data stacked from different chips, as the superposition of several independent PSF patterns cannot be corrected with the required accuracy. This leaves us with $9 \times 4 = 36$ distinct patches per one square degree pointing (see upper panels of Figs. 5.18 and 5.19), where the vertical gaps are quite narrow and hard to see. In the following, we investigate all extracted objects in a magnitude-size diagram, selecting stellar objects for the PSF anisotropy correction and suitable galaxy candidates for further analysis. We choose all objects from the stellar sequence (the exact values for the flux radii depend on the seeing of the observation) with a `SEXTRACTOR` star classification `CLASS_STAR` > 0.96, magnitudes of $18 \leq i' \leq 24$ and a signal-to-noise ratio of at least $S/N_{\min} = 50$. The signal-to-noise limit leads to an effective magnitude cut at $i' \sim 22$ (see left upper panel of Fig. 5.17). This selection leaves us with roughly 1500-2000 stars per pointing in the W1 and W3 and roughly 3500-4500 stars per pointing in the W2 and W4 fields.

First we use these stars to estimate the stellar PSF anisotropy q^* (see equation 3.33). We use a two-dimensional fifth order polynomial to fit the complete one square degree field of view, flexible enough to describe the complex PSF variations. We ignore the masked inter-gap regions. We also have experimented with the application of third order polynomial fits to the distinct subtiles of the one-square-degree-pointings, but discarded this approach because of larger systematic errors in terms of PSF anisotropy model residuals and B-modes in the two-point shear correlation function (for definition and measurement of B-modes in the two-point shear correlation function see, e.g., Van Waerbeke *et al.* 2000, 2001 or Fu *et al.* 2008). A sophisticated analysis that provides an objective measure whether to use lower or higher order polynomials in the PSF anisotropy correction is described in Rowe (2010). The residuals for the anisotropy pattern correction for two different CFHTLS pointings are shown in Figs. 5.18 and 5.19, before the lensflip⁹ (W1p2p3, see Fig. 5.18) at the MegaCam camera optics and

⁸ <http://www.ifa.hawaii.edu/~kaiser/imcat/>

⁹ <http://www.cfht.hawaii.edu/Science/CFHTLS-DATA/cfhtlsgeneralnews.html#0007>

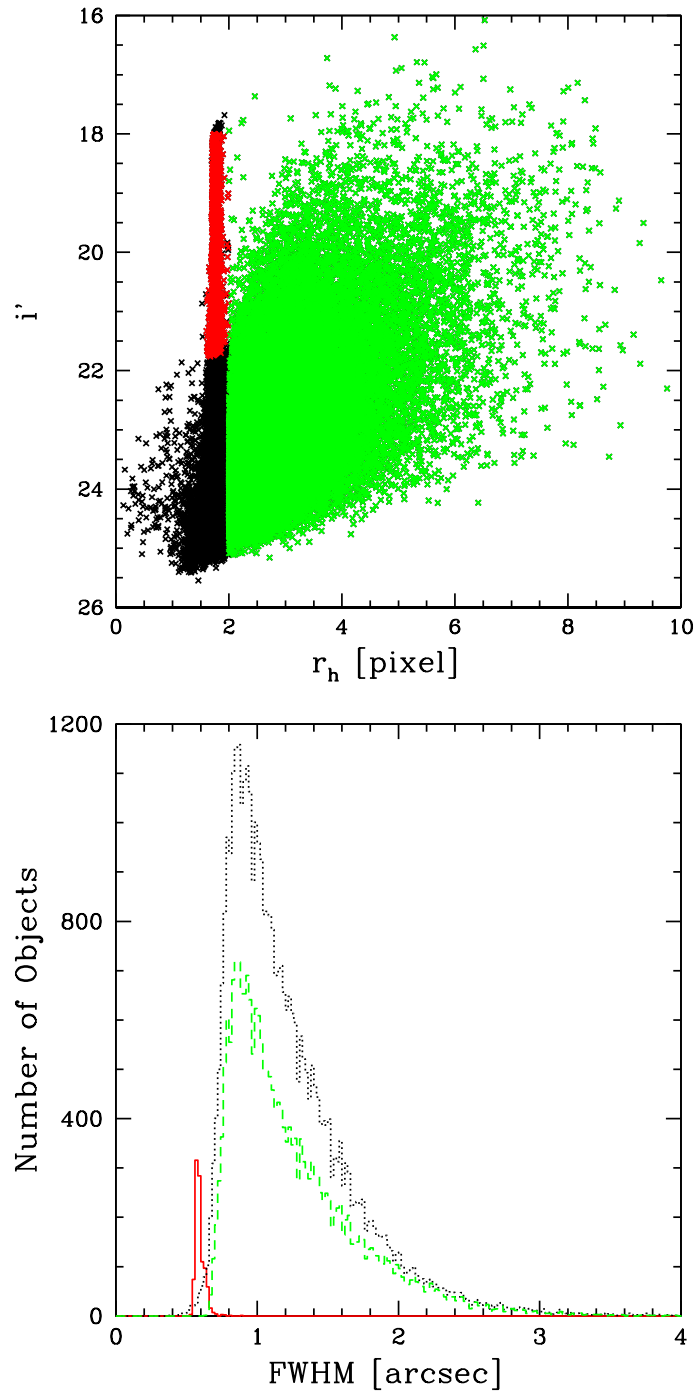


Fig. 5.17: The upper panel panel shows the distribution of the i' -band magnitudes vs. the `SExtractor` flux radius for shape measurement in the W1m1m0. The red symbols show stars which have been selected for PSF anisotropy correction, the green symbols show galaxies, which have been selected for shape catalog.

The lower panel shows the FWHM distribution of stars and galaxies. Red shows the stars selected for the PSF anisotropy correction, black the complete galaxy sample and green the cleaned galaxy sample ($S/N > 5$ and $z_{\text{phot}} \leq 2$) which is used for the weak lensing analysis. Most galaxies have a size of $> 1.4 \cdot \text{FWHM}_{\text{star}}$, allowing a bias-free shear estimate according to GREAT08 (see Bridle *et al.* 2010).

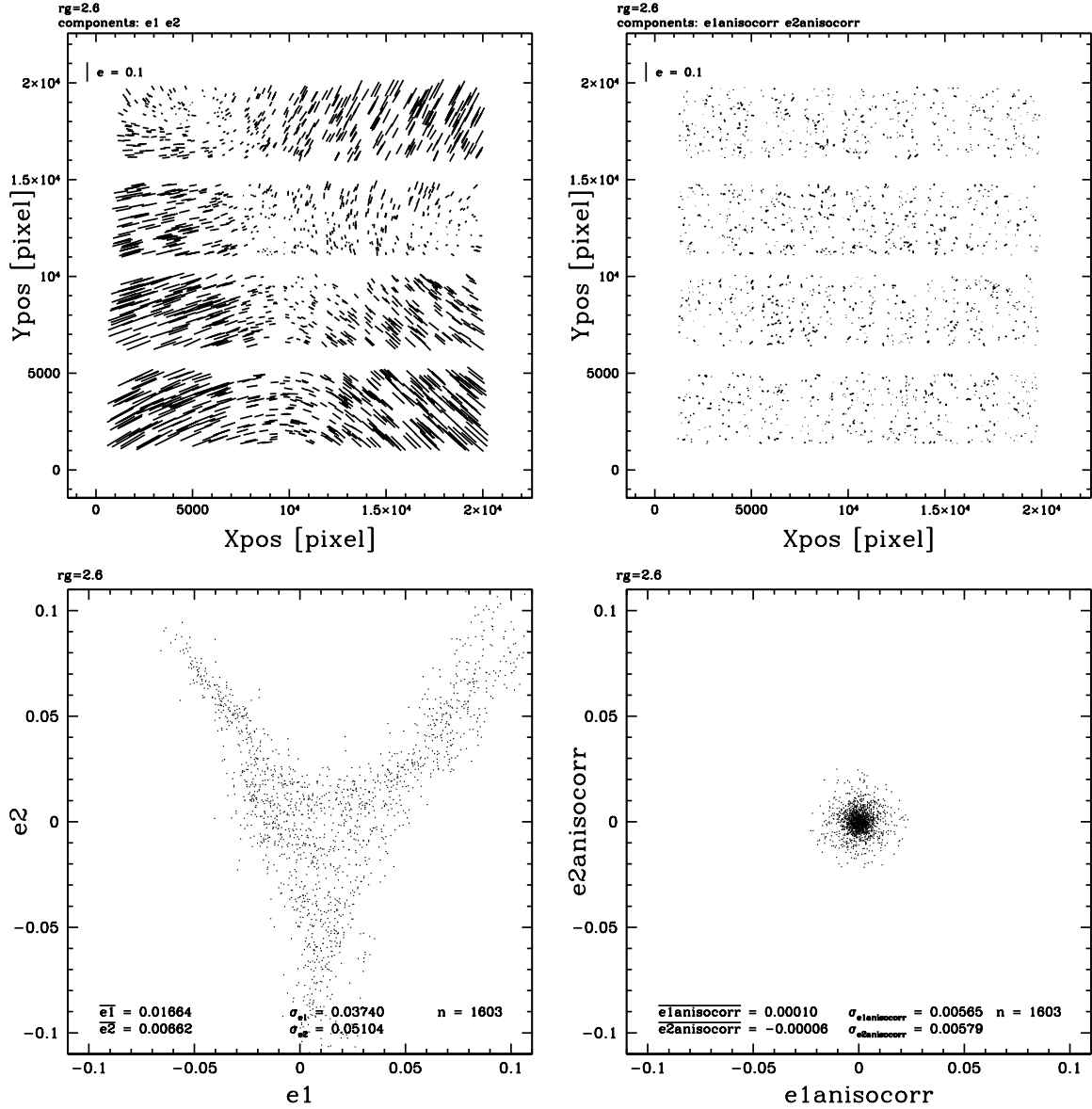


Fig. 5.18: PSF anisotropy pattern for an early (pre-lensflip) CFHTLS field (W1p2p3), see also Fig. 5.19 for a later observation. The upper left panel shows the observed uncorrected anisotropy pattern before anisotropy correction, the upper right panel shows the remaining PSF anisotropy pattern after correction with a two-dimensional PSF anisotropy model, fitted with a fifth order polynomial over the whole field of view of one square degree. The amplitude of the anisotropy is indicated by showing the length of 10% anisotropy in the upper left of the upper two panels.

The lower panels show the ellipticity distribution of stellar objects before (left) and after (right) the PSF anisotropy correction. The mean stellar ellipticities, the ellipticity dispersion and the number of fitted stars are shown in the panels.

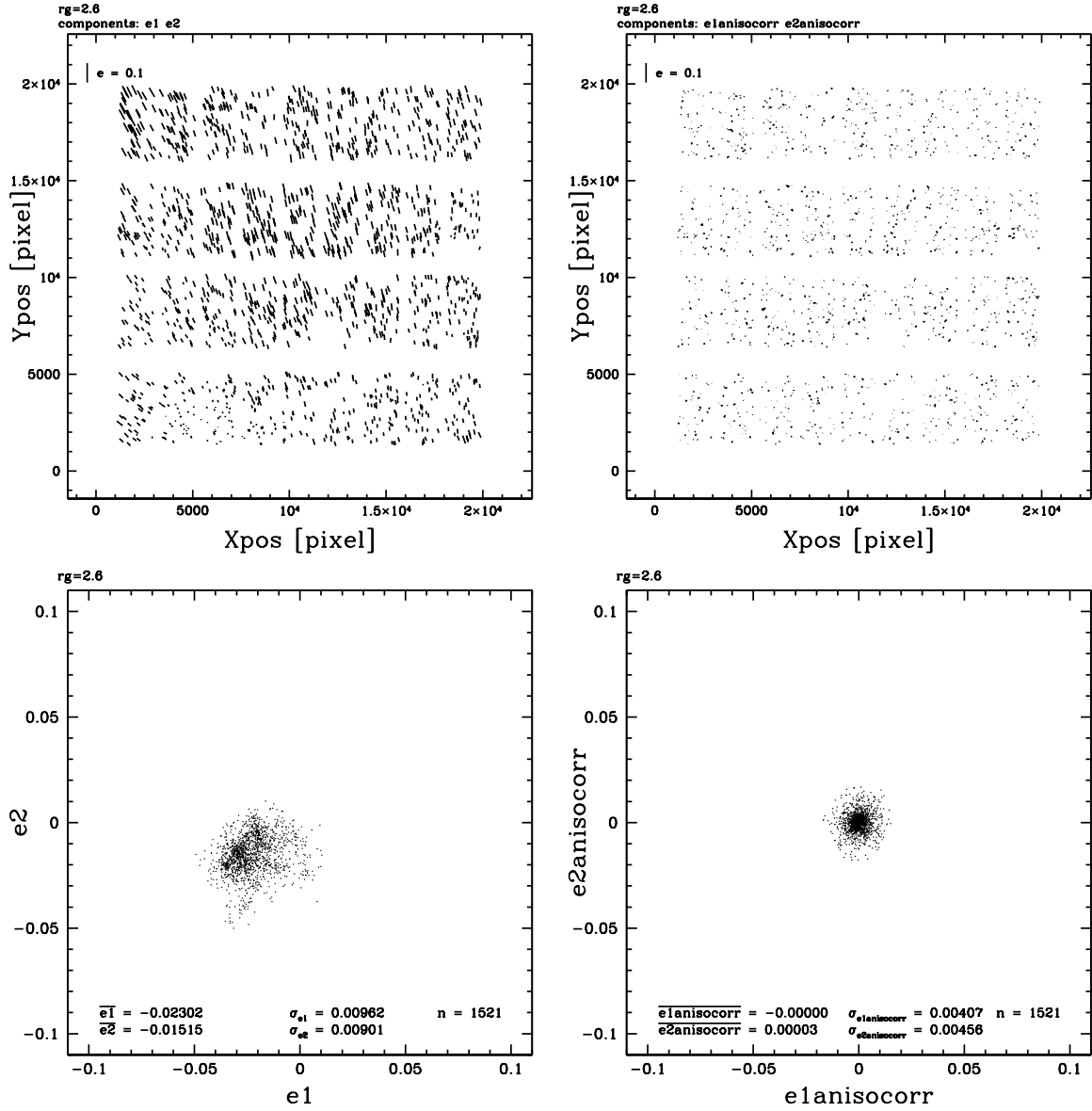


Fig. 5.19: PSF anisotropy pattern for a later (post-lensflip) CFHTLS field (W1m1m2), see also Fig. 5.18 for an early observation. The lensflip significantly changed the observed PSF anisotropy patterns of all CFHTLS observations. While the mean values for e_1 and e_2 shifted to slightly negative values, the dispersion and therefore the scatter in ellipticities significantly decreased (see the values in the lower left panel). The less irregular PSF pattern (visible in the left panels) therefore made it significantly easier to find a satisfying anisotropy correction (see the corrected ellipticities in the upper and lower right panel).

after it (W1m1m2, see Fig. 5.19). The upper panels of Figs. 5.18 and 5.19 show the positions, the amplitude and the orientations of the major axes of the ellipticities for the stellar objects with lines of defined length and orientation (a so-called whisker plot). The lengths of lines indicate the amplitude of the ellipticity, the angular orientation marks the orientation of the major axis. As reference a line indicating the 10% anisotropy level is drawn in the upper left. In the lower panels the number of the fitted stars is shown (1603 for the W1p2p3 and 1521 for the W1m1m2), as well as the mean stellar ellipticities and their dispersion. The lens flip significantly changed the image characteristics of CFHTLS observations. The anisotropy patterns for observations after the lens flip are much more regular and show a smaller amplitude in terms of ellipticity dispersion. The larger and more irregular anisotropy patterns of the pre-lensflip observations are more difficult to properly correct than the less complex patterns of later observations. Therefore, after visual inspections of every single field we decided to discard 35 fields with unsatisfactory PSF correction, keeping 89 pointings for further analysis. After modeling of the PSF anisotropy pattern, the stellar anisotropy quantities are calculated. As isotropic weight function W_{r_g} (see equation 3.32) a Gaussian with a width of r_g adjusted to the object size is chosen. As the lower panel of Fig. 5.17 shows, most galaxies follow the relation $\text{FWHM}_{\text{gal}} > 1.4 \cdot \text{FWHM}_{\text{star}}$. According to the results of the GREAT08-challenge (Bridle *et al.* 2010) this is the limit to which no bias has been observed in the KSB-implementation of Heymans. Additionally the merging with photometric redshifts and elimination of low S/N ($S/N < 5$) and high redshifts objects ($z_{\text{phot}} > 2$) remove most of the remaining galaxies with small FWHM. Tests of the TS-pipeline in the Shear TEsting Programme (STEP, see Heymans *et al.* 2006) showed a significant multiplicative bias in the analysis of the first set of simulated images (STEP1, Heymans *et al.* 2006). This bias could be almost eliminated by multiplication with a shear calibration factor $c_{\text{cal}} = 1/0.91$, leading to

$$\gamma = c_{\text{cal}} \cdot \langle \epsilon_{\text{corr}} \rangle. \quad (5.6)$$

According to the analysis of STEP2 (Massey *et al.* 2007) this bias calibration appears to be correct to $\sim 3\%$. However, the GRavitational lEnsing Accuracy Testing 2008 (GREAT08, Bridle *et al.* 2010) found, that the multiplicative shear bias can still be of the order of 5% (shown on the Heymans-KSB-implementation), present for low S/N objects with $S/N_{\text{GREAT08}} \sim 10$, more likely corresponding to $S/N_{\text{GREAT08-true}} \sim 6$. This means despite the shear calibration correction from equation (5.6), there might be a bias in the order of 5% left for objects with $S/N \sim 5$. We will address this problem later, investigating and comparing the observed signal for background objects with high and low S/N-ratio, for bright and faint background sources and for large and small flux radii, respectively, with respect to the same foreground objects.

The objects remaining in the galaxy catalog after cuts in signal-to-noise, photometric redshifts and the KSB pipeline are called the ‘shape catalog’. Due to the stricter requirements during detection for the shape catalogs, in general the photometric redshift catalogs are much larger than the corresponding shape catalogs. Therefore most shape catalog objects obtain a photometric redshift, but not vice versa. Thus the merged photometric redshift shape catalog consists of almost the same number of objects as the pure shape catalog.

The distributions of ellipticity components and absolute ellipticities are shown in Figs. 5.20 and 5.21, respectively. The red solid lines indicate the distribution of objects from the original shape catalog, the green dashed lines show the distribution of objects from the merged photo-z and shape catalog. As expected the quantities from pure shape and merged photo-z-shape catalog hardly differ. The dispersions of the ellipticity components are in all cases $\sigma_{\epsilon_1} = \sigma_{\epsilon_2} = 0.29$. These values are used for the analyses later on. The distributions themselves look similar to Gaussian profiles, but showing broader

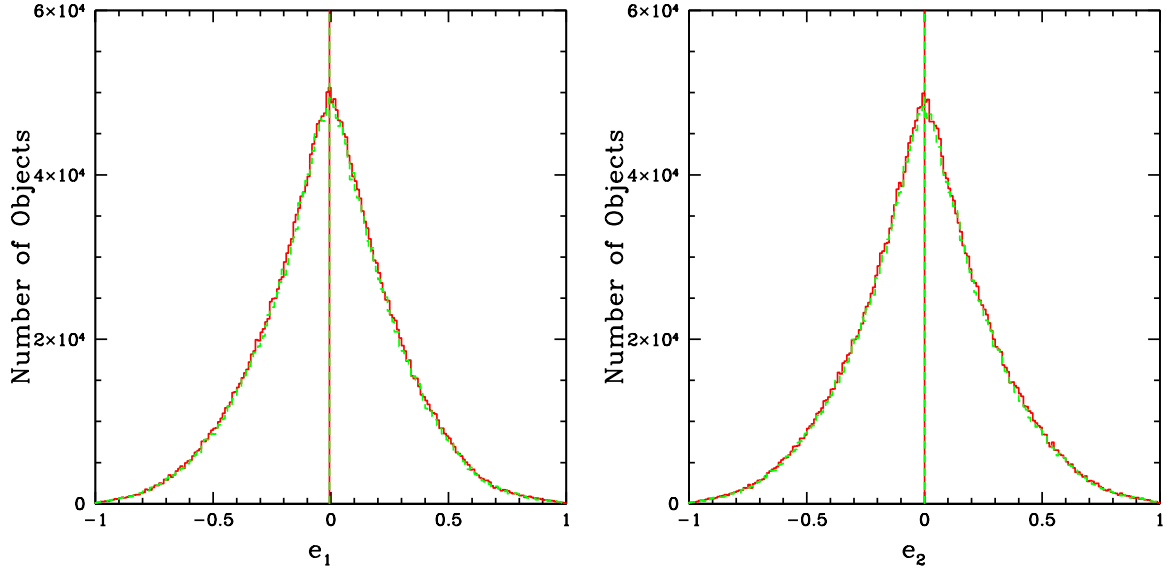


Fig. 5.20: Distribution of the ellipticity components e_1 (left panel) and e_2 (right panel) for galaxies in the shape catalog. The red solid lines shows the ellipticities in the original shape catalog, the green dashed lines shows objects from the merged shape and photo-z catalog. As can be seen the merging process hardly affects the total number. The rms-widths in all cases are equal to $\sigma_{e_1} = \sigma_{e_2} = 0.29$.

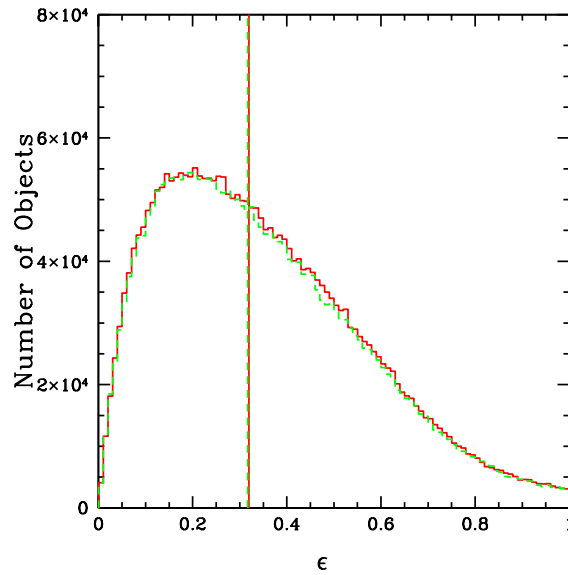


Fig. 5.21: Distribution of absolute PSF-corrected ellipticities $|e|$ for galaxies in the shape catalog. The red solid line shows the objects from the entire shape catalog, the green dashed line shows the galaxies from the merged photo-z and shape catalog. The median of the absolute ellipticity is in both cases 0.31 (see the vertical line).

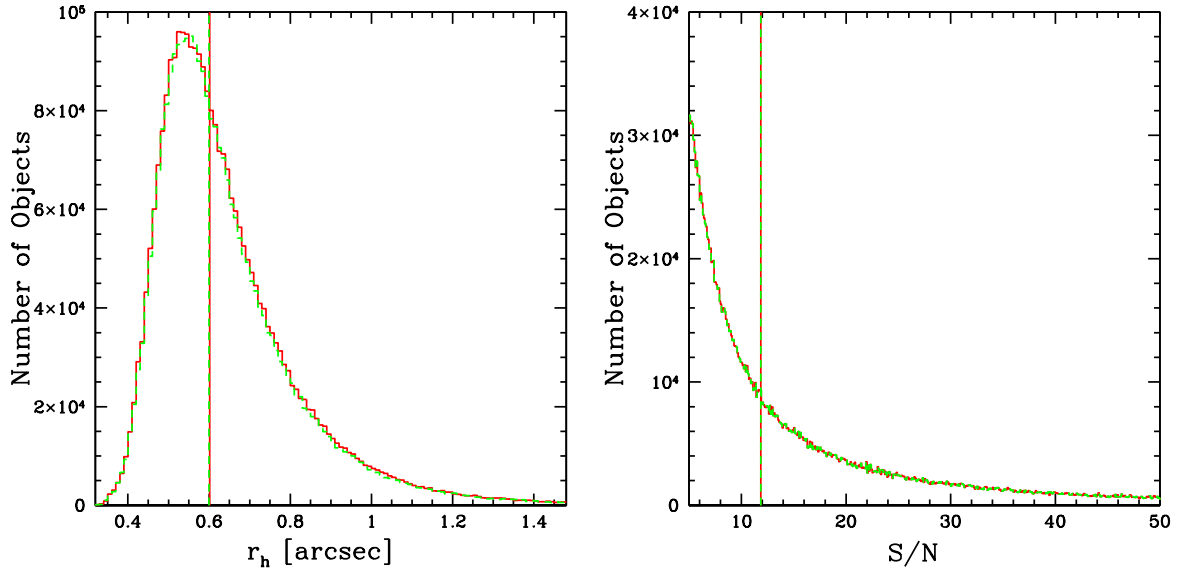


Fig. 5.22: Distribution of object sizes r_h (left panel) and S/N-ratio (right panel) for galaxies in the shape catalog. The red solid line shows the objects in the complete catalog, the green dashed line shows the objects from the merged photo-z and shape catalog. The vertical lines indicate the median for the distributions ($r_{h,\text{med}} = 0.6$ arcsec, $S/N_{\text{med}} = 11.9$).

wings than an analytic Gaussian. The median of the absolute ellipticity distribution is $|\epsilon|_{\text{med}} = 0.31$. Fig. 5.22 shows the distribution of flux radii (left panel) and S/N-ratios (right panel) for pure shape catalogs with red solid lines and for the merged photo-z-shape catalog with dashed green lines. The median of the flux radius distribution is $r_{h,\text{med}} = 0.6$ arcsec, the median for the S/N-ratio for all remaining objects (we excluded objects with $S/N \leq 5$) is 11.9.

5.5 Properties of the Galaxies in the Photometric and in the Shape Catalogs

In total our photometric catalogs consist of 17 445 504 objects, of which 11 912 636 are galaxies outside masked regions. Only considering the 89 pointings for which we obtained accurate shape catalogs, this leaves us with 8 315 162 galaxies for the foreground lens sample. The shear catalogs consist in total of 2 960 048 objects, from which 2 416 426 are in areas which are not masked, entering our background source catalog. The magnitude distribution (i' -band) of our foreground and background samples is shown in Fig. 5.23. In Fig 5.24 we show the photometric redshift distribution of our lens and source samples and compare them to the photometric redshift of Fu *et al.* (2008). Due to stricter requirements in lens-source building our source sample is fainter, leading to an earlier decline in number counts. Apart from that the distributions in general look similar.

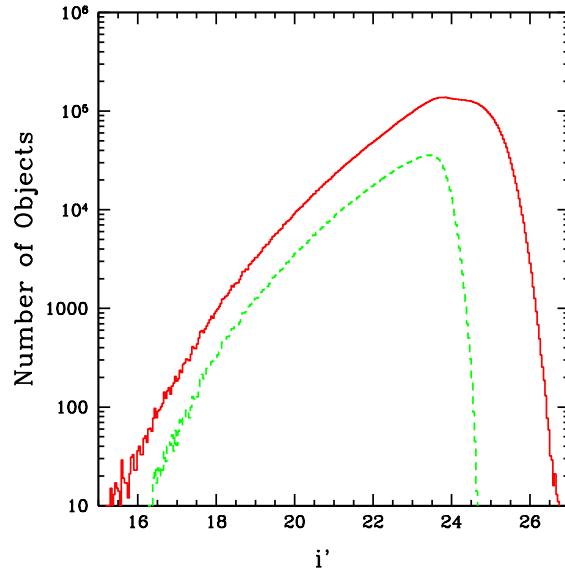


Fig. 5.23: Histogram of the i' -band magnitude for all 8 315 162 objects in our cleaned photometric redshift catalog (red solid line) and for those in the photometric redshift catalog which are not eliminated in the shape estimation procedure (green dashed line), i.e., for all 2 416 426 objects which enter our background catalog. Objects that are large and bright and those which have a low signal-to-noise ratio do not enter the shape catalog.

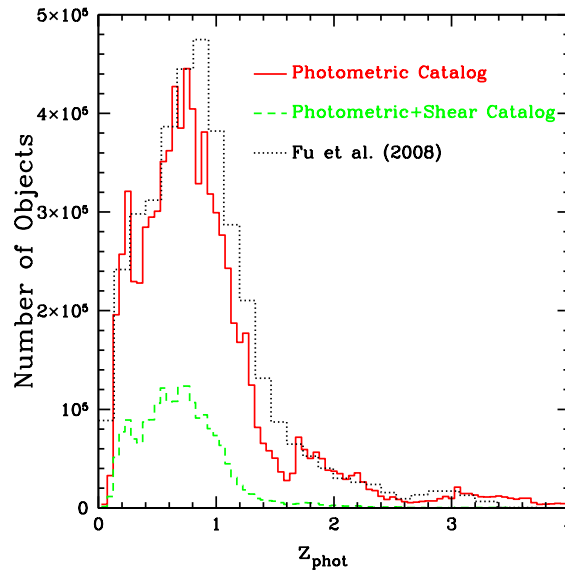


Fig. 5.24: Photometric redshift histogram for our lens sample. The red solid line shows the foreground lens sample, the dashed green line shows the background source sample. The gap and the bump at redshift ~ 1.7 is an artifact from photometric redshift calculation for objects with $i' > 24.5$. However it does not affect the lens and source samples as all sources are brighter than $i' = 24$ and we are only considering lenses with $z \leq 1$.

5.5.1 Definition of Lens and Source Galaxy Samples

As the first step we need to assign objects from our photometric catalogs to our foreground lens sample. As we intend to analyze the mass distribution of galaxies as a function of redshift, rest-frame luminosity and SED-type, photometric redshift information for the foreground lens galaxies is required. Among those galaxies from the photometric catalog sample we make the following selection for the lens sample:

$$M_r < -17 \text{ and } z_{\text{lens}} \leq 1. \quad (5.7)$$

This defines our maximum lens sample. Provided we have enough galaxies with shape estimates behind the considered lens sample, we can investigate the properties of any lens subsamples of interest. Next we need to assign our background source sample. For this we consider all galaxies with reliable shape estimates and photometric redshifts, assigned during the merging process with the photometric catalogs. Objects with photometric redshift $z_{\text{phot}} > 2$ are discarded due to several reasons. Firstly, the number of ignored objects with $z_{\text{phot}} > 2$ is rather small, as the number counts strongly drop for objects with $z > 1.5$. A second reason for this decision is the decreasing photometric redshift accuracy for redshifts $2 < z_{\text{phot}} < 3$ for observations at the depth of CFHTLS-Wide, due to the lack of NIR information. The fraction of objects at $z_{\text{phot}} > 3$, where u -band dropouts improve the redshift accuracy, is negligible. Further objects with large photometric redshift uncertainties are ignored. This leads to the following requirement for a maximum source sample:

$$\Delta_{z_{\text{phot,source}}} < 0.25 (1 + z_{\text{phot,source}}) \text{ and } z_{\text{phot,source}} \leq 2.0. \quad (5.8)$$

After these additional restrictions 4 942 433 galaxies remain in the maximum lens sample and 1 684 290 galaxies in the maximum source sample.

For the weak lensing analyses we investigate, for all considered foreground samples, the shapes of background sources within a defined radius in angular and physical scale around the lenses. As minimum and maximum angular scale we choose radii of 5 arcsec and 15 arcmin, respectively. These values correspond to physical radii of $3.3 h^{-1}$ kpc and $600 h^{-1}$ kpc at $z = 0.05$, $20 h^{-1}$ kpc and $3.8 h^{-1}$ Mpc at $z = 0.5$, and $28 h^{-1}$ kpc and $5.0 h^{-1}$ Mpc at $z = 1$. The outer angular cutoff radius of 15 arcmin, corresponding to a physical projected distance of $2.7 h^{-1}$ Mpc at $z = 0.3$, is chosen purely for computational reasons as we only evaluate the lensing signal out to a distance of $2 h^{-1}$ Mpc.

In order to disentangle foreground and background and to avoid a confusion between foreground lens and background source we require a minimal separation in redshift between lens and source of $z_s - z_d \geq \sqrt{4\Delta_{z_d}^2 + 4\Delta_{z_s}^2} \approx \sqrt{8}\Delta_z$, roughly translating into $z_s - z_d \geq 0.1$, given our photometric uncertainties of $\Delta_z \approx 0.04$. In addition the weak lensing analysis of the ultimate background is not recommendable as the weak signal contribution from these foreground-background pairs is strongly suppressed due to the geometrical constellation. Considering, e.g., an SIS, the shear signal scales with D_{ds}/D_s , the ratio of angular diameter distances between deflector and source and observer and source, respectively. For $z_s \approx z_d$ it approaches zero, steeply rising for increasing source redshift, eventually converging against 1 for $z_s \rightarrow \infty$. In order to exclude the contribution of very low signal-to noise pairs we further reject lens-source pairs with $D_{\text{ds}}/D_s < 0.1$ (cf. Fig. 5.29). Finally we want to exclude areas with large errors in the estimation of the critical surface mass density Σ_c , as the fractional error in mass density, converted from the measured shear signal, is directly proportional to the fractional error in surface mass density $\delta\Sigma_c/\Sigma_c$. Assuming Gaussian photometric redshift errors with a width of $\Delta z = 0.05 (1 + z)$ the fractional error in Σ_c does not exceed a value of 0.3 for $z_s > 1.1 \cdot z_d + 0.15$ and

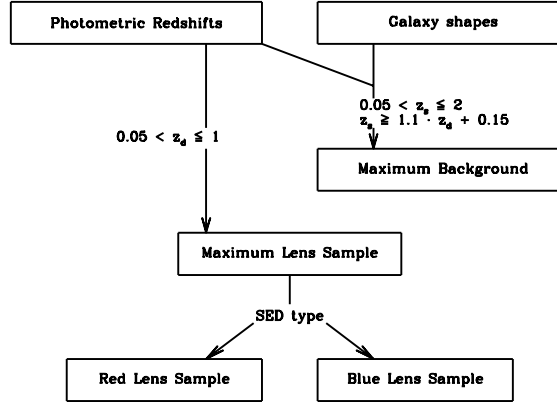


Fig. 5.25: Flowchart for our lens and background definition.

$z_d > 0.05$ (see Fig. 5.30), representing a stricter condition for the pair selection. In total our selection criteria summarize as follows (see also Fig. 5.25):

$$0.05 < z_{\text{lens}} \leq 1.0, \quad z_{\text{source}} \leq 2.0 \quad \text{and} \quad z_{\text{source}} \geq 1.1 \cdot z_{\text{lens}} + 0.15, \quad (5.9)$$

ensuring the disentanglement of foreground and background, the validity of $D_{\text{ds}}/D_{\text{s}} > 0.1$ and the fractional surface mass density error $\delta\Sigma_{\text{c}}/\Sigma_{\text{c}}$ not exceeding a value of 0.3. This leaves us with maximum number of $N_{\text{pairs}} = 601\,245\,059$ lens-source pair combinations.

5.5.2 Definition of Lens Subsamples

We want to analyze the properties of our lens sample as a function of several quantities, such as rest-frame luminosity, SED type, redshift or the environment, where the considered lens resides. We therefore firstly split our main lens sample into absolute magnitude intervals with a width of one magnitude in the range $-17 \geq M_{r'} \geq -24$ and additionally into half magnitude intervals from $-21 \geq M_{r'} \geq -24$. Further we consider four redshift intervals $0.05 < z_{\text{lens}} \leq 0.3$, $0.3 < z_{\text{lens}} \leq 0.5$, $0.5 < z_{\text{lens}} \leq 0.7$ and $0.7 < z_{\text{lens}} \leq 1.0$. Further, as we want to investigate the properties of all lenses as a function of their SED type or morphology, we need to split them into individual subsamples of red and blue galaxies. For this we follow the approach of Dahlen *et al.* (2005), using the $(B - V)$ rest-frame colors in AB-system for the galaxy classification, defining all galaxies with $(B - V) > 0.7$ as red and all galaxies with $(B - V) \leq 0.7$ as blue galaxies. We estimate the rest-frame colors using the absolute magnitude estimates derived from the best-fitting template in the photometric calculation with the PhotoZ-code. We cross-check this selection by considering the classification for the spectroscopic Luminous Red Galaxy (LRG) sample from SDSS (see Eisenstein *et al.* 2001), confirming that this classification excellently works for the LRG sample (see also Fig. 5.26). Additionally we verify our galaxy classification by considering the absolute r' -band magnitude and the apparent $(g' - r')$ - and $(r' - i')$ -colors for all galaxies. This is in agreement with Loveday *et al.* (2012), who used the absolute $(g' - r')$ -color as a function of the absolute r' -band magnitude to distinguish red from blue galaxies. For lack of individual absolute colors for all galaxies we consider the apparent $(g' - r')$ -color. At least

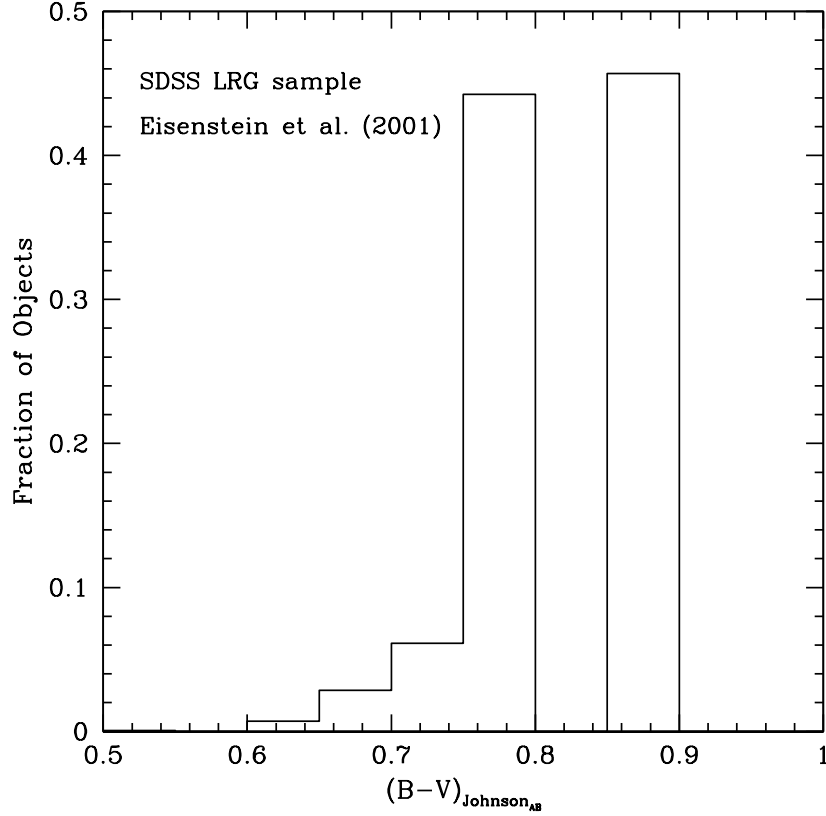


Fig. 5.26: $(B-V)$ restframe color histogram for the SDSS LRG sample (Eisenstein *et al.* 2001) in the AB-system. The $(B-V)$ -colors are taken from our SED template that best match the SDSS photometry at the spectroscopic redshift of the LRG. For almost all objects the assumption $(B-V) > 0.7$ holds, justifying the chosen galaxy classification for red and blue galaxies (see Dahlen *et al.* 2005).

looking at low redshift objects this represents a justifiable approximation, but as we will see also for higher redshifts meaningful conclusions can be extracted. Fig. 5.27 shows that red and blue galaxies populate distinct regions in the $M_r - (g' - r)$ space, indicating an at most small contamination rate for our galaxy subsamples, especially considering the higher redshift bins. Only for low redshifts there is a small overlap between red and blue galaxies. Further we plot the $(g' - r)$ - and the $(r' - i')$ -colors (see Tojeiro *et al.* 2012 for moderate redshift galaxies with $0.5 \leq z \leq 0.7$). Taking into account the results from Fig. 5.28, showing the good separation of red and blue galaxies in $(g' - r)$ - vs. $(r' - i')$ -color-space, this approves our chosen classification criterion.

As we do not only want to investigate the properties of our lens galaxies with respect to luminosity and morphology but also as a function of the environment, the galaxies populate, we need to define an estimator for the local lens environment density. For the estimation of this density we consider the relative galaxy density within a certain redshift range and projected angular separation around the investigated lens. First we consider all galaxies with $\Delta z = \pm 0.2$ in front and behind the investigated lens galaxy within a maximum angular separation of 30 arcsec from the lens and then compare the number of galaxies in this region with the total number of galaxies within this redshift bin all over the

entire one square degree pointing. By calculating the ratio of these two quantities we obtain a relative local environment density. We use this density to assign the following lens subsamples. We define:

- i) a very dense environment lens sample (10% of galaxies populating the densest environments),
- ii) a dense environment lens sample (50% of galaxies populating denser environments),
- iii) a low density environment lens sample (50% of galaxies populating lower density environments)
- iv) and a very low density environment lens sample (10% of galaxies populating the lowest density environments).

5.6 Lens Mass Errors from Photometric Redshifts and Shape Measurement Errors

In order to estimate the excess surface mass density $\Delta\Sigma$ (see equation 3.20) we use the foreground-background pair average

$$\Delta\hat{\Sigma}(R) = \langle \hat{\Sigma}_c \hat{\gamma}(R) \rangle_{\text{fg-bg-pair}} , \quad (5.10)$$

where the ‘hat’ indicates the estimates. We obtain the critical surface mass density estimate $\hat{\Sigma}_c$ from the photometric redshift estimates of the background-foreground pair and the shear estimate $\hat{\gamma}(R)$ from the background shapes, translating the angular scale θ into a physical length scale with $\hat{R} = \theta\hat{D}_d$. The relation between the true gravitational shear $\gamma(R)$ at projected distance R and its estimate $\hat{\gamma}(R)$ is given by

$$\hat{\gamma}(R) = \gamma(R) + [\gamma(\hat{R}) - \gamma(R)] + \delta\gamma_{\text{shape}} \equiv \gamma(R) + \Delta\gamma(\hat{R}, R) + \delta\gamma_{\text{shape}} . \quad (5.11)$$

We introduce a distance-independent shear estimation error $\delta\gamma_{\text{shear}}$, coming from the shape measurement error, the intrinsic shape noise and a potential shape estimation bias, where we further introduce the ‘profile error’

$$\Delta\gamma(\hat{R}, R) = \gamma(\hat{R}) - \gamma(R) = \gamma(\theta\hat{D}_d) - \gamma(\theta D_d) , \quad (5.12)$$

originating from the mixing of physical scales when translating angles into length scales. The profile error vanishes if a spectroscopic lens sample is used. The size of the profile error in general depends on the profile steepness. E.g., for a power law with $\gamma(R) \propto R^{-\alpha}$ it is given by

$$\Delta\gamma(\hat{R}, R) = \gamma \left(\frac{R^\alpha - \hat{R}^\alpha}{\hat{R}^\alpha} \right) . \quad (5.13)$$

Thus we see that the profile error increases with the steepness of the profile. Assuming an isothermal profile with $\alpha = 1$, equation (5.13) becomes

$$\Delta\gamma_t^{\text{SIS}}(\hat{R}, R) = \gamma \left(\frac{D_d - \hat{D}_d}{\hat{D}_d} \right) . \quad (5.14)$$

This means that for small redshift errors the profile error becomes

$$\left(\frac{\Delta\gamma_t^{\text{SIS}}(\hat{R}, R)}{\gamma(R)} \right)_{z_d \approx 0} = \frac{z_d - \hat{z}_d}{\hat{z}_d} = \frac{\Delta z_d}{z_d} . \quad (5.15)$$

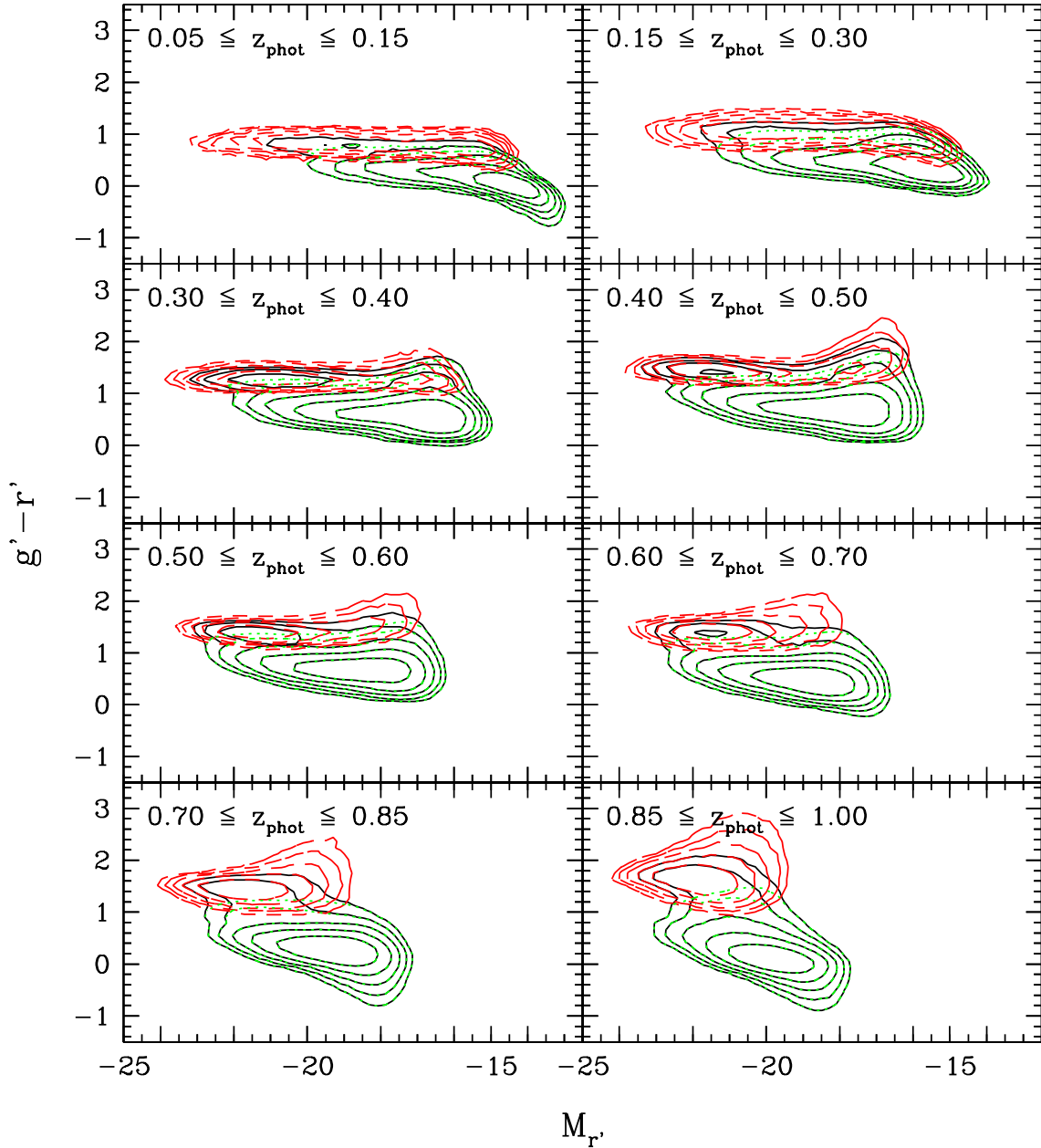


Fig. 5.27: Density contours, showing the absolute r' -band rest-frame magnitude vs. the apparent $(g' - r')$ -color for different redshift intervals. The black solid lines show the distribution of all galaxies, the red dashed lines the distribution of red galaxies and the green dotted lines the distribution of blue galaxies. As we can see, red and blue galaxies populate distinct regions in the color-magnitude space, especially for higher redshifts. For lower redshifts there is a small overlap between red and blue galaxies in the color-magnitude plane.

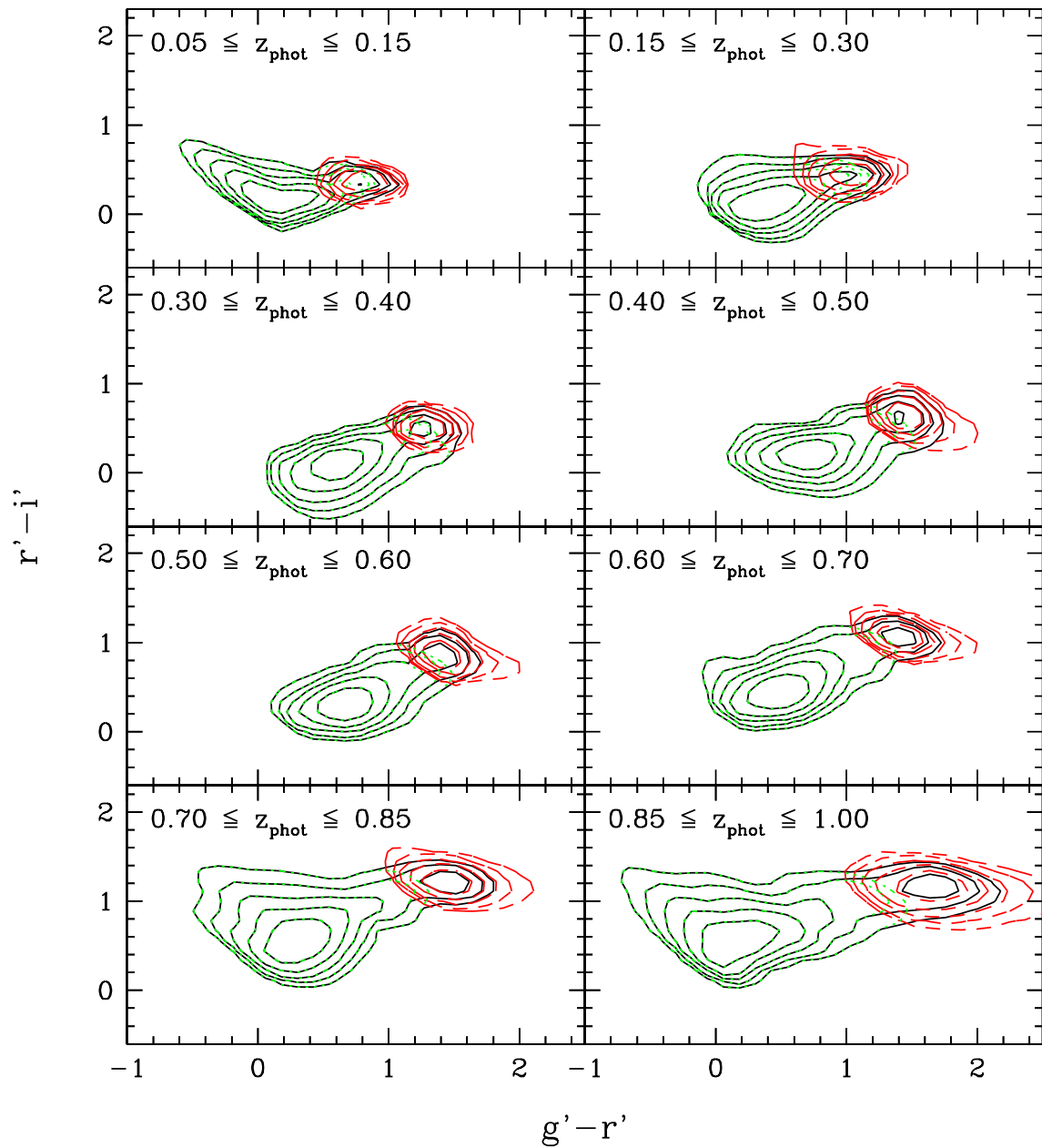


Fig. 5.28: Density contours showing the apparent $(g' - r')$ -color vs. the apparent $(r' - i')$ -color for different redshift intervals. The black solid lines show the distribution of all galaxies, the red dashed lines the distribution of red galaxies and the green dotted lines the distribution of blue galaxies. In color-space our defined red and blue galaxy samples populate distinct regions, when considering redshifts $z \geq 0.4$ in agreement with Tojeiro *et al.* (2012). For lower redshifts our $(g' - r')$ vs. $(r' - i')$ colors of red and blue galaxies overlap.

We see that already photometric redshift errors without a bias can impose a bias on the shear profile estimates. To obtain a better understanding for this we consider foreground-background pairs with a projected separation estimate \hat{R} in the lens plane and a redshift estimate \hat{z}_d . If the redshift estimate is too low ($\hat{z}_d < z_d$) the projected separation between lens and source is also underestimated ($\hat{R} < R$), i.e., sources are scattered from larger to shorter projected separations. In this case the gravitational shear will be underestimated. Analogously an overestimate of the lens redshift ($\hat{z}_d > z_d$) will lead to an overestimate of the gravitational shear signal, i.e., a possible bias depends on the redshift distribution of the analyzed lens sample. If the lens redshift distribution is flat, about the same number of galaxies are scattered down from higher redshift and scattered up from lower redshifts and the mean projected separation within a ring of diameter \hat{R} equals the true distance R . If the lens distribution has a positive slope, i.e., the lens number increases as a function of redshift, a higher number of galaxies can be scattered down to lower redshifts than scattered up. In this case the mean redshift \hat{z}_d and the mean projected separation \hat{R} and thus the gravitational shear signal are underestimated. In order to estimate the maximal bias in the measurement of the velocity distribution we performed a lensing signal simulation, scattering our photometric redshift by adding a Gaussian redshift distribution of $0.03(1+z)$. Even in the most extreme scenario (lowest redshift lenses, i.e., steep rise in the redshifts counts and asymmetric redshift scattering, as there are no lower redshift lenses which can be scattered up), we observe a bias of smaller than 4%, for larger lens redshifts the bias rapidly decreases. The number of low redshift lenses is low compared to the total number of lenses. We therefore make no attempt to correct for this bias. For a given foreground-background distance distribution the bias increases with photometric redshift scatter. In linear order the ratio of the estimator and true contribution for each pair is given by

$$\frac{\hat{\Sigma}_c \hat{\gamma}(R)}{\Sigma_c \gamma(R)} = 1 + \frac{\delta \Sigma_c}{\Sigma_c} + \frac{\Delta \gamma(\hat{R}, R)}{\gamma(R)} + \frac{\delta \gamma_{\text{shape}}}{\gamma(R)}. \quad (5.16)$$

If we define $\Delta \hat{\Sigma} = \Delta \Sigma + \delta \Delta \Sigma$ and $\hat{\Sigma}_c = \Sigma_c + \delta \Sigma_c$ and insert equation (5.16) into equation (5.10) we obtain in linear order for the error of the estimator:

$$\begin{aligned} \delta \Delta \Sigma(R) &= \left\langle \gamma(R) \Sigma_c \left[\frac{\delta \Sigma_c}{\Sigma_c} + \frac{\Delta \gamma(\hat{R}, R)}{\gamma(R)} + \frac{\delta \gamma_{\text{shape}}}{\gamma(R)} \right] \right\rangle_{\text{fg-bg-pair}} \\ &= \left\langle \gamma(R) \delta \Sigma_c + \Delta \gamma(\hat{R}, R) \Sigma_c + \delta \gamma_{\text{shape}} \Sigma_c \right\rangle_{\text{fg-bg-pair}}. \end{aligned} \quad (5.17)$$

The error of the estimator of $\Delta \Sigma$ can be used to obtain the error estimates in presence of scatter in the photometric redshifts and shape estimates. Equations (5.13)-(5.15) together with equation (5.17) explain why lens redshift errors have more severe consequences on the GGL analysis than source redshift errors. This in particular is true when considering very small lens redshifts, as for $\Delta z_d \approx 0.03$ and $z_d \approx 0.1$ the fractional error in Σ_c can easily approach an order of 30%. As for larger redshift the dependence of the lens distance D_d on the redshift flattens, the effect on the profile error also diminishes. The independent shear estimation error δ_{shape} includes intrinsic shape noise, the shape measurement error and potential systematics. As the value of $\delta \gamma_{\text{shape}}/\gamma$ is of the order of $0.3/0.002 \approx 150$ per foreground-background pair, the relative shape error exceeds the relative profile error by more than a factor of 500.

We now calculate the errors due to shape noise and photometric redshifts errors in more detail. In order to estimate the statistical error in $\gamma(R)$ and $\Delta \Sigma(R)$ the tangential shear relative to a random foreground can be used. This is shown in more detail in Section 6.3.1. For any given galaxy lens sample the background is specified by the selection criterion defined in equation (5.9). The analysis of estimating γ and $\Delta \Sigma$ is repeated, replacing the true tangential ellipticity by the shape of the background

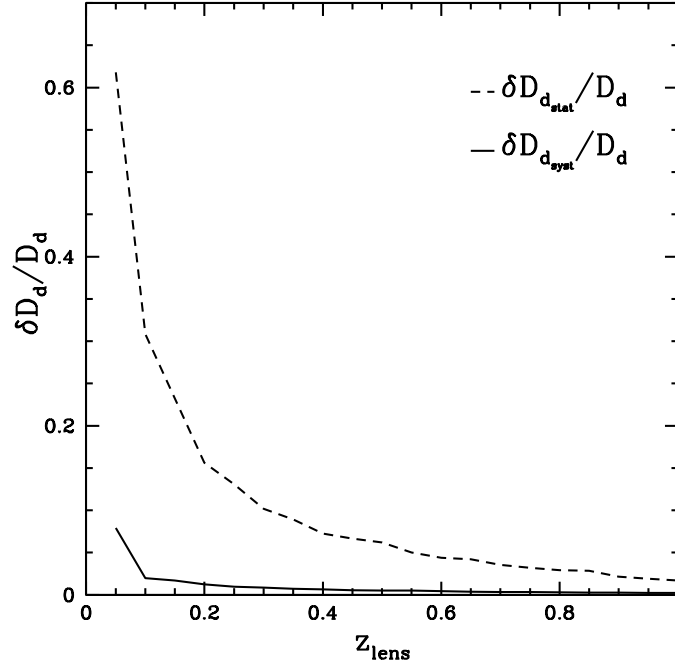


Fig. 5.29: Fractional systematic and statistical error $\delta D_d / D_d$ in the estimation of the angular distance of the lens D_d in presence of photometric redshift errors. The dashed line shows the statistical and the solid line the systematic error for a Gaussian redshift error distribution with a scatter of 0.05 $(1+z)$. The systematic error in D_d is below 10% for $z \geq 0.05$ and well below 5% for $z \geq 0.1$.

galaxy with a randomized phase or by the shape of another object in the background galaxy catalog. In order to estimate the errors introduced by the photometric redshift uncertainties we investigate the propagated systematic errors in the angular diameter distance of the deflector $\delta D_d / D_d$ and the critical surface mass density $\delta \Sigma_c / \Sigma_c$. The simulation is built in such way, to rather overestimate than underestimate the errors. This is especially true when considering very low redshifts, where scattering the photometric redshifts could easily lead to negative lens redshift values which are not realized in the observational data. The total errors can be written as the sum of the systematic error and the statistical error, e.g., for the error of the critical surface mass density Σ_c :

$$\delta \Sigma_c = \sqrt{\delta \Sigma_{c,\text{syst}}^2 + \frac{\delta \Sigma_{c,\text{stat}}^2}{n}}. \quad (5.18)$$

In order to disentangle systematic and statistical error we investigate two different sample sizes of 100 000 and 1 000 objects (see also Gruen *et al.* 2010) and solve the resulting system of equation. In both cases, the systematic error is significantly smaller than the corresponding statistical error. For a lens redshift of $z = 0.05$, we obtain a fractional error of $\delta D_d / D_d$ smaller than 10% for the lens distance, further dropping below 5% when considering higher redshifts (see also Fig. 5.29). Regarding the critical excess surface mass density, the fractional error $\delta \Sigma_c / \Sigma_c$ is larger than in the case of the angular diameter distance of the lens D_d , caused by the multiple dependence of Σ_c on the redshift (D_d , D_s and D_{ds}). However, by applying the selection criterion defined in equation (5.9), we can ensure

that the systematic errors do not exceed the 30% level (see Fig. 5.30).

We now further estimate the systematic errors for more extreme cases. Considering Σ_c , in the case of a 20% redshift bias for lens-source pairs close in redshift, we expect for lenses with $z \sim 0.7$ and a fraction of 25% in the close-redshift space a systematic error of $0.75 \cdot 1 + 0.25 \cdot 1.2 = 1.05$. This corresponds to an overestimation of $\delta\Sigma_c/\Sigma_c \sim 5\%$. Considering the other extreme at the low redshift end, the fraction of lens-source pairs is only about 5%, leading to a fractional systematic error of $0.95 \cdot 1 + 0.05 \cdot 1.2 = 1.01$, i.e., $\delta\Sigma_c/\Sigma_c = 1\%$. If we consider the complete lens-source sample we obtain $0.88 \cdot 1 + 0.12 \cdot 1.2 = 1.02$, this means we do not expect a systematic bias of $\delta\Sigma_c/\Sigma_c$ of more than 2% due to photometric redshift inaccuracies. We therefore conclude that the expected systematic errors due to photometric redshift uncertainties are small enough to be neglected.

5.7 Systematic Errors from Intrinsic Alignment

This section is directly taken from Section 3.8, Brimiouille *et al.* (2013).

Galaxies which are in the same structure and thus physically connected are not randomly distributed in orientation but rather intrinsically aligned (Hirata *et al.* 2004), for instance satellite galaxies tend to be radially aligned relative to their central galaxies. This is why intrinsic alignment (IA) is a major issue in the interpretation of cosmic shear data (see e.g. Mandelbaum *et al.* 2006b or Bridle & King 2007). The observed two-point correlation function for the ellipticity of galaxy pairs is $\langle \epsilon_i \epsilon_j^* \rangle = \langle \gamma_i \gamma_j^* \rangle + \langle \epsilon_i^S \epsilon_j^{S*} \rangle + \langle \gamma_i \epsilon_j^{S*} \rangle + \langle \epsilon_i^S \gamma_j^* \rangle$, where ϵ^S and ϵ are the unlensed and lensed ellipticities and γ_i is the cosmic shear at redshift z_i (see e.g. Joachimi & Schneider 2008). The first term on the right hand side is the desired cosmic shear signal, the second term (called II) describes the intrinsic alignment of two galaxies. Unless the two galaxies are physically associated (i.e. they are required to be at same redshift) this term is zero. The third term describes (for $z_i \leq z_j$) the correlation of a foreground gravitational shear with the intrinsic ellipticity of a background galaxy and is zero. The fourth term (called GI) describes the correlation between the intrinsic ellipticity of a foreground galaxy and the gravitational shear acting on a background galaxy.

In GGL, however, one measures the tangential alignment, i.e. the cross-correlation of a background galaxy shape and the foreground lens position. Therefore intrinsic alignment theoretically should not be an issue at all. This situation is different in case of a foreground-background mismatch due to photometric redshift errors, where the photometric redshift of the assumed background object is overestimated and the galaxy actually is embedded in the foreground structure. If the falsely assumed background galaxy is randomly oriented relative to the foreground galaxy considered, then the shear signal is just diluted and our error considerations from Section 5.6 apply. If however the background galaxy has a preferred direction to the foreground an additional source of systematic error arises. If these false ‘background’ galaxies are fainter than the foreground galaxies, they will likely be their satellites (if associated to the foreground structure) and thus will on average be radially aligned (see Agustsson & Brainerd 2006). This then leads to a false detection of the GI-signal.

The separation of GGL and intrinsic alignment is investigated in detail by Blazek *et al.* (2012). To isolate IA from the lensing signal, they exploited the fact, that the contamination of the background galaxy sample with foreground galaxies should decrease if a more distant background slice is considered. They measured the excess surface mass density $\Delta\Sigma$ associated with SDSS-LRGs using two source subsamples in two redshift slices behind the lens.

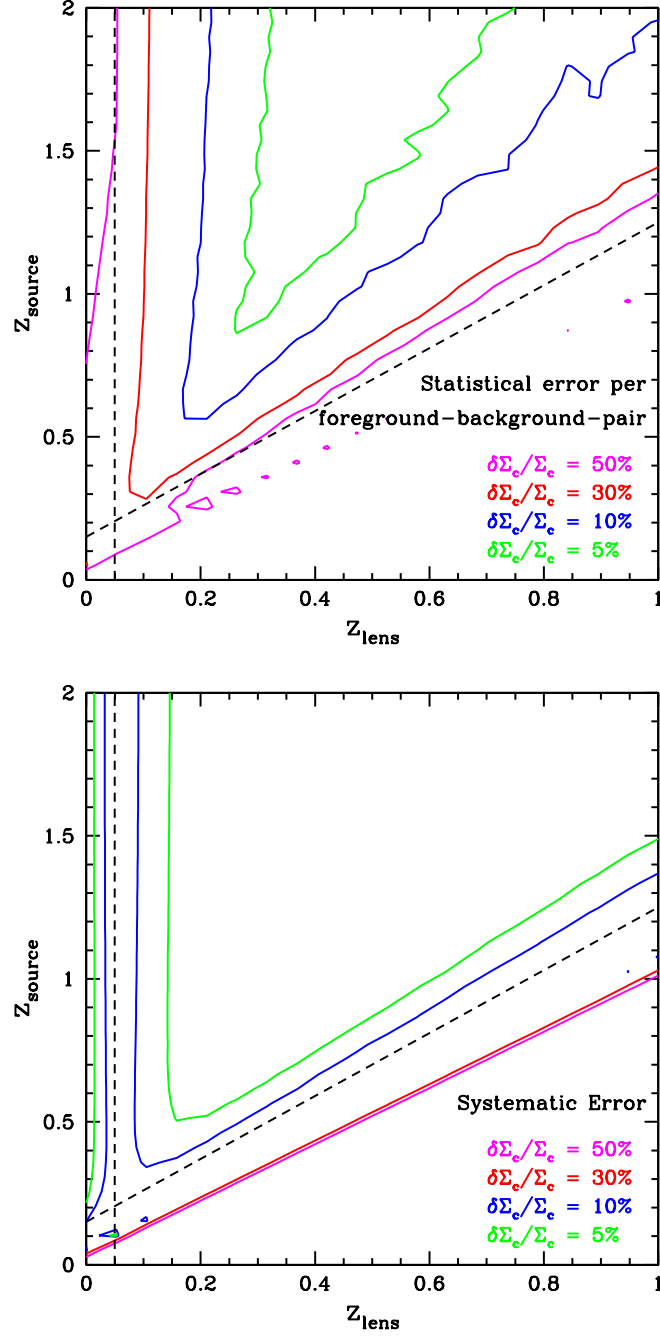


Fig. 5.30: Fractional error of the critical surface density, $\delta\Sigma_c/\Sigma_c$, in the presence of photometric redshift errors, as a function of the lens and source redshift. The upper panel shows the statistical error, the lower panel the systematic error. The photometric redshift errors in this simulation are Gaussian with a scatter of $0.05(1+z)$. The magenta and the red contours show $\delta\Sigma_c/\Sigma_c = 0.5$ and $\delta\Sigma_c/\Sigma_c = 0.3$ levels, respectively. Blue and green contours show the $\delta\Sigma_c/\Sigma_c = 0.1$ and $\delta\Sigma_c/\Sigma_c = 0.05$ levels. The fractional systematic error is below 0.3 if $z_{\text{source}} = 1.1 \cdot z_{\text{lens}} + 0.15$ (dashed black line) and $z_{\text{lens}} > 0.05$, which is the source-lens redshift requirement set in equation (5.9). The errors are in general rather overestimated than underestimated. This is especially true for very low redshift sources, where the scattering during randomization can lead to negative lens redshifts, which are not realized in the observational data.

They conclude that the size of IA for their lens sample is small (and consistent with zero, see their Figure 3). Their Figure 2 shows that for all scales larger than $100 h^{-1}$ kpc the signal extracted for two redshift subsets agrees which implies that the imprint of IA on $\Delta\Sigma$ can be neglected.

In our case we can infer the potential error due to IA from Figure 6.24 in Section 6.3. The magenta and green points show the $\Delta\Sigma$ values obtained for foreground lenses with $0.05 < z \leq 0.5$ using the shear signal from galaxies in the redshift slices of $0.6 \leq z \leq 0.73$ and $1.01 \leq z \leq 2$. Since the contamination of the $z = 1 - 2$ sample should be zero, the difference between the green and magenta points quantifies the maximal error due to IA in the low z background sample with $0.6 \leq z \leq 0.73$. All values agree within 2σ . We therefore conclude that systematic errors due to IA are small enough to be neglected.

Chapter 6

Weak Lensing Analysis

This chapter describes analyses and results which have been submitted (Brimioulle *et al.* 2013).

6.1 Measurement of the Tangential Shear

The simplest and most direct measurement in a galaxy-galaxy lensing (GGL) analysis is the measurement of the tangential shear or tangential alignment (see equation 3.29), describing the mean orientation of the major axes of considered background source galaxies. This measurement does in principle not require the knowledge of photometric redshifts, the selection of foreground and background sample can also be done with, e.g., the application of magnitude cuts for lenses and sources (see, e.g., Hoekstra *et al.* 2003, 2004 or Parker *et al.* 2007). However, without photometric redshift information the observable angular separations between lens and source cannot be converted into projected separations in physical units for individual sources, but only on average by estimating the effective redshift of the lens sample. Therefore, the observed tangential shear signal obtained in this way, represents a mixing of various physical scales, as our lens sample covers a large redshift range of $0.05 < z_{\text{phot}} \leq 1.0$. For this reason we choose to make use of the photometric redshift knowledge, measuring γ_t and directly mapping it to the physical projected distance

$$\Delta x = D_d \cdot \theta \quad (6.1)$$

and calculate a weighted mean for the tangential shear values from each individual lens-source pair. As weights we use the definition introduced by Hoekstra *et al.* (2000),

$$w = \frac{(P^g)^2}{(P^g)^2 \sigma_\varepsilon^2 + \langle \Delta \varepsilon^2 \rangle}, \quad (6.2)$$

with σ_ε being the scatter of the intrinsic galaxy ellipticities and $\sqrt{\langle \Delta \varepsilon^2 \rangle}$ the Gaussian uncertainty of the observed ellipticity measurement. The major motivation for our tangential shear analysis is the visual investigation of the main lens contribution to the tangential shear and its limitations, i.e., to which distance the shear γ_t is dominated by the considered central lens, and when the signal starts to be dominated by halos of nearby galaxies or by a parent group or cluster halo.

Weak lensing provides a very simple and comfortable opportunity to check for obvious systematics. The rotation of the source major axis by 45 degrees transforms the tangential shear γ_t into the

so-called cross-shear γ_c , also called B-mode. Gravity being a conservative force, i.e., not producing curls, the cross-shear signal is supposed to vanish. This can easily be checked. Vanishing of the cross-shear does not absolutely guarantee the absence of systematics, but on the other hand its presence is a strong indicator for remaining systematic effects.

Fig. 6.1 shows the tangential shear $\gamma_t(R)$ as a function of the projected distance R between lens and source, averaging over all galaxies and over red and blue galaxies separately. For this analysis we only consider lenses with $-20 \leq M_{r'} \leq -24$. As we can see the B-modes of all three lens samples are well consistent with zero. We estimate the velocity dispersion for the three galaxy lens samples assuming an SIS profile, only considering data points representing smaller separations than $R = 200 h^{-1}$ kpc for two reasons. Firstly, an SIS profile is not a reasonable physical assumption for larger distances as the integrated mass does not converge and secondly, by rejecting larger separations we reduce the contamination by shear contributions induced by secondary halos. In order to convert the tangential shear signal amplitude into a velocity dispersion we need to define the effective distance ratio D_{ds}/D_s for the individual lens subsamples. We estimate this quantity by calculating the weighted mean of the individual distance ratios of all lens-source pairs, using the weight defined in equation (6.2). For the inner regions the fits follow very well the profile of an SIS out to a scale of $R \sim 200 h^{-1}$ kpc, showing different amplitudes for the three lens samples. For the combined sample we find a velocity dispersion of $\sigma = 117 \pm 1 \text{ km s}^{-1}$, the red galaxy sample shows a velocity dispersion of $\sigma_{\text{red}} = 148 \pm 2 \text{ km s}^{-1}$ and the blue galaxy sample a value of $\sigma_{\text{blue}} = 99 \pm 2 \text{ km s}^{-1}$. The higher value for the red and the lower value for the blue sample are partially explained by different mean rest-frame luminosities as the combined sample has an effective luminosity of $\langle M_{r'} \rangle = -21.0$ while the red galaxy sample has $\langle M_{r'} \rangle = -21.3$ and the blue lens sample $\langle M_{r'} \rangle = -20.9$. However, the more important reason for the observed amplitude difference is given by the higher mass of elliptical galaxies compared to spiral galaxies with same luminosity. Looking at larger scales, the tangential shear profile for the complete and for the blue lens sample are still consistent within the predictions of an SIS, while the shear profile for the red galaxy sample clearly exceeds the expectation of the SIS profile. This deviation is assumed to be most likely induced by secondary halos, more strongly affecting the red galaxies' shear profile. This mirrors that the red (mainly early type) galaxies are more strongly correlated with each other and in general more often populate denser regions as galaxy groups or clusters than galaxies with bluer colors. In order to estimate the expected signal strength, we compare the observational data to the predictions of a simulated lensing survey. The details of the simulations are described in Section 3.4.4. Fig. 6.2, shows that the tangential shear expectations γ_t , assuming a BBS profile and assuming an NFW profile, respectively. Both describe observational tangential fairly well. Extracting the theoretical values for the velocity dispersion from the simulated shear profiles, we obtain $\sigma = 114 \text{ km s}^{-1}$ for the BBS combined sample and $\sigma = 115 \text{ km s}^{-1}$ for the NFW combined sample (the observational value was $\sigma = 117 \pm 1 \text{ km s}^{-1}$), $\sigma_{\text{red}} = 152 \text{ km s}^{-1}$ for the BBS red sample and $\sigma_{\text{red}} = 151 \text{ km s}^{-1}$ for the NFW red sample (the observational value was $\sigma_{\text{red}} = 148 \pm 2 \text{ km s}^{-1}$) and finally a value of $\sigma_{\text{blue}} = 92 \text{ km s}^{-1}$ for the blue BBS sample and $\sigma_{\text{blue}} = 94 \text{ km s}^{-1}$ for the blue NFW sample, with $\sigma_{\text{blue}} = 99 \pm 2 \text{ km s}^{-1}$ being the observational value. A summary is shown in Table 6.1. In particular we confirm the results of Brainerd (2010), that multiple deflection effects lead to an excess in the measured shear signal, observing that especially the simulated red galaxy shear signal significantly exceeds the predictions of an SIS on larger scales. In contrast, looking at small separations, where the 'main' lens still dominates the signal and for spiral galaxies also for larger separations, a shear excess is not observed. We will further discuss the dependence of the shear signal with respect to the environment in the later sections, then also investigating the excess surface mass

$M_{r'}$	$\langle M_{r'} \rangle$	$\sigma_{\text{true}} [\text{km s}^{-1}]$	$\sigma_{\text{sim,BBS}} [\text{km s}^{-1}]$	$\sigma_{\text{sim,NFW}} [\text{km s}^{-1}]$
Main Lens Sample				
$-24 \leq M_{r'} \leq -20$	-21.0	117 ± 1	114	115
$-24 \leq M_{r'} \leq -23$	-23.3	240 ± 4	219	239
$-23 \leq M_{r'} \leq -22$	-22.4	164 ± 4	166	175
$-22 \leq M_{r'} \leq -21$	-21.4	124 ± 2	123	123
$-21 \leq M_{r'} \leq -20$	-20.5	93 ± 2	91	87
Red Lens Sample				
$-24 \leq M_{r'} \leq -20$	-21.3	148 ± 2	152	151
$-24 \leq M_{r'} \leq -23$	-23.3	255 ± 5	237	259
$-23 \leq M_{r'} \leq -22$	-22.4	182 ± 7	186	195
$-22 \leq M_{r'} \leq -21$	-21.5	147 ± 3	150	147
$-21 \leq M_{r'} \leq -20$	-20.5	116 ± 4	125	113
Blue Lens Sample				
$-24 \leq M_{r'} \leq -20$	-20.9	99 ± 2	92	94
$-24 \leq M_{r'} \leq -23$	-23.3	205 ± 10	175	190
$-23 \leq M_{r'} \leq -22$	-22.4	138 ± 4	135	144
$-22 \leq M_{r'} \leq -21$	-21.4	109 ± 4	103	106
$-21 \leq M_{r'} \leq -20$	-20.4	87 ± 3	80	80

Table 6.1: Fit values for the velocity dispersion σ considering several luminosity bins, for observational data and BBS and NFW simulations, respectively.

density $\Delta\Sigma$.

We further investigate the tangential shear for different luminosities, splitting all three considered lens samples into four magnitude intervals for $M_{r'}$ between -24 and -20 of one magnitude width. Also in this case the observed B-modes are consistent with zero. Measuring the velocity dispersions of each individual luminosity bin, the observed decrease in velocity dispersion for fainter and therefore less massive lenses agrees well with the results of Faber & Jackson (1976) or Tully & Fisher (1977). The values for the fitted velocity dispersion σ in the considered combined lens luminosity bins are shown in Table 6.1. Further, considering the subsamples of different galaxy types but same luminosity, the conclusion of red galaxies being more massive than average or blue galaxies of the same luminosity is confirmed, as the velocity dispersions of red galaxies in all luminosity bins significantly exceed the values of their blue counterparts. Considering the combined lens sample the values for the velocity dispersions are, as expected, lower than for red galaxies, but higher than for the blue ones. The tangential shear profiles, discriminating the individual luminosity bins for all galaxies are shown in Fig. 6.3, for the red lens sample in Fig. 6.5 and finally for the blue lens sample in Fig. 6.7. We append the corresponding tangential shear plots based on BBS and NFW simulations for the individual luminosity bins for comparison in Figs. 6.4 (combined lens sample), 6.6 (red lens sample) and 6.8 (blue lens sample). The values for the shear amplitudes in the simulations mostly agree fairly well with the observational data, see Table 6.1.

Finally, we also consider the characteristics of the tangential shear profile for lenses populating

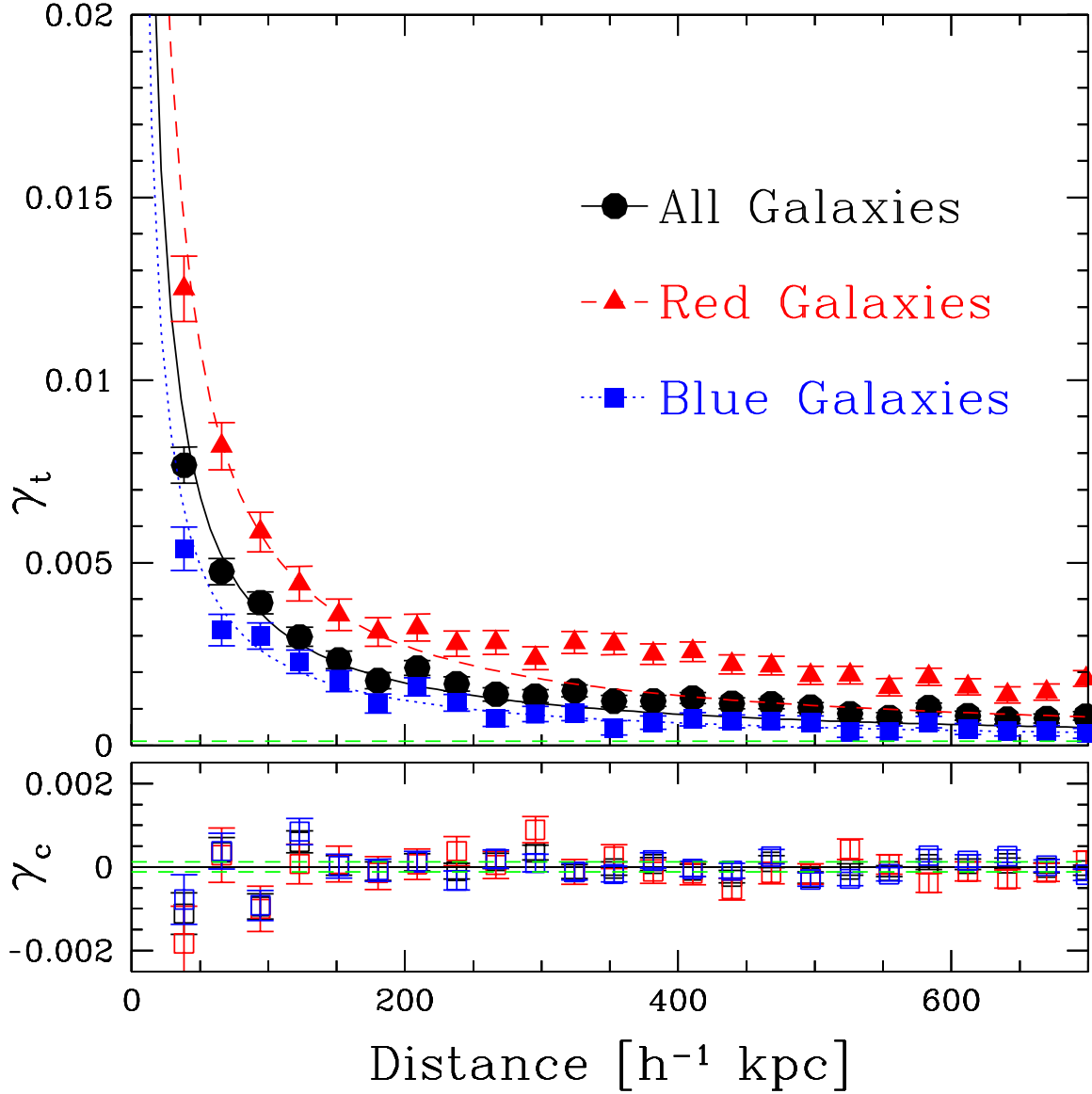


Fig. 6.1: Tangential shear γ_t for a lens sample with $-24 \leq i' \leq -20$, fitting an SIS profile for the inner part out to a scale of $R \sim 200 h^{-1}$ kpc, considering all galaxy types (black circles and solid fit-line), red (red triangles and dashed fit-line) and blue galaxies (blue squares and dotted fit-line) individually. The green dashed line indicates the $1\text{-}\sigma$ -level for remaining systematics. The signal amplitude is highest for red galaxies, exceeding the expectation for an SIS at scales larger than $R = 200 h^{-1}$ kpc. The blue galaxy sample shows the lowest tangential shear amplitude, not deviating from an SIS profile for larger separations, as spirals are mostly found in environments of lower density than cluster environment. The combined galaxy sample shows a shear profile lying between elliptical and spiral sample. The values for the velocity dispersion σ , derived by fitting an SIS out to a distance of $\sim 200 h^{-1}$ kpc, are shown in Table 6.1.

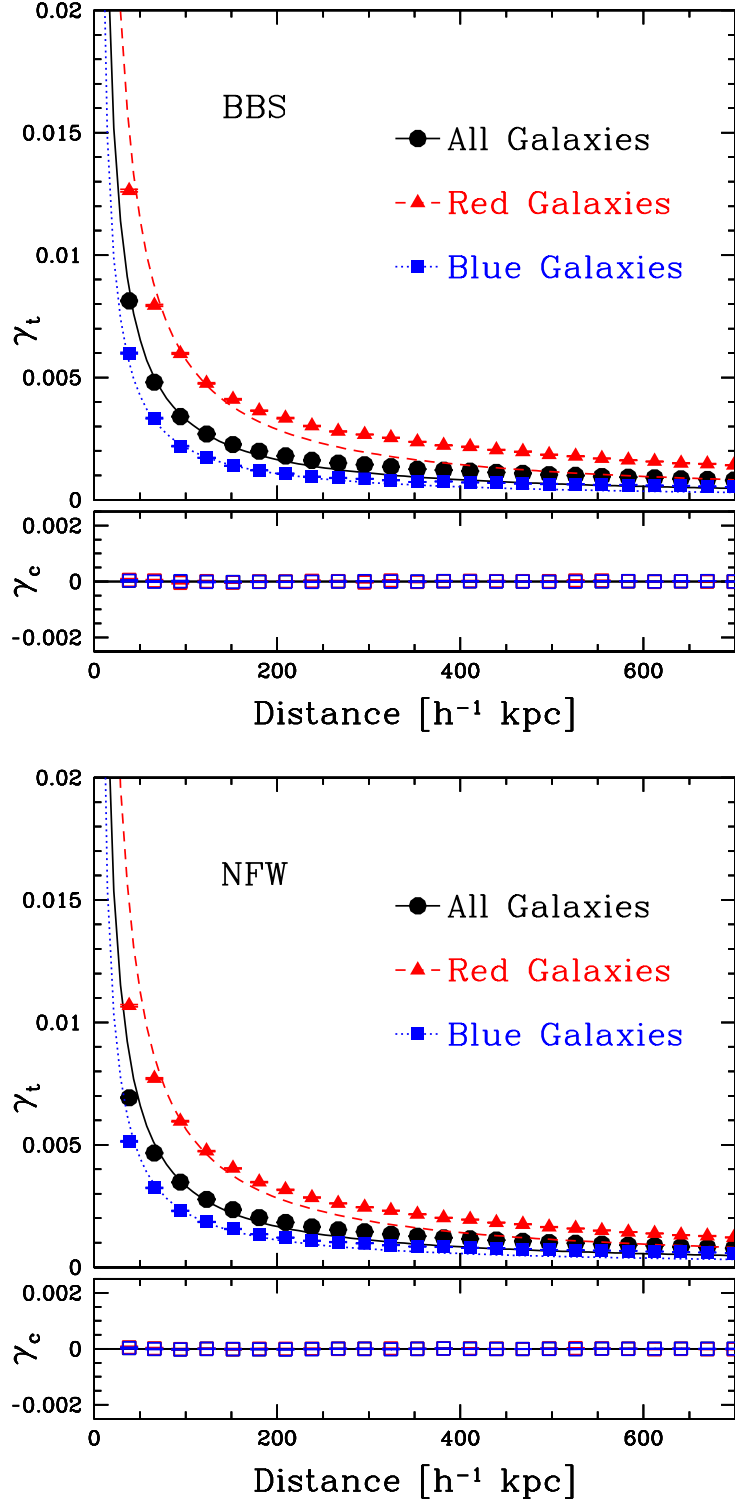


Fig. 6.2: Simulated tangential shear profile (see Section 3.4.4) for lenses with $-24 \leq i' \leq -20$. The upper panel shows the results based on the BBS simulation, the lower panel shows the results based on the NFW simulation. The tangential shear signals, based on either of both simulations, agree well with the actually observed profile (see Fig. 6.1). The values for the velocity dispersion σ , derived by fitting an SIS out to a distance of $\sim 200 h^{-1}$ kpc, are shown in Table 6.1.

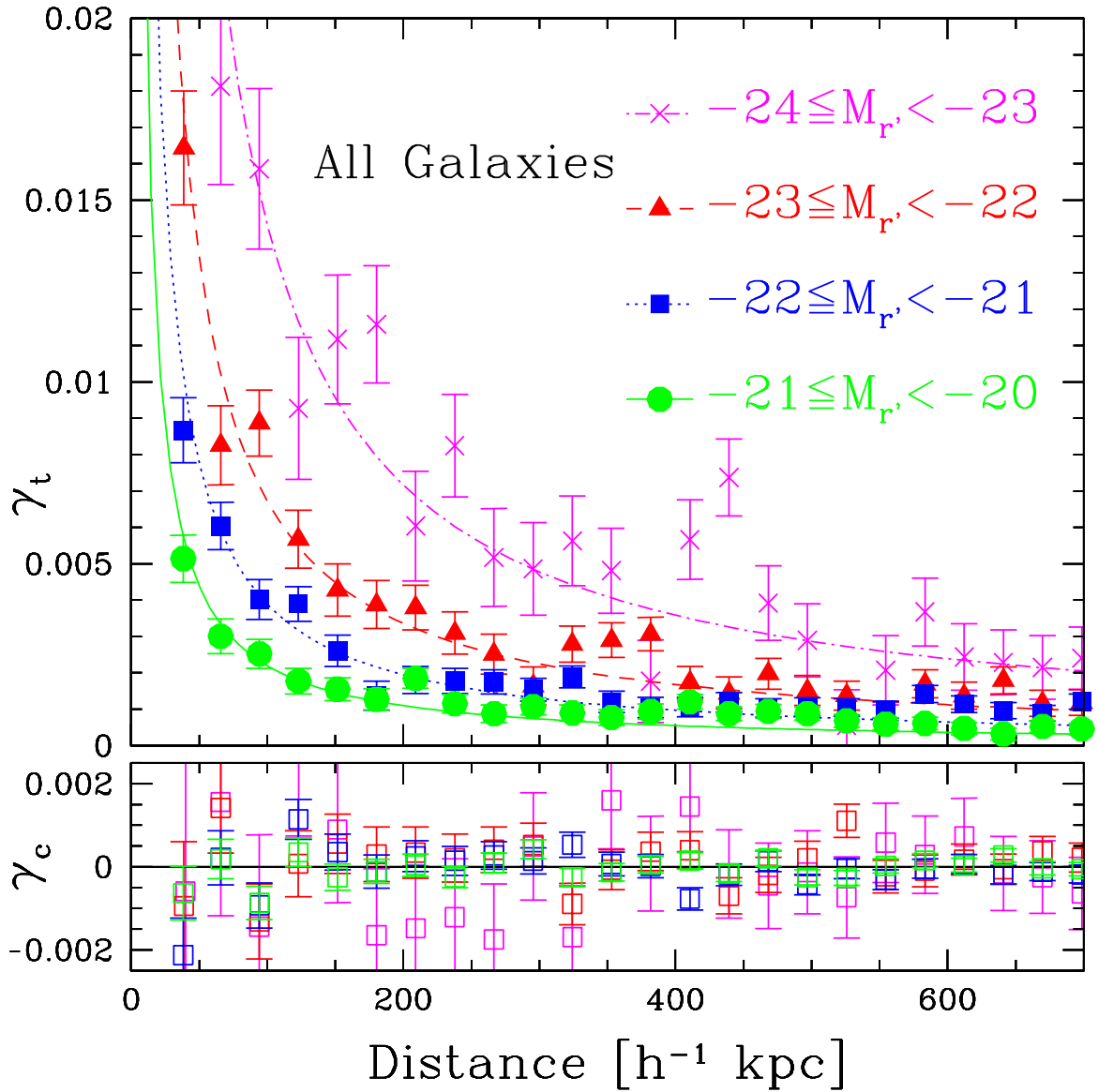


Fig. 6.3: Tangential shear profiles for the complete lens sample, discriminating four luminosity bins for $-24 \leq i' \leq -23$ in magenta (crosses, dashed-dotted fit-line), $-23 \leq i' \leq -22$ in red (triangles, dashed fit-line), $-22 \leq i' \leq -21$ in blue (squares, dotted fit-line) and finally $-21 \leq i' \leq -20$ in green (circles, solid fit-line). The estimated values for the velocity dispersions decrease with decreasing luminosity, as predicted by the Faber-Jackson or Tully-Fisher relation. The values for the velocity dispersion σ , derived by fitting an SIS out to a distance of $\sim 200 h^{-1}$ kpc, are shown in Table 6.1.

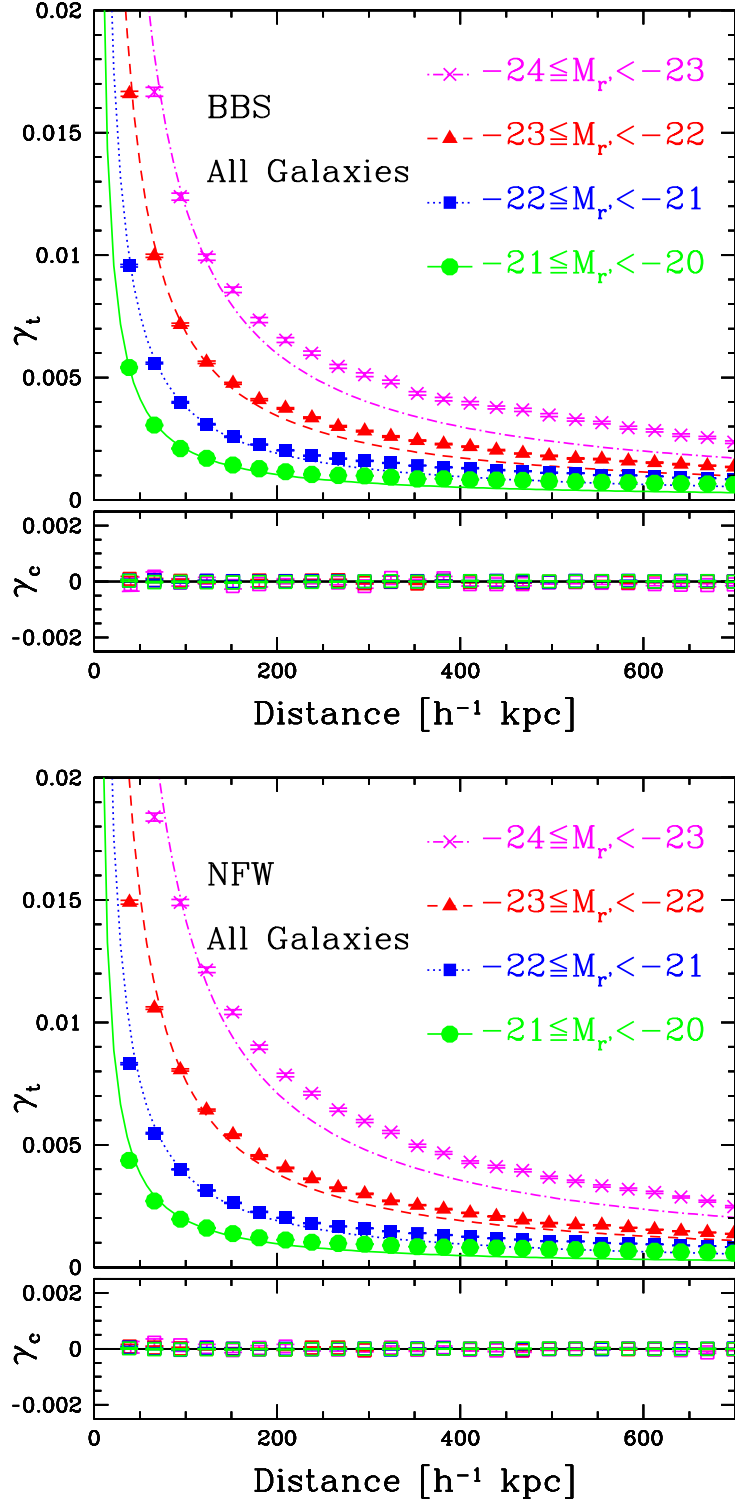


Fig. 6.4: Simulated tangential shear γ for all lenses, showing the profiles for individual luminosity bins with $-24 \leq i' \leq -20$. The upper panel shows the results of the BBS simulation, the lower panel of the NFW simulation. The simulations are widely consistent with the observational data. The values for the velocity dispersion σ , derived by fitting an SIS out to a distance of $\sim 200 h^{-1}$ kpc, are shown in Table 6.1.

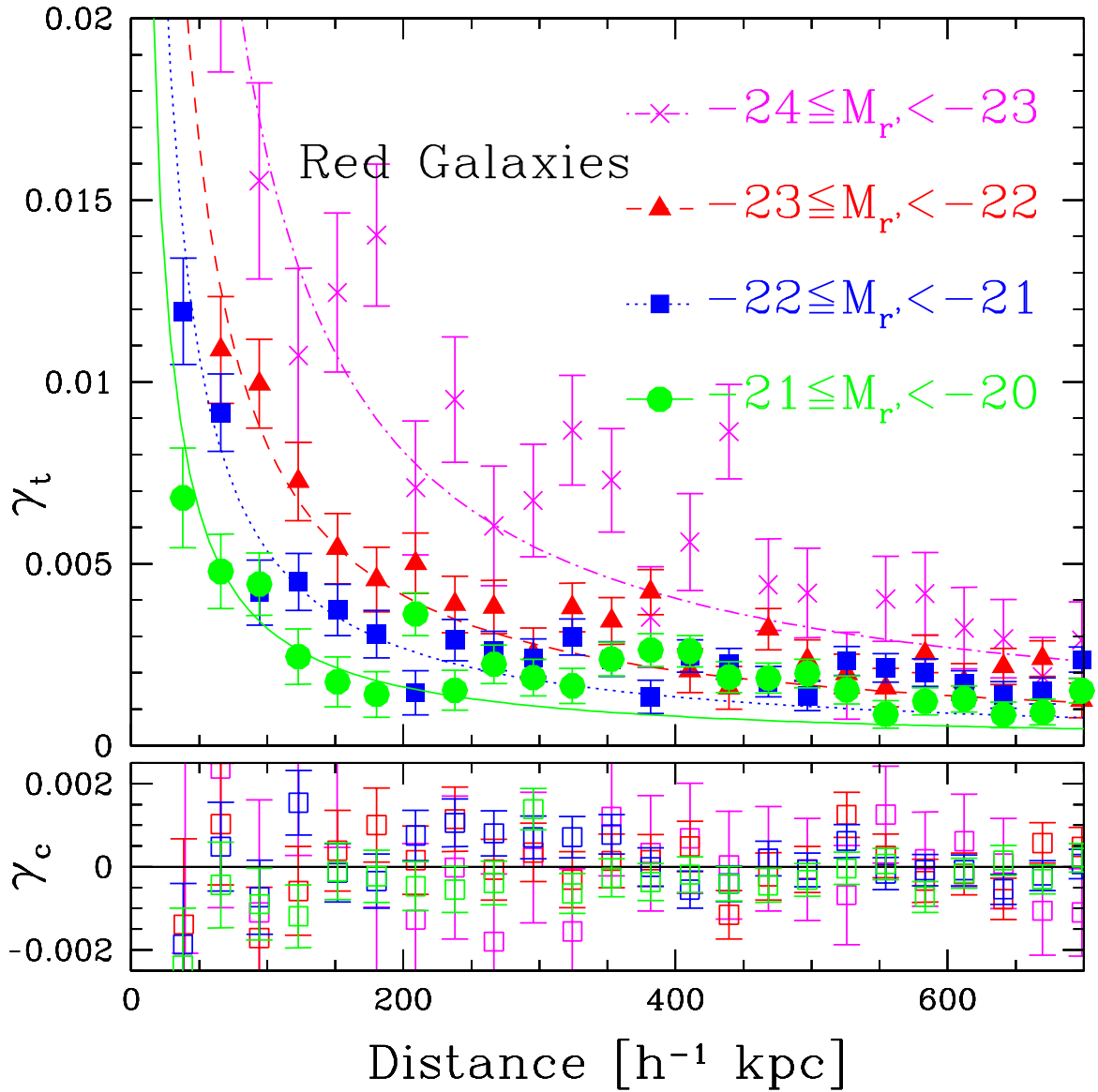


Fig. 6.5: Tangential shear profiles for the red lens sample, discriminating four luminosity bins for $-24 \leq i' \leq -23$ in magenta (crosses, dashed-dotted fit-line), $-23 \leq i' \leq -22$ in red (triangles, dashed fit-line), $-22 \leq i' \leq -21$ in blue (squares, dotted fit-line) and finally $-21 \leq i' \leq -20$ in green (circles, solid fit-line). The estimated values for the velocity dispersions decrease with decreasing luminosity, as predicted by the Faber-Jackson. All values for σ are higher than for the combined lens sample. The values for the velocity dispersion σ , derived by fitting an SIS out to a distance of $\sim 200 h^{-1}$ kpc, are shown in Table 6.1.

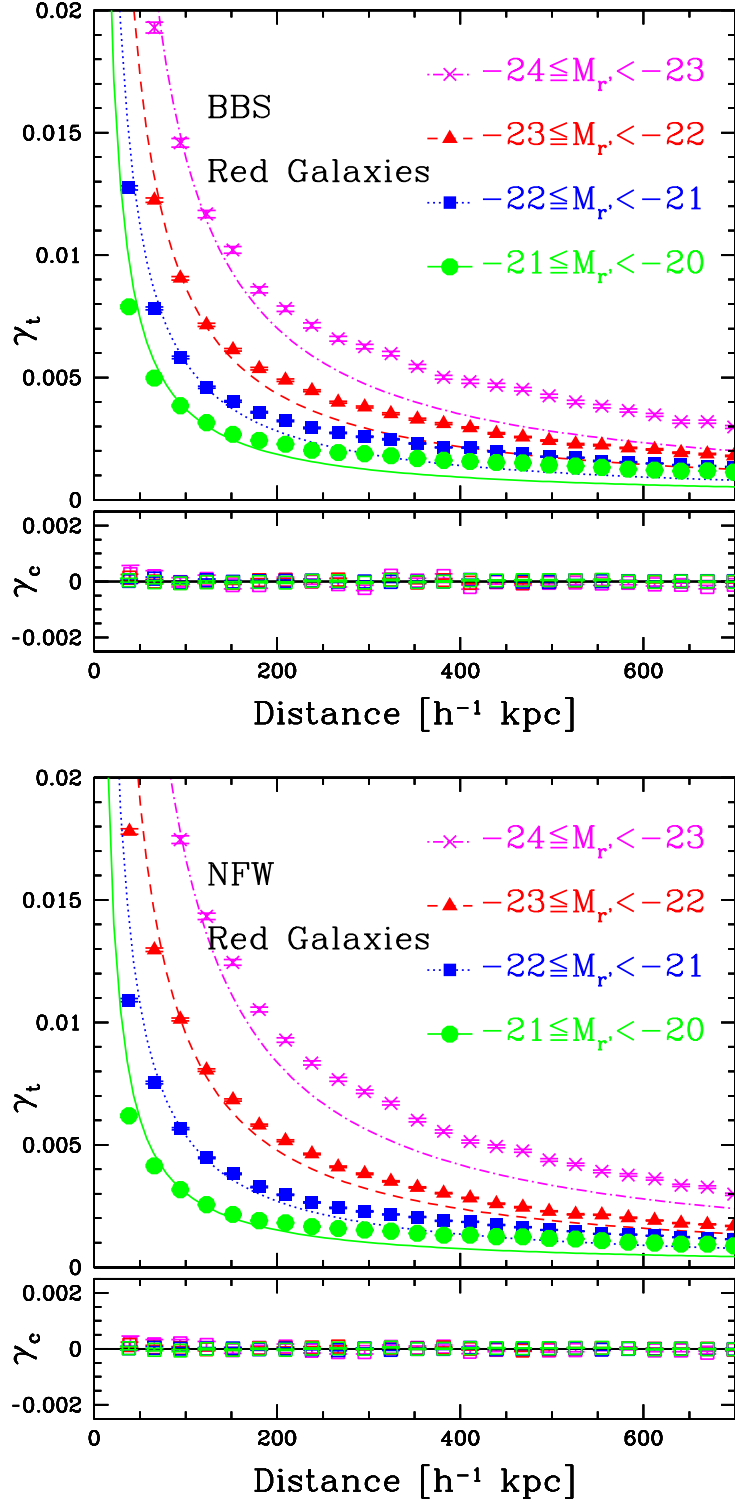


Fig. 6.6: Simulated tangential shear γ for red lenses, showing the profiles for individual luminosity bins with $-24 \leq i' \leq -20$. The upper panel shows the results of the BBS simulation, the lower panel of the NFW simulation. The simulations are widely consistent with the observational data. The values for the velocity dispersion σ , derived by fitting an SIS out to a distance of $\sim 200 h^{-1}$ kpc, are shown in Table 6.1.

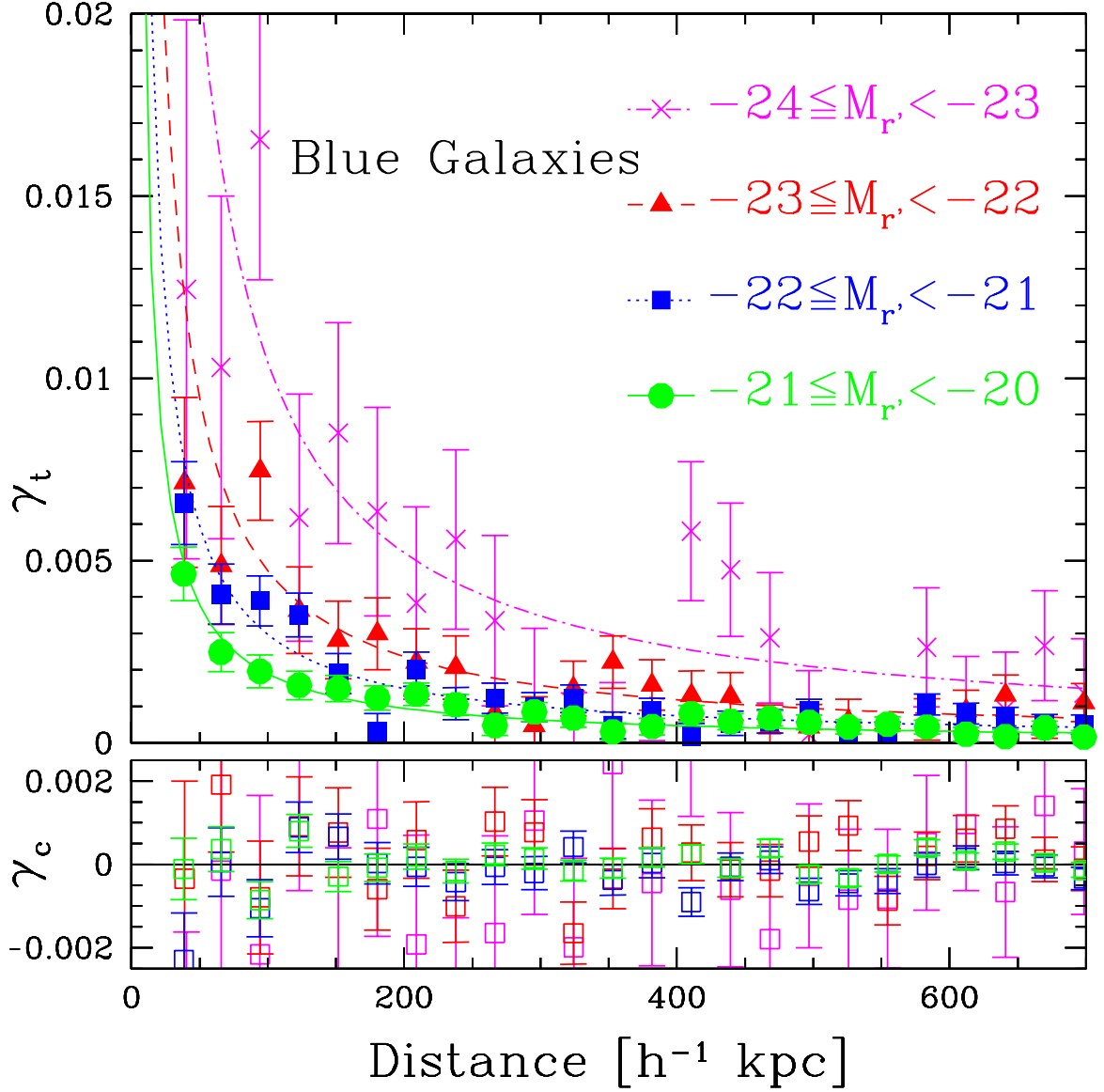


Fig. 6.7: Tangential shear profiles for the blue lens sample, discriminating four luminosity bins for $-24 \leq i' \leq -23$ in magenta (crosses, dashed-dotted fit-line), $-23 \leq i' \leq -22$ in red (triangles, dashed fit-line), $-22 \leq i' \leq -21$ in blue (squares, dotted fit-line) and finally $-21 \leq i' \leq -20$ in green (circles, solid fit-line). The estimated values for the velocity dispersions decrease with decreasing luminosity, as predicted by the Tully-Fisher relation. All values for σ are lower than for the combined lens sample. The values for the velocity dispersion σ , derived by fitting an SIS out to a distance of $\sim 200 h^{-1}$ kpc, are shown in Table 6.1.

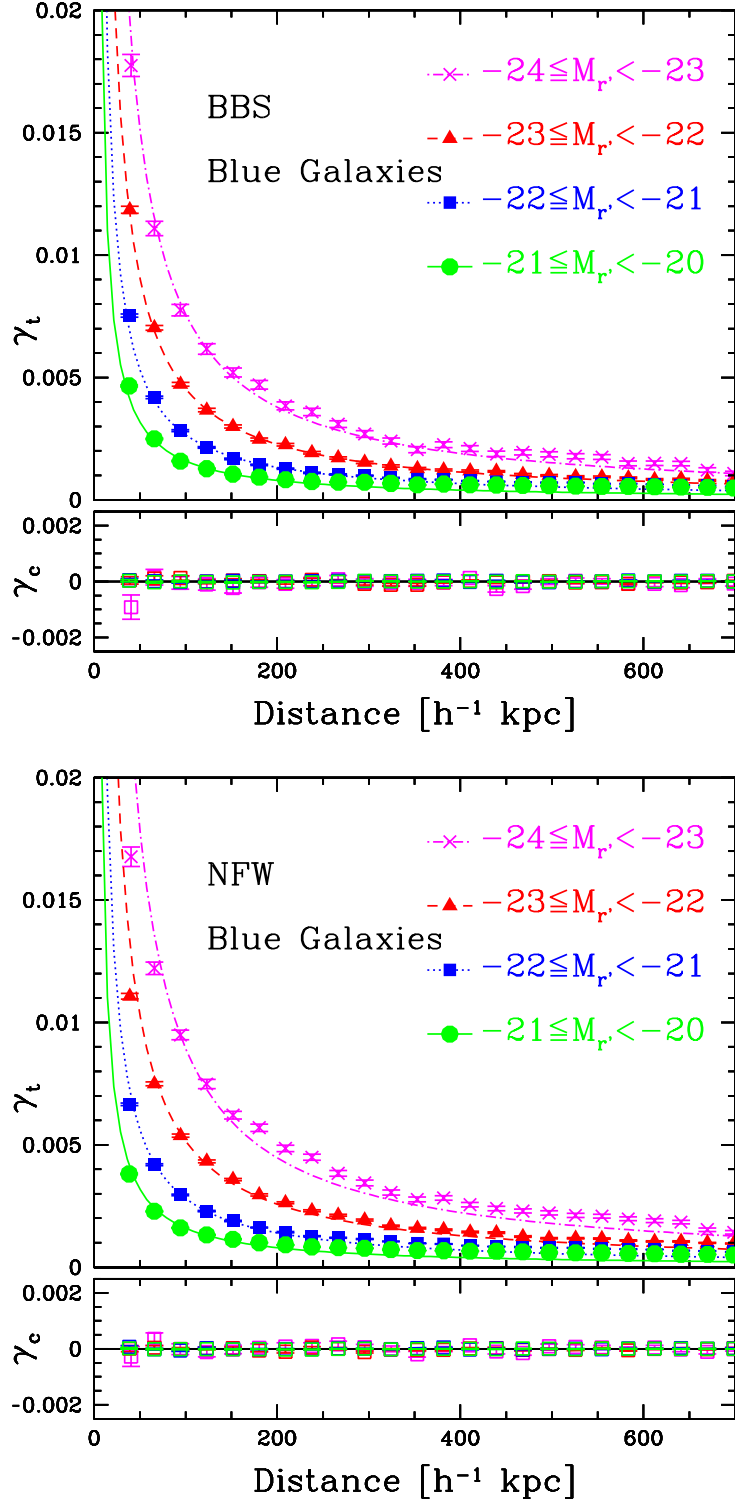


Fig. 6.8: Simulated tangential shear γ_t for blue lenses, showing the profiles for individual luminosity bins with $-24 \leq i' \leq -20$. The upper panel shows the results of the BBS simulation, the lower panel of the NFW simulation. The simulations are widely consistent with the observational data. The values for the velocity dispersion σ , derived by fitting an SIS out to a distance of $\sim 200 h^{-1}$ kpc, are shown in Table 6.1.

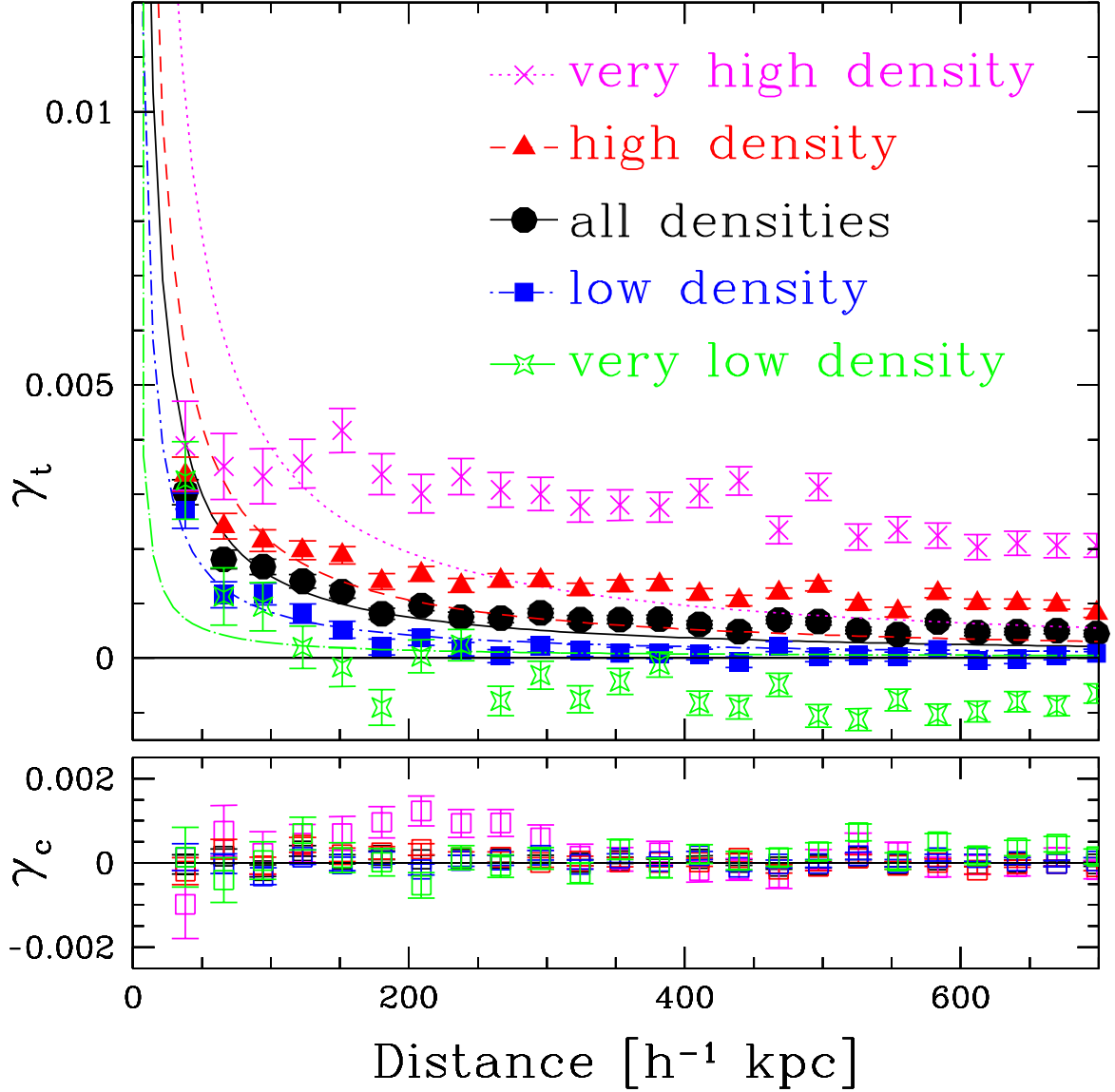


Fig. 6.9: Tangential shear profile for the combined lens sample with $-24 \leq i' \leq -17$, distinguishing between environment of different density (see Section 5.5.2 for the exact definition). The SIS fits are obtained within a projected separation of $R = 200 h^{-1}$ kpc. The combined lens sample, consisting of all lenses in all environments, is shown with black circles and black solid fit-line as reference (see also Fig. 6.1). Blue (squares, dashed-dotted fit-line) and green (diamonds, solid fit-line) show lenses in environment with low and very low density, red (triangles, dashed fit-line) and magenta (crosses, dotted fit-line) show lenses in high and very high density environment. We see that the amplitude increases with environment density. Further the contribution of the secondary halos significantly increases with environment density. This is negligible for low density samples, but strongly enhances the shear signal on large scales in high density environments, even leading to an almost constant signal in the very high density environment.

environments of different density. Following the definition in Section 5.5.2 we distinguish between lenses in high, low, very high and very low density environments. As Fig. 6.9 shows, the observed tangential profiles in the different environments significantly differ in amplitude and in large scale behavior. The lowest signal is observed for lenses populating the very low density environment, not only showing the lowest amplitude, but dropping to zero very soon and even showing a constantly negative E-mode for scales $R > 400 h^{-1}$ kpc. This indicates that the average convergence at the edge of the considered circle is higher than the mean convergence enclosed by this circle (see equation 3.19). For the low density lens sample we find that the amplitude is higher than for the very low density case, the profile nicely follows an SIS on shorter scales, then dropping down to zero but not showing negative values. In both low density cases there is hardly any impact of nearby halos visible in the signal (as expected when the environment is poor). The mean density lens sample consisting of all lenses in all environments follows nicely an SIS out to a scale of $R = 200 - 300 h^{-1}$ kpc, even showing a small excess in γ_t . This effect is even stronger considering the high density lens sample, which shows a further increase in shear amplitude, exceeding the predictions of an SIS already for projected separations $R > 150 - 200 h^{-1}$ kpc at a higher level. The very high density sample finally hardly shows any dependence of shear on projected separation. On one hand the profile shows the highest amplitude of all considered environment subsamples and on the other hand the amplitude remains approximately constant on all considered scale out to a distance of $R = 700 h^{-1}$ kpc. This flat behavior is also confirmed in our 3D-LOS-projected lensing signal simulations (see Fig. 6.43 in Section 6.5), where we see that this flatness originates in the multiple gravitational deflections on brighter nearby galaxies in the close environment.

6.2 Measurement of the Excess Surface Mass Density

6.2.1 Measurement of $\Delta\Sigma$ for Several Luminosity Intervals

Now we ultimately make use of photometric redshift information and multiply the tangential shear with the critical surface mass density Σ_c , which depends on the geometrical constellation, i.e., the angular diameter distances and therefore the redshifts. This converts $\gamma_t(R)$ into the excess surface mass density $\Delta\Sigma(R)$ (see equation 3.20), directly mapping the investigated projected surface mass densities. Also for the estimation of $\Delta\Sigma$ we use the weighted mean (see equation 6.2) of all considered lens-source pairs. For all investigated lens samples, on scales out to $1 h^{-1}$ Mpc, we fit the excess surface mass density for illustrative reasons with a power law,

$$\Delta\Sigma(R) = A [R/1\text{Mpc}]^{-\alpha} . \quad (6.3)$$

In this fit an exponent of $\alpha = 1$ corresponds to an isothermal profile. In Fig. 6.10 the excess surface mass density is shown for all lenses in black, red lenses in red and blue lenses in blue. The drawn picture perfectly mirrors the results from Fig. 6.1, confirming the higher masses for elliptical galaxies in comparison to spiral galaxies, the combined sample lying in between. In the following we analyze the magnitude dependence of the excess surface mass density $\Delta\Sigma$ for four luminosity intervals of half a magnitude width with $-21 \geq i' \geq -23$ and five luminosity bins of one magnitude width with $-23 \geq i' \geq -24$ and $-17 \geq i' \geq -21$, respectively.

We show the $\Delta\Sigma$ -profiles in Fig. 6.11, confirming the results from the tangential shear measurement. As expected, also the amplitude of $\Delta\Sigma$ strongly depends on the luminosity (and thus on the mass) of

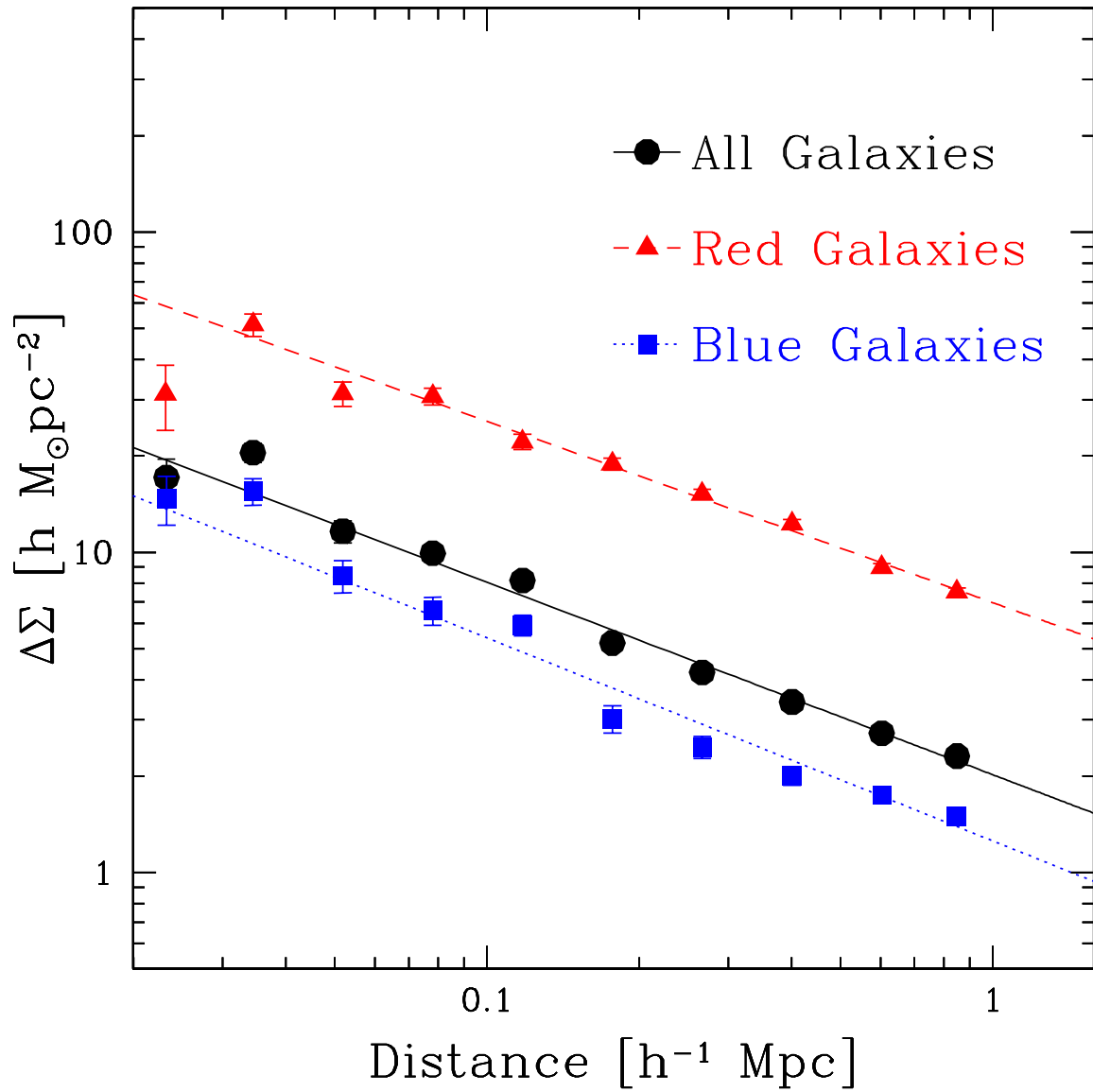


Fig. 6.10: Excess surface mass density $\Delta\Sigma$ for the complete luminosity sample with $-24 \leq i' \leq -17$ for all lenses (black circles), red (red triangles) and blue lenses (blue squares). The profiles are self-similar, showing a significantly higher amplitude considering red galaxies (red dashed line) than blue galaxies (blue dotted lines), the overall sample lying in between (black solid line).

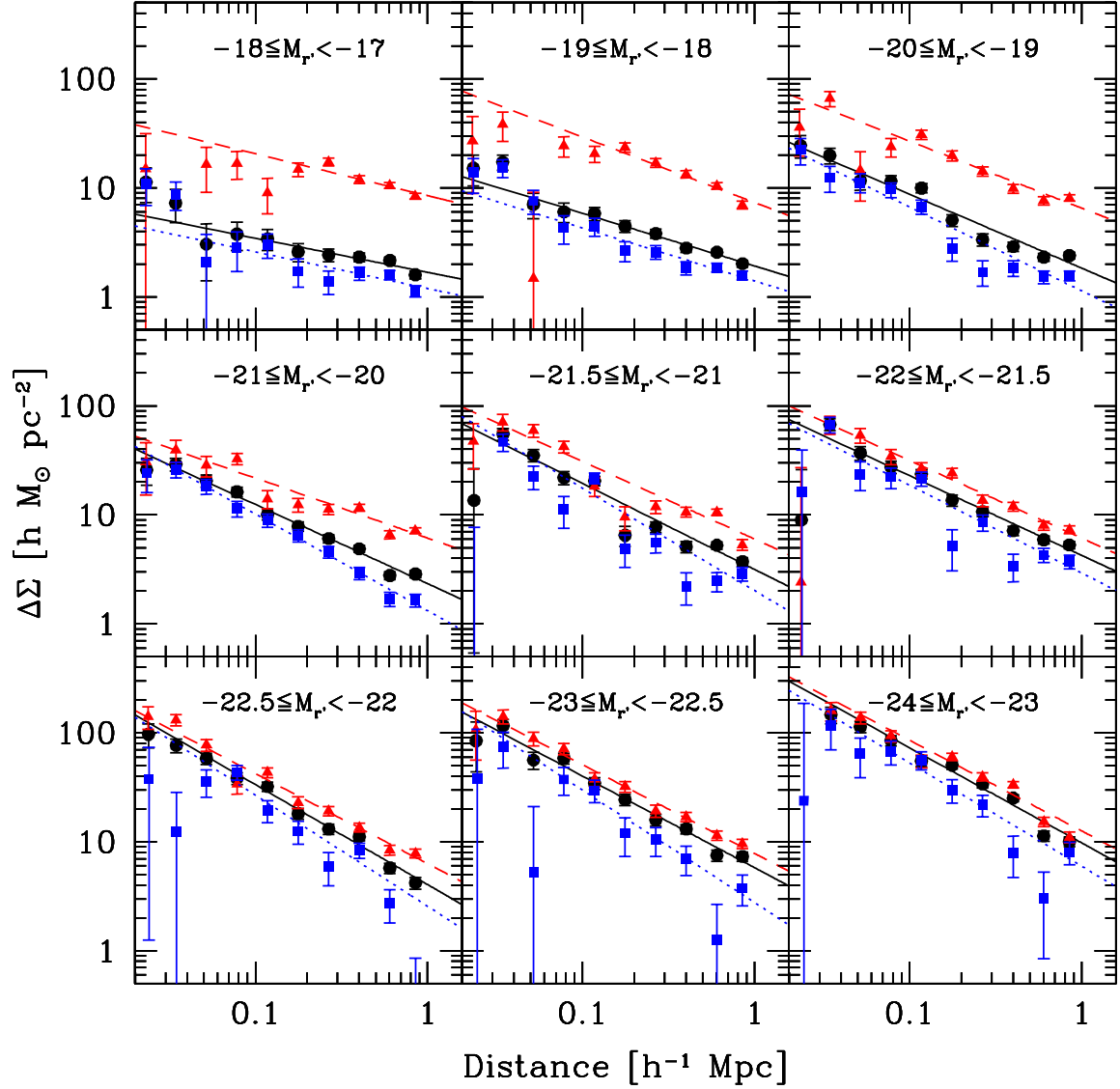


Fig. 6.11: Excess surface mass density for individual luminosity bins. The combined galaxy type sample is shown with black circles and solid fit-line, the red galaxy lens sample is shown with red triangles and dashed fit-line and the blue lens sample is shown with blue squares and dotted fit-line. In every single luminosity bin the red galaxy amplitudes of the surface mass profiles exceed the values of the blue ones. As can be seen in the upper row the lensing signal in the fainter luminosity bins is dominated by blue lenses, outnumbering their red counterparts. The fraction of red lenses increases with luminosity leading to a rapprochement between the combined lens and the red lens profile. This trend continues until, regarding the brightest luminosity bins, the signal is red SED dominated.

the considered lenses, increasing with luminosity, as the tangential shear already did before. Investigating the combined galaxy sample we further find that the profile slope increases from $\alpha \sim 0.3$ for luminosities $-17 > M_{r'} > -18$ to $\alpha \sim 0.9$ for galaxies with $-24 > M_{r'} > -23$. Consisting of higher masses for same luminosity, the amplitude of the excess surface mass density $\Delta\Sigma$ is higher for red than for blue galaxies in every single investigated luminosity bin. We see that for high luminosities the total lens signal is dominated by red galaxies, outnumbering their blue counterparts. This relation turns into its opposite when considering intervals with decreasing luminosity, as the fraction of blue galaxies significantly increases. Therefore in the faintest considered luminosity bins finally, the $\Delta\Sigma$ profiles are dominated by blue lenses. However, the increasing difference between red and blue lens profiles is remarkable. While in the brightest luminosity bins the amplitude of $\Delta\Sigma$ for both galaxy types are similar, regarding the faintest luminosity bins the red galaxy signal is significantly higher than for blue lenses. This indicates a combination of significantly higher mass of red low luminosity galaxies than of blue ones of same luminosity and a more strongly pronounced preference of red low mass galaxies to reside in denser environments. Further addressing the question about observable evolution in our lens sample, we repeat our measurement of $\Delta\Sigma$ in all luminosity bins, restricting our lens sample to a redshift range of $z_{\text{phot}} \leq 0.3$. As Fig. 6.12 shows, we do not observe a significant difference in the lensing signal for lenses with $0.05 < z_{\text{phot}} \leq 0.3$ and $0.05 < z_{\text{phot}} \leq 1.0$.

We compare the results for the excess surface mass density $\Delta\Sigma$ with the literature. Mandelbaum *et al.* (2006c) analyzed $\Delta\Sigma$ from SDSS-data and investigated individual luminosity bins with $-22.5 \leq M_{r',\text{SDSS}} \leq -17.0$. For the foreground sample Mandelbaum *et al.* (2006c) used spectroscopic redshift information, for the background sample photometric redshifts were applied for bright galaxies ($r'_{\text{SDSS}} < 21$) and a statistical redshift distribution for fainter sources. In comparison to Mandelbaum *et al.* (2006c) this work covers a much smaller area, but consists of a significantly deeper dataset. In the following we consider and compare the corresponding luminosity bins. As in contrast to Mandelbaum *et al.* (2006c) our rest-frame magnitudes are, firstly, not given in AB but in the Vega system and, secondly, not calculated with a Hubble parameter of $H_0 = 100 \text{ km s}^{-1} \text{ Mpc}^{-1}$ but with $H_0 = 72 \text{ km s}^{-1} \text{ Mpc}^{-1}$, in order to adjust for these differences we need to apply a magnitude offset of roughly $\Delta \text{mag} = -0.55$ to our rest-frame magnitudes for the comparison of the results.

Considering the blue galaxy sample, the results agree rather well, yet fairly noisy. This is not the case when considering the red lens sample. For the luminosities bins up to $M_{r'} \sim -21$ we constantly measure a higher amplitude. Decreasing with increasing luminosity, the measured excess finally vanishes for magnitudes of $M_{r'} \sim -21.5$. Considering brighter red lens samples this trend continues, leading to lower measured amplitudes for the remaining luminosity bins. However, in their later work Mandelbaum *et al.* (2008) (see also Dutton *et al.* 2010) do find a higher signal for faint galaxies, which agrees with our results.

As a further reference we have a look at the results of van Uitert *et al.* 2011, who investigated the GGL signal for data based on the Red Sequence Cluster Survey (RCS) 2, making use of data overlapping with the SDSS-DR7. In the work of van Uitert *et al.* 2011 for the lens sample spectroscopic redshift information from the SDSS was used, while the shear estimates were extracted from the significantly deeper CFHT r' -band data in the RCS2. The comparison of the corresponding luminosity bins shows that our measurements for the excess surface mass density agree well with the results of van Uitert *et al.* (2011).

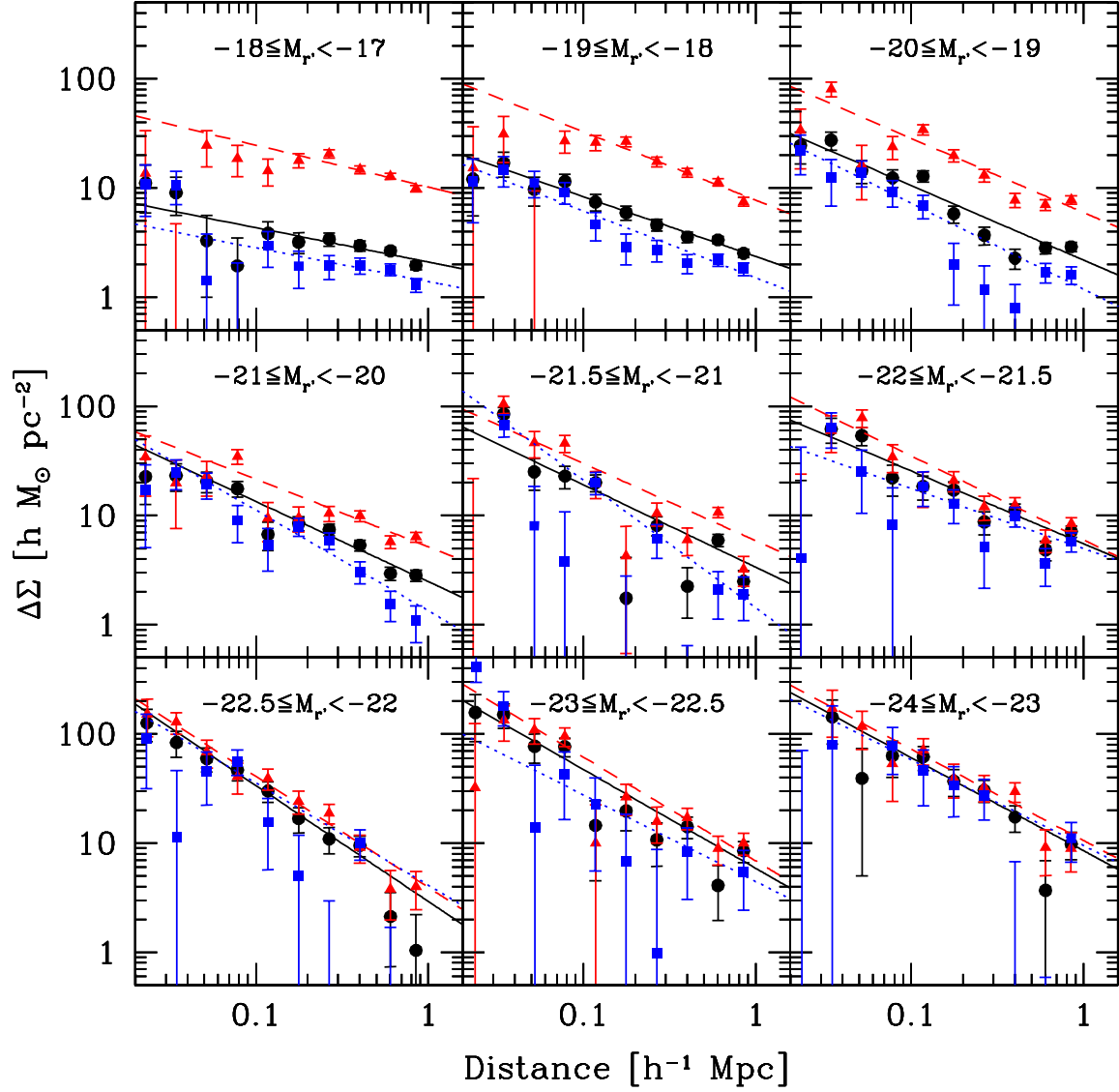


Fig. 6.12: Excess surface mass density $\Delta\Sigma$ for individual luminosity bins (see also Fig. 6.11), restricting the lens sample to $z_{\text{phot}} \leq 0.3$. We do not observe significant differences to the results for the complete lens sample considering lenses with redshifts up to $z_{\text{phot}} = 1$.

6.2.2 Investigation of Halo Parameter Scaling Relations

L- σ -Scaling Based on Fits to $\Delta\Sigma$

The amplitude of the observed excess surface mass density provides a very simple estimate for the mean values of the halo profile parameter for the investigated lens sample. The SIS being the simplest halo profile, the corresponding measurement of the velocity dispersion gives the most direct estimate of the halo mass magnitude. Recalling equation (3.50), we see that $\Delta\Sigma_{\text{SIS}}$ only depends on the velocity dispersion and the projected distance from the lens. As we want to derive σ for the single galaxy halo, we only take radial bins into account, where the contribution of nearby galaxies can be ignored. We therefore restrict our σ -fits to maximum distances of $R \sim 100 h^{-1}$ kpc. Thus only considering the inner part of the galactic halos, the assumption of an SIS as the galaxy halo profile appears to be a justifiable simplification. For the fits we consider all luminosity bins with $-24 \leq M_r \leq -17$ and fit the velocity dispersions for the combined lens sample, but also for the red and blue lens samples separately. First we address the influence of the local environment density on the scaling relation of the velocity dispersion. As we see in Fig. 6.13 for massive lenses at the bright end of our lens sample, the environment density does not play a major role, since the central halo signal is too dominating, completely covering the contribution of secondary halos. However, approaching the faint luminosity end we see a slightly growing weak dependency, fainter lenses in denser environments show slightly enhanced values for σ compared to lenses in less dense environments. This might indicate that the assumption of an undisturbed halo profile is not entirely true anymore, when considering $\Delta\Sigma$ in projected distances of $R \sim 100 h^{-1}$ kpc from low-mass lenses in denser environments. More likely this effect is due to the change of the fraction of red and blue galaxies, as in dense environments the red galaxies are relatively more abundant and thus increase the $\Delta\Sigma$ -amplitude of the combined sample. Though, the scaling relation is only mildly affected. Compared to the combined lens sample relation of $\sigma \propto L_r^{0.29 \pm 0.02}$ we measure a scaling of $\sigma \propto L_r^{0.31 \pm 0.03}$ for the low density density sample and a scaling of $\sigma \propto L_r^{0.27 \pm 0.02}$ for the high density sample. Using these scaling relations for galaxies in average environments (meaning that all galaxies, independent of local environment density are considered) we find for a L^* -galaxy ($L^* = 1.6 \times 10^{10} h^{-2} L_{r,\odot}$, corresponding to $M_r \sim -21.7$ in Vega system) a velocity dispersion of $\sigma^* = 135 \pm 2 \text{ km s}^{-1}$ when looking at all galaxies, $\sigma^* = 141 \pm 2 \text{ km s}^{-1}$ for all galaxies in high density environments and a value of $\sigma^* = 132 \pm 2 \text{ km s}^{-1}$ for galaxies in low density environments. Analyzing the velocity dispersions for the different SED types (see left panel of Fig. 6.14), we find that red and blue galaxies show the same scaling behavior, $\sigma_{\text{red}} \propto L_r^{0.24 \pm 0.03}$ and $\sigma_{\text{blue}} \propto L_r^{0.23 \pm 0.03}$, respectively, agreeing well with the predictions of the Faber-Jackson (Faber & Jackson 1976) and Tully-Fisher relation (Tully & Fisher 1977). However, given the higher mass of red galaxies for galaxies of same luminosities, the red galaxy sample shows a significantly higher amplitude. As bright galaxies are red SED dominated and for decreasing luminosity the fraction of blue galaxies significantly increases, we see a transition between both straight lines, leading to the steeper $\sigma - L$ -scaling relation of $\sigma \propto L_r^{0.29 \pm 0.02}$, when not explicitly considering the galaxy type and treating all galaxies of the combined lens sample (representing a mix of both galaxy types) equally. For a L^* -galaxy we find a velocity dispersion of $\sigma_{\text{red}}^* = 162 \pm 2 \text{ km s}^{-1}$ for red and a value of $\sigma_{\text{blue}}^* = 115 \pm 3 \text{ km s}^{-1}$ for blue galaxies.

Until now we investigated the velocity dispersion as a function of the rest-frame luminosity, ignoring that luminosity evolves with look-back time and thus redshift. We now account for the evolution of luminosity, assuming that $L \propto (1+z)$. While this is correct for passively evolving red galaxies (see,

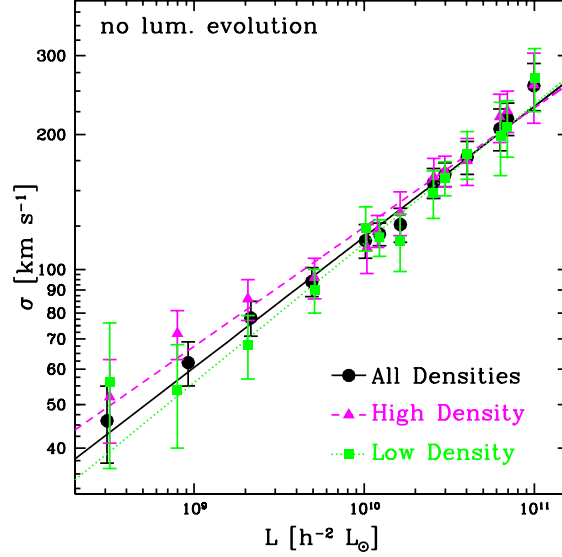


Fig. 6.13: Velocity dispersion σ as function of the absolute luminosity. We determine the velocity dispersion by fitting an SIS out to a scale of $100 h^{-1}$ kpc to the excess surface mass density $\Delta\Sigma$ in separate luminosity bins (see Fig. 6.11). We show the combined morphology samples in different environments, magenta triangles (dashed fit-line) in dense environments, green squares (dotted fit-line) in environments of low density and black circles (solid fit-line) in all environments. The results for bright galaxies are in perfect agreement, but for faint, i.e., low mass galaxies we see a mass excess increasing with environment density as already observed before (see Fig. 6.9).

e.g., Saglia *et al.* 2010 or Bernardi *et al.* 2010), blue galaxies evolve more rapidly. As for an accurate estimate a star formation history is needed, which cannot be extracted sufficiently well from $u^*g'r'i'z'$ photometry, we use also the evolution $L \propto (1+z)$ for blue galaxies as a lower limit. As we see in the right panel of Fig. 6.14, the amplitudes of the scaling increase to values of $\sigma^* = 150 \pm 2 \text{ km s}^{-1}$ for the combined lens sample, $\sigma_{\text{red}}^* = 173 \pm 2 \text{ km s}^{-1}$ for the red lens sample and $\sigma_{\text{blue}}^* = 123 \pm 3 \text{ km s}^{-1}$ for the blue galaxies. However the slope of the $L_r - \sigma$ -relation remains hardly changed. We find for both SED types a scaling behavior corresponding to the Faber-Jackson or Tully-Fisher relation, $\sigma_{\text{red}} \propto L^{0.25 \pm 0.03}$ for red and $\sigma_{\text{blue}} \propto L^{0.24 \pm 0.03}$ for blue galaxies, while the galaxy type transition for the combined lens sample leads to the steeper scaling relation of $\sigma \propto L^{0.29 \pm 0.02}$. The values for the scaling relations also are shown in Table 6.2. A closer inspection of red and blue data points in both panels of Fig. 6.14 reveals that for a luminosity of $L \sim 6 - 7 \times 10^{10} h^{-2} L_{\odot}$ two red data points are decreased relative to the red SED linear fit and that one blue data point is increased relative to the blue SED linear fit. This could point to a problem in contamination of the red and blue samples with blue and red galaxies at this luminosity.

Assuming an SIS profile (see equation 3.43), the velocity dispersion σ_{halo} obtained from the weak lensing analysis (out to $100 h^{-1}$ kpc) describes the circular velocity $v_{\text{circ,halo}} = \sigma_{\text{halo}} \cdot \sqrt{2}$ of the dark matter halo. The impact of baryons that might change the profile is negligible for the value of σ_{halo} since baryonic effects happen on smaller scales only.

Gerhard *et al.* (2001) (see their fig. 2) studied the circular velocity curves of local ellipticals with

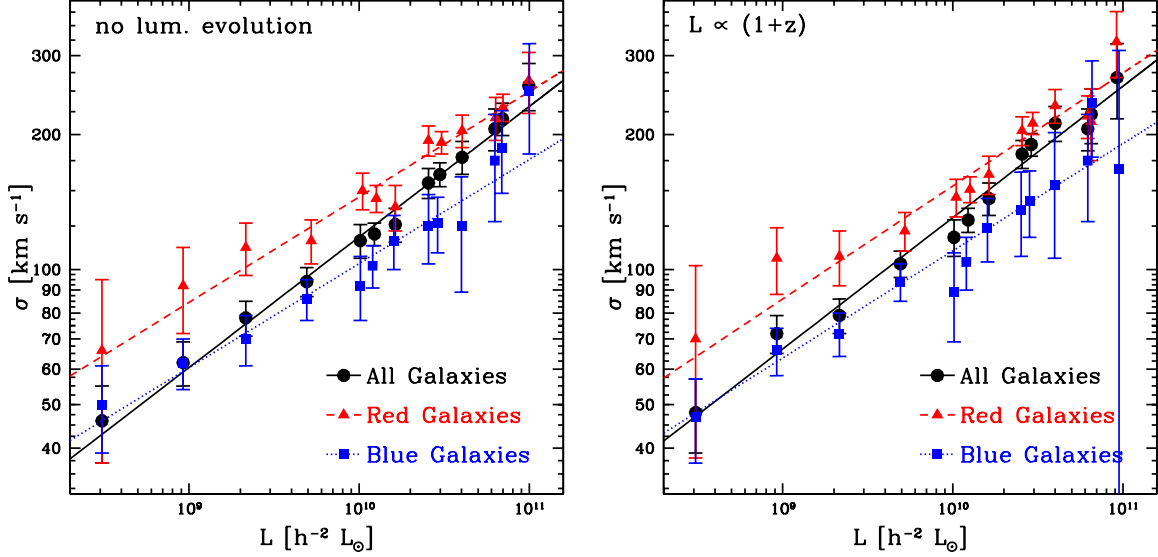


Fig. 6.14: Velocity dispersion σ as function of the absolute luminosity, without (left panel) and with luminosity evolution according to $L \propto (1+z)$ (right panel). The σ values are obtained by SIS-fits out to a scale of $100 h^{-1}$ kpc to $\Delta\Sigma$ in separate luminosity bins (see Fig. 6.11). The complete lens sample is shown in black (circles and solid fit-line), the red galaxy sample in red (triangles and dashed fit-line) and the blue galaxy sample in blue (squares and dotted fit-line). The luminosity evolution only changes the amplitude but not the scaling behavior.

stellar dynamics out to a few (≤ 3) effective radii. They constrained the anisotropy profiles $\beta(r)$ (see Binney & Tremaine 1987) of the stellar orbits and obtained that the mean values for β are typically between 0.2 and 0.4. The detailed dynamical models yield a relation between the central stellar velocity dispersion and the maximal rotation velocity profile of

$$\sigma_{\text{star}} = 0.66 v_{\text{max}}^{\text{dyn}} . \quad (6.4)$$

The radii where these maximal velocities are reached are of order 0.5 times the effective radii. The rotation velocities for larger radii ($> R_e$) are flat and have values of $\approx 0.9 v_{\text{max}}^{\text{dyn}}$. If one sets these ‘asymptotic values’ equal to the halo circular velocity we obtain

$$v_{\text{circ,halo}} = \sqrt{2} \sigma_{\text{halo}}^{\text{WL}} = 0.9 v_{\text{max}}^{\text{dyn}} = 0.9 \cdot 1/0.66 \sigma_{\text{star}}$$

or

$$\sigma_{\text{halo}}^{\text{WL}} = 0.96 \sigma_{\text{star}} . \quad (6.5)$$

If one sets the maximal circular velocity equal to the halo circular velocity one obtains

$$\sigma_{\text{halo}}^{\text{WL}} = 1.07 \sigma_{\text{star}} . \quad (6.6)$$

In Fig. 6.15 we compare how the measured velocity dispersion σ_{star} of LRGs compare with predictions from our WL-analysis for red galaxies, based on Eisenstein *et al.* (2001) and Gallazzi *et al.* (2006), i.e., we add the best-fitting lines for the $\sigma_{\text{halo}}^{\text{WL}}$ -luminosity relation, rescaled with 1/0.96 (in magenta)

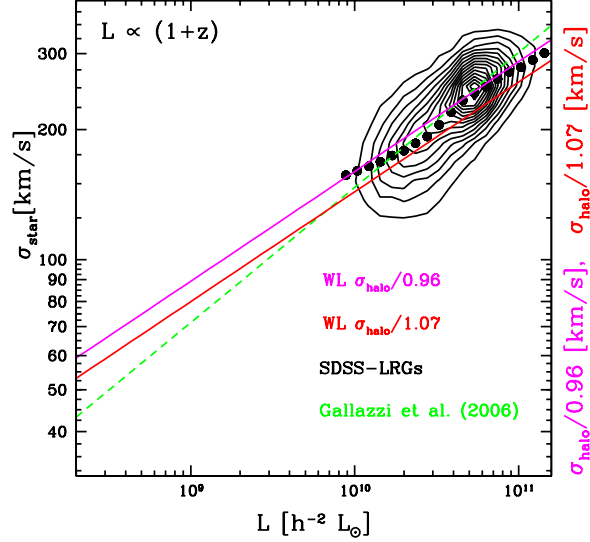


Fig. 6.15: Velocity dispersion σ for red galaxies as a function of absolute magnitude. The red circles and fit-line show our weak lensing result, divided by 1.07, taking into account that velocity dispersions derived by stellar motions are about 7% lower than halo velocity dispersions. We compare our result with a spectroscopic LRG sample based on Eisenstein *et al.* (2001), only considering LRGs with redshifts of $0.05 < z < 0.3$ and uncertainties in σ of $0.03 < d\sigma_{\text{star}}/\sigma_{\text{star}} < 0.1$ (black circles and contours), and with the results from Gallazzi *et al.* (2006) (green dashed fit-line).

and $1/1.07$ (in red). We have added the relation between the σ_{star} and evolution corrected luminosities of SDSS-LRGs (Eisenstein *et al.* 2001) obtained from Gallazzi *et al.* (2006) as green dashed line. This relation is however obtained from fitting a linear relation of velocity dispersions vs. absolute magnitude to the overall LRG sample. In the lensing analysis we first average the signal within some (small) luminosity bin and then study the signal. To treat the LRG-galaxies in a similar way we have obtained the σ_{star} -values from the SDSS data base and estimated the luminosity evolved redshift zero absolute magnitudes in the r-band (from SED-fits and a luminosity evolution proportional to $1+z$) and obtained the mean stellar velocity dispersion within equidistant luminosity intervals. For this we only include galaxies with redshifts between 0.05 and 0.3 and with secure velocity dispersion estimates $0.03 < d\sigma_{\text{star}}/\sigma_{\text{star}} < 0.1$. The results are plotted with filled black circles, whereas the density contours for all considered galaxies are shown in black. We see that $0.96 \sigma_{\text{star}} \leq \sigma_{\text{halo}}^{\text{WL}} \leq 1.07 \sigma_{\text{star}}$ holds at least for luminosities above $10^{10} h^{-2} L_{\odot}$. Therefore the halo velocity is between the maximal circular velocity found around $0.5 R_e$ and 90 per cent of this value which equals the velocity of galaxies at a few effective radii. This indicates that at least for galaxies above this luminosity threshold the halo indeed is isothermal on scales out to $100 h^{-1}$ kpc.

L- r_{200} - and L- M_{200} -Scaling Based on Fits to $\Delta\Sigma$

We now investigate halo parameters based on the NFW profile, firstly considering the virial radius r_{200} . We calculate the values for r_{200} from a one-dimensional fit, assuming the mass-concentration

relation $c \propto M^{-0.084}$ of Duffy *et al.* (2008) (see also equation 3.81). Also in this case we only use scales up to a distance of $100 h^{-1}$ kpc from the the $\Delta\Sigma$ -profile. The result is shown in Fig. 6.16. We see that apparently a simple power law is no longer able to fit r_{200} over the whole luminosity range, as, regarding data points with $L < 10^{10} h^{-2} L_{\odot}$, the scaling behavior of r_{200} becomes clearly shallower. Possible explanations are a contamination in the faint luminosity region by neighboring galaxy halos, a change in the scaling of the virial radius (see, e.g., Kormendy & Bender 2012 due to transition between different red galaxy populations, leading to an almost luminosity independent mass) or a modification of the concentration-mass relation in this regime. The circumstance that the velocity dispersion σ does not show this ‘broken’ scaling behavior indicates that contamination by secondary galaxy halos should not be the reason for this observation. Assuming that the mass concentration relation of Duffy *et al.* (2008) is correct implies that the $r_{200} - L$ relation cannot be described by a single-power law anymore, but instead with double-power laws and a break at around $L = 10^{10} h^{-2} L_{\odot}$, i.e., the mean mass-to-light ratio of galaxies within a luminosity interval would indeed be minimal at this break luminosity. This is in agreement with results from abundance matching (AM) techniques and some satellite kinematic results (see fig. 1 Dutton *et al.* 2010), in particular with the results of More *et al.* (2011) (see their fig. 5) who also obtained a change of slope for the red galaxies’ $M_{200} - L$ relation at a luminosity of about $10^{10} h^{-2} L_{\odot}$. However this result in Fig. 6.16 only holds if the concentration is only weakly changing with virial mass. On the other hand, instead, an approximate single-power law r_{200} -luminosity relation could be reconciled, requiring the concentration to steeply rise for luminosities smaller than $10^{10} h^{-2} L_{\odot}$. We will investigate these two alternatives in more detail in Section 6.4.3. Because of the apparently broken r_{200} -luminosity scaling relation we measure the power law slope only for galaxies brighter than $10^{10} h^{-2} L_{\odot}$. For the virial radius we obtain power laws of $r_{200}^{\text{red}} \propto L^{0.33 \pm 0.04}$ for red and $r_{200}^{\text{blue}} \propto L^{0.36 \pm 0.07}$ for blue galaxies without luminosity evolution and of $r_{200}^{\text{red}} \propto L^{0.38 \pm 0.04}$ and $r_{200}^{\text{blue}} \propto L^{0.40 \pm 0.08}$ for luminosities evolving with $(1+z)$. If galaxies are not separated into blue and red SED types we obtain (for the combined sample) $r_{200} \propto L^{0.39 \pm 0.03}$, ignoring luminosity evolution, and $r_{200} \propto L^{0.37 \pm 0.04}$, assuming a $(1+z)$ scaling. As before the steeper scaling is due to the fact that the amplitudes for the $r_{200} - L$ scalings are different for red and blue galaxies and the fractional mix of red and blue galaxies changes as a function of absolute luminosity.

We translate the result for r_{200} to the virial velocity v_{200} in Fig. 6.17 using equation (3.67). The right panel of Fig. 6.17 shows v_{200} versus luminosity for our blue galaxy sample (blue data points) and the power law fit for $L > 10^{10} h^{-2} L_{\odot}$ (blue dotted line). Reyes *et al.* (2011) have measured v_{200} for SDSS disk (and thus blue SED-type dominated) galaxies as a function of stellar mass. In order to compare their result to ours we translate their stellar mass estimate (back) to luminosity. For local disk galaxies (the Reyes *et al.* 2011 disk galaxies have redshifts between 0.02 and 0.1) an average mass-to-light ratio of $M_*/L_r = 1 M_{\odot}/L_{\odot}$ appears to be a good description. On one hand this can be seen in fig. 1 of van Uitert *et al.* (2011) by comparing their blue histograms on the vertical to the horizontal axis showing the luminosity distribution and stellar mass distribution of blue SDSS-galaxies. This is in agreement with Bell *et al.* (2003), if one takes into account that our local (see Fig. 5.27) galaxies have a $(g-r)$ -color of approximately 0.3 – 0.4 at the bright end (which are the galaxies in common with Reyes *et al.* 2011). The same result is obtained from Kauffmann *et al.* (2003), fig. 14, upper right panel, taking into account that our local blue galaxies are dominated by absolute magnitudes fainter than $M_r = -21$. For the three luminosity intervals provided by Reyes *et al.* (2011) their data points (translated to luminosity) agree well with ours (see

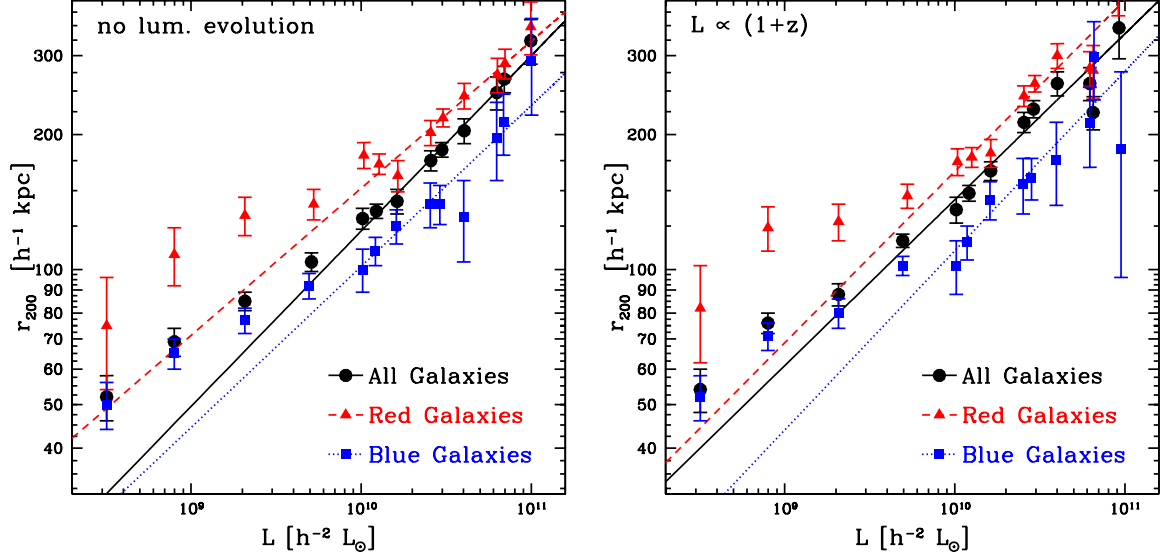


Fig. 6.16: r_{200} as a function of absolute luminosity. The left panel shows the result without, the right panel with luminosity evolution $L \propto (1+z)$. The red triangles and dashed fit-lines denote red galaxies, the blue squares and dotted fit-lines blue galaxies and the black circles and solid fit-lines all galaxies. We see that a single-power law apparently is no longer able to fit the scaling relation. Therefore only data points with $L > 10^{10} h^{-2} L_{\odot}$ are used for the determination of the scaling relation. For the combined lens sample, r_{200} scales with $L^{0.39 \pm 0.04}$ ignoring and $L^{0.43 \pm 0.04}$ including luminosity evolution.

Fig. 6.17, right panel). We have a larger dynamic range and can extend our analysis down to a few times $10^9 L_{\odot}$. In an analogous way we have translated the Dutton *et al.* (2010) model for the v_{200} -stellar mass relation to the v_{200} -luminosity relation, agreeing well with our result, but possibly showing a slightly shallower slope.

Confident that for the considered absolute magnitude and redshift range we can properly translate our absolute luminosities into stellar mass estimates for red galaxies, we use $\log_{10}(M_{*}) = 1.093 \log_{10} L_r - 0.573$ (which was used by Dutton *et al.* 2010 and derived from Gallazzi *et al.* 2006), inserting luminosity evolution corrected luminosities. Our results for v_{200} are shown in red in Fig. 6.17, together with the model of Dutton *et al.* (2010), being the same to a remarkable level. Only the results for the second and third brightest luminosity interval lie below for reasons we already speculated about. On top we have added the result for v_{opt} as obtained from the Gallazzi *et al.* (2006) $\sigma - L$ relation, using the prefactors of Dutton *et al.* (2010) for the relation between velocity dispersion and rotation velocity. We conclude that for luminosities between 10^{10} and $6 \times 10^{10} h^{-2} L_{\odot}$, the mass density profile of ellipticals is not only isothermal out to $100 h^{-1}$ kpc (as shown before), but also out to the virial radius. For higher luminosities, the virial velocity exceeds the optical velocity.

Finally translating our virial radii into virial masses we show results with and without luminosity evolution correction in the left and right panels of Fig. 6.18. We continue using only galaxies with $L > 10^{10} h^{-2} L_{\odot}$ for the power law fits (added as red dashed and blue dotted lines). For the

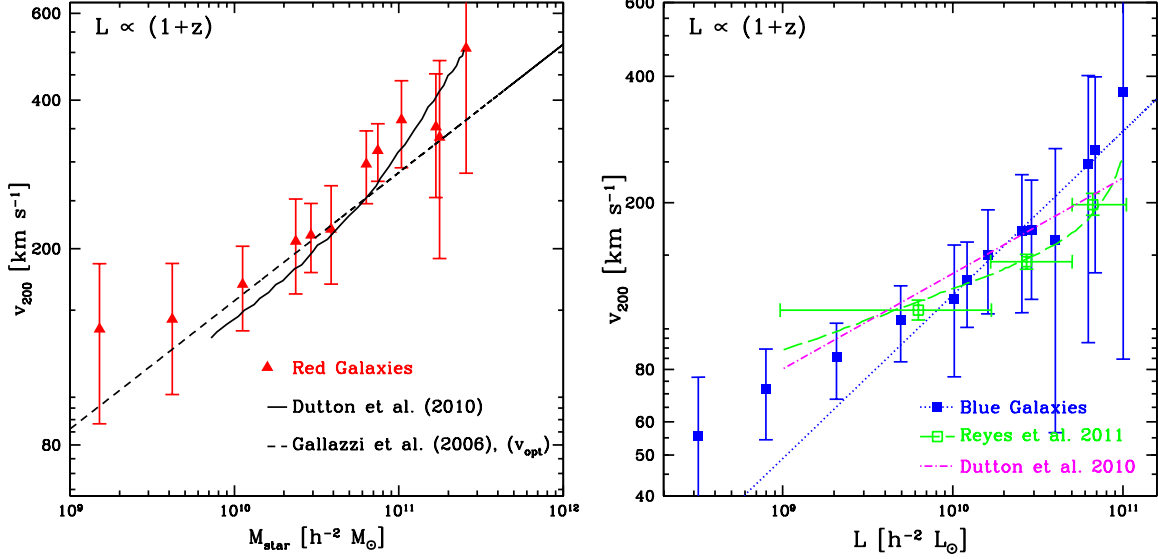


Fig. 6.17: Circular velocity v_{200} as a function of absolute luminosity for our blue galaxy sample (blue filled squares, blue dotted fit-line). Analogously to the fit of r_{200} we only use data points with $L > 10^{10} h^{-2} L_{\odot}$ for the determination of the scaling relation fit. Our measurements agree quite well with the results of Reyes *et al.* (2011) (green empty squares, green long-dashed line) and Dutton *et al.* (2010) (magenta dashed-dotted line).

In the left panel we show the circular velocity for our red galaxy sample in red. On top we add the model from Dutton *et al.* (2010) as a solid line and the result for v_{opt} of Gallazzi *et al.* (2006) as a dashed line.

combined sample we obtain $M_{200} \propto L^{1.21 \pm 0.10}$ and $M_{200} \propto L^{1.12 \pm 0.11}$ for the case without and with luminosity evolution correction. This scaling agrees with the results of Guzik & Seljak (2002) within their larger uncertainties ($M \propto L_r^{1.34 \pm 0.17}$). We have further included the results of Hoekstra *et al.* (2005) as magenta points, also well agreeing with our blue sample. This agreement appears reasonable since the Hoekstra *et al.* (2005) sample contains isolated galaxies, thus mostly consisting of blue galaxies. In addition we have considered the excess surface mass density profiles of van Uitert *et al.* (2011) (see their fig. 8), and translated them into virial mass estimates in the same way as we did for our work. These estimates are shown as green points. They agree well with our red sample results, again being reasonable since the van Uitert *et al.* (2011) sample is dominated by red galaxies. All results obtained for r_{200} and M_{200} are summarized in Table 2.

At last we translate our $M_{200} - L$ relation from the right panel of Fig. 6.18 into the M_{200} versus stellar mass relation (MSR), again using the relation $\log_{10}(M_*) = 1.093 \log_{10} L_r - 0.573$ as above. The result is shown in Fig. 6.19. The virial-to-stellar mass ratio (shown as red points) is almost constant (at ~ 100) for a decade in stellar mass (10^{10} to $10^{11} h^{-2} M_{\odot}$) and increases for lower stellar masses. This result precisely agrees with the Dutton *et al.* (2010) model shown as the black solid curve. At the high stellar mass end the MSR appears to only slightly increase (if at all) with stellar mass. This saturation is in agreement with the results of van Uitert *et al.* (2011) (green points, taken from their fig. 14, and converting their stellar masses to $H_0 = 100 \text{ km s}^{-1} \text{ Mpc}^{-1}$, as in this Figure the stellar masses are given for $H_0 = 70 \text{ km s}^{-1} \text{ Mpc}^{-1}$ and the virial masses are given for

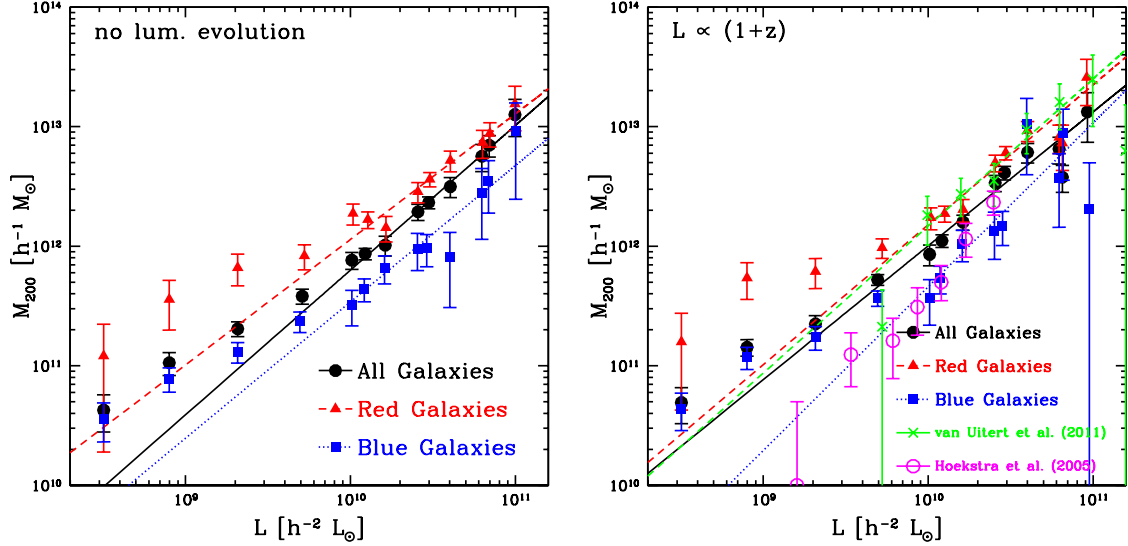


Fig. 6.18: M_{200} as a function of luminosity. The left panel shows the result without, the right panel with luminosity evolution $L \propto (1+z)$. Red triangles and dashed fit-lines denote red galaxies, blue squares and dotted fit-lines blue galaxies and black circles and solid fit-lines all galaxies. We see as expected the same scaling behavior as for r_{200} (see Fig. 6.16). Only data points with $L > 10^{10} h^{-2} L_{\odot}$ are used for the determination of the scaling relation. For the complete lens sample the M_{200} scales with $L^{1.21 \pm 0.10}$ ignoring and $L^{1.31 \pm 0.13}$ including luminosity evolution. We included the results from van Uiter *et al.* (2011) in the right panel (green crosses), observing good agreement, given that their analysis describes a red SED-type dominated lens sample.

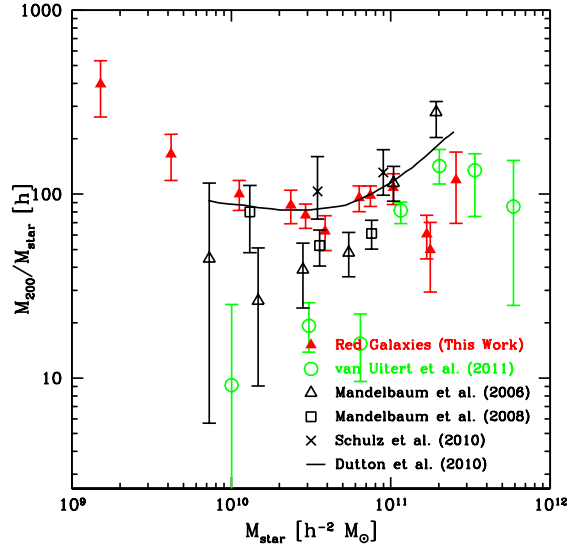


Fig. 6.19: Stellar Mass versus M_{200}/M_{star} -ratio for red galaxies converted to $z = 0$. The red triangles denote our red galaxies. We have added the results of Mandelbaum *et al.* (2006c) (open triangles), Mandelbaum *et al.* (2008) (open squares) and Dutton *et al.* (2010) (black solid line), see also fig. 1 in Dutton *et al.* (2010). We further include the results of van Uiter *et al.* (2011) from their fig. 14 as green open circles.

Without luminosity evolution, $L_{r'}^* = 1.6 \times 10^{10} h^{-2} L_{r',\odot}$						
Sample	σ^* [km s ⁻¹]	η_σ	r_{200}^* [h^{-1} kpc]	$\eta_{r_{200}}$	M_{200}^* [$10^{11} h^{-1} M_\odot$]	$\eta_{M_{200}}$
All	135 ± 2	0.29 ± 0.02	146 ± 2	0.39 ± 0.03	11.1 ± 0.4	1.21 ± 0.10
Red	162 ± 2	0.24 ± 0.03	177 ± 3	0.33 ± 0.04	18.6 ± 0.8	1.05 ± 0.12
Blue	115 ± 3	0.23 ± 0.03	120 ± 2	0.36 ± 0.07	5.8 ± 0.5	1.14 ± 0.20
With luminosity evolution, $L_{r'}^* = 1.6 \times 10^{10} h^{-2} L_{r',\odot}$						
Sample	σ^* [km s ⁻¹]	η_σ	r_{200}^* [h^{-1} kpc]	$\eta_{r_{200}}$	M_{200}^* [$10^{11} h^{-1} M_\odot$]	$\eta_{M_{200}}$
All	150 ± 2	0.29 ± 0.02	170 ± 2	0.37 ± 0.04	17.0 ± 0.6	1.12 ± 0.11
Red	173 ± 2	0.25 ± 0.03	198 ± 3	0.38 ± 0.04	26.1 ± 1.1	1.17 ± 0.13
Blue	123 ± 3	0.24 ± 0.03	133 ± 3	0.40 ± 0.08	8.7 ± 0.6	1.37 ± 0.25

Table 6.2: Best fits for the scaling relations of the velocity dispersion σ , assuming an SIS and for the r_{200} and M_{200} , assuming an NFW profile without and with luminosity evolution. The SIS fits have been extracted from all all luminosity bins, the fits for the NFW profiles only include luminosities brighter than $L = 10^{10} h^{-1} L_\odot$.

$H_0 = 100 \text{ km s}^{-1} \text{ Mpc}^{-1}$ according to van Uitert, private communication) which also saturates at a value of about 100 to 150. The points of van Uitert *et al.* (2011) for low stellar masses seem however very low, even being below the early results of Mandelbaum *et al.* (2006c). However, since the van Uitert *et al.* (2011) M_{200} versus luminosity relation derived by us from their $\Delta\Sigma$ results agree well with ours, the difference can only be due to a different relation for the stellar masses (especially considering that van Uitert *et al.* 2011 aim to add up the total stellar mass, i.e., not only that of the central galaxy but also that of its satellites).

6.3 Checks for Systematic Errors from γ_t and $\Delta\Sigma$ Measurements

In order in to verify the integrity of our lensing sample and to confirm that our lensing results are devoid of significant systematic errors, we perform several systematic tests. These tests also include measurement of the tangential shear γ and the excess surface mass density $\Delta\Sigma$ for specific subsamples of lenses and sources. We demonstrate that there is no weak lensing signal if we replace foreground galaxies by stellar objects or random points and that our measured lensing signal amplitudes do not show a significant dependence on source magnitude, S/N-ratio or size. We also show, that misassignment of foreground objects to the background does not introduce a bias of more than ~ 1 to 2% to the measurements of velocity dispersions. The contribution of faint not detected galaxies in the neighborhood of more massive galaxies does not significantly affect the shear measurement of the massive galaxies and can be neglected.

6.3.1 Shear Estimates Relative to Stars and Random Points

In our first test we measure the tangential shear γ_t (see equation 3.29 and also Section 6.1 for the data analysis itself), with respect to stellar foreground samples and randomized lens-source-samples. As these objects cannot act as gravitational lenses, in absence of systematics any measured tangential shear and cross-shear are supposed to vanish, when averaging the lensing signals, measured with respect to these positions. First we analyze the tangential shear γ_t with respect to stellar foreground samples. As foreground catalog we choose all stars, selected for the PSF anisotropy correction performed with the KSB-pipeline. This leaves us with a total number of 247 589 stars, with

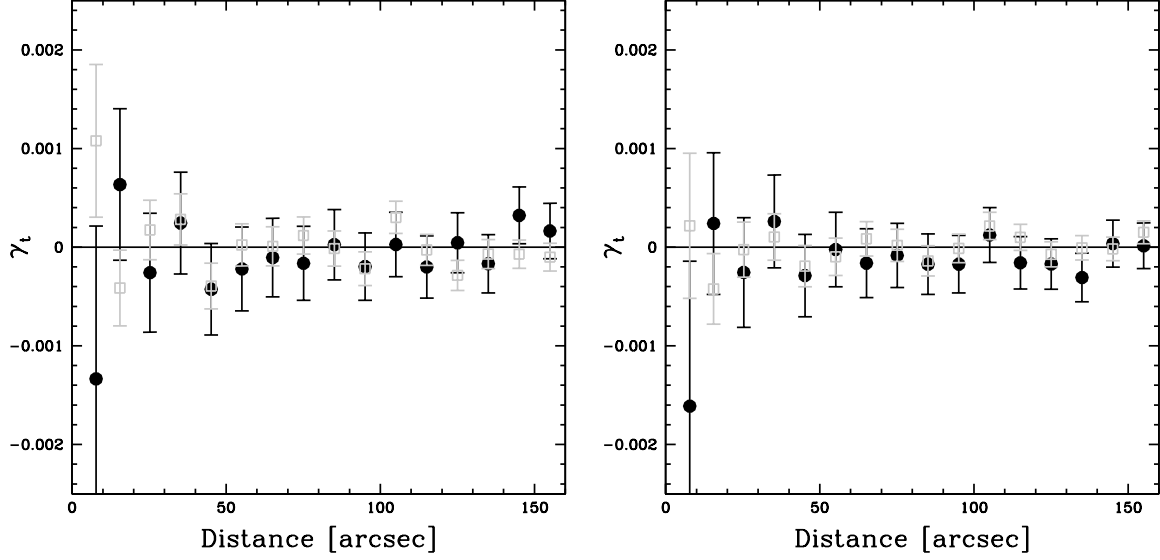


Fig. 6.20: Measured tangential shear γ_t , with respect to stellar foreground. The left panel shows the result for a stellar foreground sample with magnitudes of $18 < i' < 22$, $S/N \geq 50$ and a `SExtractor` star classification > 0.96 , as used for the KSB shear correction. The right panel shows a foreground sample, consisting of stars with $18 < i' < 22$ and a `SExtractor` stars classifier > 0.96 , without S/N-cut. The tangential shear is shown with filled black circles, the cross-shear with empty grey squares. All measured values are consistent with zero.

magnitudes of $18 \lesssim i' \lesssim 22$ (the exact values depend on the S/N-ratio) and a `SExtractor` star classification of greater than 0.96. As we see in the left panel of Fig. 6.20, both the tangential shear γ_t displayed as filled black circles and the cross-shear γ_c displayed as empty grey squares are well consistent with zero. As a further test we assign a second, larger stellar sample, selecting all stars with magnitudes of $18 < i' < 22$ and a `SExtractor` star classification of greater of 0.96, without S/N-cuts or restrictions by the KSB-pipeline. This leaves us with a stellar foreground sample consisting of a higher total number of 471 066 objects. The result is shown in the right panel of Fig. 6.20. Also in this case all measured values are consistent with zero.

As a further test, examining the tangential shear, we measure the alignment with respect to a random foreground sample. As random points are not related to physically existing objects and thus cannot act as gravitational lenses, the signal obviously has to vanish in the same way, as already observed for the stellar foreground sample. In order to create this random catalog, we dice random points all over the area of the CFHTLS-Wide, only considering objects in areas, which have not been masked out. In this way we ensure, that we are tracing the same area as the original (photometric) foreground sample in the actual scientific analysis. The left panel of Fig. 6.21 shows that the measured values for γ_t and γ_c are perfectly consistent with zero. As a final test we keep our original foreground lens sample and modify our background source sample. For the background sources we keep the original positions, but randomize the shape values for all objects by permutation. In this way we conserve the originally observed ellipticity distribution, but erase any gravitational imprint by the foreground lenses. We see in the right panel of Fig. 6.21 that the E- and B-modes vanish as expected.

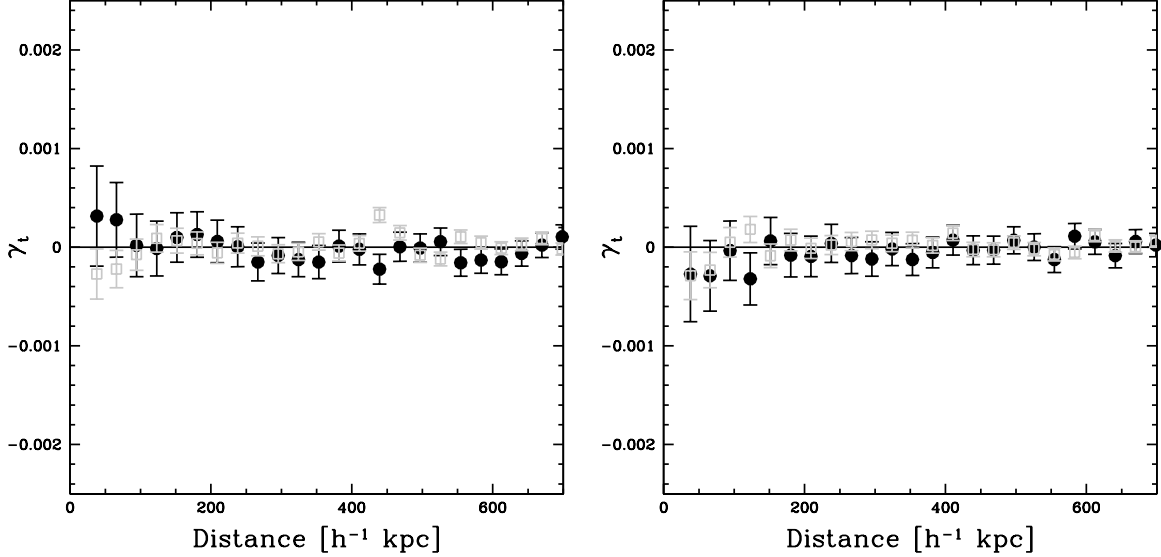


Fig. 6.21: Measured tangential shear for randomized lens-source pairs with γ_t as filled black circles and γ_c as open grey squares. The left panel shows the result, analyzing the random position foreground sample, the right panel shows the analysis for the background with randomly permuted shape values. All signals are consistent with zero.

6.3.2 Signal Dilution from Contamination of the Background Sample

A contamination of the background sample with objects from the foreground can lead to a significant dilution of the observed gravitational signal. An estimate of the contamination rate can be done, by investigating the number of objects around photometric foreground objects as a function of the projected separation. For this analysis we measure the background density of all objects around galaxies from our foreground catalog within a radius of $\sim 2 h^{-1}$ Mpc (see Mandelbaum *et al.* 2005). Only background objects fulfilling our selection criterion shown in equation (5.9) are considered. The result is shown in Fig. 6.22. We see that on short scales the density is only slightly enhanced, showing an excess of below 3% on very short scales. This value drops below 2% on a scale of roughly $200 h^{-1}$ kpc and below 1% for scales larger than $\sim 450 h^{-1}$ kpc. As already mentioned a possible explanation is the accidental assignment of foreground galaxies to the background. The assignment of foreground objects to the background can significantly dilute the observed lensing, as no gravitational imprint is carried by this class of objects. The situation even can get worse, when objects physically associated to the considered gravitational lens are assigned as source, introducing a false gravitational shear signature.

This means that in the worst case the velocity dispersions can be systematically underestimated by ~ 1 to 2% on very short scales and less than $\sim 1\%$ for larger scales due to by background contamination by foreground objects. Besides contamination of the background sample a further possible explanation for galaxy excess around the foreground galaxies is provided by the magnification bias, lowering the detection threshold for galaxies situated at close projected distances from the foreground lens.

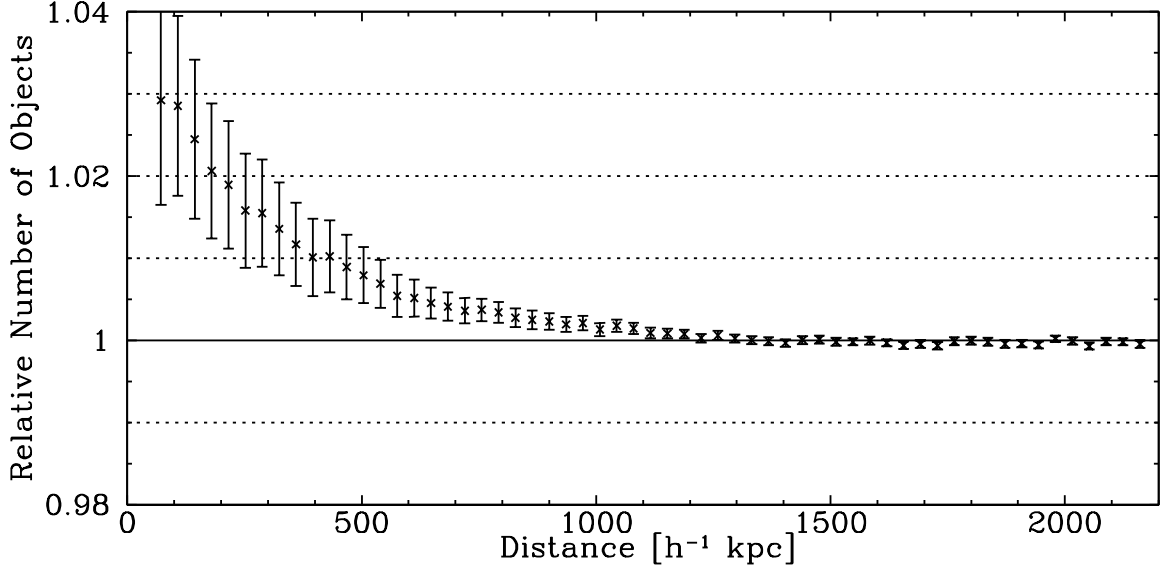


Fig. 6.22: Relative background density around galaxies from the foreground sample (normalized by background density around random foreground points). Being between 2 and 3% for very short projected separations the excess density falls below 2% for distances larger than $\sim 200 h^{-1}$ kpc and below 1% for distances larger than $\sim 450 h^{-1}$ kpc.

6.3.3 Signal Contribution of Undetected Low Mass Nearby Galaxies

A further effect which can lead to an overestimated lensing signal for the foreground sample is the presence of undetected low-mass galaxies in the direct vicinity of massive lens galaxies. While for lower redshifts low mass galaxies in general can be resolved quite well, for larger redshifts they might not be detectable as individual galaxies anymore. This can lead to an assignment of the galaxy's mass to the only observable main lens, which might result in an overestimate of the halo mass for the observed galaxy. In order to estimate the increase in the gravitational signal, we analyze the theoretical expectable excess surface mass densities $\Delta\Sigma$, predicted by simulations (see Section 3.4.4 for the details of the simulations and Section 6.2 for details to the analysis of $\Delta\Sigma$). For the simulations we choose two different foreground lens sample setups and compare the outcome. First we estimate the unbiased gravitational lensing signal by the central galaxy halos. For this we only consider lenses with rest-frame luminosities brighter than $M_r \sim -21$ and ignore the contribution of fainter galaxies in the simulations. In a second step we include fainter low mass nearby galaxies in the simulations and measure their contribution to $\Delta\Sigma$. As a cross-check the individual signals of the low mass galaxies are investigated separately for the fainter luminosity bins. However, the main intention is to measure the contamination of the brighter luminosity bins by faint unresolved companions. For this we consider the luminosity bins with $-21 > M_r > -24$, measuring the excess surface mass density $\Delta\Sigma$ for isolated central lenses and for central lenses including faint nearby galaxies with $M_r > -21$. As we see in Fig. 6.23 the contribution of unresolved nearby galaxies to the main central galaxy halo signals is negligible.

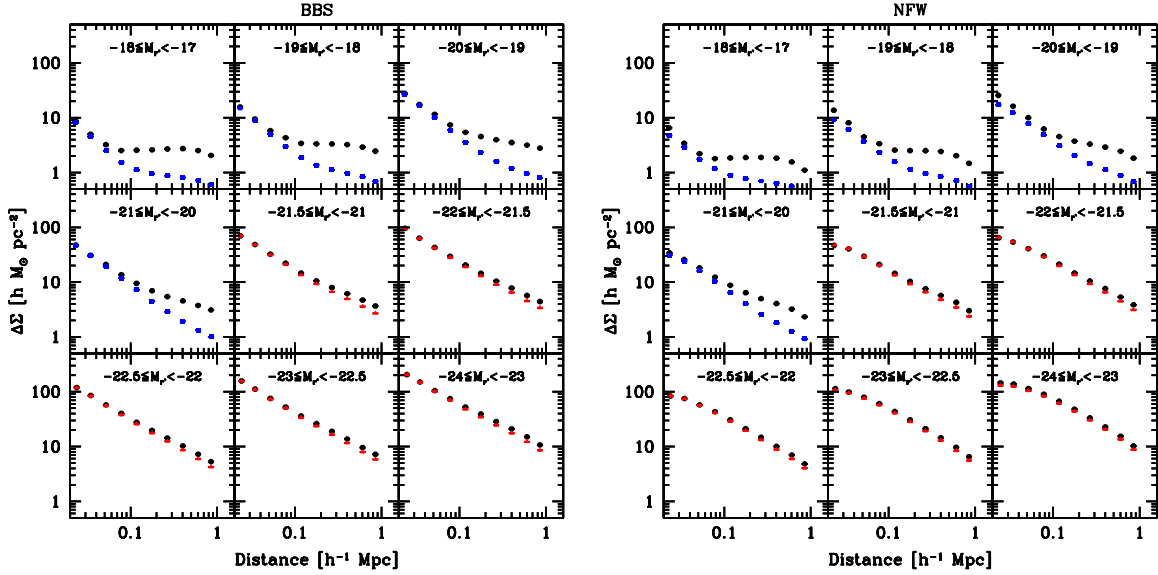


Fig. 6.23: Estimate of the contamination of the lensing signal by unresolved nearby galaxies. The left panel shows the BBS simulation, the right panel the NFW simulation. The red triangles show the excess surface mass density $\Delta\Sigma$ for the uncontaminated pure central galaxy sample for lenses brighter than $M_L \sim -21$, the black circles include the signal contribution for fainter nearby galaxies. As we see, the contribution of low mass nearby galaxies to the excess surface mass density of massive galaxies is negligible. For comparison we also show simulations for the fainter luminosity bins only consisting of the faint galaxy sample, but excluding the brighter ones (blue squares). As the simulations already showed only on short scales the lensing signal is described by the considered central lens while on larger scales it is dominated by the environment.

6.3.4 Systematic Checks by Analyzing the Shear Signal on Subsamples

As a further test we analyze the shear signal for specific source subsamples, checking the results for consistency. For this we divide our source sample and analyze the individual source subsamples with respect to the same foreground. Splitting the foreground in principle would also provide a possible systematic check, but unfortunately, as a cause for differing analysis results, systematics and evolutionary effects are hard to disentangle.

As a first test we want to investigate the proper scaling of the lensing signal with photometric redshifts. In order to avoid systematic side effects by the dynamical lens-source assignment, due to asymmetric sample properties, we redefine our lens and source samples for this analysis. We restrict our foreground lens sample to a photometric redshift of $0.05 < z_{\text{phot}} \leq 0.5$ and our background source sample to a redshift of $0.6 \leq z_{\text{phot}} \leq 2.0$. The intention is to ensure that all source samples ‘see’ the same lens sample. We split the source sample into four different redshift bins (see Table 6.3) and calculate the tangential alignment γ_t and the excess surface mass density $\Delta\Sigma$ for all subsamples. The result for the tangential shear γ_t is shown in the left panel of Fig. 6.24. The amplitude of the tangential alignment does not provide a direct answer to the equality of the four source samples, as the signal amplitude still depends on the distance ratio $D_{\text{ds}}/D_{\text{ds}}$. But as we see from the best-fitting values for the velocity dispersion σ , assuming an SIS profile within $200 h^{-1}$ kpc ($\sigma = 121 \pm 5 \text{ km s}^{-1}$

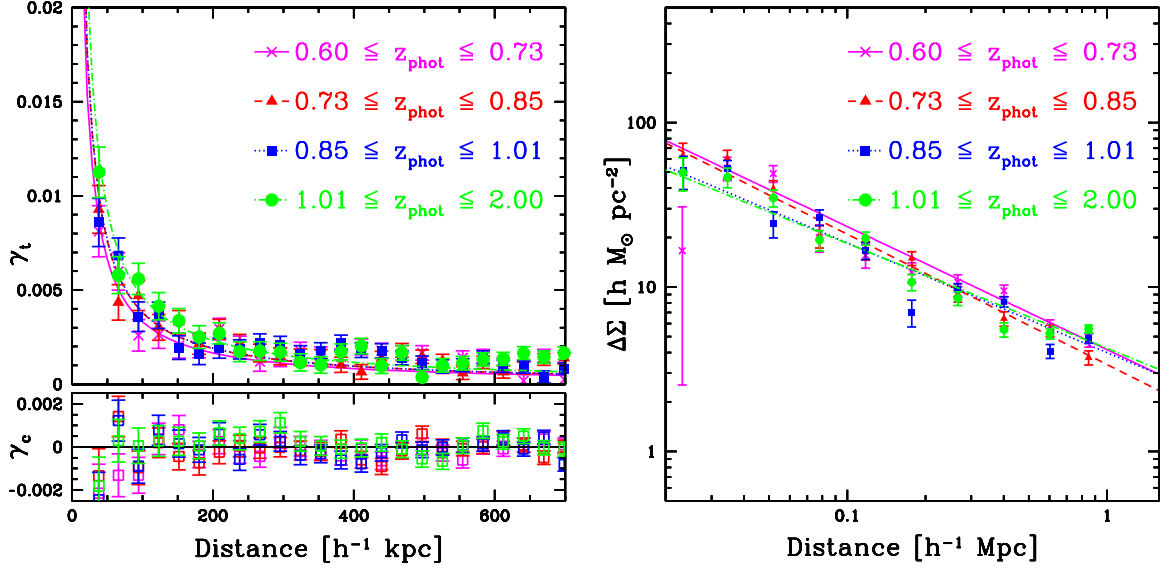


Fig. 6.24: Redshift scaling, obtained from the tangential shear analysis (left panel) and from the excess surface mass density (right panel). We observe background galaxies in different photometric redshift bins ($0.60 \leq z_{\text{phot}} \leq 0.73$ with magenta crosses and solid fit-line, $0.73 \leq z_{\text{phot}} \leq 0.85$ with red triangles and dashed fit-line, $0.85 \leq z_{\text{phot}} \leq 1.01$ with blue squares and dotted fit-line and $1.01 \leq z_{\text{phot}} \leq 2.00$ with green circles and dashed-dotted fit-line). The γ_t -profiles are not directly comparable, due to different D_d/D_{ds} -ratios for the different redshift bins. The velocity dispersions can be estimated assuming effective values for the distance ratios for an SIS-fit. The best-fitting values are shown in Table 6.3. If directly calculating $\Delta\Sigma$, the distance ratios are already implicitly accounted for, due to the dependence on the critical surface mass density Σ_c (see equation 3.8). The obtained velocity dispersions and $\Delta\Sigma$ -profiles agree well within the uncertainties.

for $0.60 \leq z_{\text{phot}} \leq 0.73$, $\sigma = 124 \pm 4 \text{ km s}^{-1}$ for $0.73 \leq z_{\text{phot}} \leq 0.85$, $\sigma = 118 \pm 3 \text{ km s}^{-1}$ for $0.85 \leq z_{\text{phot}} \leq 1.01$ and $\sigma = 124 \pm 3 \text{ km s}^{-1}$ for $1.01 \leq z_{\text{phot}} \leq 2.00$) the results agree well within the uncertainties. In contrast, the amplitude of the excess surface mass density $\Delta\Sigma$ provides a direct visual possibility for comparison, as $\Delta\Sigma$ already includes the distance ratio D_d/D_{ds} . As we see in the right panel of Fig. 6.24 the signals of the four considered background samples are consistent with each other.

As a second systematic test, concerning the tangential shear and the excess surface mass density, we analyze the influence of apparent source luminosity. For this we return to the original photometric foreground lens sample, consisting of all objects with $0.05 < z_{\text{phot}} \leq 1.0$. We divide the background source sample into two subsamples with higher and lower source luminosities, creating two lens-source subsamples with equal pair numbers. The tangential shear γ_t is shown in the left panel of Fig. 6.25, the corresponding fit-values for the velocity dispersion, $\sigma = 115 \pm 2 \text{ km s}^{-1}$ for the bright source sample and $\sigma = 119 \pm 1 \text{ km s}^{-1}$ derived from the SIS-fit on the inner $200 h^{-1} \text{ kpc}$, are added to Table 6.3. The excess surface mass density $\Delta\Sigma$ is shown in the right panel of Fig. 6.25, confirming very good agreement for $\Delta\Sigma$, comparing the surface mass profiles for both luminosity subsamples.

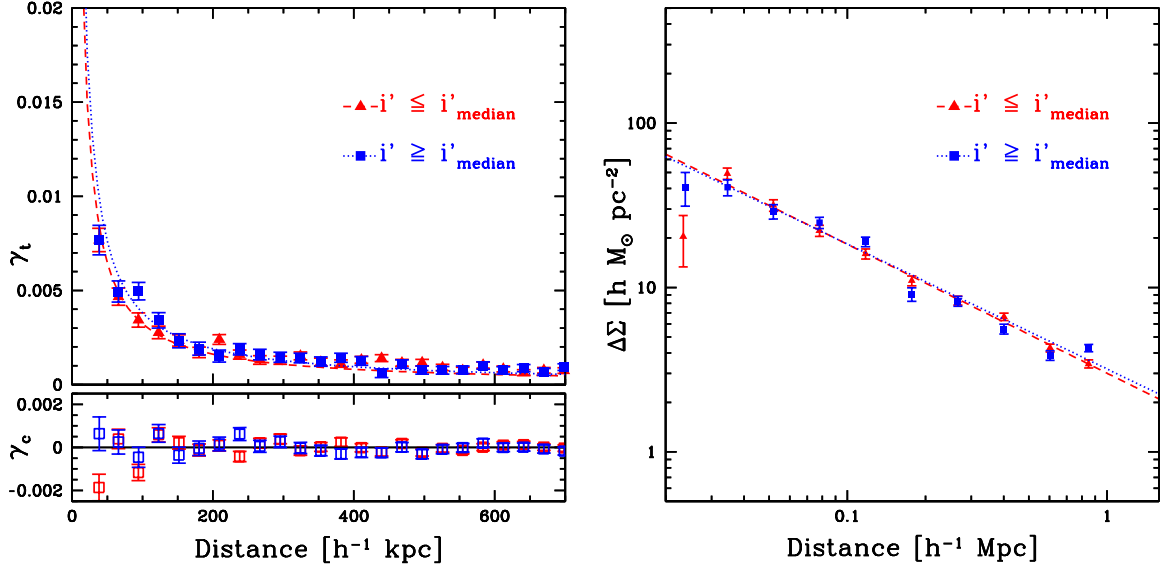


Fig. 6.25: Systematic check, comparing the tangential shear γ (left panel) and the excess surface mass density $\Delta\Sigma$ for sources of different luminosities. The red triangles and dashed fit-lines show the results for the brighter source sample, the blue squares and dotted fit-lines show the results for the fainter sources. The fitted values for σ are shown in Table 6.3. As the right panel directly shows, the mass density profiles for both subsamples are in very good agreement.

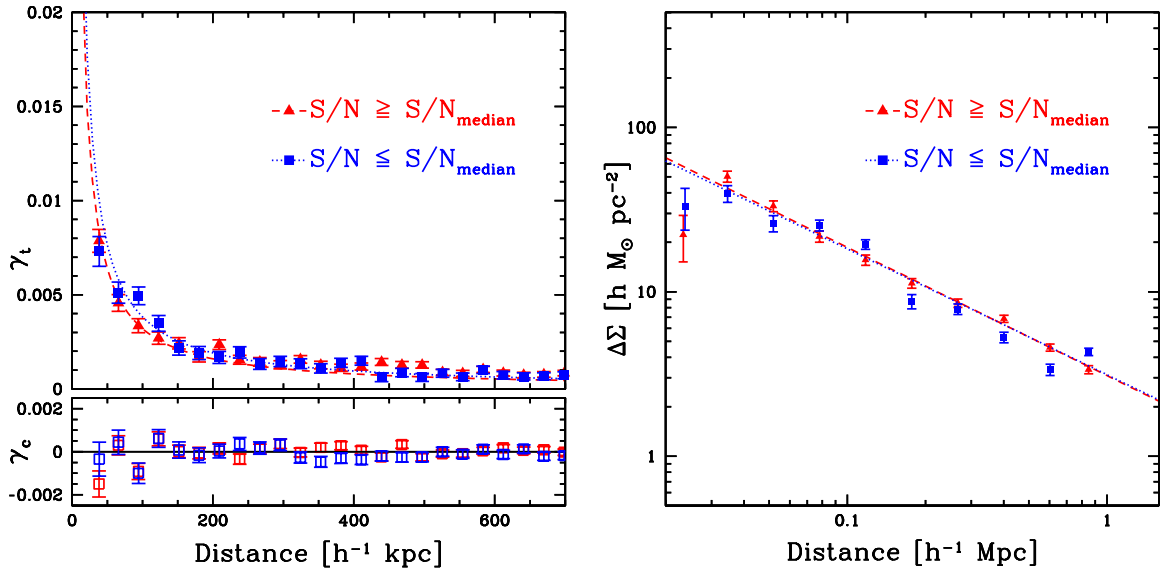


Fig. 6.26: Systematic check, comparing the tangential shear γ (left panel) and the excess surface mass density $\Delta\Sigma$ for sources of different signal-to-noise ratios. The red triangles and dashed fit-lines show the results for the higher S/N sample, the blue squares and dotted fit-lines show the results for the lower S/N sources. The fitted values for σ are shown in Table 6.3. As the right panel directly shows, the mass density profiles for both subsamples are in very good agreement. The results directly reflect the measurements for the brighter and fainter source samples.

sample	z_{fg}	Background selection	$\langle M_{r'} \rangle$	$\langle z_{\text{fg}} \rangle_{\text{pair}}$	$\langle z_{\text{bg}} \rangle_{\text{pair}}$	N_{fg}	N_{bg}	N_{pair}	σ [km s $^{-1}$]
$L_{\text{bg}1}$	$0.05 < z_{\text{fg}} \leq 0.5$	$0.60 \leq z_{\text{bg}} \leq 0.73$	-21.0	0.29	0.67	277 219	292 900	17 230 313	121 ± 5
$L_{\text{bg}2}$	$0.05 < z_{\text{fg}} \leq 0.5$	$0.73 \leq z_{\text{bg}} \leq 0.85$	-21.0	0.32	0.78	277 577	283 754	19 174 161	124 ± 4
$L_{\text{bg}3}$	$0.05 < z_{\text{fg}} \leq 0.5$	$0.85 \leq z_{\text{bg}} \leq 1.01$	-21.0	0.32	0.92	277 513	273 113	18 325 822	118 ± 3
$L_{\text{bg}4}$	$0.05 < z_{\text{fg}} \leq 0.5$	$1.01 \leq z_{\text{bg}} \leq 2.00$	-21.0	0.32	1.20	277 598	260 978	17 531 415	124 ± 3
$L_{\text{bg,bright}}$	$0.05 < z_{\text{fg}} \leq 1.0$	$r' \leq 23.06$	-21.0	0.38	0.81	1 711 502	1 035 270	67 033 496	115 ± 2
$L_{\text{bg,faint}}$	$0.05 < z_{\text{fg}} \leq 1.0$	$r' > 23.06$	-21.0	0.48	1.04	1 811 810	626 348	67 025 398	119 ± 1
$L_{\text{rh,big}}$	$0.05 < z_{\text{fg}} \leq 1.0$	$r_{\text{h}} \leq 3.17$	-21.0	0.40	0.87	1 772 769	890 184	67 031 724	117 ± 2
$L_{\text{rh,small}}$	$0.05 < z_{\text{fg}} \leq 1.0$	$r_{\text{h}} > 3.17$	-21.0	0.42	0.92	1 791 460	771 434	67 027 170	116 ± 2
$L_{\text{sn,high}}$	$0.05 < z_{\text{fg}} \leq 1.0$	$S/N \geq 9.34$	-21.0	0.37	0.80	1 695 097	1 037 322	67 029 067	115 ± 2
$L_{\text{sn,low}}$	$0.05 < z_{\text{fg}} \leq 1.0$	$S/N < 9.34$	-21.0	0.48	1.04	1 819 346	624 296	67 029 827	119 ± 1

Table 6.3: Results for the systematics check by splitting the background sample (redshift, apparent luminosity, object size and S/N-ratio) and analyzing the subsamples with respect to the same foreground sample. The table shows effective lens luminosities and foreground/background-redshifts, number of lenses, sources and lens-source pairs and the velocity dispersions σ from the SIS-fit to the inner region ($R \leq 200 h^{-1}$ kpc.)

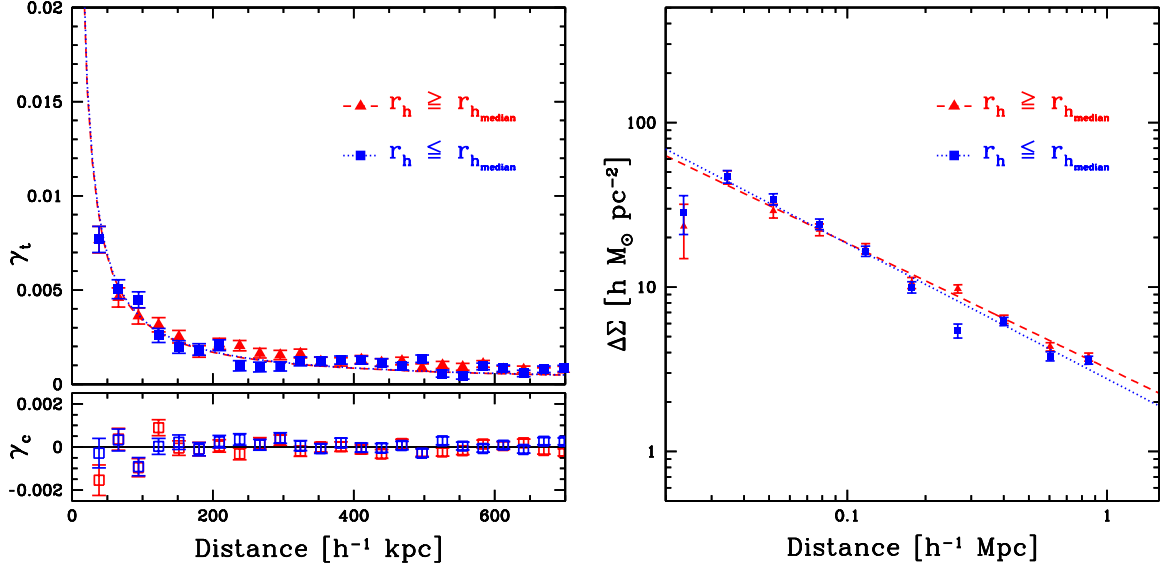


Fig. 6.27: Systematic check, comparing the tangential shear γ_t (left panel) and the excess surface mass density $\Delta\Sigma$ for sources of different half-light radii. The red triangles and dashed fit-lines show the results for the larger background object sample, the blue squares and dotted fit-lines show the results for the smaller source sample. The fitted values for σ are shown in Table 6.3. The results are in good agreement.

We further investigate γ_t and $\Delta\Sigma$ as a function of the signal-to-noise ratio of our background sources. We therefore split our background sample analogously to the previous test, concerning the luminosities. The sample properties, including σ -fit ($\sigma = 115 \pm 2 \text{ km s}^{-1}$ for the high S/N-background and $\sigma = 119 \pm 1 \text{ km s}^{-1}$ for the low S/N-background), are added to Table 6.3. The results are shown in Fig. 6.26. The fact, that luminosities and signal-to-noise ratios are related in a direct way, is reflected by the sample properties, as, e.g., effective lens and source redshifts $\langle z_{\text{fg}} \rangle_{\text{pair}}$ and $\langle z_{\text{bg}} \rangle_{\text{pair}}$ and further by the best-fitting values for the velocity dispersion σ . Looking at the $\Delta\Sigma$ -profiles the results for both subsamples are in good agreement.

Finally, we take the influence of the background object sizes into consideration, dividing our sources into two samples with higher larger and smaller half-light radius r_h . The tangential shear and excess surface density profiles are shown in Fig. 6.27. The measured values for the velocity dispersions of $\sigma = 117 \pm 2 \text{ km s}^{-1}$ for the larger source sample analysis and $\sigma = 116 \pm 2 \text{ km s}^{-1}$ for the smaller sources (see also Table 6.3), as well as the observed $\Delta\Sigma$ -profiles for both subsamples are in good agreement.

6.4 Maximum Likelihood Analysis

The previous analyses of the gravitational lensing signal, the measurement of the tangential shear γ_t and the measurement of the excess surface mass density $\Delta\Sigma$, ignored the impact of additional galaxy halos and thus described the observable cumulative galaxy halo profiles, composed of the central galaxy halo, neighboring secondary galaxy halos, and potentially parent group or cluster halo. In this

section we want to quantify the properties of the single galaxy halos, measuring the lensing signal out to a scale of $2 h^{-1}$ Mpc in case of BBS. Since the integrated mass for the NFW profile diverges for infinite radii and the integrated mass value within a radius of $1 h^{-1}$ Mpc already exceeds the total BBS mass, assuming reference halo parameters of $\sigma^* \sim 130 \text{ km s}^{-1}$, $s^* \sim 200 h^{-1} \text{ kpc}$, $c^* \sim 6$ and $r_{200}^* \sim 130 h^{-1} \text{ kpc}$, we limit the NFW maximum likelihood analysis to a maximum separation of $400 h^{-1} \text{ kpc}$. This distance corresponds to $\approx 1 r_{200}$ for bright and $\approx 5 r_{200}$ for faint galaxies. Since at these scales the original NFW profile hardly differs from a truncated NFW profile (see Baltz *et al.* 2009), the not-finite total NFW masses do not affect our results. At scales of $400 h^{-1} \text{ kpc}$ the lensing signal of the neighboring halos becomes comparable to the signal of the investigated one. I.e., we need to model all the halos simultaneously. For this we follow the approach of Schneider & Rix (1997), and perform a maximum likelihood analysis, assuming analytic two-parametric profiles for the galaxy halos. We apply scaling relations for the halo parameters with respect to the luminosity of our fiducial galaxy and derive the best-fitting parameters for each profile by comparison of the predicted shear values with the observed ones (see Section 3.4.3). Thus we fully treat multiple deflections and reproduce the observable cumulative lensing signal from the independent single galaxy deflections. For the luminosity of the fiducial galaxy we choose $L_{r'}^* = 1.6 \times 10^{10} h^{-2} L_{r',\odot}$.

6.4.1 Truncated Isothermal Sphere (BBS)

For the maximum likelihood analysis we first consider the profile of a truncated isothermal sphere (Brainerd *et al.* 1996, see also Section 3.4.1), representing a slightly more sophisticated profile than the singular isothermal sphere (see Section 3.4.1). It consists of an additional parameter, the truncation radius s , enabling a finite estimate of the total galaxy halo mass. A maximum likelihood means the complete and proper treatment of every single lens, dealing with lenses spanning a wide range of luminosities and therefore masses. Therefore it is indispensable to make some assumptions about the scaling relations of the profile parameters with luminosity, in this way tracing the considered lenses back to a fiducial lens with luminosity L^* . We apply the scaling relations as already discussed in Section 3.4.2 in equations (3.76) and (3.77).

The analysis in Section 6.2.2 suggests a scaling parameter of 0.29 ± 0.02 for the σ -luminosity-scaling relation. We cross-check this value and run a maximum likelihood analysis, assuming an SIS and only considering lens-source pairs with a maximal projected distance of $200 h^{-1} \text{ kpc}$. As the fit variable we use the velocity dispersion σ and its scaling parameter η_σ with luminosity. The contamination by secondary galaxy halos is significantly reduced as each galaxy halo is treated separately in this investigation. The maximum likelihood analysis leaves us with a best-fitting value of $\eta_\sigma = 0.31 \pm 0.02$ (see black contours in Fig. 6.28). Assuming luminosity evolution with $(1+z)$ increases the values for the fiducial velocity dispersion σ^* but does not affect the scaling relation. Combining this value with our previous results from the $\Delta\Sigma$ measurement we thus adopt a value of $\eta_\sigma = 0.3$ for the BBS maximum likelihood analysis. In order to choose an appropriate scaling relation for the truncation radius s we follow our result from Section 6.2.2 of $M \propto L_{r'}^{1.2 \pm 0.02}$ for the virial masses. Although NFW and BBS masses are not identical, we assume similar luminosity scalings to hold and apply $M \propto L^{1.2}$ in agreement with Hoekstra *et al.* (2004). Given that $M_{\text{BBS}} \propto \sigma^2 s$ (see equation 3.60) this leads to a scaling parameter of $\eta_s = 0.6$ for the truncation radius s . This scaling behavior corresponds to a scaling relation of $s \propto \sigma^2$.

On the other hand, recalling the result shown in Fig. 6.14, the scaling parameter depended on the considered SED type. To be more specific the value of $\eta_\sigma = 0.29$ only was valid for a combined lens

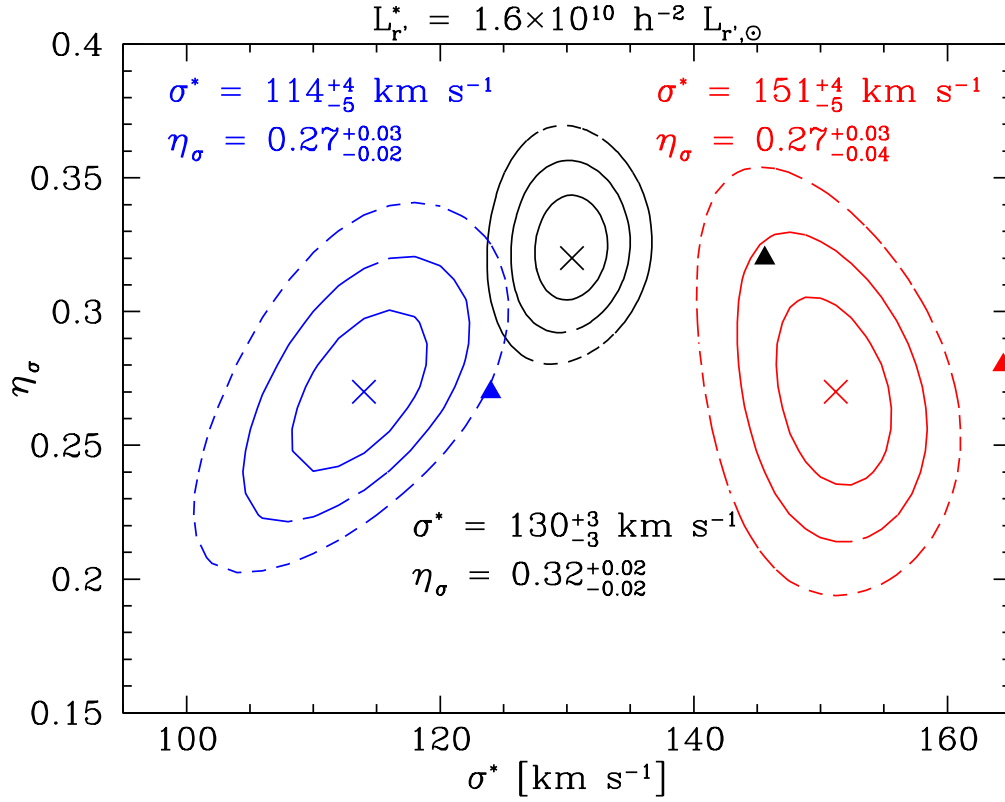


Fig. 6.28: Maximum likelihood result for the scaling relation of the velocity dispersion σ without luminosity evolution (68.3%, 95.5% and 99.7% confidence levels), for the combined sample in black and discriminating between blue galaxies in blue and red galaxies in red. The values for the red and blue samples are lower than for the combined, confirming the result from Fig. 6.14. The filled triangles indicate the best-fitting values, assuming a luminosity evolution with $(1+z)$.

sample, while for red and blue galaxies separately the value was significantly lower, following much closer the predictions of the Faber-Jackson or Tully-Fisher relation ($L \propto \sigma^4$). We therefore investigate η_σ for both galaxy types separately in maximum likelihood analyses. For these analyses the parameters of one galaxy type are examined at one time, while for the other galaxy type fixed values for the fiducial parameters at L^* are used and scaled with luminosity. This means we assume fixed values σ^* and η_σ for the blue galaxies and run a maximum likelihood to constrain the corresponding values for red galaxies and vice versa. The obtained parameters then are refed into a further iteration of the maximum likelihood analysis, repeating the procedure until the calculations converge. In this way we obtain values of $\eta_\sigma = 0.27_{-0.04}^{+0.03}$ for the red galaxies and $\eta_\sigma = 0.27_{-0.02}^{+0.03}$ for the blue galaxies, also shown in Fig. 6.28.

We investigate the BBS profile for several lens samples, first giving the mean properties of the combined lens sample, subsequently discriminating the lenses into red and blue galaxies and finally also investigating the galaxy properties as a function of the environment the galaxies reside in. First of all we consider the combined galaxy type lens sample, populating all environments, and assume no evolution of luminosities with redshift. The applied scaling assumptions for this analysis are $\sigma \propto L^{0.3}$ and $s \propto L^{0.6}$. For an L^* -galaxy we measure a velocity dispersion of $\sigma^* = 131_{-2}^{+2} \text{ km s}^{-1}$ and a trunca-

tion radius of $s^* = 184_{-14}^{+17} h^{-1}$ kpc, leading to a total mass of $M_{\text{total,BBS}}^* = 2.4_{-0.2}^{+0.3} \times 10^{12} h^{-1} M_{\odot}$.

Next we address the general properties of the red and blue lens samples independently. The scaling parameter $\eta_{\sigma} = 0.3$, used in the maximum likelihood analysis for the combined lens sample, implicitly takes into account that red and blue galaxy masses for the same luminosity significantly differ and that bright and faint galaxies in our lens sample are dominated by different SED types. As the independent analysis of both SED types explicitly includes this mass difference and the transition, a value of $\eta_{\sigma} = 0.3$ would lead to an overcorrection in the scaling behavior. Combining the results from Section 6.2.2 as seen in Figs. 6.14 and 6.28 with the maximum likelihood results, we therefore apply a scaling parameter of $\eta_{\sigma} = 0.25$ for red and for blue galaxies in the independent analyses. The observed transition from red to blue SED-type domination for decreasing masses also is supposed to affect the truncation radius s . Given that the original approach corresponds to $s \propto \sigma^2$ we therefore apply a value of $\eta_s = 0.5$ for both galaxy types in all separate investigations. According to equation (3.73), this corresponds to a mass-independent M/L -ratio. In order to analyze red and blue galaxies separately, we apply the same iteration algorithm as before, when calculating the maximum likelihood for the scaling relation for the velocity dispersion σ , assuming an SIS profile. The red lens sample exceeds the values of the combined sample for both profile parameters, yielding a velocity dispersion of $\sigma_{\text{red}}^* = 149_{-3}^{+3} \text{ km s}^{-1}$ and truncation radius of $s^{*,\text{red}} = 337_{-37}^{+43} h^{-1}$ kpc. This leads to a significantly larger total mass of $M_{\text{total,BBS}}^{*,\text{red}} = 5.5_{-0.8}^{+0.9} \times 10^{12} h^{-1} M_{\odot}$. For the blue lens sample we obtain much lower values of $\sigma_{\text{blue}}^* = 118_{-5}^{+4} \text{ km s}^{-1}$ for the velocity dispersion and $s^{*,\text{blue}} = 84_{-14}^{+13} h^{-1}$ kpc for the truncation radius, corresponding to an expected significantly lower total galaxy halo mass of $M_{\text{total,BBS}}^{*,\text{blue}} = 8.6_{-2.2}^{+1.9} \times 10^{11} h^{-1} M_{\odot}$. These results also are visualized in the upper left panel of Fig. 6.29.

As we have seen in Section 6.5.2, the lens environment is not a variable without influence on the galaxy properties. We therefore repeat the BBS maximum likelihood analysis, considering a combined, a red and a blue lens sample in low density and high density environment, and compare the best-fitting values to the corresponding results from the ‘all densities’ analysis. For the lens samples in different environments we use the definitions from Section 5.5.2. For the lens samples of same SED type, but populating different environments, the environment density hardly influences the velocity dispersion of the galaxies. In other words this means that the central galaxy matter density mainly depends on their luminosity but not on their environment. Considering the truncation radii the opposite is the case. In denser environments s significantly increases and therefore the total mass significantly grows with density. This observation is valid for all SED types. These results are also shown in the lower panels of Fig. 6.29. In particular in dense structures parent group or cluster halos might exist in addition to plenty of secondary overlapping galaxy halos. As we do not account for individual group or cluster halos their mass is assigned to the corresponding galaxies. Further the parent halo might smear out the observable change in slope at the truncation radius. Both effects can lead an overestimation of the truncation radius and therefore the total mass does not appear impossible. The best-fitting values for all BBS maximum likelihood results are summarized in Table 6.4.

In the following we additionally take passive evolution of our lens galaxies into account, assuming an evolution of the luminosity with redshift corresponding to $L \propto (1+z)$. Under this assumption the velocity dispersion of our L^* -galaxy significantly increases to a value of $\sigma^* = 144_{-2}^{+3} \text{ km s}^{-1}$ for all lens galaxies and a truncation radius of $s^* = 253_{-20}^{+23} h^{-1}$ kpc. This corresponds to an increased total

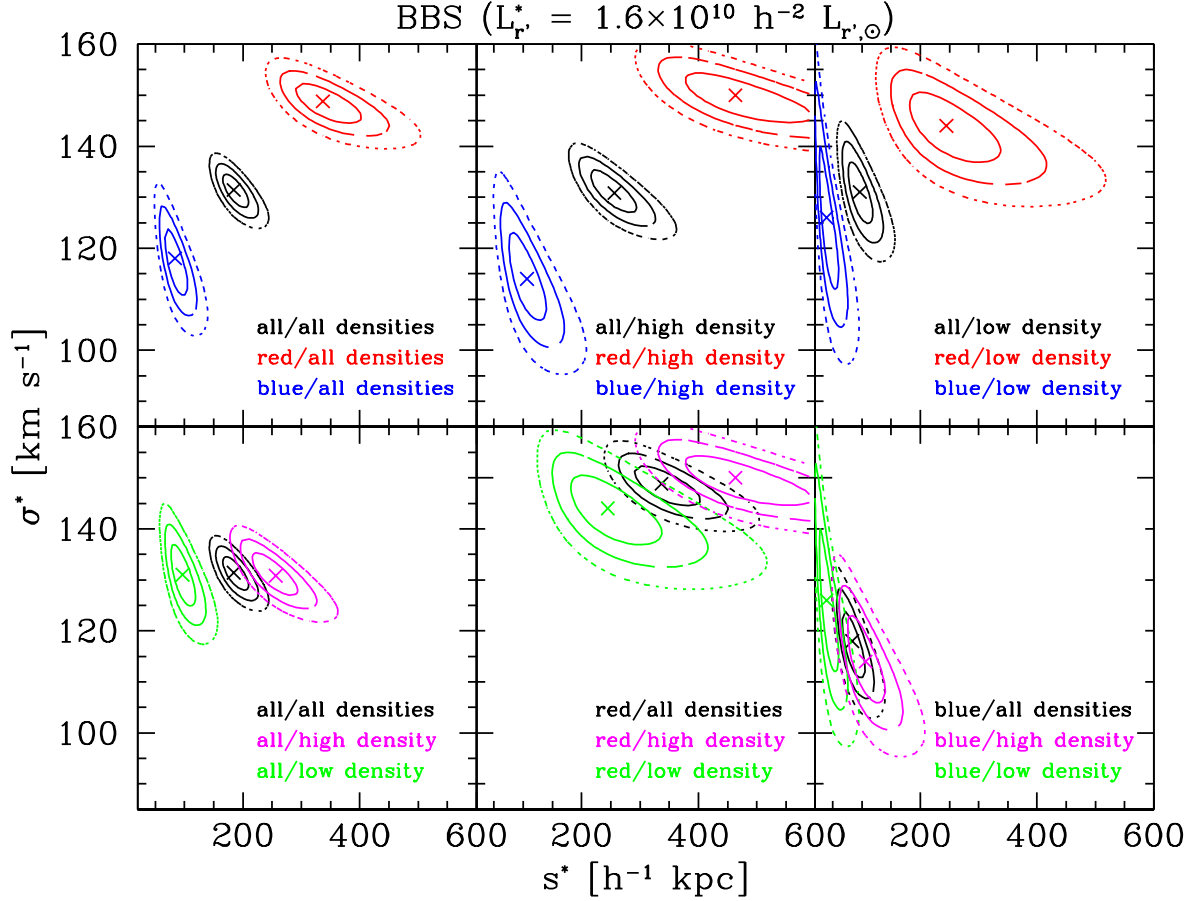


Fig. 6.29: Maximum likelihood analysis for the BBS profile. The solid, the long-dashed and the short-dashed contours show the 68.3%, the 95.4% and the 99.7% confidence levels. We select the lens samples with respect to galaxy SED and environment density. The crosses indicate the best-fitting parameters. In the upper row the different galaxy SEDs are compared to each other in the corresponding environments (all densities in the upper left panel, high density in the upper middle panel and low density in the upper right panel). We see that for all environments red galaxies (in red) exceed blue galaxies (in blue) in both, velocity dispersion σ^* and truncation radius s^* . The combined lens sample (in black) lies in between. In the lower row we compare the influence of the environment on each of the galaxy types (all densities in black, high density in magenta and low density in green), the combined lens sample shown in the lower left panel, the red lens sample in the lower middle panel and the blue lens sample shown in the lower right panel. As we see the velocity dispersion is hardly influenced by the environment density. This indicates that the central galaxy matter density mainly depends on the luminosity and not the environment. In contrast the truncation radii significantly increase with environment density.

mass of $M_{\text{total,BBS}}^* = 3.9_{-0.4}^{+0.5} \times 10^{12} h^{-1} M_{\odot}$. Regarding red and blue galaxies separately we obtain a velocity dispersion of $\sigma_{\text{red}}^* = 161_{-3}^{+3} \text{ km s}^{-1}$ and a truncation radius of $s^{*,\text{red}} = 414_{-48}^{+49} h^{-1} \text{ kpc}$, corresponding to a total mass of $M_{\text{total,BBS}}^{*,\text{red}} = 7.9_{-1.2}^{+1.2} \times 10^{12} h^{-1} M_{\odot}$ for a red L^* -galaxy and a velocity dispersion of $\sigma_{\text{blue}}^* = 126_{-5}^{+5} \text{ km s}^{-1}$ and a truncation radius of $s^{*,\text{blue}} = 108_{-17}^{+19} h^{-1} \text{ kpc}$, corresponding to a total mass of $M_{\text{total,BBS}}^{*,\text{blue}} = 1.3_{-0.3}^{+0.3} \times 10^{12} h^{-1} M_{\odot}$ for a blue L^* -galaxy. The results assuming luminosity evolution are added to Table 6.4.

6.4.2 Universal Density Profile (NFW)

As a further discussed possible galaxy halo profile, we now consider the universal density profile (see also Section 3.4.1), better known as NFW profile, which was introduced by Navarro *et al.* (1996). The NFW profile also consists of two independent parameters, the concentration parameter c and the virial radius r_{200} . As already for the BBS profile we have to think about the scaling relations to be applied. Recalling the results of Guzik & Seljak (2002), but also our result from Section 6.2.2 that $M \propto L^{1.2}$, combined with equation (3.65) for the M_{200} , we obtain a scaling relation of $r_{200} \propto L^{0.4}$ (see equation 3.79 in Section 3.4.2). In order to properly scale the concentration parameter c , we follow the results of Duffy *et al.* (2008) (see equation 3.81).

In the NFW likelihood analysis we again first investigate the complete lens sample, ignoring any possible evolution of the galaxy luminosities with redshift. For these conditions we obtain for the L^* -galaxy a concentration parameter of $c^* = 6.4_{-0.7}^{+0.9}$ and a virial radius of $r_{200}^* = 133_{-2}^{+3} h^{-1} \text{ kpc}$. These values correspond to a virial mass of $M_{200}^* = 7.6_{-0.3}^{+0.5} \times 10^{11} h^{-1} M_{\odot}$.

In order to disentangle the contribution of red and blue galaxies we also run likelihood analyses for both SED types separately, in the same manner as described for the BBS profile. Recalling that the assumed scaling parameters for BBS analyses for the different SED types separately corresponded to a mass-independent M/L -ratio, we adjust the value of $\eta_{r_{200}}$ for all separate-SED analyses to a value of $\eta_{r_{200}} = 1/3$. These scaling parameters also perfectly reflect the values we obtained in Section 6.2.2. We find that the concentrations of red and blue galaxies do not strongly differ, at least considering galaxies around the fiducial luminosity. However, this can not be generalized for all luminosity or mass ranges, respectively, as we will see in Section 6.4.3. In contrast to the observation of the concentration parameter, the virial radii of red and blue galaxies significantly differ, confirming the large difference in halo mass, as observed in the BBS analyses. For red galaxies we measure a concentration parameter of $c^{*,\text{red}} = 6.4_{-0.8}^{+0.7}$ and a virial radius of $r_{200}^{*,\text{red}} = 160_{-4}^{+3} h^{-1} \text{ kpc}$, corresponding to a virial mass $M_{200}^{*,\text{red}} = 1.2_{-0.1}^{+0.1} \times 10^{12} h^{-1} M_{\odot}$. Complementary, we obtain a concentration parameter of $c^{*,\text{blue}} = 7.0_{-1.6}^{+1.9}$ and virial radius of $r_{200}^{*,\text{blue}} = 115_{-5}^{+4} h^{-1} \text{ kpc}$ for the blue galaxies. This translate into a virial mass of $M_{200}^{*,\text{blue}} = 5.0_{-0.6}^{+0.5} \times 10^{11} h^{-1} M_{\odot}$. The results are also shown in the upper row of Fig. 6.30.

If we now investigate the evolution of the NFW profile parameters with the density of the environment, we do not observe a strong dependency of the concentration parameter c , which only slightly increases with decreasing density. While the concentration of galaxies appears slightly enhanced in low density environments, the concentration hardly differs between mean and high density environments. The opposite is the case, however, when considering the virial radii. The virial radii strongly increase with environment density. This corresponds to a significant increase in the

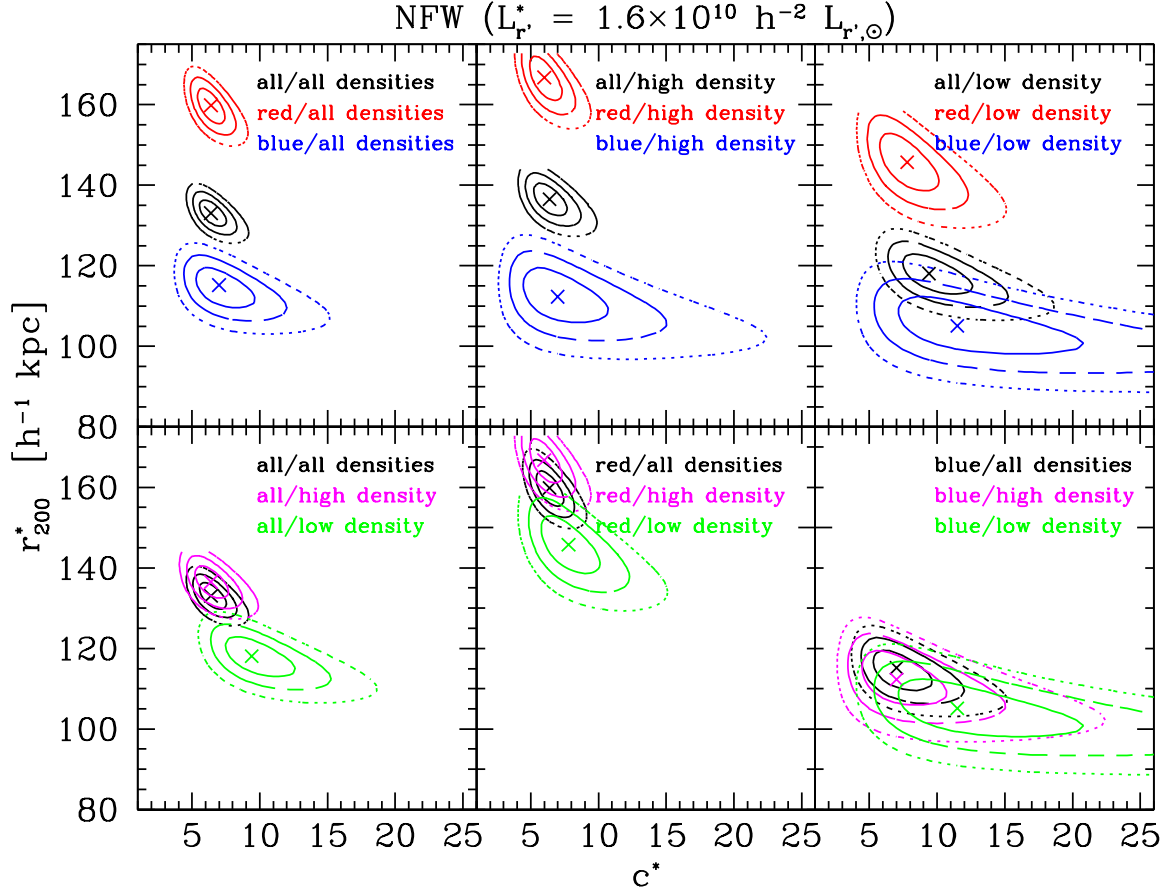


Fig. 6.30: Maximum likelihood analysis for the NFW profile. The solid, the long-dashed and the short-dashed contours show the 68.3%, the 95.4% and the 99.7% confidence levels. We select the lens samples with respect to galaxy SED and environment density. The crosses indicate the best-fitting parameters.

In the upper row the different galaxy SEDs are compared to each other in the corresponding environments (all densities in the upper left panel, high density in the upper middle panel and low density in the upper right panel). We see that for all environments all galaxy types show very similar concentration c in the same environment for the L^* -galaxy, while the virial radii r_{200} for red galaxies (in red) are significantly higher than for blue galaxies (in blue). The combined lens sample (in black) consistently lies in between.

In the lower row we compare the influence of the environment on each of the galaxy types (all densities in black, high density in magenta and low density in green), the combined type lens sample shown in the lower left panel, the red lens sample in the lower middle panel and the blue lens sample shown in the lower right panel. As we see the concentration parameter is hardly influenced by the environment density, being almost identical in all densities and high density, but slightly enhanced in low density environment. The increase of the halo mass with environment density is also observed for the NFW profile, indicated by the increase of r_{200} .

virial masses, reflecting the results from the BBS analyses. The environment density dependencies also are shown in the lower row of Fig. 6.30. The best-fitting parameter for the NFW likelihood analyses are added to Table 6.4.

Now we also assume that the galaxy luminosities evolve with $L \propto (1+z)$. This slightly reduces the concentration parameter to a value of $c^* = 5.4_{-0.6}^{+0.8}$, but strongly enhances the value of the virial radius to $r_{200}^* = 158_{-2}^{+3} h^{-1}$ kpc, corresponding to a larger virial mass of $M_{200}^* = 1.2_{-0.1}^{+0.1} \times 10^{12} h^{-1} M_{\odot}$ for the complete lens sample. Investigating red galaxies separately, we measure a concentration parameter of $c^{*,\text{red}} = 6.2_{-0.7}^{+0.8}$ and a virial radius of $r_{200}^{*,\text{red}} = 183_{-4}^{+4} h^{-1}$ kpc. This corresponds to a virial mass of $M_{200}^{*,\text{red}} = 1.9_{-0.1}^{+0.1} \times 10^{12} h^{-1} M_{\odot}$. Looking at our blue galaxy sample, we obtain a concentration parameter of $c^{*,\text{blue}} = 6.2_{-1.4}^{+1.7}$ and a virial radius of $r_{200}^{*,\text{blue}} = 135_{-6}^{+4} h^{-1}$ kpc, leading to a virial mass of $M_{200}^{*,\text{blue}} = 8.0_{-1.1}^{+0.7} \times 10^{11} h^{-1} M_{\odot}$.

As we investigated two different halo profiles, we want to check the consistency of the results from our BBS and NFW likelihood analyses. For this purpose we compare the corresponding masses from the BBS and from the NFW analyses, enclosed by the same radius. We choose this radius to be the virial radius, as obtained in the NFW analysis. The corresponding mass in the NFW case is M_{200}^* , see equation (3.65). The corresponding mass for the BBS profile is calculated according to equation (3.59). Assuming a BBS profile, for the combined galaxy lens sample we obtain a mass of $M_{\text{BBS}}^*(r_{200}^*) = 9.2_{-0.9}^{+1.1} \times 10^{11} h^{-1} M_{\odot}$, representing a slightly higher value than the NFW value of $M_{200}^* = 7.6_{-0.3}^{+0.5} \times 10^{11} h^{-1} M_{\odot}$. For the combined lens sample in lower and higher density environments, the characteristic behavior is the same. This results in $M_{\text{BBS}}^*(r_{200}^*) = 10.1_{-1.4}^{+1.4} \times 10^{11} h^{-1} M_{\odot}$ compared to $M_{200}^* = 8.3_{-0.5}^{+0.5} \times 10^{11} h^{-1} M_{\odot}$ for the high density case and $M_{\text{BBS}} = 10.1_{-1.4}^{+1.4} \times 10^{11} h^{-1} M_{\odot}$ for the low density case. Considering the masses of red and blue galaxies independently, we also see for red lenses that the BBS masses inside r_{200} are slightly enhanced, while looking at the blue lenses the corresponding two mass values hardly differ anymore. However, considering the uncertainties, the results agree within 1σ .

If we now further compare the BBS and NFW masses, including luminosity evolution with redshift, $L \propto (1+z)$, we obtain a BBS-mass of $M_{\text{BBS}}^*(r_{200}^*) = 1.4_{-0.1}^{+0.1} \times 10^{12} h^{-1} M_{\odot}$ compared to an NFW-mass of $M_{200}^* = 1.3_{-0.1}^{+0.1} \times 10^{12} h^{-1} M_{\odot}$ for all lens galaxies, a BBS-mass of $M_{\text{BBS}}^{*,\text{red}}(r_{200}^{*,\text{red}}) = 2.1_{-0.2}^{+0.3} \times 10^{12} h^{-1} M_{\odot}$ compared to an NFW-mass of $M_{200}^{*,\text{red}} = 1.9_{-0.1}^{+0.1} \times 10^{12} h^{-1} M_{\odot}$ for red galaxies and a BBS-mass of $M_{\text{BBS}}^{*,\text{blue}}(r_{200}^{*,\text{blue}}) = 7.2_{-1.5}^{+1.8} \times 10^{11} h^{-1} M_{\odot}$ compared to an NFW-mass of $M_{200}^{*,\text{blue}} = 8.0_{-1.1}^{+0.7} \times 10^{11} h^{-1} M_{\odot}$ for blue galaxies. All measured values for the masses and halo parameters are summarized in Table 6.4.

Taking the results of Wright & Brainerd (2000) into account, which show that isothermal profiles indeed have a tendency in yielding higher masses than NFW profiles for the same given gravitational shear within the virial radius, a consistent picture is drawn.

6.4.3 Extraction of Scaling Relations from Maximum Likelihood Analyses

Mass-to-Light-Ratio

In the analyses based on the BBS profile in the previous sections, we assumed a mass-luminosity-scaling relation with $M \propto L^{1.2}$, being equivalent to a scaling of the mass-to-light ratio of $M/L \propto L^{0.2}$.

Without luminosity evolution, $L_{r'}^* = 1.6 \times 10^{10} h^{-2} L_{r',\odot}$									
type	density	σ^* [km s ⁻¹]	s^* [h ⁻¹ kpc]	c^*	r_{200}^* [h ⁻¹ kpc]	$M_{\text{total,BBS}}^*$ [10 ¹¹ h ⁻¹ M _⊙]	M_{200}^* [10 ¹¹ h ⁻¹ M _⊙]	$M_{\text{BBS}}^*(r_{200}^*)$ [10 ¹¹ h ⁻¹ M _⊙]	$M_{\text{total,BBS}}^*/L_{r'}^*$ [h M _⊙ /L _{r',⊙}]
all	all	131 ⁺² ₋₂	184 ⁺¹⁷ ₋₁₄	6.4 ^{+0.9} _{-0.7}	133 ⁺³ ₋₂	23.2 ^{+2.8} _{-2.5}	7.6 ^{+0.5} _{-0.3}	9.2 ^{+1.1} _{-0.9}	178 ⁺²² ₋₁₉
all	high	131 ⁺³ ₋₃	256 ⁺²⁴ ₋₂₆	6.4 ^{+1.0} _{-1.0}	137 ⁺³ ₋₃	32.2 ^{+4.5} _{-4.8}	8.3 ^{+0.5} _{-0.5}	10.1 ^{+1.4} _{-1.4}	248 ⁺³⁵ ₋₃₇
all	low	131 ⁺⁴ ₋₅	96 ⁺¹⁵ ₋₁₅	9.4 ^{+2.4} _{-1.7}	118 ⁺⁴ ₋₄	12.1 ^{+2.6} _{-2.8}	5.3 ^{+0.5} _{-0.5}	6.8 ^{+1.4} _{-1.5}	93 ⁺²⁰ ₋₂₂
red	all	149 ⁺³ ₋₃	337 ⁺⁴³ ₋₃₇	6.4 ^{+0.7} _{-0.8}	160 ⁺³ ₋₄	54.9 ^{+9.2} _{-8.2}	12.4 ^{+0.7} _{-0.9}	15.5 ^{+2.6} _{-1.7}	422 ⁺⁷¹ ₋₆₃
red	high	150 ⁺³ ₋₄	464 ⁺⁷⁵ ₋₆₈	6.0 ^{+1.0} _{-0.9}	167 ⁺⁴ ₋₅	76.6 ^{+15.4} _{-15.3}	14.1 ^{+1.0} _{-1.3}	16.8 ^{+3.4} _{-2.4}	589 ⁺¹¹⁹ ₋₁₁₈
red	low	144 ⁺⁵ ₋₆	245 ⁺⁶⁴ ₋₅₂	7.8 ^{+1.6} _{-1.7}	146 ⁺⁵ ₋₆	37.3 ^{+12.3} _{-10.5}	9.4 ^{+1.0} _{-1.2}	12.8 ^{+4.0} _{-2.9}	287 ⁺⁹⁵ ₋₈₅
blue	all	118 ⁺⁴ ₋₅	84 ⁺¹³ ₋₁₄	7.0 ^{+1.9} _{-1.6}	115 ⁺⁴ ₋₅	8.6 ^{+1.9} _{-2.2}	5.0 ^{+0.5} _{-0.6}	5.1 ^{+1.1} _{-1.3}	66 ⁺¹⁵ ₋₁₇
blue	high	114 ⁺⁵ ₋₆	107 ⁺²² ₋₂₃	7.0 ^{+3.1} _{-2.3}	112 ⁺⁶ ₋₆	10.2 ^{+3.0} _{-3.3}	4.6 ^{+0.7} _{-0.7}	5.3 ^{+1.5} _{-1.7}	78 ⁺²³ ₋₂₅
blue	low	126 ⁺⁸ ₋₉	40 ⁺¹¹ ₋₈	11.5 ^{+6.5} _{-3.9}	105 ⁺⁶ ₋₆	4.7 ^{+1.9} _{-1.6}	3.8 ^{+0.6} _{-0.6}	3.6 ^{+1.4} _{-1.3}	36 ⁺¹⁴ ₋₁₂

With luminosity evolution, $L_{r'}^* = 1.6 \times 10^{10} h^{-2} L_{r',\odot}$									
type	density	σ^* [km s ⁻¹]	s^* [h ⁻¹ kpc]	c^*	r_{200}^* [h ⁻¹ kpc]	$M_{\text{total,BBS}}^*$ [10 ¹¹ h ⁻¹ M _⊙]	M_{200}^* [10 ¹¹ h ⁻¹ M _⊙]	$M_{\text{BBS}}^*(r_{200}^*)$ [10 ¹¹ h ⁻¹ M _⊙]	$M_{\text{total,BBS}}^*/L_{r'}^*$ [h M _⊙ /L _{r',⊙}]
all	all	144 ⁺³ ₋₂	253 ⁺²³ ₋₂₀	5.4 ^{+0.8} _{-0.6}	158 ⁺³ ₋₂	38.5 ^{+5.1} _{-4.1}	12.7 ^{+0.7} _{-0.5}	13.7 ^{+1.8} _{-1.1}	296 ⁺³⁹ ₋₃₂
red	all	161 ⁺³ ₋₃	414 ⁺⁴⁹ ₋₄₈	6.2 ^{+0.8} _{-0.7}	183 ⁺⁴ ₋₄	78.7 ^{+12.3} _{-12.1}	18.6 ^{+1.2} _{-1.2}	20.9 ^{+3.2} _{-2.1}	605 ⁺⁹⁵ ₋₉₃
blue	all	126 ⁺⁵ ₋₅	108 ⁺¹⁹ ₋₁₇	6.2 ^{+1.7} _{-1.4}	135 ⁺⁴ ₋₆	12.6 ^{+3.2} _{-3.0}	8.0 ^{+0.7} _{-1.1}	7.2 ^{+1.8} _{-1.5}	97 ⁺²⁵ ₋₂₃

Table 6.4: Best-fitting values from the likelihood analyses, velocity dispersion σ , truncation radius s and total halo mass $M_{\text{total,BBS}}$ from the BBS analysis, concentration parameter c , virial radius r_{200} and virial mass M_{200} from the NFW analysis, completed by the BBS mass at the NFW- r_{200} and the total mass-to-light-ratio $M_{\text{total,BBS}}/L_{r',\odot}$. The upper table shows the values without luminosity evolution, the lower table with luminosity evolution according to $L \propto (1+z)$.

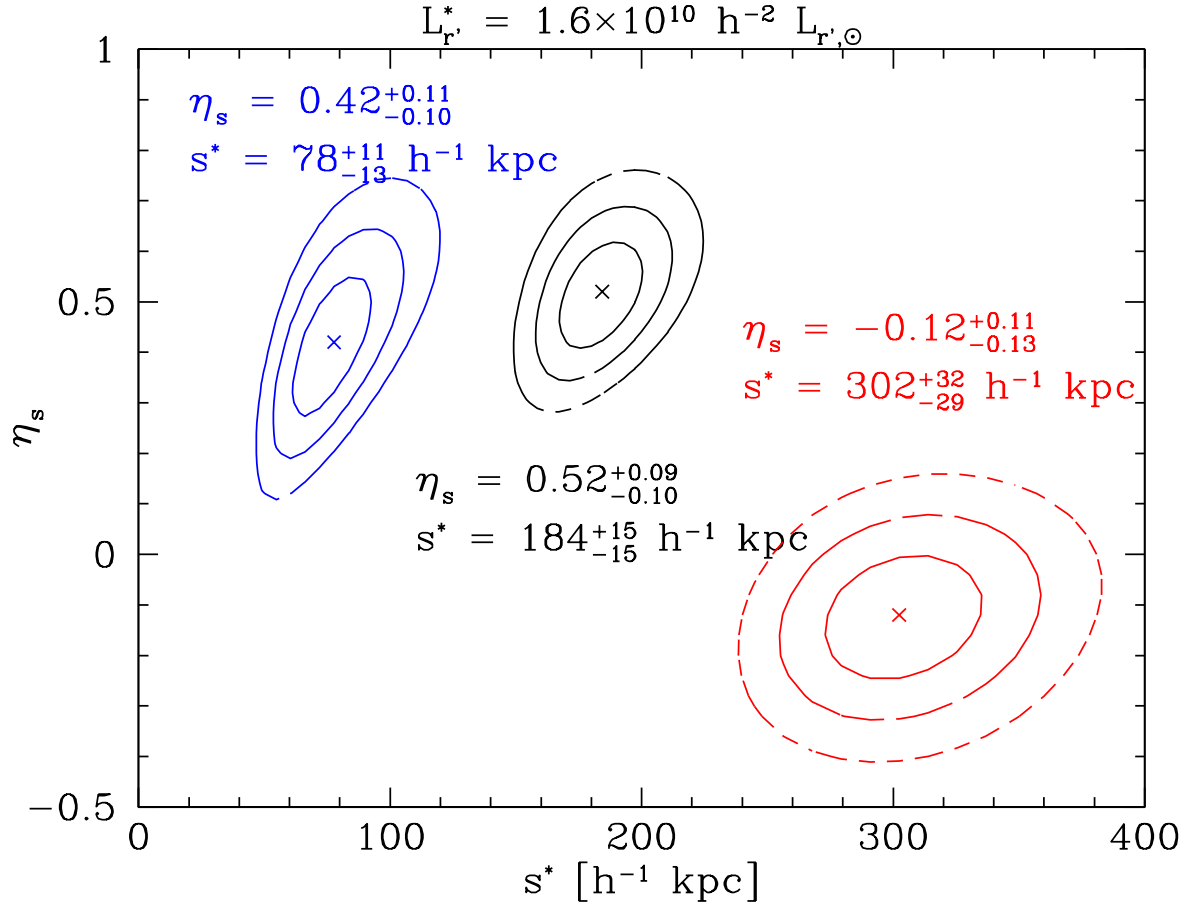


Fig. 6.31: Maximum likelihood results for the scaling relation of the BBS truncation radius s , investigating blue (left) and red galaxies (right) separately. The solid lines show the 68.3%, the long-dashed lines the 95.4% and the short-dashed line the 99.7% confidence levels, the crosses indicates the best-fitting parameters. For the combined sample (black contours) we find a best-fitting scaling parameter of $\eta_s = 0.52^{+0.09}_{-0.10}$ for s , which corresponds to a best-fitting scaling parameter of $\eta_{M/L} = 0.12^{+0.10}_{-0.11}$, for blue galaxies (blue contours) we find $\eta_s^{\text{blue}} = 0.42^{+0.11}_{-0.10}$ and for red galaxies (red galaxies) we obtain $\eta_s^{\text{red}} = -0.12^{+0.11}_{-0.13}$.

Given the stability of the scaling relation of the velocity dispersion σ with luminosity, we now fix the velocity dispersion to the observed value of $\sigma^* = 131 \text{ km s}^{-1}$ from the BBS likelihood analysis for a L^* -galaxy and use the scaling factor η_s of the truncation radius with luminosity as a free parameter. I.e., we now run a likelihood analysis with the truncation s and the scaling factor η_s as fit parameters. Recalling that the total BBS mass scales as $M \propto \sigma^2 s$ (see equation 3.60), this leads to a scaling factor for the mass-to-light ratio of

$$\eta_{M/L} = 2 \cdot \eta_\sigma + \eta_s - 1. \quad (6.7)$$

As the black contours in Fig. 6.31 show, the likelihood analysis for the complete lens sample yields a scaling factor of $\eta_s = 0.52^{+0.09}_{-0.10}$ with unchanged truncation radius s . Therefore the total halo mass remains unaffected. Combining this result with the assumed scaling factor $\eta_\sigma = 0.30 \pm 0.02$ we obtain a scaling relation of $M/L \propto L^{\eta_{M/L}}$ with $\eta_{M/L} = 0.12^{+0.10}_{-0.11}$. The estimation of the scaling relation for the individual galaxy types is challenging, as the transition point, where the profile turns from a decrease with second order to a decrease with fourth order in distance, is smeared out by the contribution of

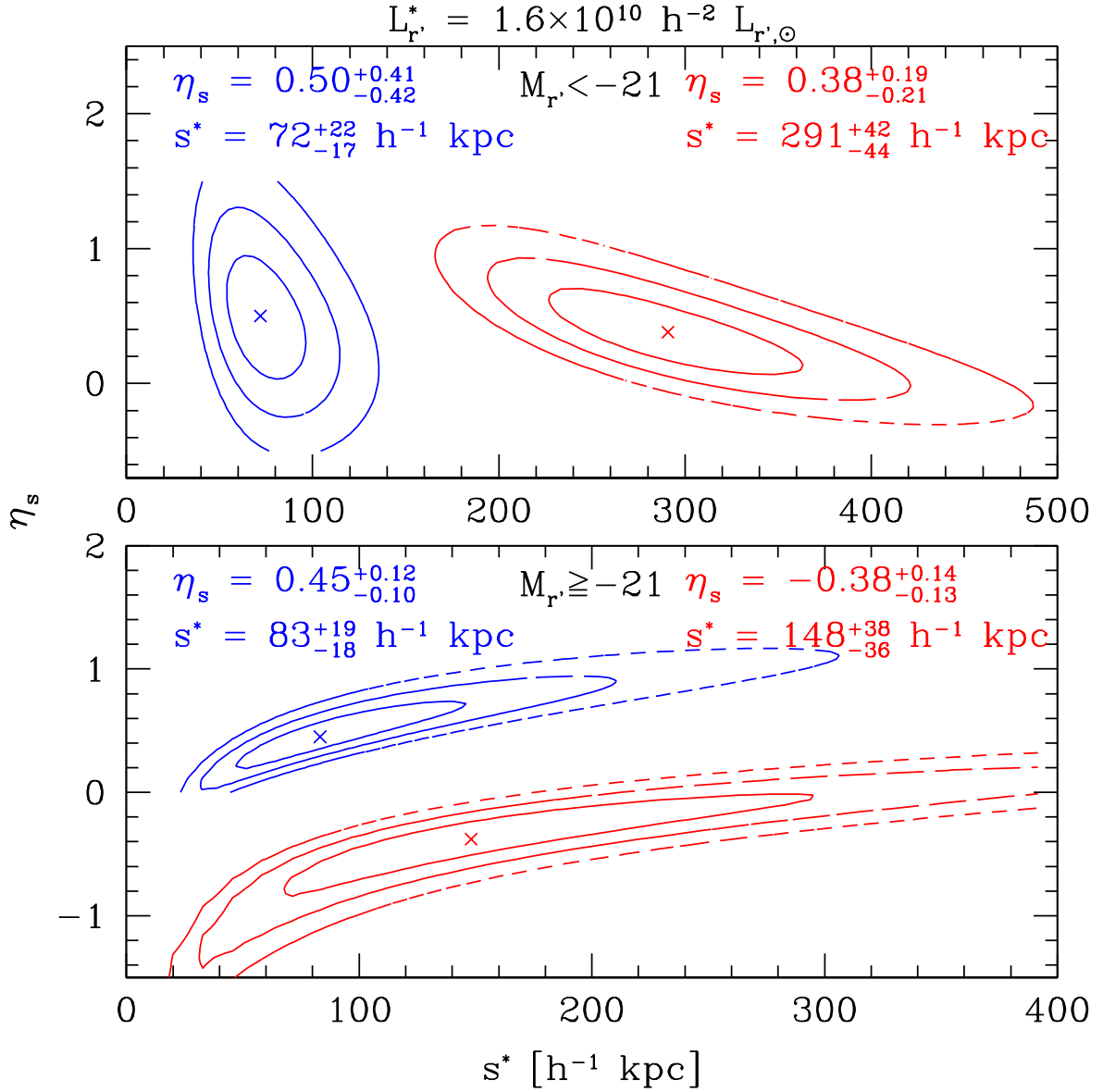


Fig. 6.32: Maximum likelihood results for the scaling relation of the BBS truncation radius s , investigating blue (blue contours) and red (red contours), bright (upper panel) and faint galaxies (lower panel) separately. The solid, the long-dashed and the short-dashed contours show the 68.3%, the 95.4% and the 99.7% confidence levels. As we see in the upper panel, the truncation radii s of all galaxies brighter than $M_r = -21$, independent from the SED-type, show a scaling behavior which agrees well with the assumptions ($\eta_s = 0.5$), while for galaxies fainter than $M_r = -21$ this is only the case for blue galaxies. Red galaxies show an inverted scaling behavior. This implies increasing radii with decreasing luminosity, corresponding to an almost luminosity independent total mass. This phenomenon could be explained by assuming a transition from a further red galaxy population with higher mass for same luminosity, which dominates for faint galaxies, but dies out with increasing luminosity.

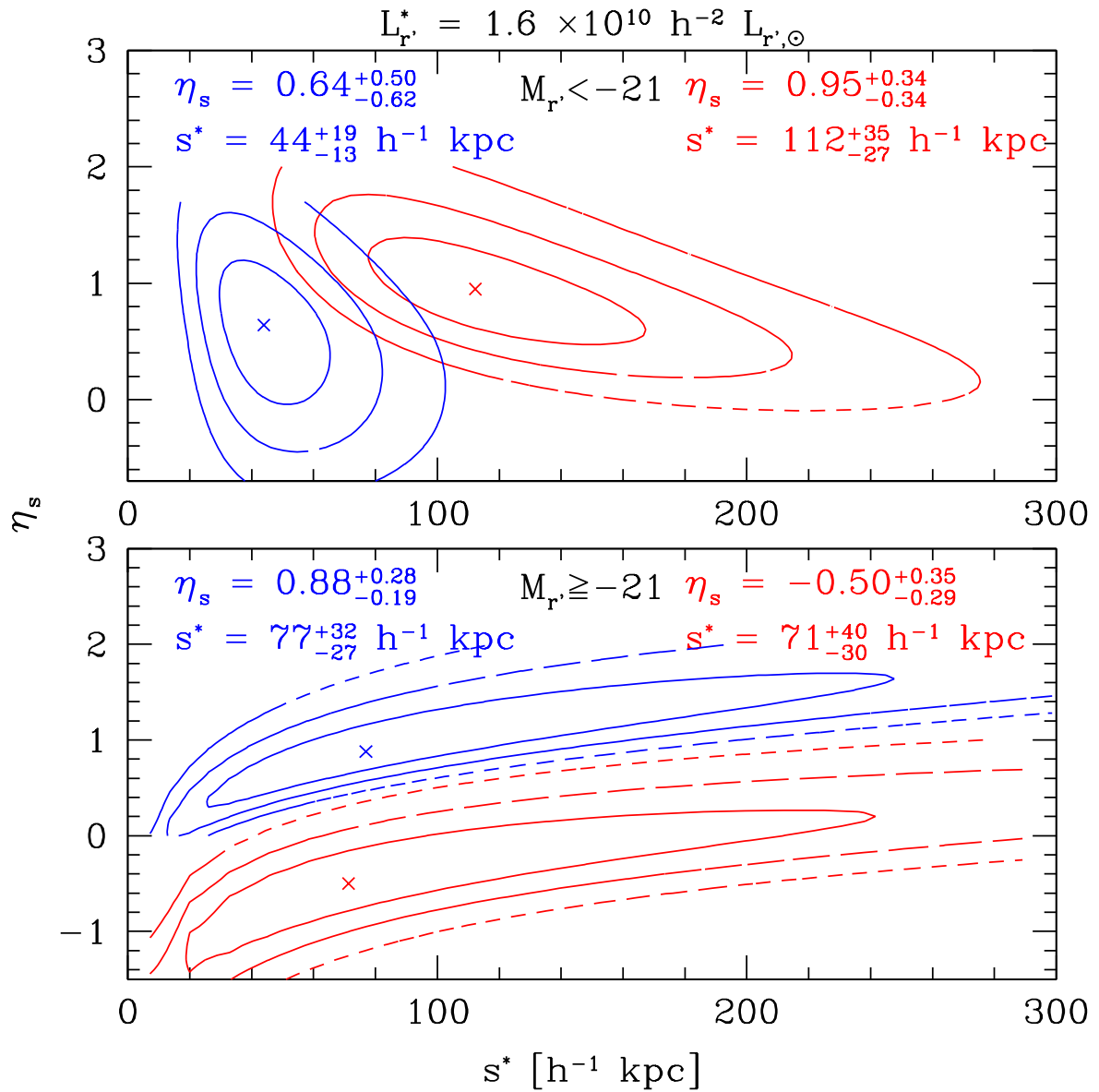


Fig. 6.33: Same as Fig. 6.32, but for lenses in low density environments. As we see the deviating scaling behavior of fainter red galaxies is not an environmental phenomenon. The truncation radii of bright red and blue but also of faint red galaxies show a scaling behavior widely consistent to $s \propto L^{0.5}$, while the faint red lenses agree with a luminosity independent mass.

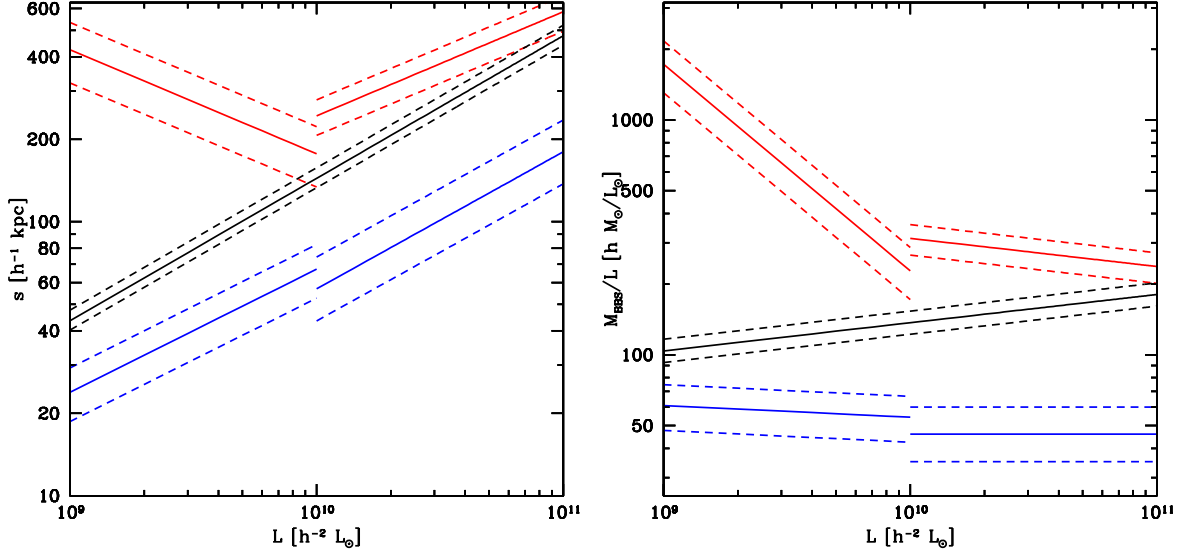


Fig. 6.34: Truncation radius s (left panel) and M/L -ratio (right panel), calculated for red (in red) and blue galaxies (in blue) according to the scaling relation of Fig. 6.32. The solid lines denote the best fit, the dashed lines denote the 68.3%-confidence levels. We observe a negative s -slope for faint red galaxies and a positive s -slope for bright red and all blue galaxies. This leads to a strong increase in the M/L -ratio for faint red galaxies, while the universally positive s -slope for blue galaxies leads to an approximately luminosity independent M/L -ratio. The discontinuities at $L = 10^{10} h^{-1} L_{\odot}$ are numerical artifacts, due to assuming a sudden change in the scaling relation and not exactly knowing where this change occurs. However, both sides of the fits still agree within 1σ . We included for comparison the single-power scaling for the combined sample in both panels in black ($s \propto L^{0.52}$, $M/L \propto L^{1.12}$, see Figure 6.31).

many neighboring galaxy halos and occasionally group or cluster halos. While a reasonable estimation for the truncation radii of massive galaxies is still possible, the measurements in the low-mass regime become very difficult. This becomes obvious when investigating the scaling behavior of the truncation radius s for blue and red galaxies separately (see Fig. 6.31). While for blue galaxies the observed scaling behavior ($\eta_s^{\text{blue}} = 0.42^{+0.10}_{-0.11}$) is consistent with our expectations, for red galaxies the scaling relation is at first look surprising, indicating a growth in the truncation radii for decreasing luminosities ($\eta_s^{\text{red}} = -0.12^{+0.11}_{-0.13}$). In order to determine the origin of this feature, we further divide our lens samples into brighter and fainter galaxies and repeat the maximum likelihood analysis for the scaling behavior of s . First investigating the scaling relation for massive galaxies we only consider lenses with magnitudes $M_r < -21$ in the fitting loop, while for fainter galaxies we assume the standard scaling behavior with $\eta_s = 0.5$. As we see in the upper panel of Fig. 6.32, in this case, for both, red and blue galaxies, the results for the scaling relation agree well with the expectations from the analysis of the ‘all luminosities’ samples ($\eta_s^{\text{red,bright}} = 0.38^{+0.19}_{-0.21}$ for red and $\eta_s^{\text{blue,bright}} = 0.50^{+0.41}_{-0.42}$ for blue galaxies). However, this result is not confirmed when considering the fainter part of the lens sample, fitting galaxies with $M_r > -21$ and running the brighter lenses with the standard value of $\eta_s = 0.5$ (see lower panel of Fig. 6.32). While for the blue galaxies the scaling relation is still consistent with the previous assumptions and results ($\eta_s^{\text{blue,faint}} = 0.45^{+0.12}_{-0.10}$), the result for the red sample is surprising and irritating. For that specific sample we measure a value of $\eta_s^{\text{red,faint}} = -0.38^{+0.14}_{-0.13}$.

Thus implies an inverted scaling relation, leading to increasing galaxy radii for decreasing luminosity. Since the velocity dispersion is decreasing with decreasing luminosity this implies that the masses are only slowly decreasing with luminosity. This is in agreement with the halo mass vs. stellar mass relation from Guo *et al.* (2010) (based on abundance matching). Their fig. 2 (upper panel) shows that the halo mass decreases only slowly with stellar mass for stellar masses $\leq 10^{10} h^{-2} L_{\odot}$. To exclude that environment structures are the cause of this rise of the truncation radius with decreasing luminosity, we repeat the analyses on a more restricted lens sample, only consisting of galaxies in environments with low local density. However, this approach indeed confirms the previous results. While for bright galaxies in low density environments the observed scaling behavior is in agreement with our expectations ($\eta_s^{\text{red,bright,low}} = 0.95^{+0.34}_{-0.34}$ for red and $\eta_s^{\text{blue,bright,low}} = 0.64^{+0.50}_{-0.62}$ for blue galaxies, see upper panel of Fig. 6.33), regarding the faint lens sample this is in principle only true for blue galaxies ($\eta_s^{\text{blue,faint,low}} = 0.88^{+0.28}_{-0.19}$, see lower panel of Fig. 6.33). Also in low density environments faint red galaxies appear to scale inversely ($\eta_s^{\text{red,faint,low}} = -0.50^{+0.35}_{-0.29}$). In summary our results indicate that the M/L -ratio for red galaxies steeply decreases for increasing luminosities considering galaxies fainter than $L \sim 10^{10} h^{-1} L_{\odot}$ and then turns into a further, but shallower decrease for more massive galaxies, while for blue galaxies the M/L -ratio is approximately constant (see Fig. 6.34).

Concentration-Mass-Relation

A further scaling relation of interest is represented by the scaling of the concentration parameter c of the NFW profile with luminosity and consequently with mass. In order to constrain the scaling behavior we fix the expected virial radius r_{200} and its scaling ($\eta_{r_{200}} = 0.4$ for the combined and $\eta_{r_{200}} = 1/3$ for the separate SED samples) and perform an NFW maximum likelihood analysis, fitting the scaling exponent η_c of the concentration parameter with luminosity. For the combined lens sample we obtain a value of $\eta_c = -0.07^{+0.11}_{-0.11}$. This is also shown in Fig. 6.35 (black contours). Assuming a scaling of the mass-to-light ratio according to $M_{200}/L \propto L^{0.2}$ this leads to a scaling relation between concentration and mass of $c \propto M_{200}^{0.06^{+0.09}_{-0.09}}$, for $M_{200}/L \propto L^{0.12}$ this leads to $c \propto M_{200}^{0.06^{+0.10}_{-0.10}}$, both being consistent with the results of Duffy *et al.* (2008) ($\eta_{c,\text{Duffy}} = 0.084 \pm 0.06$). Further we also investigate possible differences in the scaling behavior of the concentration parameter for the different SED types. The analysis of the red lens sample results in a very similar, but slightly shallower scaling relation of $c \propto L^{-0.04^{+0.10}_{-0.13}}$. In contrast, the scaling relation for the blue lens sample turns out to be steeper, although with only marginal significance, following a relation of $c \propto L^{-0.34^{+0.24}_{-0.26}}$. The concentration-luminosity relation can be easily translated into a concentration-mass relation, assuming a certain M_{200}/L -ratio, but as we see the difference between $M_{200}/L \propto L^{0.2}$ and $M_{200}/L \propto L^{0.12}$ hardly changes the result. If we apply the scaling relations for the SED types independently, we see that the almost identical concentrations of red and blue galaxies cannot be generalized, but only happen to be valid for luminosities close to L^* . While due to the very shallow scaling relation for red galaxies the concentration remains approximately constant with mass, the concentration parameter for massive blue galaxies is rather low, strongly increasing with decreasing mass. Therefore in the massive regime red galaxies exceed their blue counterparts in concentration, while the relation turns into its opposite when moving to the low mass regime. In Fig. 6.37 the concentration parameter is illustrated as a function of the virial mass.

The measurements of the virial radii r_{200} in the $\Delta\Sigma$ analyses showed indications for a modified scaling behavior of the M/L -ratio (see Section 6.4.3) and thus the r_{200} or of the concentration

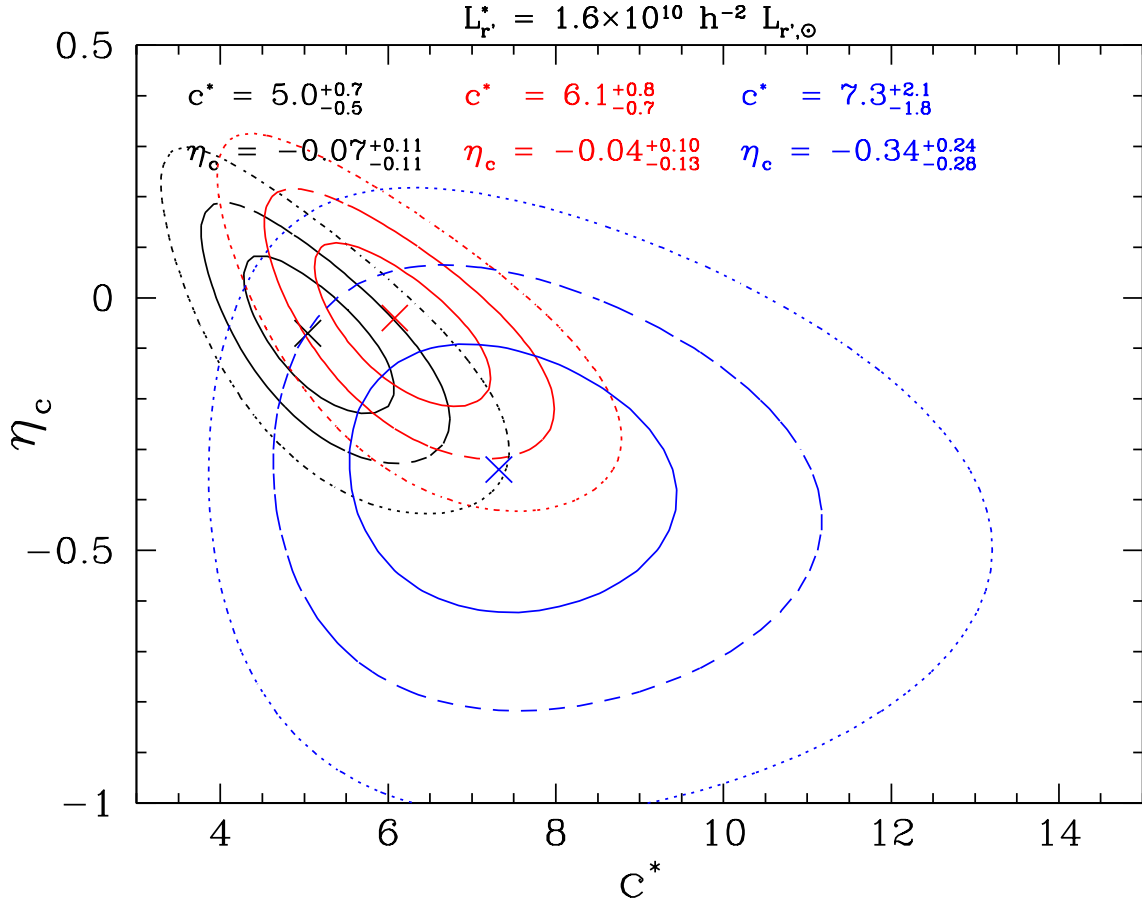


Fig. 6.35: Maximum likelihood result for the concentration-luminosity relation, for combined (in black), red (in red) and blue galaxies (in blue) separately. The solid, the long-dashed and the short-dashed contours show the 68.3%, the 95.4% and the 99.7% confidence levels. The scaling for the red lens galaxies is very flat, being quite similar to the combined sample, leading to an almost constant concentration parameter over the investigated luminosity range. In contrast, the scaling relation for the blue lens sample is steeper, although with only marginal significance.

parameter, when considering galaxies at the faint luminosity end of our lens sample. First we investigate the possibility, that the M_{200}/L -scaling does not change. We therefore run NFW maximum likelihood analyses, allowing independent concentration parameter scaling relations for galaxies brighter and fainter than $L = 10^{10} h^{-2} L_{\odot}$. Indeed the best-fitting values for both luminosity regimes clearly differ as can be seen in the upper panel of Fig. 6.36. Looking at the brighter galaxy samples, we find values of η_c which are similar ($\eta_c^{\text{red,bright}} = 0.02^{+0.06}_{-0.06}$ for red galaxies and $\eta_c^{\text{blue,bright}} = -0.28^{+0.15}_{-0.17}$) to those obtained in the analysis without discrimination in luminosity. This picture dramatically changes when considering the faint lens fraction. Taking the large uncertainties into account the results only are mildly inconsistent with the previous ones. However, considering the absolute values ($\eta_c^{\text{red,faint}} = -1.52^{+1.12}_{-1.36}$ for red galaxies and $\eta_c^{\text{blue,faint}} = -1.14^{+0.99}_{-1.56}$), there is a strong indication for a steeper scaling relation for the concentration parameter c when investigating luminosities fainter than $10^{10} h^{-2} L_{\odot}$. In order to assure that we do not observe an environmental or multi-deflection effect we repeat the maximum likelihood analysis with a low density environment

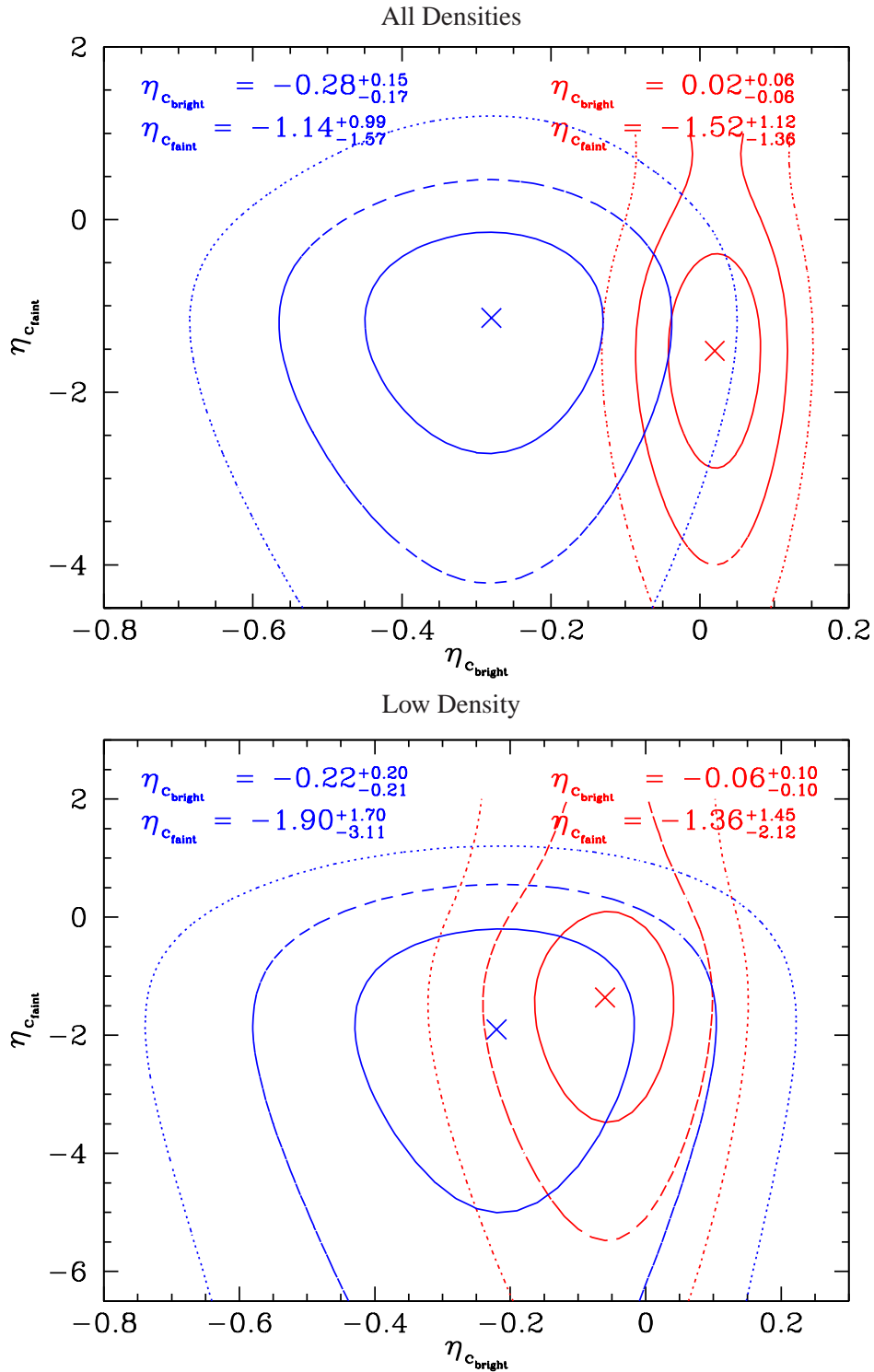


Fig. 6.36: Concentration-luminosity-relation for bright (x-axis) and faint galaxies (y-axis) separately, distinguishing between galaxies in all environments (upper panels) and galaxies in low density environment (lower panel). The solid, the long-dashed and the short-dashed contours show the 68.3%, the 95.4% and the 99.7% confidence levels. The blue contours show blue, the red contours red galaxies. The scaling parameters η_c for the bright sample are very similar to the obtained values with differentiation in luminosity (see also Fig. 6.35). However, the analysis of the faint fraction of our lens sample indicates a much steeper concentration-luminosity-relation ($\eta_c < -1$).

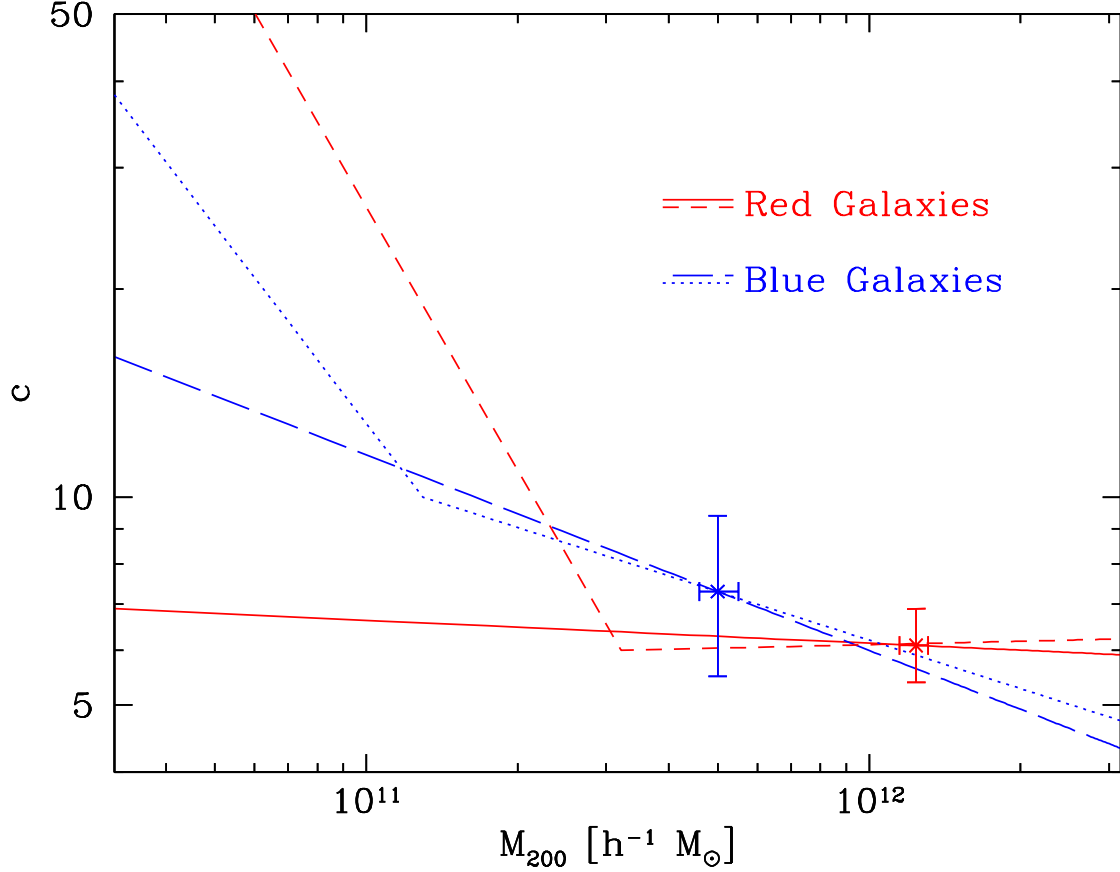


Fig. 6.37: Scaling relations for the concentration parameter with M_{200} , assuming a scaling of M_{200} with $L^{1.2}$. The red solid line and the blue long-dashed line show the best-fitting scaling relation assuming a universal slope for all luminosities or masses, respectively (see Fig. 6.35). In this case at high masses red galaxies are more concentrated than blue galaxies of the same mass, while for decreasing masses the opposite is true. The red short-dashed line and the blue dotted line show the scaling behavior for the concentration parameter, assuming a significant increase in steepness of the concentration-luminosity-relation at $L = 10^{10} h^{-1} L_{\odot}$ (see Fig. 6.36).

lens sample. As the lower panel of Fig. 6.36 shows, with values of $\eta_c^{\text{red,bright,low}} = -0.06^{+0.10}_{-0.11}$ and $\eta_c^{\text{red,faint,low}} = -1.36^{+1.45}_{-2.12}$ for brighter and fainter red galaxies and $\eta_c^{\text{blue,bright,low}} = -0.22^{+0.20}_{-0.21}$ and $\eta_c^{\text{blue,faint,low}} = -1.90^{+1.70}_{-3.11}$ for brighter and fainter blue galaxies, despite the excessive uncertainties, the analysis confirms the previous result.

We also investigate the possibility that, due to a change in the M_{200}/L -scaling, the r_{200} scaling shows a ‘broken’ power law behavior with different slopes for luminosities brighter and fainter than $L_{\nu} = 10^{10} h^{-2} L_{\odot}$. For this we repeat the maximum likelihood analysis, assuming that the concentration-mass relation of Duffy *et al.* (2008) holds, and fit r_{200} and its scaling with luminosity for red and blue galaxies brighter and fainter than $M_{\nu} = 20.5$ separately. The scaling of the r_{200} indeed appears to change with luminosity. This change is stronger for red than for blue galaxies, while for blue galaxies it is only modest. We cross-check the results repeating the same likelihood

analysis for the lens sample in low density environment, obtaining the same result.

6.4.4 Comparison of the Results

Parker *et al.* (2007) analyzed an area of 22 deg^2 CFHTLS i' -band, but without photometric redshift estimation, using the i' -band magnitude for lens and source selection. All galaxies with $19 < i' < 22$ were defined as lenses and all galaxies with $22.5 < i' < 24$ were defined as sources, applying a photometric distribution based on Brown *et al.* (2003) from the COMBO-17 for the lens sample and Ilbert *et al.* (2006) from the CFHTLS-Deep for the source sample. Assuming a truncation radius of $185 \pm 30 h^{-1}$ kpc based on Hoekstra *et al.* (2004), they found for an $L_{r'}^* = 1.6 \times 10^{10} h^{-2} L_{r',\odot}$ -galaxy a velocity dispersion of $\sigma^* = 137 \pm 11 \text{ km s}^{-1}$ and a rest-frame mass-to-light ratio of $M^*/L_{r'}^* = 173 \pm 34 h M_{\odot}/L_{\odot}$. Comparing these values with our results of $\sigma^* = 131_{-2}^{+2} \text{ km s}^{-1}$ and $M_{\text{total,BBS}}^*/L_{r'}^* = 178_{-19}^{+22} M_{\odot}/L_{\odot}$, we observe good agreement. Analyzing RCS2-data, based on CHFT- r' -band photometry and mainly consisting of red galaxies, van Uitert *et al.* (2011) found for a $L_R^* = 10^{10} h^{-1} L_{R,\odot}$ -galaxy, including luminosity evolution, a virial mass of $M_{\text{vir}} = 7.2 \pm 1.5 \times 10^{11} h^{-1} M_{\odot}$. Converting our result for the M_{200} from the red lenses NFW maximum likelihood analysis, we obtain a value of $M_{\text{vir}} = 7.3 \pm 0.5 \times 10^{11} h^{-1} M_{\odot}$, in good agreement with van Uitert *et al.* (2011).

6.4.5 Consistency of Maximum Likelihood and $\Delta\Sigma$ -Fit Results

Comparing our investigations of the excess surface mass density $\Delta\Sigma$ in Section 6.2.2 with those from the maximum likelihood in Section 6.4 analyses, we obtain following results. Assuming an SIS or BBS profile, respectively, we derived values for velocity dispersion of $\sigma^* = 135 \pm 2 \text{ km s}^{-1}$ for the combined lens sample, $\sigma_{\text{red}}^* = 162 \pm 2 \text{ km s}^{-1}$ for red galaxies and $\sigma_{\text{blue}}^* = 115 \pm 3 \text{ km s}^{-1}$ for blue galaxies from $\Delta\Sigma$, while the maximum likelihood analyses delivered values of $\sigma^* = 131_{-2}^{+2} \text{ km s}^{-1}$ for the combined galaxy sample, $\sigma_{\text{red}}^* = 149_{-3}^{+3} \text{ km s}^{-1}$ for red galaxies and $\sigma_{\text{blue}}^* = 118_{-5}^{+4} \text{ km s}^{-1}$ for blue galaxies. Except for the red lens sample, the results are thus in good agreement. The same conclusions hold when including the assumption of luminosity evolution with redshift according to $L \propto (1+z)$. In this case we measured velocity dispersions of $\sigma^* = 150 \pm 2 \text{ km s}^{-1}$ for the combined lens samples, $\sigma_{\text{red}}^* = 173 \pm 2 \text{ km s}^{-1}$ for red galaxies and $\sigma_{\text{blue}}^* = 123 \pm 3 \text{ km s}^{-1}$ for blue galaxies from $\Delta\Sigma$ compared to values of $\sigma^* = 144_{-2}^{+3} \text{ km s}^{-1}$ for the combined sample, $\sigma_{\text{red}}^* = 161_{-3}^{+3} \text{ km s}^{-1}$ for the red galaxy sample and $\sigma_{\text{blue}}^* = 123_{-3}^{+3} \text{ km s}^{-1}$ for the blue galaxy sample from the maximum likelihood analyses.

However the situation looks different when investigating the halo parameters based on an NFW profile, the virial radius r_{200}^* and the virial mass M_{200} . While the maximum likelihood analyses yield values of $r_{200}^* = 133_{-2}^{+3} h^{-1} \text{ kpc}$ for the combined lens sample, $r_{200}^{*,\text{red}} = 160_{-4}^{+3} h^{-1} \text{ kpc}$ for the red lens sample and $r_{200}^{*,\text{blue}} = 115_{-5}^{+4} h^{-1} \text{ kpc}$ for the blue lens sample, except for blue galaxies the investigation of $\Delta\Sigma$ delivers systematically higher results, as in that case we obtain values of $r_{200}^* = 146 \pm 2 h^{-1} \text{ kpc}$ for the combined galaxy sample, $r_{200}^{*,\text{red}} = 177 \pm 3 h^{-1} \text{ kpc}$ for red galaxies and $r_{200}^{*,\text{blue}} = 120 \pm 2 h^{-1} \text{ kpc}$ for the blue galaxies.

In order to understand the systematic difference of $\sim 10\%$ in the measurements, we additionally run simulations (BBS and NFW), continuously restricting the lens sample. First only considering lenses with absolute luminosities of $M_{r'} < -21$ and in the following only taking lenses into account with $M_{r'} < -23$, we further restrict the latter lens sample to those galaxies populating low density environments by only considering galaxies with less than five neighbors within a projected distance

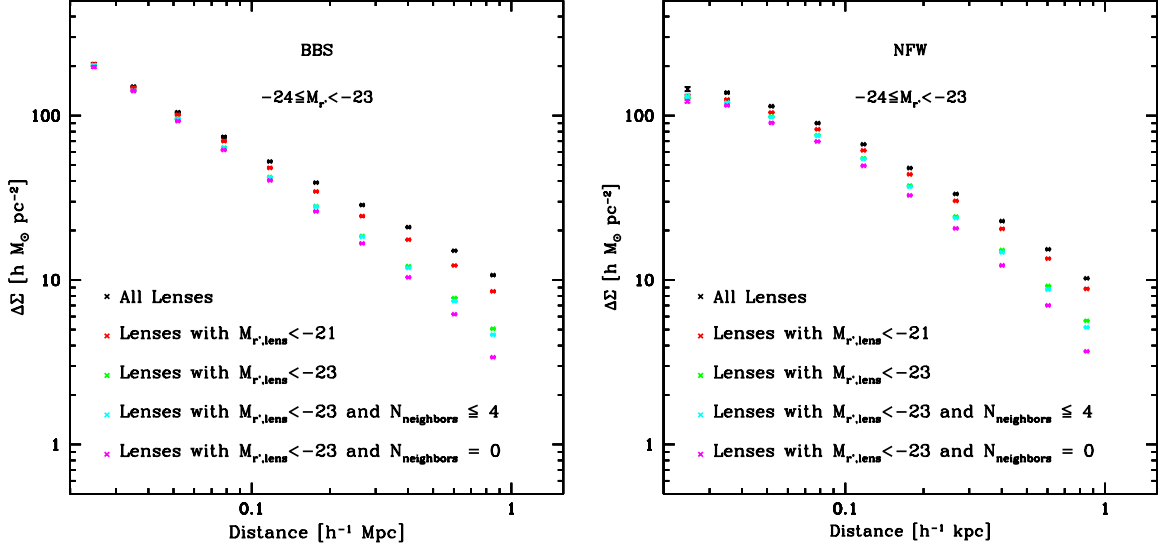


Fig. 6.38: Excess surface mass density $\Delta\Sigma$ extracted from lens galaxies with $-23 < M_r \leq -24$ calculated from simulated lens signals. The black dots show simulations including lenses with all magnitude, red dots only include lenses with $M_r \leq -21$, green dots only include lenses with $M_r < -23$, cyan dots additionally restrict the lens sample to maximum neighbor number of 4 galaxies within a projected distance of $720 h^{-1}$ kpc and finally the magenta plots only show lenses these lenses without any neighbor within this projected distance. We see that in the case of a BBS profile (left panel) multiple deflection affect the signal amplitude only on larger scales, while assuming an NFW profile (right panel) the signal amplitude already at very low scale is biased high about 20%.

of $720 h^{-1}$ kpc and finally only isolated galaxies without any other galaxy within the same projected distance. In this way we incrementally reduce the influence of multiple deflections. After this the obtained artificial shape catalogs were used to measure the predicted profiles of the excess surface mass density for all cases. For this investigation we focus in particular on the analysis of lenses within a magnitude range of $-23 > M_r \geq -24$. As we can see in Fig. 6.38, independent of the considered galaxy halo profile, on large scales multiple deflections significantly boost the amplitude of the measured $\Delta\Sigma$ profile, as expected, due to group/cluster halo and secondary nearby galaxy halos. However, the result is more surprising when looking at small projected separations. While the amplitude of the BBS $\Delta\Sigma$ remains almost undisturbed by multiple deflection on small scales, considering an NFW profile the opposite is the case. In fact, the amplitude of $\Delta\Sigma$ is increased by $\sim 20\%$ in comparison to the undisturbed single galaxy halo. This can be understood, if we take into account that the BBS and NFW slopes behave differently as a function of luminosity. The NFW profile slopes become significantly steeper for scales larger than the scale radius r_s . As the scale radius changes as a function of luminosity, so does the profile slope, i.e., we start summing up profile contributions with different slopes. In contrast, the slopes of isothermal profiles do not change with luminosity. This implies that we can measure unbiased values for the velocity dispersion σ from the $\Delta\Sigma$ profile, while NFW based parameters, as the virial radius r_{200} , systematically might be biased high, when not explicitly considering a galaxy lens sample residing in low density environments.

6.5 Comparison of Observed $\Delta\Sigma$ -Profiles to Expectations from Lensing Simulations

6.5.1 Combined, Red and Blue Lens Samples in Average Environment

In order to check our results for consistency in theoretical aspects, we compare the excess surface mass density with the predictions of the 3D-LOS-projected lensing signal simulations based on BBS and NFW profiles as described in Section 3.4.4. We do the complete analysis the same way as for the observed data, feeding the synthetic catalogs with original positions, luminosities and photometric redshifts, but with the analytically simulated, computed shear values γ . However, the application of single-power law profiles for BBS and NFW profiles leads to underestimated amplitudes of the simulated excess surface mass densities for the fainter luminosity bins. Therefore in the simulations we assume a constant truncation radius for red galaxies fainter than $M_r = -21$ and change the r_{200} -scaling of the NFW-profile similar to the results from Section 6.4.3 to a double-power law fit ($\eta_{r_{200},\text{bright}}^{\text{red}} = \eta_{r_{200},\text{bright}}^{\text{blue}} = 1/3$, $\eta_{r_{200},\text{faint}}^{\text{red}} = 0$ and $\eta_{r_{200},\text{faint}}^{\text{blue}} = 0.21$) for galaxies brighter and fainter than $L_{r'} = 10^{10} h^{-2} L_{\odot}$. The results are shown in Fig. 6.39. As we can see the measured $\Delta\Sigma$ profiles of the observed data in general agree quite well with the predictions of the simulations, especially for the brighter luminosity bins. For the faintest luminosity bins, applying single-power law fits, we find that the profile only agreed well on larger scales, showing higher values for small separations than the simulations suggest. Especially the NFW predictions, being even lower than the BBS ones, underestimate the observations for low-mass lenses. This might indicate that the assumed scaling relations for the profile parameters are not perfectly fine-tuned or that the scaling relations follow a modified law for less massive galaxies. However, applying double-power-law fits, the simulated profiles also agree well for the fainter luminosity bins. In order to visually disentangle the contribution of the considered ‘central’ lens and additional halos from the neighborhood to the lensing signal, we calculate the theoretical $\Delta\Sigma$ profile for a single galaxy halo (BBS and NFW, respectively), scaled to the effective luminosity for every single bin, add them in Fig. 6.39 and compare them to the observed signal. For luminosities $M_r \leq -20$ we find that the excess surface mass density is dominated by the central lenses out to distances of $R \sim 100 h^{-1}$ kpc. On larger scales the influence of the secondary galaxy halos begins to rise and the halo profile turns into a cumulative profile, composed of central halo, neighboring halos and group or cluster halo. For increasing luminosity the impact of the neighboring galaxy halos shifts to larger distances and the difference between single and cumulative halo profile continuously diminishes. In general, in the inner profile parts the BBS profiles appear to fit the observed surface mass profiles better than the NFW profiles, especially considering the inner parts of the galaxy halos for small projected separations between lens and source. A possible explanation is provided by the consideration of the baryonic matter in the galaxies in addition to the NFW dark matter halo, giving a boost in the galaxy core matter distribution.

We extend our analysis, discriminating red and blue lenses, now also investigating the contribution of both galaxy types to the simulated surface excess mass density. For this purpose we further append the predictions of the BBS and NFW profiles for both lens samples separately. We already noticed that for the combined galaxy type lens sample observation and simulation agree well. This conclusion also holds for blue and bright red lens galaxies separately. However, we notice a growing difference between data and simulation with decreasing luminosity for the red lens sample. Taking into account that faint red galaxies, in contrast to blue galaxies, most likely have a preference to

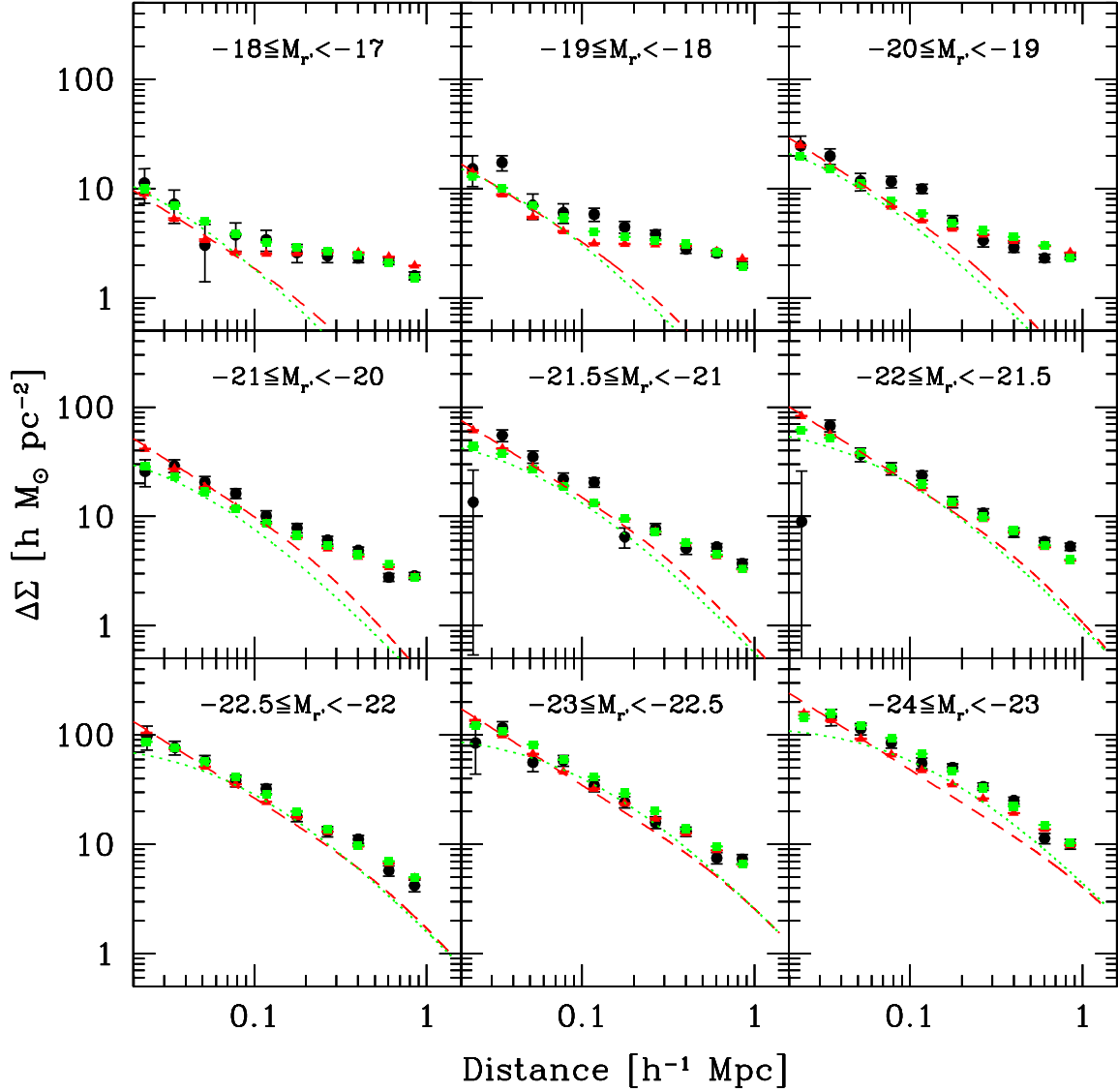


Fig. 6.39: Excess surface mass density $\Delta\Sigma$ for all lenses in luminosity bins. We compare the observed surface mass density profiles (black circles) to the predictions of the double-power law simulations, assuming BBS (red triangles) and NFW galaxy halos (green squares). The profiles in general agree quite well. In order to disentangle the central halo from the cumulative halo profile we add BBS (red dashed line) and NFW (green dotted line) analytic single halos for every single luminosity bin. The profile on large scales is higher than expected for an isolated galaxy in the fainter luminosity bins, where the central halo only dominates out to scales of $\sim 100 h^{-1}$ kpc before turning into the cumulative profile. The difference between central and cumulative halo strongly decreases with increasing luminosity.

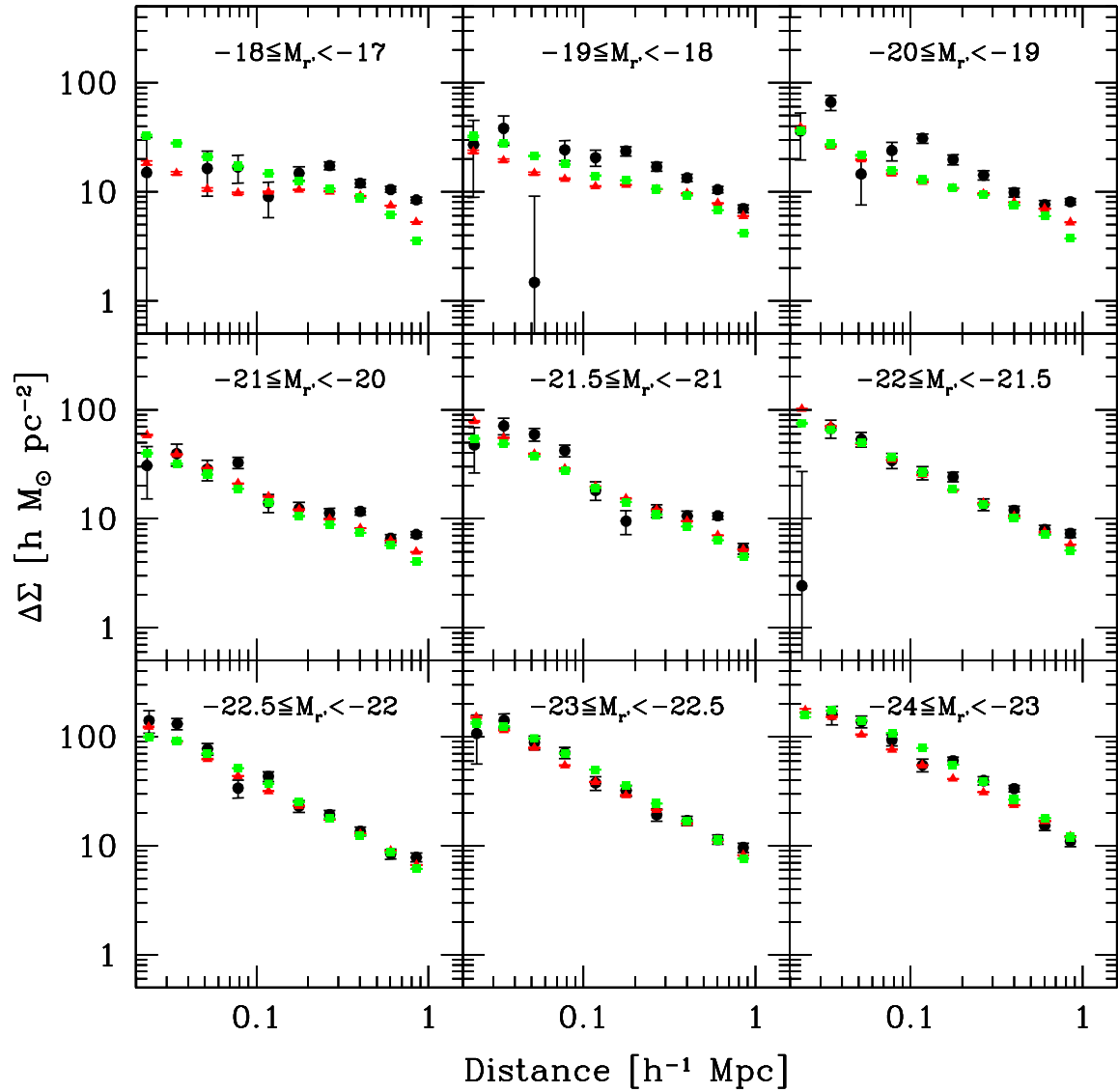


Fig. 6.40: Excess surface mass density for the red lens sample. Black circles are the observed data points, red triangles come from the BBS and green squares from the NFW double-power law simulations. Simulations and observation agree well for brighter lenses (middle and lower row). For fainter elliptical galaxies the simulations underestimate the observed signal, BBS more strongly than NFW.

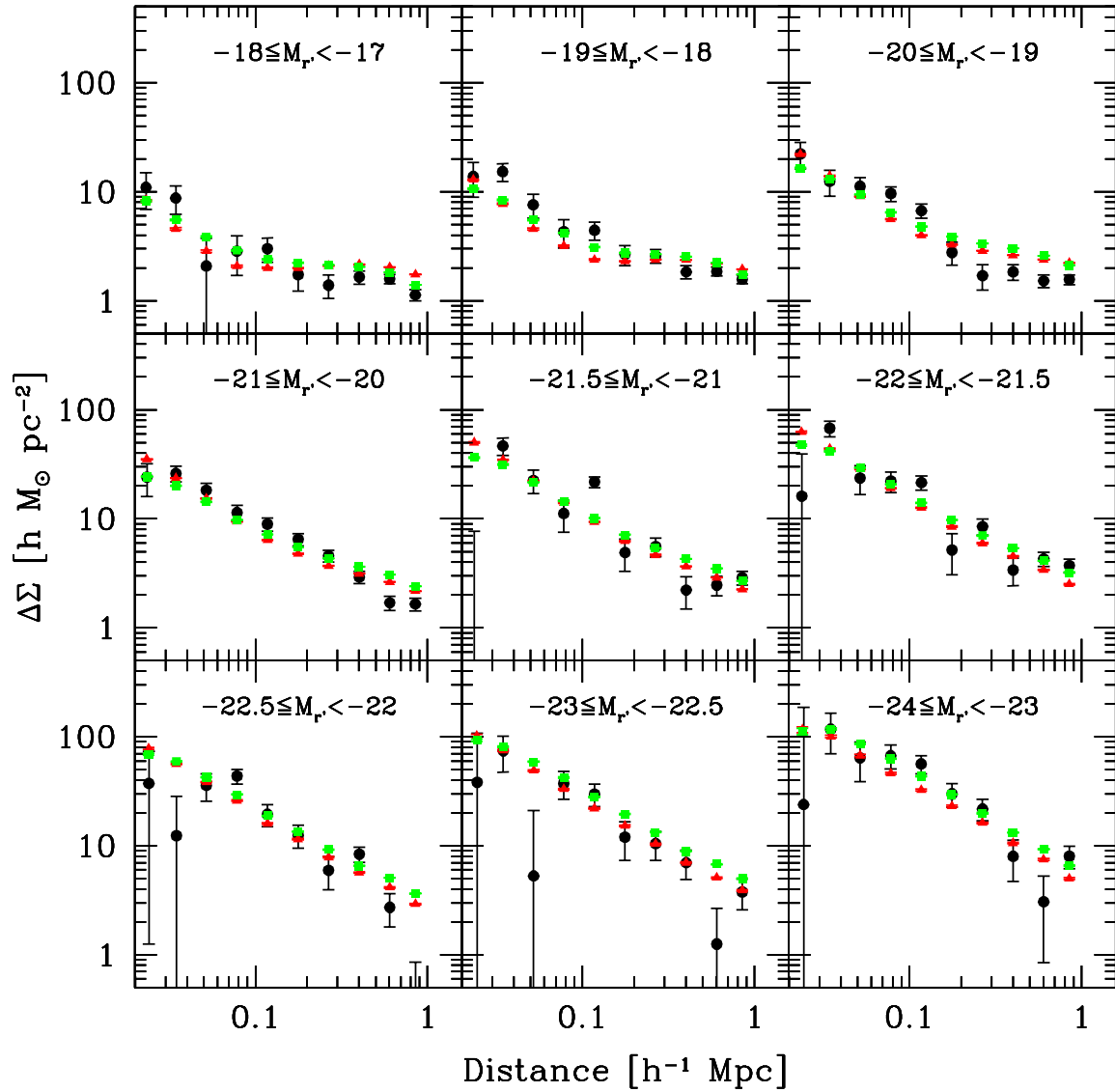


Fig. 6.41: Excess surface mass density for the blue lens sample. Black circles are the observed data points, red triangles come from the BBS and green squares from the NFW double-power law simulations. The simulations agree well with the observed mass profiles, especially in the bright lens regime (middle and lower row). For the faintest lenses the simulation only slightly underestimate the observed mass profile, however the difference between observation and simulation is clearly smaller than for red lenses.

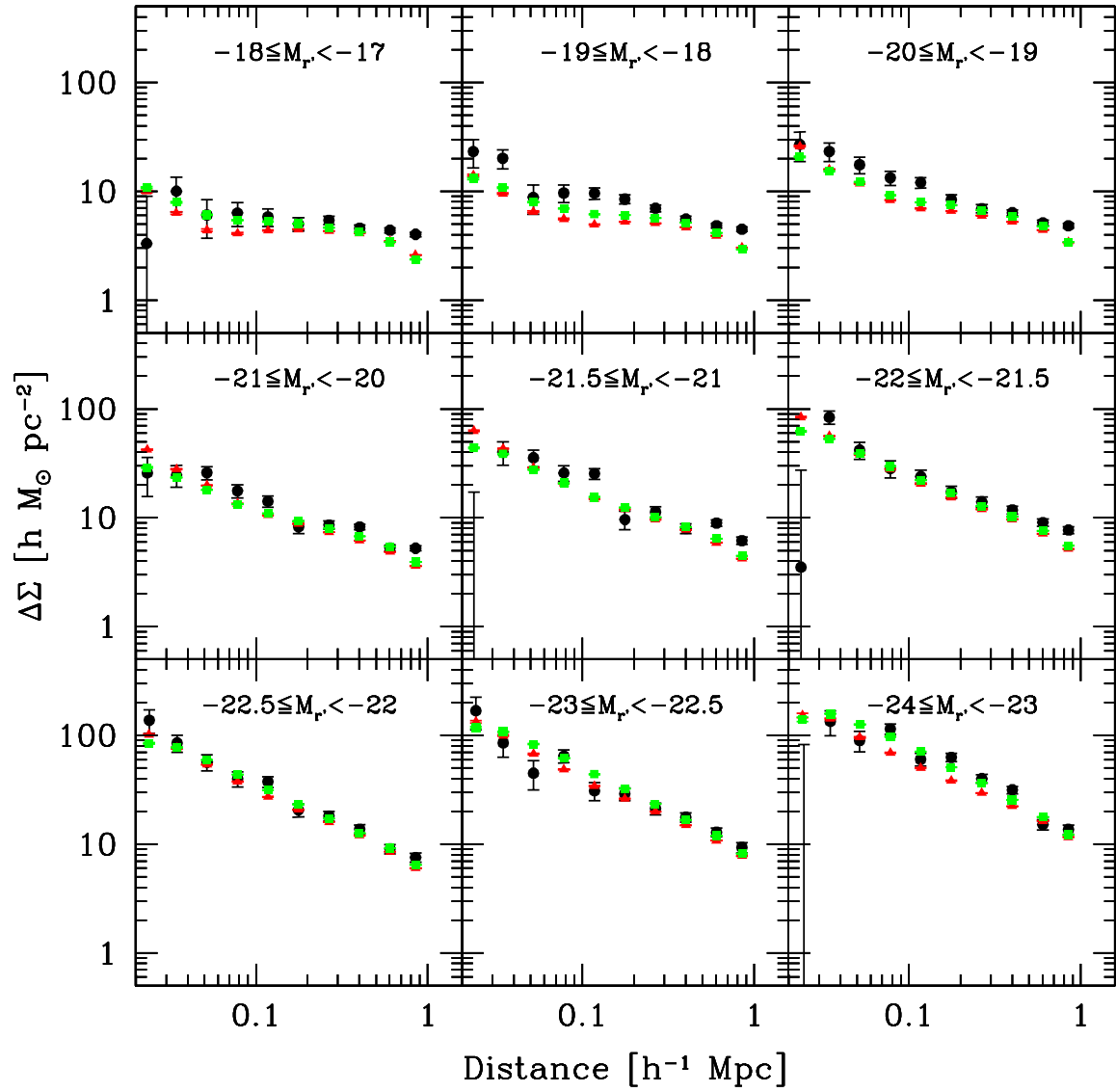


Fig. 6.42: Excess surface mass density for the lens sample in high density environments. Black circles are the observed data points, red triangles come from the BBS and green squares from the NFW double-power law simulations. Observations and simulations agree very well for all luminosities.

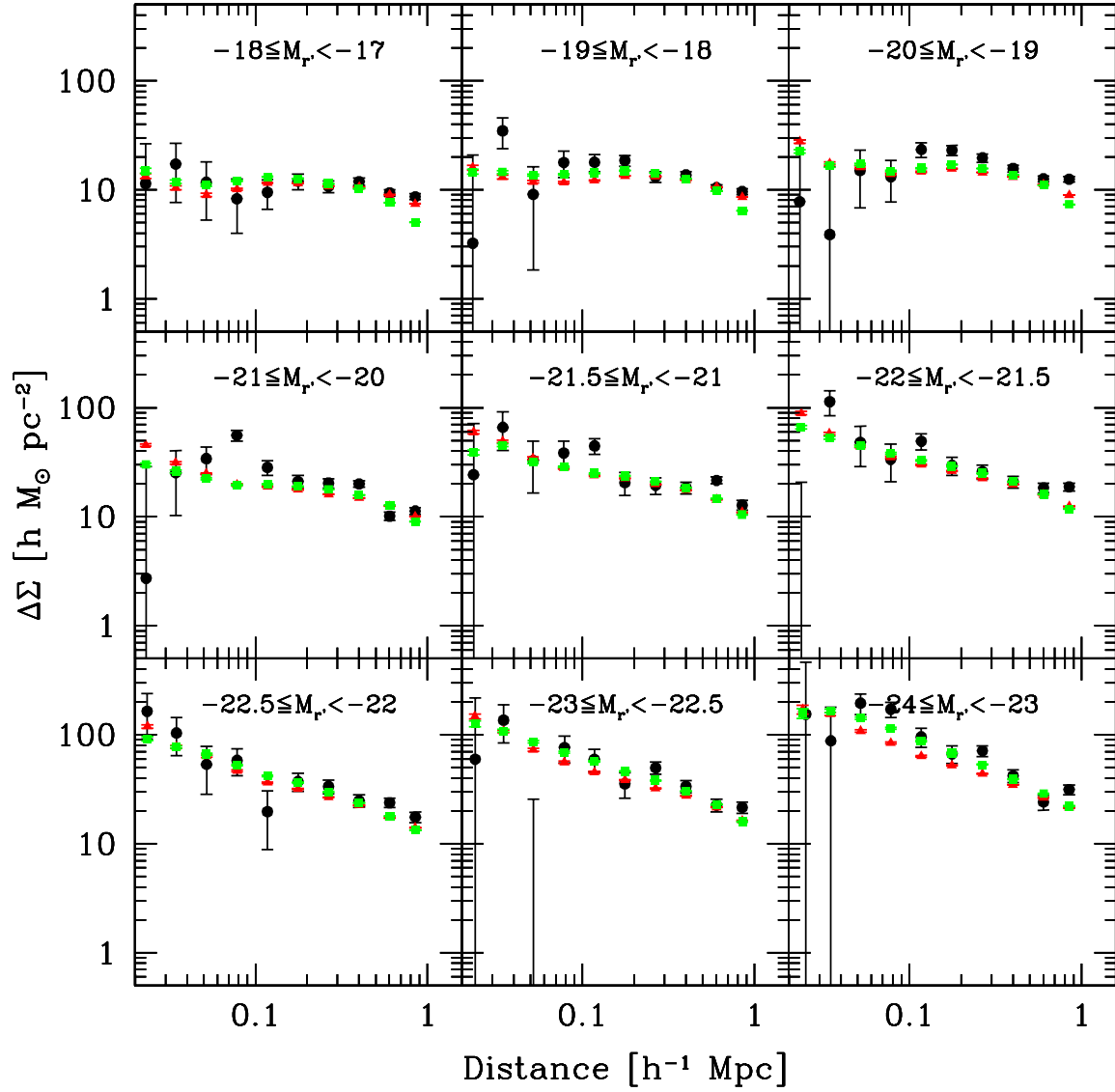


Fig. 6.43: Excess surface mass density for the lens sample in very high density environments. Black circles are the observed data points, red triangles come from the BBS and green squares from the NFW double-power law simulations. Observations and simulations agree very well for all luminosities.

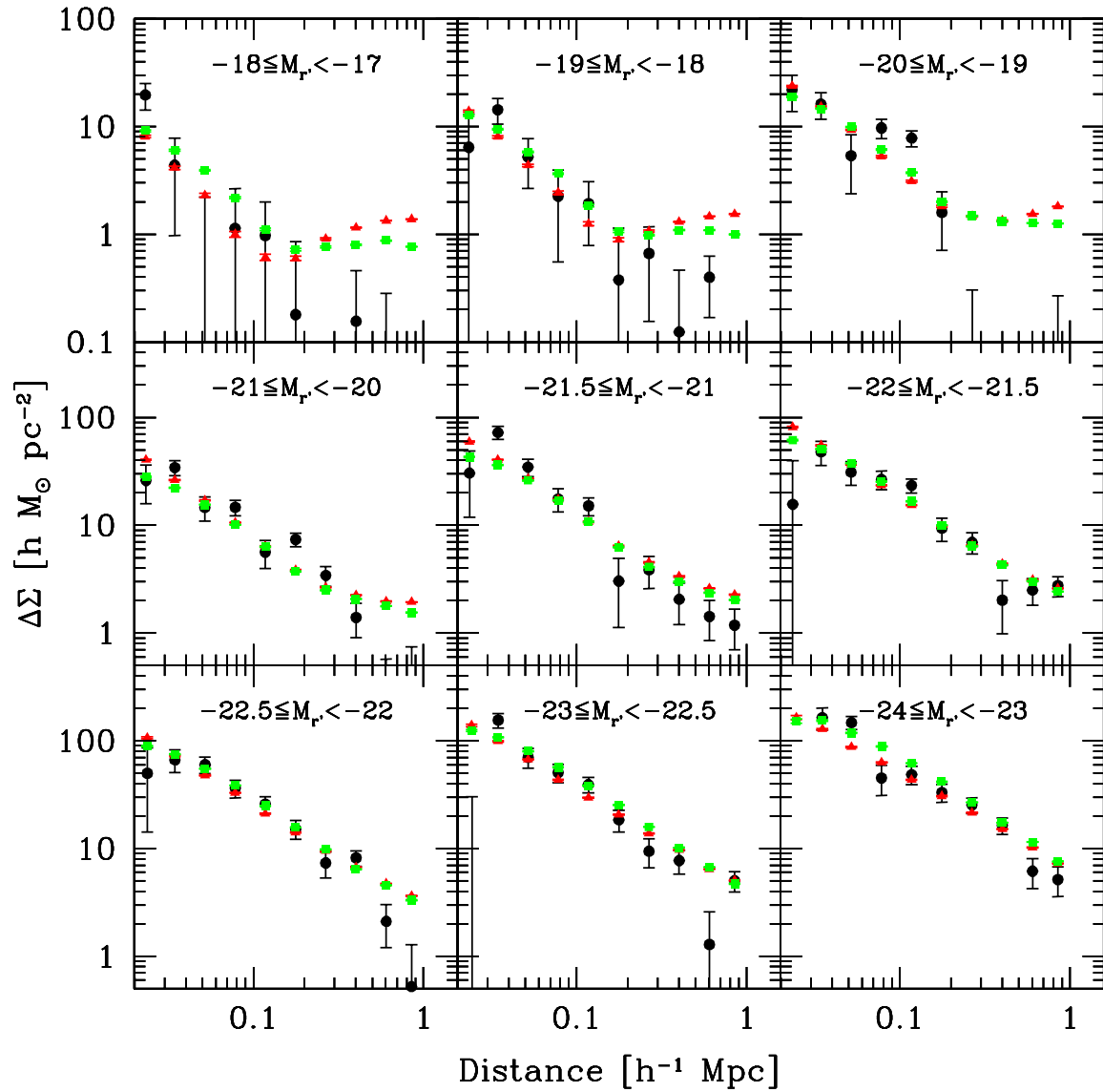


Fig. 6.44: Excess surface mass density for the lens sample in low density environments. Black circles are the observed data points, red triangles come from the BBS and green squares from the NFW double-power law simulations. The profiles are steeper than for high density environment. The observations and simulation in general agree very well.

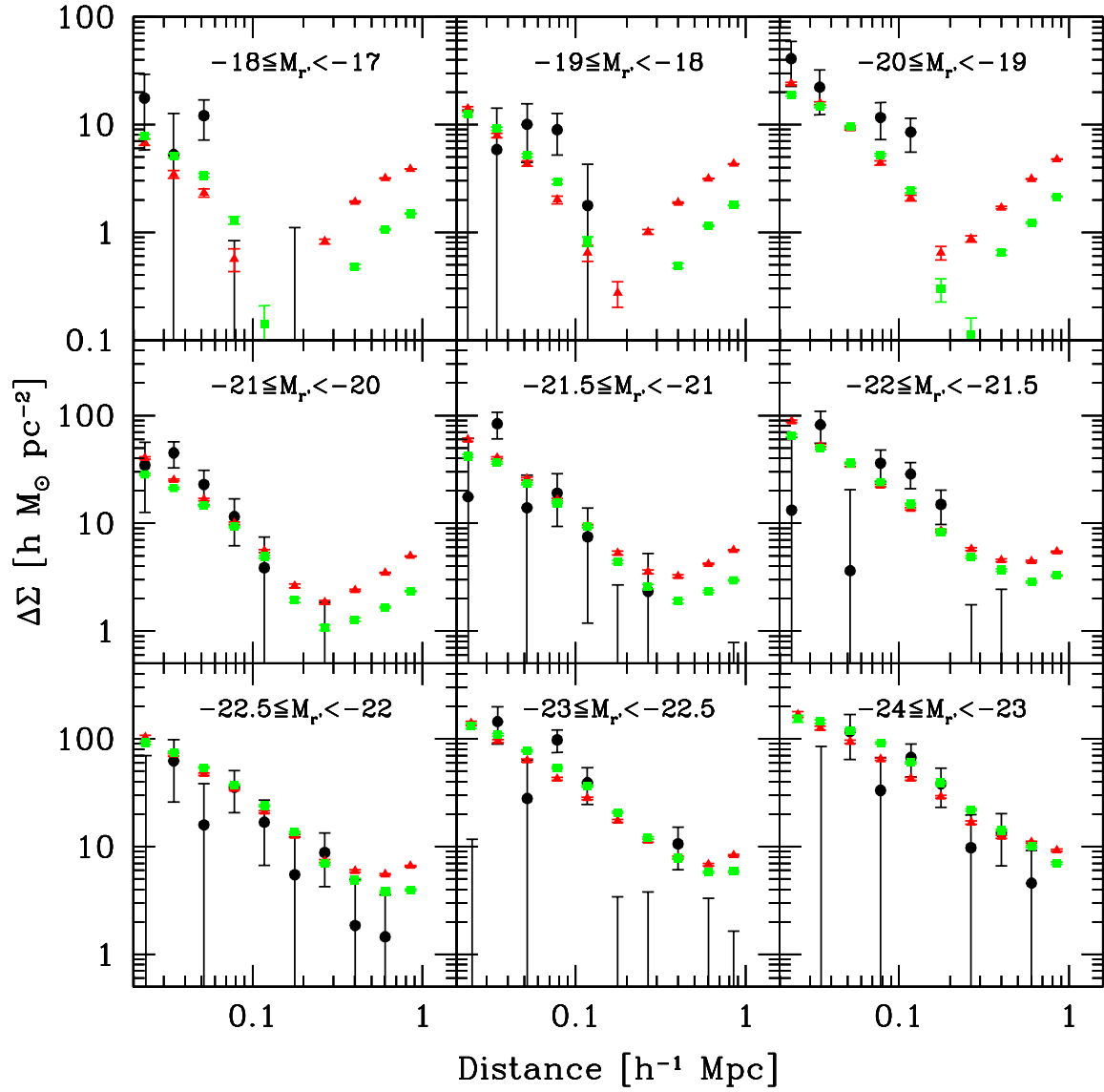


Fig. 6.45: Excess surface mass density for the lens sample in very low density environments. Black circles are the observed data points, red triangles come from the BBS and green squares from the NFW double-power law simulations. Simulation and observation agree well, yet fairly noisy.

reside in group or cluster environments, meaning environments of higher than average density, this effect becomes understandable. While for blue galaxies the assumption of the cumulative halo being the composition of many individual galaxy halos appears to be sufficiently accurate, apparently the observed red galaxy mass profiles include an additional contribution of the parent group or cluster halo. Another explanation is provided by the assumption that the assumed scaling relations reasonably describe the behavior of blue galaxies, but the scaling of red galaxies starts to deviate for lower masses.

6.5.2 Combined Lens Sample in Over- and Underdense Environments

In order to gain a better understanding of galaxy surface mass profiles as a function of environment density, we further measure the excess surface mass density $\Delta\Sigma$ for the combined lens sample in environments of different density (as defined in Section 5.5.2). We again directly compare the observational data with predictions of the simulations based on BBS and NFW profiles. Considering the galaxy sample composed of galaxies living in high density environments (see Fig. 6.42), we see that simulations and observations mostly agree fairly well. In general, the profiles are the flatter, the denser the environment is (see Figs. 6.42 and 6.43 for galaxies in high and very high density environments). This is evident as on larger scales the signal is dominated by neighboring galaxies (also from brighter luminosity bins) and the environment, and the denser the environment the higher the total mass and thus the profile in the outskirts is.

Considering lenses in lower than average density environments, we have to note that the decreasing signal-to-noise ratio makes the analysis more difficult. This especially becomes relevant when looking at larger scales around faint galaxies. In general the $\Delta\Sigma$ profiles are steeper than for galaxies in denser environments. The observed and simulated $\Delta\Sigma$ agree well with each other as can be seen Fig. 6.44. For larger separations and less massive lenses the simulations now start to overestimate the observed data. However, due to the low signal-to-noise (the lens density is low by definition and thus also affects the lens-source pair numbers) the exact value for $\Delta\Sigma$ in these regions is very hard to tell. It becomes even more difficult for very low environment density galaxy samples (see Fig. 6.45). While for brighter bins observations and simulations still agree well, for the faintest bins the observational data are noise-dominated, making it practically impossible to make a statement. However, the results are not inconsistent on scales $< 200 h^{-1}$ kpc.

Summarizing the comparisons between observations and simulations in environments of different densities, we see fairly good agreement between expectation and observation. Assuming that the mass-to-light ratio increases for galaxies fainter than $L_{\nu} = 10^{10} h^{-2} L_{\odot}$, the analyzed system appears to be well understood. We find that the profile slopes of the excess surface mass density $\Delta\Sigma$ increase with decreasing environment density and with increasing central lens luminosity. The first effect is caused by the increased excess surface mass density at larger scales due to the higher total mass in comparison to the central galaxy mass. The second effect is caused by the increased central galaxy mass in comparison to the total mass of the environment, thus down-weighting the environmental influence and acting in the opposite direction. In general, both BBS and NFW profiles almost equally well describe the observed galaxy halo profiles, which makes it difficult to decide, which profile the actual dark matter halos follow. Only in the fainter bins the BBS and NFW signal start to differ, due to differently modeled scaling relations for galaxies fainter than $10^{10} h^{-2} L_{\odot}$.

Chapter 7

Summary and Conclusions

We presented a GGL analysis based on 89 deg² multi-color data ($u^*g'r'i'z'$) obtained in the CFHT Legacy Survey Wide (CFHTLS-Wide), carried out with the Canada-France-Hawaii Telescope (CFHT) in Hawaii.

Based on the downloaded and subsequently reduced imaging data (including creation of science and weight frames and image masks to indicate photometrically corrupted or contaminated photometric image areas), we adapted the PSF properties for all bands of each pointing by applying a global convolution with a carefully selected Gaussian kernel, thus matching the PSF patterns in order to ensure meaningful galaxy colors. We subsequently used these PSF-matched frames to create multi-color catalogs for all 124 pointings, containing the positions and PSF-corrected fluxes and magnitudes for the $u^*g'r'i'z'$ photometry, using the `SExtractor` software with a detection threshold of 2σ above the background on at least four contiguous pixels. These multi-color catalogs represent the basis for the calculation and estimation of accurate photometric redshifts, required for a precise GGL analysis. We applied a two-step calibration procedure for the photometric zeropoint and offset determination. In the first step we adjusted the zeropoint offset for the detection band (in all cases chosen to be the i' -band, being the deepest exposure), by determining the galactic extinction from the Schlegel maps and applying the corresponding extinction value, thus dereddening the observed i' -band magnitudes and fluxes. The stellar zeropoint calibration of the remaining photometric images (u^* -, g' -, r' - and z' -band) is performed by comparison with the stellar colors predicted by the Pickles star library (Pickles 1998), adjusting the offsets of the u^* -, g' -, r' - and z' -band in such a way that the observed stellar colors from the measured fluxes in the multi-color catalogs correspond to the predicted ones. This step homogenizes all investigated CFHTLS pointings in terms of zeropoints and already significantly improves the accuracy of the estimated photometric redshifts, both in terms of rms and catastrophic outlier rate. In the second step we improve the accuracy of the photometric redshift estimation by applying a further zeropoint calibration based on the comparison with spectroscopic redshifts, obtained from the VVDS-Deep (W1), VVDS-F22 (W4), the DEEP2-survey (W3) and additionally obtained spectra in the W2. We derived the spectroscopic zeropoint offsets on all spectroscopically covered pointings separately and calculated the median values of all pointings within one large tile (i.e. W1, W2, W3, W4) in order to apply the median values to spectroscopically not covered pointings. In this way we obtained a photometric redshift sample consisting of in total 11 912 636 objects with a photometric redshift accuracy of $\Delta z / (1 + z_{\text{spec}}) = 0.036$ or $\sigma_{\Delta z / (1 + z_{\text{spec}})} = 0.033$ and a catastrophic outlier rate of $\eta = 2.0\%$ for objects

with magnitudes $i' \leq 22.5$, calculated with the photometric redshift code PhotoZ of Bender *et al.* (2001). As the spectroscopic limiting magnitude in the CFHTLS-Wide fields W1 and W3 allowed a further verification of objects with magnitudes of $22.5 < i' \leq 24$, we investigated the origin of the redshift accuracy deterioration by comparing the accuracy with the results of the significantly deeper CFHTLS-Deep fields D1 and D3, concluding that the increasing photometric noise is the main reason for the decreasing accuracy and that a possible increase in the spectral variety of high redshift galaxies does not appear to play a significant role.

For our subsequent weak lensing analysis we extracted shape catalogs from the CFHTLS-Wide i' -band images, using the KSB-pipeline (see Kaiser *et al.* 1995 and Hoekstra *et al.* 1998). The source extraction was performed with SExtractor using a detection limit of 3σ above the background on at least four contiguous pixels. In order to correct the PSF anisotropy, on all i' -band images we selected not-saturated stars from the stellar sequences with magnitudes $18 < r' < 24$ and a minimum signal-to-noise ratio of $S/N=50$. The finally obtained corrected ellipticities from the KSB-pipeline are in the end multiplied with a shear calibration factor of $c_{\text{cal}} = 1/0.91$ in order to compensate a bias in this KSB-pipeline, discovered in the Shear TEsting Programme (STEP, see Heymans *et al.* 2006). After visual inspection we rejected 35 pointings with dissatisfactory shear correction, further excluding objects with low signal-to-ratio ($SN \leq 5$), thus obtaining a total number of 89 pointings with corrected source shape estimates consisting of a total number of 2 416 426 objects with photometric redshifts and shape estimates.

We used our photometric redshifts and our shear catalogs to perform a GGL analysis. We assigned our shear catalog objects to the background and our photometric redshift catalog objects to the foreground as for the gravitational lenses shape information is not required. We omitted lens-source pairs with high probability of significant systematic errors in angular distances and critical surface density and also pairs with low separation in redshift space due to low lensing strength and possible mismatch between foreground and background. Therefore we required for the lens sample $0.05 < z_d \leq 1$, for the source sample $0.05 < z_s \leq 2$ and for a pair assignment $z_s \geq 1.1 \cdot z_d + 0.15$. This left us with maximum lens and source samples of 4 942 433 and 1 684 290 objects, respectively.

In our weak lensing analysis we first investigated the tangential shear signal γ_t for several specific lens samples on a projected separation scale of $25 h^{-1}$ kpc to $1 h^{-1}$ Mpc. As expected we find that the lensing signal increases with rest-frame luminosity of the considered lenses. Analyzing individual SED types separately, we find that for given luminosity the mass of a red galaxy is higher than for a blue galaxy. On first view the considered tangential shear profile appears to be consistent with the prediction of a singular isothermal sphere (SIS), however this observation strongly depends on the considered lens sample, or to be more precise, on the environment the considered lens resides in. Especially the environment density leaves a significant imprint on the tangential shear signal when considering larger scales. While in low density environments on short scales the central lens is dominating and on larger scales the signal drops down to values close to zero, with increasing density the lensing signal value continuously increases, until for very high density lenses the signal approximately is a constant signal on a scale out to several hundred kpc. This perfectly confirms the results of Brainerd (2010), analyzing the impact of multiple deflections in GGL. Estimating the velocity dispersion from the γ_t -amplitude we obtain that red galaxies show values for σ exceeding the results for average galaxies with same luminosities by 25% , while σ -values for blue galaxies are

15-20% below the average.

The combination of photometric redshifts and galaxy shapes allowed us to investigate the excess surface mass density $\Delta\Sigma$, having an amplitude which does not explicitly depend on the geometrical constellation due to the angular diameter distances of lenses and sources. The comparison with the literature only shows partial consistence, especially when comparing with the results of Mandelbaum *et al.* (2006c). While the results concerning blue galaxies agree very well, we obtained profiles for $\Delta\Sigma$ for our red galaxies showing higher amplitudes for the faintest lenses and lower amplitudes for the brightest lenses. However, the later results of Mandelbaum *et al.* (2008) agree well with our analysis. Further comparing our analysis with the results of van Uitert *et al.* (2011) we find good agreement for most luminosity bins. We used the amplitudes of $\Delta\Sigma$ for several lens luminosity bins to extract scaling relations for several halo profile parameters as the velocity dispersion σ based on the SIS or BBS profile and the virial radius and mass r_{200} and M_{200} based on the NFW profile. We find, for red and blue galaxies separately, scaling relation of $\sigma^{\text{red}} \propto L^{0.23 \pm 0.03}$ and $\sigma^{\text{blue}} \propto L^{0.24 \pm 0.03}$, in good agreement with the Faber-Jackson relation ($\sigma \propto L^{0.25}$, Faber & Jackson 1976). The extraction of the scaling relation for a combined SED sample yields a steeper scaling behavior of $\sigma \propto L^{0.29 \pm 0.02}$, caused by the transition from red to blue dominated SEDs when considering decreasing luminosities. These scaling relations are also confirmed when running a corresponding maximum likelihood analysis ($\eta_{\sigma}^{\text{red}} = 0.27_{-0.02}^{+0.03}$ for red galaxies, $\eta_{\sigma}^{\text{blue}} = 0.27_{-0.04}^{+0.03}$ for blue galaxies and $\eta_{\sigma} = 0.31_{-0.03}^{+0.02}$ for the combined galaxy sample). We compared the results of our red galaxy sample to spectroscopic results for a LRG sample based on Eisenstein *et al.* (2001) and to results from Gallazzi *et al.* (2006). We observe a remarkable agreement, given the fundamentally different nature of the investigation methods. Investigating r_{200} we find $\eta_{r_{200}}^{\text{red}} = 0.33 \pm 0.04$ for red galaxies, $\eta_{r_{200}}^{\text{blue}} = 0.36 \pm 0.07$ for blue galaxies and, due to the SED transition, a steeper $\eta_{r_{200}} = 0.39 \pm 0.04$ for the combined lens sample. The corresponding measurements for M_{200} yield scaling indices of $\eta_{M_{200}}^{\text{red}} = 1.05 \pm 0.12$ for red galaxies, $\eta_{M_{200}}^{\text{blue}} = 1.14 \pm 0.20$ for blue galaxies and $\eta_{M_{200}} = 1.21 \pm 0.10$ for the combined sample. This is in good agreement with the results of Guzik & Seljak (2002) ($M \propto L_r^{1.34 \pm 0.17}$). However, we find that a single-power law only properly describes the scaling relations when excluding luminosity bins with $L < 10^{10} h^{-1} L_{\odot}$, as the amplitude in this range significantly exceeds the predictions of the power law fit. This either indicates a slower decrease in virial radius and mass (leading to an increasing mass-to-light ratio for low-mass galaxies) or a significant increase of the concentration parameter c for low-mass galaxies, thus boosting the lensing signal amplitude. Calculating the circular velocity v_{200} from r_{200} for our blue galaxy sample, we also find good agreement with the results of Reyes *et al.* (2011) and Dutton *et al.* (2010). Further our results for the red galaxy M/L -ratios agree well with the results of Mandelbaum *et al.* (2008), Dutton *et al.* (2010) and van Uitert *et al.* (2011). We measured the mass vs. stellar mass ratio for red galaxies over 2.5 decades in stellar mass and found a minimum for this ratio at $M_{\text{star}} \sim 3 - 4 \times 10^{10} h^{-2} M_{\odot}$. The existence and location of this minimum is consistent with results from abundance matching (see Guo *et al.* 2010 and Dutton *et al.* 2010). For lower stellar masses the mass vs. stellar mass ratio strongly increases.

We performed maximum likelihood analyses based on the method described by Schneider & Rix (1997), assuming a BBS (Brainerd *et al.* 1996) and an NFW (Navarro *et al.* 1996) profile and analyzing our lens galaxy properties as a function of SED type and environment density. We applied scaling relations according to Guzik & Seljak (2002) and Hoekstra *et al.* (2004) for the total mass, Duffy *et al.* (2008) for the concentration parameter and our own results from $\Delta\Sigma$ for σ and r_{200} . For

the combined lens sample we find for an NFW profile best-fitting parameters of $c^* = 6.4^{+0.9}_{-0.7}$ and $r_{200}^* = 133^{+3}_{-2} h^{-1}$ kpc, corresponding to a virial mass of $M_{200}^* = 7.6^{+0.5}_{-0.3} \times 10^{10} h^{-1} M_{\odot}$. Considering red galaxies the value for r_{200}^* is about 20% higher while for blue galaxies it is about 15% lower, corresponding to a 60% higher M_{200} for red and a 35% lower M_{200} for blue galaxies. Assuming a BBS profile for the combined lens sample we obtain a velocity of $\sigma^* = 131^{+2}_{-3} \text{ km s}^{-1}$ and a truncation radius of $s^* = 184^{+17}_{-14} h^{-1}$ kpc, corresponding to a total mass of $M_{\text{total,BBS}}^* = 2.32^{+0.28}_{-0.25} \times 10^{12} h^{-1} M_{\odot}$. Focussing on red galaxies, we find that σ^* is about 15% and s about 80% higher, leading to a mass excess of $\sim 130\%$ in comparison to the average galaxy, while for blue galaxies σ is about 10% and s about 50% lower, leading to a mass deficit of $\sim 60\%$ in comparison to the average galaxy. Investigating the influence of the environment density on the galaxy properties we find that, assuming a BBS profile, the velocity dispersion hardly shows any dependence, while the truncation radii significantly increase with environmental density. This implies that the central galaxy matter density mainly depends on the galaxy luminosity, but hardly on the environment. Assuming an NFW profile, we also only see weak dependence of the concentration parameter c on the environment, while r_{200} rapidly increases with increasing density. The increasing values for s and for r_{200} with density lead to significantly higher masses for galaxies in high density environments. As we did not explicitly include cluster halos in our maximum likelihood analyses, but assumed all clustered structures to be the sum of galaxy halos, the mass of an additional independent cluster halo would be assigned to the individual galaxies. This could lead to a mass overestimate for red galaxies or galaxies in dense regions in general. Further we did not discriminate between central galaxies and satellites in our analysis and thus are not sensitive to the level that satellite galaxies are stripped and central galaxies grow in mass, but instead measure the average mass for a given luminosity as a function of environment density. If we take into account that the total mass-to-light ratio increases from galaxies to groups (and galaxy clusters) (van Uitert *et al.* 2011, Sheldon *et al.* 2009), this increase of average halo masses is expected.

Encouraged by the robustness of the previously obtained scaling relations, we further applied maximum likelihood analyses to determine the scaling relations for the truncation radius s and the concentration parameter c . In the first investigation we fixed the values for σ^* and η_{σ} , thus fitting the truncation radius s^* and its scaling index η_s with luminosity. We obtained a value of $\eta_s = 0.52^{+0.09}_{-0.10}$, leading to a scaling of the mass-to-light ratio of $M/L \propto L^{0.12^{+0.10}_{-0.11}}$. Also the obtained scaling index for s , considering blue galaxies is well consistent with the assumption of a luminosity-independent M/L -ratio. Investigating our red lens sample, the situation is more complicated. While for brighter red galaxies ($M_r < -21$) the constant M/L -ratio still fits well, for the fainter red galaxies the radii appear to increase with decreasing luminosity, implying a luminosity independent mass. This could be explained by the assumption of an additional different red galaxy population with higher mass for given luminosity, dominating at the low mass end but fading away with increasing mass.

We investigated the scaling behavior of the concentration parameter c with the absolute luminosity as a function of SED type by running maximum likelihood analyses with fixed values for r_{200} and its scaling index $\eta_{r_{200}}$ with luminosity. We assumed that the r_{200} can universally be described as a single-power law function of the luminosity. We obtained values of $\eta_c = -0.07^{+0.11}_{-0.11}$ for our lens sample as a whole, consistent with the results of Duffy *et al.* (2008). Looking at red galaxies separately, we found a slightly shallower relation with $\eta_c^{\text{red}} = -0.04^{+0.10}_{-0.11}$ while the relation for blue galaxies is steeper with marginal significance ($\eta_c^{\text{blue}} = -0.34^{+0.24}_{-0.26}$). This would lead to a

significant increase of the concentration with decreasing luminosity and thus mass. Translating the concentration-luminosity-relation into a concentration-mass-relation, we see that massive red galaxies exceed their blue counterparts in concentration while for lower mass galaxies the relation turns into its opposite.

As the analysis of the r_{200} -scaling relation indicated a change in the scaling behavior when considering galaxies with $L < 10^{10} h^{-2} L_{\odot}$, we discussed two possible explanations, a change in the $c - L$ -relation and the effect on the $c - L$ -relation assuming a modified $r_{200} - L$ relation due to a change in the $M - L$ -scaling relation. First we assumed a single-power law for the $r_{200} - L$ relation and applied a maximum likelihood analysis, allowing two independent scaling indices $\eta_{c_{\text{bright}}}$ and $\eta_{c_{\text{faint}}}$ for the concentration in both luminosity ranges. Indeed the maximum likelihood analyses confirmed this assumption. While for galaxies with $L > 10^{10} h^{-1} L_{\odot}$ the analysis yields values well agreeing with the previous results, for the fainter galaxies a significantly stronger increase in the concentration is suggested ($\eta_{c_{\text{faint}}} < -1$). This is also confirmed by repeating the analysis using a low density lens sample. Alternatively, we assumed the concentration-mass relation obtained by Duffy *et al.* (2008) to hold and independently fitted the slopes of the $r_{200} - L$ -relation for bright and faint galaxies. Indeed we find that in this case the scaling behaviors differ, more strongly for red than for blue galaxies, confirming the results for the M/L -scaling derived by the measurements of the BBS truncation radius s . However, if we use different slopes for the $r_{200} - L$ relation, the maximum likelihood results yield $c - L$ relations which are much more compatible with single-power law $c - L$ -relations.

Finally we created two simulated master lens samples, performing simulations based on the maximum likelihood results from our BBS and our NFW analyses. We repeated the measurements of the tangential shear γ_t and for the excess surface mass density $\Delta\Sigma$ as a function of the absolute galaxy luminosity and SED type. Comparing the results of the observational data with the results based on simulations, we observe in general good agreement, especially when considering galaxies brighter than $M_r = -20$. However, for fainter galaxies we obtain lower amplitudes from the simulated results than suggested by the observational data when assuming single-power law scaling relations. This indicates a modification in the scaling relations when investigating fainter lens galaxies or insufficient consideration of high density effects, especially appearing in the low mass regime. We therefore repeated the simulations, assuming double-power law scaling relations for the truncation radii s and the virial radii r_{200} with respect to the absolute galaxy luminosity and reanalyzed the simulated lensing signals. The newly obtained simulated $\Delta\Sigma$ -profiles now agree well with the observed profiles for almost all considered luminosity and environment density bins.

Bibliography

- Adelman-McCarthy, J. K. & et al. 2007: *The SDSS Photometric Catalog, Release 5 (Adelman-McCarthy+, 2007)*, VizieR Online Data Catalog, 2276, 0
- Agustsson, I. & Brainerd, T. G. 2006: *The Orientation of Satellite Galaxies: Evidence of Elongation in the Direction of the Host*, ApJ, 644, L25
- Astier, P., Guy, J., Regnault, N., Pain, R., Aubourg, E., Balam, D., Basa, S., Carlberg, R. G., Fabbro, S., Fouchez, D., Hook, I. M., et al. 2006: *The Supernova Legacy Survey: measurement of Ω_M , Ω_Λ and w from the first year data set*, A&A, 447, 31
- Baltz, E. A., Marshall, P., & Oguri, M. 2009: *Analytic models of plausible gravitational lens potentials*, Journal of Cosmology and Astro-Particle Physics, 1, 15
- Bamford, S. P., Aragón-Salamanca, A., & Milvang-Jensen, B. 2006: *The Tully-Fisher relation of distant field galaxies*, MNRAS, 366, 308
- Bartelmann, M. 1996: *Arcs from a universal dark-matter halo profile.*, A&A, 313, 697
- Bartelmann, M. & Schneider, P. 2001: *Weak gravitational lensing*, Phys. Rep., 340, 291
- Baum, W. A. 1962: *Photoelectric Magnitudes and Red-Shifts*, in IAU Symposium, Vol. 15, Problems of Extra-Galactic Research, ed. G. C. McVittie, 390
- Bell, E. F., McIntosh, D. H., Katz, N., & Weinberg, M. D. 2003: *The Optical and Near-Infrared Properties of Galaxies. I. Luminosity and Stellar Mass Functions*, ApJS, 149, 289
- Bender, R. 1988: *Velocity anisotropies and isophote shapes in elliptical galaxies*, A&A, 193, L7
- Bender, R., Appenzeller, I., Böhm, A., Drory, N., Fricke, K. J., Gabasch, A., Heidt, J., Hopp, U., Jäger, K., Kümmel, M., Mehlert, D., et al. 2001: *The FORS Deep Field: Photometric Data and Photometric Redshifts*, in Deep Fields, Springer, Berlin, ed. S. Cristiani, A. Renzini, & R. E. Williams, 96
- Bender, R., Burstein, D., & Faber, S. M. 1992: *Dynamically hot galaxies. I - Structural properties*, ApJ, 399, 462
- Benítez, N. 2000: *Bayesian Photometric Redshift Estimation*, ApJ, 536, 571
- Bernardi, M., Shankar, F., Hyde, J. B., Mei, S., Marulli, F., & Sheth, R. K. 2010: *Galaxy luminosities, stellar masses, sizes, velocity dispersions as a function of morphological type*, MNRAS, 404, 2087

- Bertin, E. & Arnouts, S. 1996: *SExtractor: Software for source extraction.*, A&AS, 117, 393
- Bhattacharya, S., Habib, S., Heitmann, K., & Vikhlinin, A. 2013: *Dark Matter Halo Profiles of Massive Clusters: Theory versus Observations*, ApJ, 766, 32
- Binney, J. & Tremaine, S. 1987, Galactic dynamics
- Blazek, J., Mandelbaum, R., Seljak, U., & Nakajima, R. 2012: *Separating intrinsic alignment and galaxy-galaxy lensing*, Journal of Cosmology and Astro-Particle Physics, 5, 41
- Bolzonella, M., Miralles, J.-M., & Pelló, R. 2000: *Photometric redshifts based on standard SED fitting procedures*, A&A, 363, 476
- Boulade, O., Charlot, X., Abbon, P., Aune, S., Borgeaud, P., Carton, P.-H., Carty, M., Da Costa, J., Deschamps, H., Desforge, D., Eppellé, D., et al. 2003: *MegaCam: the new Canada-France-Hawaii Telescope wide-field imaging camera*, in Society of Photo-Optical Instrumentation Engineers (SPIE) Conference Series, Vol. 4841, Society of Photo-Optical Instrumentation Engineers (SPIE) Conference Series, ed. M. Iye & A. F. M. Moorwood, 72–81
- Brainerd, T. G. 2010: *Multiple Weak Deflections in Galaxy-Galaxy Lensing*, ApJ, 713, 603
- Brainerd, T. G., Blandford, R. D., & Smail, I. 1996: *Weak Gravitational Lensing by Galaxies*, ApJ, 466, 623
- Bridle, S., Balan, S. T., Bethge, M., Gentile, M., Harmeling, S., Heymans, C., Hirsch, M., Hosseini, R., Jarvis, M., Kirk, D., Kitching, T., et al. 2010: *Results of the GREAT08 Challenge: an image analysis competition for cosmological lensing*, MNRAS, 405, 2044
- Bridle, S. & King, L. 2007: *Dark energy constraints from cosmic shear power spectra: impact of intrinsic alignments on photometric redshift requirements*, New Journal of Physics, 9, 444
- Brimioulle, F., Lerchster, M., Seitz, S., Bender, R., & Snigula, J. 2008: *Photometric redshifts for the CFHTLS-Wide*, ArXiv e-prints, 0811.3211v1
- Brimioulle, F., Seitz, S., Lerchster, M., Bender, R., & Snigula, J. 2013: *Dark Matter Halo Properties from Galaxy-Galaxy Lensing*, ArXiv e-prints, 1303.6287v1
- Brown, M. L., Taylor, A. N., Bacon, D. J., Gray, M. E., Dye, S., Meisenheimer, K., & Wolf, C. 2003: *The shear power spectrum from the COMBO-17 survey*, MNRAS, 341, 100
- Bruzual A., G. & Charlot, S. 1993: *Spectral evolution of stellar populations using isochrone synthesis*, ApJ, 405, 538
- Bullock, J. S., Kolatt, T. S., Sigad, Y., Somerville, R. S., Kravtsov, A. V., Klypin, A. A., Primack, J. R., & Dekel, A. 2001: *Profiles of dark haloes: evolution, scatter and environment*, MNRAS, 321, 559
- Cappellari, M., Scott, N., Alatalo, K., Blitz, L., Bois, M., Bournaud, F., Bureau, M., Crocker, A. F., Davies, R. L., Davis, T. A., de Zeeuw, P. T., et al. 2012: *The Atlas3D project - XIX. Benchmark for early-type galaxies scaling relations from 260 dynamical models: mass-to-light ratio, dark matter, Fundamental Plane and Virial Plane*, ArXiv e-prints, 1208.3522v1

- Carroll, B. W. & Ostlie, D. A. 1996, *An Introduction to Modern Astrophysics*
- Carter, D. 1978: *The structure of the isophotes of elliptical galaxies*, MNRAS, 182, 797
- Coleman, G. D., Wu, C.-C., & Weedman, D. W. 1980: *Colors and magnitudes predicted for high redshift galaxies*, ApJS, 43, 393
- Collister, A. A. & Lahav, O. 2004: *ANNz: Estimating Photometric Redshifts Using Artificial Neural Networks*, PASP, 116, 345
- Coupon, J., Ilbert, O., Kilbinger, M., McCracken, H. J., Mellier, Y., Arnouts, S., Bertin, E., Hudelot, P., Schultheis, M., Le Fèvre, O., Le Brun, V., et al. 2009: *Photometric redshifts for the CFHTLS T0004 deep and wide fields*, A&A, 500, 981
- Dahlen, T., Mobasher, B., Somerville, R. S., Moustakas, L. A., Dickinson, M., Ferguson, H. C., & Giavalisco, M. 2005: *The Evolution of the Optical and Near-Infrared Galaxy Luminosity Functions and Luminosity Densities to $z \sim 2$* , ApJ, 631, 126
- Darnell, T., Bertin, E., Gower, M., Ngeow, C., Desai, S., Mohr, J. J., Adams, D., Daves, G. E., Gower, M., Ngeow, C., Desai, S., et al. 2009: *The Dark Energy Survey Data Management System: The Coaddition Pipeline and PSF Homogenization*, in *Astronomical Society of the Pacific Conference Series*, Vol. 411, *Astronomical Data Analysis Software and Systems XVIII*, ed. D. A. Bohlender, D. Durand, & P. Dowler, 18
- Davies, R. L., Efstathiou, G., Fall, S. M., Illingworth, G., & Schechter, P. L. 1983: *The kinematic properties of faint elliptical galaxies*, ApJ, 266, 41
- Davis, M., Faber, S. M., Newman, J., Phillips, A. C., Ellis, R. S., Steidel, C. C., Conselice, C., Coil, A. L., Finkbeiner, D. P., Koo, D. C., Guhathakurta, P., et al. 2003: *Science Objectives and Early Results of the DEEP2 Redshift Survey*, in *Society of Photo-Optical Instrumentation Engineers (SPIE) Conference Series*, Vol. 4834, *Society of Photo-Optical Instrumentation Engineers (SPIE) Conference Series*, ed. P. Guhathakurta, 161–172
- Davis, M., Guhathakurta, P., Konidaris, N. P., Newman, J. A., Ashby, M. L. N., Biggs, A. D., Barmby, P., Bundy, K., Chapman, S. C., Coil, A. L., Conselice, C. J., et al. 2007: *The All-Wavelength Extended Groth Strip International Survey (AEGIS) Data Sets*, ApJ, 660, L1
- de Vaucouleurs, G. 1948: *Recherches sur les Nebuleuses Extragalactiques*, *Annales d'Astrophysique*, 11, 247
- de Vaucouleurs, G. 1953: *On the distribution of mass and luminosity in elliptical galaxies*, MNRAS, 113, 134
- de Vaucouleurs, G. 1958: *Photoelectric photometry of the Andromeda nebula in the UBV system*, ApJ, 128, 465
- dell'Antonio, I. P. & Tyson, J. A. 1996: *Galaxy Dark Matter: Galaxy-Galaxy Lensing in the Hubble Deep Field*, ApJ, 473, L17

- Drory, N., Feulner, G., Bender, R., Botzler, C. S., Hopp, U., Maraston, C., Mendes de Oliveira, C., & Snigula, J. 2001: *The Munich Near-Infrared Cluster Survey - I. Field selection, object extraction and photometry*, MNRAS, 325, 550
- Duffy, A. R., Schaye, J., Kay, S. T., & Dalla Vecchia, C. 2008: *Dark matter halo concentrations in the Wilkinson Microwave Anisotropy Probe year 5 cosmology*, MNRAS, 390, L64
- Dutton, A. A., Conroy, C., van den Bosch, F. C., Prada, F., & More, S. 2010: *The kinematic connection between galaxies and dark matter haloes*, MNRAS, 407, 2
- Einstein, A. 1914: *Die formale Grundlage der allgemeinen Relativitätstheorie*, Sitzungsberichte der Königlich Preußischen Akademie der Wissenschaften (Berlin), Seite 1030-1085., 1030
- Einstein, A. 1915: *Die Feldgleichungen der Gravitation*, Sitzungsberichte der Königlich Preußischen Akademie der Wissenschaften (Berlin), Seite 844-847., 844
- Eisenstein, D. J., Annis, J., Gunn, J. E., Szalay, A. S., Connolly, A. J., Nichol, R. C., Bahcall, N. A., Bernardi, M., Burles, S., Castander, F. J., Fukugita, M., et al. 2001: *Spectroscopic Target Selection for the Sloan Digital Sky Survey: The Luminous Red Galaxy Sample*, AJ, 122, 2267
- Erben, T., Hildebrandt, H., Lerchster, M., Hudelot, P., Benjamin, J., van Waerbeke, L., Schrabback, T., Brimiouille, F., Cordes, O., Dietrich, J. P., Holhjem, K., et al. 2009: *CARS: the CFHTLS-Archive-Research Survey. I. Five-band multi-colour data from 37 sq. deg. CFHTLS-wide observations*, A&A, 493, 1197
- Erben, T., Schirmer, M., Dietrich, J. P., Cordes, O., Habertzettl, L., Hetterscheidt, M., Hildebrandt, H., Schmithuesen, O., Schneider, P., Simon, P., Deul, E., et al. 2005: *GaBoDS: The Garching-Bonn Deep Survey. IV. Methods for the image reduction of multi-chip cameras demonstrated on data from the ESO Wide-Field Imager*, Astronomische Nachrichten, 326, 432
- Erben, T., Van Waerbeke, L., Bertin, E., Mellier, Y., & Schneider, P. 2001: *How accurately can we measure weak gravitational shear?*, A&A, 366, 717
- Etherington, I. M. H. 1933: *On the Definition of Distance in General Relativity.*, Philosophical Magazine, 15, 761
- Faber, S. M. & Jackson, R. E. 1976: *Velocity dispersions and mass-to-light ratios for elliptical galaxies*, ApJ, 204, 668
- Fernández Lorenzo, M., Cepa, J., Bongiovanni, A., Castañeda, H., Pérez García, A. M., Lara-López, M. A., Pović, M., & Sánchez-Portal, M. 2009: *Evolution of the optical Tully-Fisher relation up to $z = 1.3$* , A&A, 496, 389
- Feulner, G., Gabasch, A., Salvato, M., Drory, N., Hopp, U., & Bender, R. 2005: *Specific Star Formation Rates to Redshift 5 from the FORS Deep Field and the GOODS-S Field*, ApJ, 633, L9
- Feulner, G., Hopp, U., & Botzler, C. S. 2006: *Integrated specific star formation rates of galaxies, groups, and clusters: a continuous upper limit with stellar mass?*, A&A, 451, L13
- Freeman, K. C. 1970: *On the Disks of Spiral and so Galaxies*, ApJ, 160, 811

- Friedmann, A. 1924: *Über die Möglichkeit einer Welt mit konstanter negativer Krümmung des Raumes*, Zeitschrift für Physik, 21, 326
- Fu, L., Semboloni, E., Hoekstra, H., Kilbinger, M., van Waerbeke, L., Tereno, I., Mellier, Y., Heymans, C., Coupon, J., Benabed, K., Benjamin, J., et al. 2008: *Very weak lensing in the CFHTLS wide: cosmology from cosmic shear in the linear regime*, A&A, 479, 9
- Gabasch, A., Bender, R., Seitz, S., Hopp, U., Saglia, R. P., Feulner, G., Snigula, J., Drory, N., Appenzeller, I., Heidt, J., Mehlert, D., et al. 2004a: *The evolution of the luminosity functions in the FORS Deep Field from low to high redshift. I. The blue bands*, A&A, 421, 41
- Gabasch, A., Goranova, Y., Hopp, U., Noll, S., & Pannella, M. 2008: *A deep i-selected multiwaveband galaxy catalogue in the COSMOS field*, MNRAS, 383, 1319
- Gabasch, A., Hopp, U., Feulner, G., Bender, R., Seitz, S., Saglia, R. P., Snigula, J., Drory, N., Appenzeller, I., Heidt, J., Mehlert, D., et al. 2006: *The evolution of the luminosity functions in the FORS deep field from low to high redshift. II. The red bands*, A&A, 448, 101
- Gabasch, A., Salvato, M., Saglia, R. P., Bender, R., Hopp, U., Seitz, S., Feulner, G., Pannella, M., Drory, N., Schirmer, M., & Erben, T. 2004b: *The Star Formation Rate History in the FORS Deep and GOODS-South Fields*, ApJ, 616, L83
- Gallazzi, A., Charlot, S., Brinchmann, J., & White, S. D. M. 2006: *Ages and metallicities of early-type galaxies in the Sloan Digital Sky Survey: new insight into the physical origin of the colour-magnitude and the Mg_2 - σ_V relations*, MNRAS, 370, 1106
- Garilli, B., Le Fèvre, O., Guzzo, L., Maccagni, D., Le Brun, V., de la Torre, S., Meneux, B., Tresse, L., Franzetti, P., Zamorani, G., Zanichelli, A., et al. 2008: *The Vimos VLT deep survey. Global properties of 20,000 galaxies in the $I_{AB} < 22.5$ WIDE survey*, A&A, 486, 683
- Gerhard, O., Kronawitter, A., Saglia, R. P., & Bender, R. 2001: *Dynamical Family Properties and Dark Halo Scaling Relations of Giant Elliptical Galaxies*, AJ, 121, 1936
- Griffiths, R. E., Casertano, S., Im, M., & Ratnatunga, K. U. 1996: *Weak gravitational lensing around field galaxies in Hubble Space Telescope survey images*, MNRAS, 282, 1159
- Gruen, D., Brimiouille, F., Seitz, S., Lee, C.-H., Young, J., Koppenhoefer, J., Eichner, T., Riffeser, A., Vikram, V., Weidinger, T., & Zenteno, A. 2013: *Weak lensing analysis of RXC J2248.7-4431*, ArXiv e-prints, 1304.0764v1
- Gruen, D., Seitz, S., Koppenhoefer, J., & Riffeser, A. 2010: *Bias-free Shear Estimation Using Artificial Neural Networks*, ApJ, 720, 639
- Guo, Q., White, S., Li, C., & Boylan-Kolchin, M. 2010: *How do galaxies populate dark matter haloes?*, MNRAS, 404, 1111
- Guzik, J. & Seljak, U. 2002: *Virial masses of galactic haloes from galaxy-galaxy lensing: theoretical modelling and application to Sloan Digital Sky Survey data*, MNRAS, 335, 311

- Heymans, C., Van Waerbeke, L., Bacon, D., Berge, J., Bernstein, G., Bertin, E., Bridle, S., Brown, M. L., Clowe, D., Dahle, H., Erben, T., et al. 2006: *The Shear Testing Programme - I. Weak lensing analysis of simulated ground-based observations*, MNRAS, 368, 1323
- Hildebrandt, H., Erben, T., Kuijken, K., van Waerbeke, L., Heymans, C., Coupon, J., Benjamin, J., Bonnett, C., Fu, L., Hoekstra, H., Kitching, T. D., et al. 2012: *CFHTLenS: improving the quality of photometric redshifts with precision photometry*, MNRAS, 2386
- Hirata, C. M., Mandelbaum, R., Seljak, U., Guzik, J., Padmanabhan, N., Blake, C., Brinkmann, J., Budávári, T., Connolly, A., Csabai, I., Scranton, R., et al. 2004: *Galaxy-galaxy weak lensing in the Sloan Digital Sky Survey: intrinsic alignments and shear calibration errors*, MNRAS, 353, 529
- Hoekstra, H., Franx, M., & Kuijken, K. 2000: *Hubble Space Telescope Weak-Lensing Study of the $z=0.83$ Cluster MS 1054-03*, ApJ, 532, 88
- Hoekstra, H., Franx, M., Kuijken, K., Carlberg, R. G., & Yee, H. K. C. 2003: *Lensing by galaxies in CNO2 fields*, MNRAS, 340, 609
- Hoekstra, H., Franx, M., Kuijken, K., & Squires, G. 1998: *Weak Lensing Analysis of CL 1358+62 Using Hubble Space Telescope Observations*, ApJ, 504, 636
- Hoekstra, H., Hsieh, B. C., Yee, H. K. C., Lin, H., & Gladders, M. D. 2005: *Virial Masses and the Baryon Fraction in Galaxies*, ApJ, 635, 73
- Hoekstra, H., Mellier, Y., van Waerbeke, L., Semboloni, E., Fu, L., Hudson, M. J., Parker, L. C., Tereno, I., & Benabed, K. 2006: *First Cosmic Shear Results from the Canada-France-Hawaii Telescope Wide Synoptic Legacy Survey*, ApJ, 647, 116
- Hoekstra, H., Yee, H. K. C., & Gladders, M. D. 2004: *Properties of Galaxy Dark Matter Halos from Weak Lensing*, ApJ, 606, 67
- Hoekstra, H., Yee, H. K. C., Gladders, M. D., Barrientos, L. F., Hall, P. B., & Infante, L. 2002: *A Measurement of Weak Lensing by Large-Scale Structure in Red-Sequence Cluster Survey Fields*, ApJ, 572, 55
- Hudson, M. J., Gwyn, S. D. J., Dahle, H., & Kaiser, N. 1998: *Galaxy-Galaxy Lensing in the Hubble Deep Field: The Halo Tully-Fisher Relation at Intermediate Redshift*, ApJ, 503, 531
- Ilbert, O., Arnouts, S., McCracken, H. J., Bolzonella, M., Bertin, E., Le Fèvre, O., Mellier, Y., Zamorani, G., Pellò, R., Iovino, A., Tresse, L., et al. 2006: *Accurate photometric redshifts for the CFHT legacy survey calibrated using the VIMOS VLT deep survey*, A&A, 457, 841
- Jarrett, T. H., Chester, T., Cutri, R., Schneider, S., Skrutskie, M., & Huchra, J. P. 2000: *2MASS Extended Source Catalog: Overview and Algorithms*, AJ, 119, 2498
- Joachimi, B. & Schneider, P. 2008: *The removal of shear-ellipticity correlations from the cosmic shear signal via nulling techniques*, A&A, 488, 829
- Kaiser, N. 1995: *Nonlinear cluster lens reconstruction*, ApJ, 439, L1

- Kaiser, N., Squires, G., & Broadhurst, T. 1995: *A Method for Weak Lensing Observations*, ApJ, 449, 460
- Kauffmann, G., Heckman, T. M., White, S. D. M., Charlot, S., Tremonti, C., Brinchmann, J., Bruzual, G., Peng, E. W., Seibert, M., Bernardi, M., Blanton, M., et al. 2003: *Stellar masses and star formation histories for 10^5 galaxies from the Sloan Digital Sky Survey*, MNRAS, 341, 33
- Kinney, A. L., Calzetti, D., Bica, E., & Storchi-Bergmann, T. 1994: *The Reddening law outside the local group galaxies: The case of NGC 7552 and NGC 5236*, ApJ, 429, 172
- Kinney, A. L., Calzetti, D., Bohlin, R. C., McQuade, K., Storchi-Bergmann, T., & Schmitt, H. R. 1996: *Template Ultraviolet to Near-Infrared Spectra of Star-forming Galaxies and Their Application to K-Corrections*, ApJ, 467, 38
- Kleinheinrich, M., Schneider, P., Rix, H.-W., Erben, T., Wolf, C., Schirmer, M., Meisenheimer, K., Borch, A., Dye, S., Kovacs, Z., & Wisotzki, L. 2006: *Weak lensing measurements of dark matter halos of galaxies from COMBO-17*, A&A, 455, 441
- Klypin, A. A., Trujillo-Gomez, S., & Primack, J. 2011: *Dark Matter Halos in the Standard Cosmological Model: Results from the Bolshoi Simulation*, ApJ, 740, 102
- Kormendy, J. & Bender, R. 2012: *A Revised Parallel-sequence Morphological Classification of Galaxies: Structure and Formation of S0 and Spheroidal Galaxies*, ApJS, 198, 2
- Le Fèvre, O., Mellier, Y., McCracken, H. J., Foucaud, S., Gwyn, S., Radovich, M., Dantel-Fort, M., Bertin, E., Moreau, C., Cuillandre, J.-C., Pierre, M., et al. 2004: *The VIRMOS deep imaging survey. I. Overview, survey strategy, and CFH12K observations*, A&A, 417, 839
- Le Fèvre, O., Vettolani, G., Garilli, B., Tresse, L., Bottini, D., Le Brun, V., Maccagni, D., Picat, J. P., Scaramella, R., Scodreggio, M., Zanichelli, A., et al. 2005: *The VIMOS VLT deep survey. First epoch VVDS-deep survey: 11 564 spectra with $17.5 \leq IAB \leq 24$, and the redshift distribution over $0 \leq z \leq 5$* , A&A, 439, 845
- Lerchster, M., Seitz, S., Brimiouille, F., Fassbender, R., Rovilos, M., Böhringer, H., Pierini, D., Kilbinger, M., Finoguenov, A., Quintana, H., & Bender, R. 2011: *The massive galaxy cluster XMMU J1230.3+1339 at $z \sim 1$: colour-magnitude relation, Butcher-Oemler effect, X-ray and weak lensing mass estimates*, MNRAS, 411, 2667
- Lilly, S. J., Le Fèvre, O., Renzini, A., Zamorani, G., Scodreggio, M., Contini, T., Carollo, C. M., Hasinger, G., Kneib, J.-P., Iovino, A., Le Brun, V., et al. 2007: *z COSMOS: A Large VLT/VIMOS Redshift Survey Covering $0 < z < 3$ in the COSMOS Field*, ApJS, 172, 70
- Loveday, J., Norberg, P., Baldry, I. K., Driver, S. P., Hopkins, A. M., Peacock, J. A., Bamford, S. P., Liske, J., Bland-Hawthorn, J., Brough, S., Brown, M. J. I., et al. 2012: *Galaxy and Mass Assembly (GAMA): ugriz galaxy luminosity functions*, MNRAS, 420, 1239
- Luppino, G. A. & Kaiser, N. 1997: *Detection of Weak Lensing by a Cluster of Galaxies at $Z = 0.83$* , ApJ, 475, 20

- Magnier, E. A. & Cuillandre, J.-C. 2004: *The Elixir System: Data Characterization and Calibration at the Canada-France-Hawaii Telescope*, PASP, 116, 449
- Mandelbaum, R., Hirata, C. M., Broderick, T., Seljak, U., & Brinkmann, J. 2006a: *Ellipticity of dark matter haloes with galaxy-galaxy weak lensing*, MNRAS, 370, 1008
- Mandelbaum, R., Hirata, C. M., Ishak, M., Seljak, U., & Brinkmann, J. 2006b: *Detection of large-scale intrinsic ellipticity-density correlation from the Sloan Digital Sky Survey and implications for weak lensing surveys*, MNRAS, 367, 611
- Mandelbaum, R., Hirata, C. M., Seljak, U., Guzik, J., Padmanabhan, N., Blake, C., Blanton, M. R., Lupton, R., & Brinkmann, J. 2005: *Systematic errors in weak lensing: application to SDSS galaxy-galaxy weak lensing*, MNRAS, 361, 1287
- Mandelbaum, R., Seljak, U., & Hirata, C. M. 2008: *A halo mass–concentration relation from weak lensing*, Journal of Cosmology and Astro-Particle Physics, 8, 6
- Mandelbaum, R., Seljak, U., Kauffmann, G., Hirata, C. M., & Brinkmann, J. 2006c: *Galaxy halo masses and satellite fractions from galaxy-galaxy lensing in the Sloan Digital Sky Survey: stellar mass, luminosity, morphology and environment dependencies*, MNRAS, 368, 715
- Mannucci, F., Basile, F., Poggianti, B. M., Cimatti, A., Daddi, E., Pozzetti, L., & Vanzi, L. 2001: *Near-infrared template spectra of normal galaxies: k-corrections, galaxy models and stellar populations*, MNRAS, 326, 745
- Maraston, C. 1998: *Evolutionary synthesis of stellar populations: a modular tool*, MNRAS, 300, 872
- Massey, R., Heymans, C., Bergé, J., Bernstein, G., Bridle, S., Clowe, D., Dahle, H., Ellis, R., Erben, T., Hettterscheidt, M., High, F. W., et al. 2007: *The Shear Testing Programme 2: Factors affecting high-precision weak-lensing analyses*, MNRAS, 376, 13
- Matkovic, A. & Guzmán, R. 2007: *Faber-Jackson Relation for dwarf E/S0 Galaxies*, in Revista Mexicana de Astronomía y Astrofísica, vol. 27, Vol. 29, Revista Mexicana de Astronomía y Astrofísica Conference Series, ed. R. Guzmán, 107–109
- McKay, T. A., Sheldon, E. S., Racusin, J., Fischer, P., Seljak, U., Stebbins, A., Johnston, D., Frieman, J. A., Bahcall, N., Brinkmann, J., Csabai, I., et al. 2001: *Galaxy Mass and Luminosity Scaling Laws Determined by Weak Gravitational Lensing*, ArXiv Astrophysics e-prints, 0108013v1
- Miller, S. H., Bundy, K., Sullivan, M., Ellis, R. S., & Treu, T. 2011: *The Assembly History of Disk Galaxies. I. The Tully-Fisher Relation to $z \sim 1.3$ from Deep Exposures with DEIMOS*, ApJ, 741, 115
- More, S., van den Bosch, F. C., Cacciato, M., Skibba, R., Mo, H. J., & Yang, X. 2011: *Satellite kinematics - III. Halo masses of central galaxies in SDSS*, MNRAS, 410, 210
- Navarro, J. F., Frenk, C. S., & White, S. D. M. 1996: *The Structure of Cold Dark Matter Halos*, ApJ, 462, 563
- Navarro, J. F., Frenk, C. S., & White, S. D. M. 1997: *A Universal Density Profile from Hierarchical Clustering*, ApJ, 490, 493

- Nigoche-Netro, A., Aguerri, J. A. L., Lagos, P., Ruelas-Mayorga, A., Sánchez, L. J., & Machado, A. 2010: *The Faber-Jackson relation for early-type galaxies: dependence on the magnitude range*, A&A, 516, A96
- Parker, L. C., Hoekstra, H., Hudson, M. J., van Waerbeke, L., & Mellier, Y. 2007: *The Masses and Shapes of Dark Matter Halos from Galaxy-Galaxy Lensing in the CFHT Legacy Survey*, ApJ, 669, 21
- Pickles, A. J. 1998: *A Stellar Spectral Flux Library: 1150-25000 Å*, PASP, 110, 863
- Pizagno, J., Prada, F., Weinberg, D. H., Rix, H.-W., Harbeck, D., Grebel, E. K., Bell, E. F., Brinkmann, J., Holtzman, J., & West, A. 2005: *Dark Matter and Stellar Mass in the Luminous Regions of Disk Galaxies*, ApJ, 633, 844
- Prada, F., Klypin, A. A., Cuesta, A. J., Betancort-Rijo, J. E., & Primack, J. 2012: *Halo concentrations in the standard Λ cold dark matter cosmology*, MNRAS, 423, 3018
- Press, W. H. & Schechter, P. 1974: *Formation of Galaxies and Clusters of Galaxies by Self-Similar Gravitational Condensation*, ApJ, 187, 425
- Reyes, R., Mandelbaum, R., Gunn, J. E., Nakajima, R., Seljak, U., & Hirata, C. M. 2011: *Optical-to-virial velocity ratios of local disk galaxies from combined kinematics and galaxy-galaxy lensing*, ArXiv e-prints, 1110.4107v2
- Robertson, H. P. 1935: *Kinematics and World-Structure*, ApJ, 82, 284
- Rowe, B. 2010: *Improving PSF modelling for weak gravitational lensing using new methods in model selection*, MNRAS, 404, 350
- Saglia, R. P., Sánchez-Blázquez, P., Bender, R., Simard, L., Desai, V., Aragón-Salamanca, A., Milvang-Jensen, B., Halliday, C., Jablonka, P., Noll, S., Poggianti, B., et al. 2010: *The fundamental plane of EDisCS galaxies. The effect of size evolution*, A&A, 524, A6
- Schneider, P. 2006a, Einführung in die extragalaktische Astronomie und Kosmologie
- Schneider, P. 2006b: *Part 3: Weak gravitational lensing*, in Saas-Fee Advanced Course 33: Gravitational Lensing: Strong, Weak and Micro, ed. G. Meylan, P. Jetzer, P. North, P. Schneider, C. S. Kochanek, & J. Wambsganss, 269–451
- Schneider, P., Ehlers, J., & Falco, E. E. 1992, Gravitational Lenses
- Schneider, P. & Rix, H.-W. 1997: *Quantitative Analysis of Galaxy-Galaxy Lensing*, ApJ, 474, 25
- Schneider, P. & Seitz, C. 1995: *Steps towards nonlinear cluster inversion through gravitational distortions. I: Basic considerations and circular clusters*, A&A, 294, 411
- Schrabback, T., Erben, T., Simon, P., Miralles, J.-M., Schneider, P., Heymans, C., Eifler, T., Fosbury, R. A. E., Freudling, W., Hettterscheidt, M., Hildebrandt, H., et al. 2007: *Cosmic shear analysis of archival HST/ACS data. I. Comparison of early ACS pure parallel data to the HST/GEMS survey*, A&A, 468, 823

- Seitz, C. & Schneider, P. 1995: *Steps towards nonlinear cluster inversion through gravitational distortions II. Generalization of the Kaiser and Squires method.*, A&A, 297, 287
- Seitz, C. & Schneider, P. 1997: *Steps towards nonlinear cluster inversion through gravitational distortions. III. Including a redshift distribution of the sources.*, A&A, 318, 687
- Seitz, S. & Schneider, P. 1996: *Cluster lens reconstruction using only observed local data: an improved finite-field inversion technique.*, A&A, 305, 383
- Seitz, S. & Schneider, P. 2001: *A new finite-field mass reconstruction algorithm*, A&A, 374, 740
- Seitz, S., Schneider, P., & Ehlers, J. 1994: *Light propagation in arbitrary spacetimes and the gravitational lens approximation*, Classical and Quantum Gravity, 11, 2345
- Seljak, U. 2002: *Constraints on galaxy halo profiles from galaxy-galaxy lensing and Tully-Fisher/Fundamental Plane relations*, MNRAS, 334, 797
- Semboloni, E., Mellier, Y., van Waerbeke, L., Hoekstra, H., Tereno, I., Benabed, K., Gwyn, S. D. J., Fu, L., Hudson, M. J., Maoli, R., & Parker, L. C. 2006: *Cosmic shear analysis with CFHTLS deep data*, A&A, 452, 51
- Shaw, L. D., Weller, J., Ostriker, J. P., & Bode, P. 2006: *Statistics of Physical Properties of Dark Matter Clusters*, ApJ, 646, 815
- Sheldon, E. S., Johnston, D. E., Frieman, J. A., Scranton, R., McKay, T. A., Connolly, A. J., Budavári, T., Zehavi, I., Bahcall, N. A., Brinkmann, J., & Fukugita, M. 2004: *The Galaxy-Mass Correlation Function Measured from Weak Lensing in the Sloan Digital Sky Survey*, AJ, 127, 2544
- Sheldon, E. S., Johnston, D. E., Masjedi, M., McKay, T. A., Blanton, M. R., Scranton, R., Wechsler, R. H., Koester, B. P., Hansen, S. M., Frieman, J. A., & Annis, J. 2009: *Cross-correlation Weak Lensing of SDSS Galaxy Clusters. III. Mass-to-Light Ratios*, ApJ, 703, 2232
- Smoot, G. F., Bennett, C. L., Kogut, A., Wright, E. L., Aymon, J., Boggess, N. W., Cheng, E. S., de Amici, G., Gulkis, S., Hauser, M. G., Hinshaw, G., et al. 1992: *Structure in the COBE differential microwave radiometer first-year maps*, ApJ, 396, L1
- Spinelli, P. F., Seitz, S., Lerchster, M., Brimiouille, F., & Finoguenov, A. 2012: *Weak-lensing mass estimates of galaxy groups and the line-of-sight contamination*, MNRAS, 420, 1384
- Strauss, M. A., Weinberg, D. H., Lupton, R. H., Narayanan, V. K., Annis, J., Bernardi, M., Blanton, M., Burles, S., Connolly, A. J., Dalcanton, J., Doi, M., et al. 2002: *Spectroscopic Target Selection in the Sloan Digital Sky Survey: The Main Galaxy Sample*, AJ, 124, 1810
- Tojeiro, R., Percival, W. J., Wake, D. A., Maraston, C., Skibba, R. A., Zehavi, I., Ross, A. J., Brinkmann, J., Conroy, C., Guo, H., Manera, M., et al. 2012: *The progenitors of present-day massive red galaxies up to $z \sim 0.7$ - finding passive galaxies using SDSS-I/II and SDSS-III*, MNRAS, 424, 136
- Tully, R. B. & Fisher, J. R. 1977: *A new method of determining distances to galaxies*, A&A, 54, 661

- Tyson, J. A., Valdes, F., Jarvis, J. F., & Mills, Jr., A. P. 1984: *Galaxy mass distribution from gravitational light deflection*, ApJ, 281, L59
- van Uitert, E., Hoekstra, H., Velander, M., Gilbank, D. G., Gladders, M. D., & Yee, H. K. C. 2011: *Galaxy-galaxy lensing constraints on the relation between baryons and dark matter in galaxies in the Red Sequence Cluster Survey 2*, A&A, 534, A14
- Van Waerbeke, L., Mellier, Y., Erben, T., Cuillandre, J. C., Bernardeau, F., Maoli, R., Bertin, E., McCracken, H. J., Le Fèvre, O., Fort, B., Dantel-Fort, M., et al. 2000: *Detection of correlated galaxy ellipticities from CFHT data: first evidence for gravitational lensing by large-scale structures*, A&A, 358, 30
- Van Waerbeke, L., Mellier, Y., Radovich, M., Bertin, E., Dantel-Fort, M., McCracken, H. J., Le Fèvre, O., Foucaud, S., Cuillandre, J.-C., Erben, T., Jain, B., et al. 2001: *Cosmic shear statistics and cosmology*, A&A, 374, 757
- Verheijen, M. A. W. 2001: *The Ursa Major Cluster of Galaxies. V. HI Rotation Curve Shapes and the Tully-Fisher Relations*, ApJ, 563, 694
- Vogt, N. P., Koo, D. C., Phillips, A. C., Wu, K., Faber, S. M., Willmer, C. N. A., Simard, L., Weiner, B. J., Illingworth, G. D., Gebhardt, K., Gronwall, C., et al. 2005: *The DEEP Groth Strip Survey. I. The Sample*, ApJS, 159, 41
- Walker, A. G. 1937: *On Milne's Theory of World-Structure*, Proceedings of the London Mathematical Society, s2-42, 90
- Weiner, B. J., Phillips, A. C., Faber, S. M., Willmer, C. N. A., Vogt, N. P., Simard, L., Gebhardt, K., Im, M., Koo, D. C., Sarajedini, V. L., Wu, K. L., et al. 2005: *The DEEP Groth Strip Galaxy Redshift Survey. III. Redshift Catalog and Properties of Galaxies*, ApJ, 620, 595
- Williams, M. J., Bureau, M., & Cappellari, M. 2010: *The Tully-Fisher relations of early-type spiral and S0 galaxies*, MNRAS, 409, 1330
- Wright, C. O. & Brainerd, T. G. 2000: *Gravitational Lensing by NFW Halos*, ApJ, 534, 34

Appendix A

Zeropoint Corrections

In this appendix the zeropoint corrections, derived from calibration on the Pickles star library (Pickles 1998) and from calibration on spectroscopic redshifts, for all filters of all analyzed CFHTLS-WIDE pointings are listed.

Table A.1: Zeropoint corrections for the all filters of all analyzed CFHTLS pointings.

pointing	stellar offsets					spectroscopic offsets				
	u^*	g'	r'	i'	z'	u^*	g'	r'	i'	z'
W1m2m3	-0.20	-0.06	-0.06	0.00	0.00	0.015	0.02	0.00	0.00	-0.005
W1m2m2	-0.17	0.00	-0.09	0.00	0.02	0.015	0.02	0.00	0.00	-0.005
W1m2m1	-0.30	0.01	-0.12	0.00	-0.05	0.015	0.02	0.00	0.00	-0.005
W1m2m0	-0.52	-0.13	-0.23	0.00	-0.06	0.015	0.02	0.00	0.00	-0.005
W1m2p1	-0.23	0.00	-0.06	0.00	0.02	0.015	0.02	0.00	0.00	-0.005
W1m2p2	-0.22	-0.03	0.06	0.00	0.03	0.015	0.02	0.00	0.00	-0.005
W1m2p3	-0.23	0.00	0.06	0.00	0.10	0.015	0.02	0.00	0.00	-0.005
W1m1m3	-0.21	-0.12	-0.05	0.00	-0.10	0.015	0.02	0.00	0.00	-0.005
W1m1m2	-0.22	0.01	0.09	0.00	0.00	0.015	0.02	0.00	0.00	-0.005
W1m1m1	-0.33	-0.02	-0.21	0.00	-0.09	0.015	0.02	0.00	0.00	-0.005
W1m1m0	-0.28	-0.05	0.00	0.00	0.02	0.015	0.02	0.00	0.00	-0.005
W1m1p1	-0.38	-0.02	0.05	0.00	0.00	0.015	0.02	0.00	0.00	-0.005
W1m1p2	-0.20	-0.11	-0.13	0.00	0.03	0.015	0.02	0.00	0.00	-0.005
W1m1p3	-0.05	-0.07	-0.14	0.00	0.17	0.015	0.02	0.00	0.00	-0.005
W1m0m3	-0.34	-0.07	-0.02	0.00	-0.02	0.015	0.02	0.00	0.00	-0.005
W1m0m2	-0.31	-0.01	-0.42	0.00	0.05	0.015	0.02	0.00	0.00	-0.005
W1m0m1	-0.35	-0.14	-0.13	0.00	-0.05	0.015	0.02	0.00	0.00	-0.005
W1m0m0	-0.21	-0.01	0.00	0.00	-0.01	0.015	0.02	0.00	0.00	-0.005
W1m0p1	-0.34	-0.13	-0.14	0.00	0.00	0.015	0.02	0.00	0.00	-0.005
W1m0p2	-0.30	-0.13	-0.14	0.00	0.00	0.015	0.02	0.00	0.00	-0.005
W1m0p3	-0.26	-0.09	-0.10	0.00	-0.02	0.015	0.02	0.00	0.00	-0.005
W1p1m3	-0.39	-0.12	-0.14	0.00	-0.03	0.015	0.02	0.00	0.00	-0.005
W1p1m2	-0.34	-0.05	-0.02	0.00	0.05	0.015	0.02	0.00	0.00	-0.005

pointing	stellar offsets					spectroscopic offsets				
	u^*	g'	r'	i'	z'	u^*	g'	r'	i'	z'
W1p1m1	-0.36	-0.08	-0.04	0.00	0.03	0.015	0.02	0.00	0.00	-0.005
W1p1m0	-0.33	-0.06	-0.02	0.00	-0.01	0.015	0.02	0.00	0.00	-0.005
W1p1p1	-0.30	-0.05	-0.06	0.00	0.08	0.015	0.02	0.00	0.00	-0.005
W1p1p2	-0.22	-0.01	-0.09	0.00	0.08	0.015	0.02	0.00	0.00	-0.005
W1p1p3	-0.19	-0.01	-0.13	0.00	0.09	0.015	0.02	0.00	0.00	-0.005
W1p2m3	-0.25	-0.03	-0.07	0.00	-0.44	0.015	0.02	0.00	0.00	-0.005
W1p2m2	-0.41	-0.10	-0.05	0.00	0.00	0.015	0.02	0.00	0.00	-0.005
W1p2m1	-0.53	-0.01	-0.06	0.00	0.00	0.015	0.02	0.00	0.00	-0.005
W1p2m0	-0.26	-0.01	0.00	0.00	0.07	0.015	0.02	0.00	0.00	-0.005
W1p2p1	-0.20	-0.09	-0.01	0.00	0.12	0.015	0.02	0.00	0.00	-0.005
W1p2p2	-0.30	-0.10	-0.06	0.00	0.08	0.01	0.04	0.01	0.00	0.00
W1p2p3	-0.22	-0.04	0.04	0.00	0.08	-0.02	0.01	0.03	0.00	-0.01
W1p3m3	-0.43	-0.08	-0.17	0.00	-0.08	0.015	0.02	0.00	0.00	-0.005
W1p3m2	-0.40	-0.12	-0.11	0.00	0.00	0.015	0.02	0.00	0.00	-0.005
W1p3m1	-0.38	-0.05	-0.07	0.00	0.09	0.015	0.02	0.00	0.00	-0.005
W1p3m0	-0.42	-0.12	-0.05	0.00	0.00	0.015	0.02	0.00	0.00	-0.005
W1p3p1	-0.35	-0.13	-0.10	0.00	0.04	0.015	0.02	0.00	0.00	-0.005
W1p3p2	-0.42	-0.14	-0.14	0.00	0.01	0.02	0.03	-0.01	0.00	-0.02
W1p3p3	-0.39	-0.04	0.00	0.00	0.10	0.03	-0.01	-0.02	0.00	0.01
W1p4m3	-0.39	-0.09	-0.14	0.00	0.06	0.015	0.02	0.00	0.00	-0.005
W1p4m2	-0.32	-0.11	-0.10	0.00	0.02	0.015	0.02	0.00	0.00	-0.005
W1p4m1	-0.51	-0.14	-0.13	0.00	-0.06	0.015	0.02	0.00	0.00	-0.005
W1p4m0	-0.39	-0.14	-0.09	0.00	0.00	0.015	0.02	0.00	0.00	-0.005
W1p4p1	-0.41	-0.04	-0.03	0.00	0.09	0.015	0.02	0.00	0.00	-0.005
W1p4p2	-0.31	0.01	0.03	0.00	0.11	0.015	0.02	0.00	0.00	-0.005
W1p4p3	-0.44	-0.11	-0.01	0.00	-0.07	0.015	0.02	0.00	0.00	-0.005
W2m1m1	-0.39	-0.15	-0.02	0.00	0.00	-0.05	-0.01	-0.01	0.00	0.02
W2m1m0	-0.43	-0.04	-0.03	0.00	-0.05	-0.05	-0.01	-0.01	0.00	0.02
W2m1p1	-0.40	-0.15	-0.14	0.00	0.00	-0.05	-0.01	-0.01	0.00	0.02
W2m1p2	-0.56	-0.16	-0.15	0.00	-0.06	-0.05	-0.01	-0.01	0.00	0.02
W2m1p3	-0.46	-0.05	-0.05	0.00	-0.03	-0.05	-0.01	-0.01	0.00	0.02
W2m0m1	-0.40	-0.13	-0.14	0.00	-0.08	-0.05	-0.01	-0.01	0.00	0.02
W2m0m0	-0.29	-0.07	0.05	0.00	0.01	-0.05	-0.01	-0.01	0.00	0.02
W2m0p1	-0.44	-0.16	-0.03	0.00	-0.01	-0.05	0.01	0.00	0.00	0.03
W2m0p2	-0.40	-0.11	0.00	0.00	0.00	-0.09	-0.04	-0.03	0.00	0.00
W2m0p3	-0.42	-0.08	-0.14	0.00	-0.02	-0.05	-0.05	0.02	0.00	0.04
W2p1m1	-0.20	-0.07	-0.10	0.00	-0.01	-0.05	-0.01	-0.01	0.00	0.02
W2p1m0	-0.36	-0.08	-0.05	0.00	0.02	-0.05	-0.01	-0.01	0.00	0.02
W2p1p1	-0.39	-0.04	-0.08	0.00	0.05	-0.01	0.01	0.03	0.00	0.01
W2p1p2	-0.49	-0.09	-0.05	0.00	0.07	-0.05	-0.02	-0.02	0.00	-0.02
W2p1p3	-0.31	-0.04	0.00	0.00	0.07	-0.11	0.01	-0.02	0.00	0.01
W2p2m1	-0.23	-0.11	-0.04	0.00	0.05	-0.05	-0.01	-0.01	0.00	0.02
W2p2m0	-0.46	-0.13	-0.11	0.00	0.00	-0.05	-0.01	-0.01	0.00	0.02

pointing	stellar offsets					spectroscopic offsets				
	u^*	g'	r'	i'	z'	u^*	g'	r'	i'	z'
W2p2p1	-0.44	-0.07	-0.03	0.00	-0.03	-0.13	-0.07	-0.06	0.00	0.01
W2p2p2	-0.36	0.01	0.11	0.00	0.06	0.07	0.05	0.03	0.00	0.04
W2p2p3	-0.42	-0.02	-0.05	0.00	0.06	-0.05	-0.01	-0.01	0.00	0.02
W2p3m1	-0.32	-0.04	-0.04	0.00	0.13	-0.05	-0.01	-0.01	0.00	0.02
W2p3m0	-0.39	-0.07	-0.05	0.00	-0.01	-0.05	-0.01	-0.01	0.00	0.02
W2p3p1	-0.30	-0.06	0.00	0.00	0.06	0.03	-0.02	-0.03	0.00	0.03
W2p3p2	-0.39	-0.13	-0.03	0.00	0.05	0.05	0.00	0.00	0.00	0.05
W2p3p3	-0.30	-0.08	-0.06	0.00	0.09	-0.05	-0.01	-0.01	0.00	0.02
W3m3m3	-0.43	-0.10	-0.12	0.00	0.01	-0.025	-0.015	0.01	0.00	0.00
W3m3m2	-0.42	-0.07	-0.13	0.00	0.03	-0.025	-0.015	0.01	0.00	0.00
W3m3m1	-0.33	-0.04	0.00	0.00	0.08	-0.025	-0.015	0.01	0.00	0.00
W3m3m0	-0.26	-0.09	-0.10	0.00	-0.02	-0.025	-0.015	0.01	0.00	0.00
W3m3p1	-0.06	0.03	-0.06	0.00	0.08	-0.025	-0.015	0.01	0.00	0.00
W3m3p2	-0.30	-0.02	-0.12	0.00	0.01	-0.025	-0.015	0.01	0.00	0.00
W3m2m3	-0.33	-0.07	-0.01	0.00	-0.01	-0.025	-0.015	0.01	0.00	0.00
W3m2m2	-0.37	-0.08	0.03	0.00	0.05	-0.025	-0.015	0.01	0.00	0.00
W3m2m1	-0.31	-0.09	0.08	0.00	0.24	-0.025	-0.015	0.01	0.00	0.00
W3m2m0	-0.18	0.03	0.06	0.00	0.24	-0.025	-0.015	0.01	0.00	0.00
W3m2p1	-0.16	-0.01	-0.12	0.00	0.07	-0.025	-0.015	0.01	0.00	0.00
W3m2p2	-0.26	-0.04	-0.08	0.00	-0.02	-0.025	-0.015	0.01	0.00	0.00
W3m1m3	-0.48	-0.09	-0.16	0.00	0.07	-0.05	-0.03	0.03	0.00	0.02
W3m1m2	-0.41	-0.01	0.05	0.00	0.06	0.02	0.00	0.00	0.00	-0.19
W3m1m1	-0.35	-0.02	-0.02	0.00	-0.03	-0.025	-0.015	0.01	0.00	0.00
W3m1m0	-0.21	-0.14	-0.02	0.00	-0.28	-0.025	-0.015	0.01	0.00	0.00
W3m1p1	-0.25	0.02	-0.08	0.00	0.03	-0.025	-0.015	0.01	0.00	0.00
W3m1p2	-0.29	-0.02	-0.12	0.00	0.05	-0.025	-0.015	0.01	0.00	0.00
W3m0m3	-0.13	-0.01	-0.03	0.00	-0.02	0.02	0.01	0.02	0.00	0.06
W3m0m2	-0.40	-0.04	-0.06	0.00	0.04	-0.02	0.06	0.04	0.00	-0.07
W3m0m1	-0.32	-0.12	-0.07	0.00	-0.02	-0.025	-0.015	0.01	0.00	0.00
W3m0m0	-0.39	-0.07	-0.05	0.00	-0.01	-0.025	-0.015	0.01	0.00	0.00
W3m0p1	-0.31	-0.07	-0.11	0.00	-0.01	-0.025	-0.015	0.01	0.00	0.00
W3m0p2	-0.30	-0.02	-0.02	0.00	-0.01	-0.025	-0.015	0.01	0.00	0.00
W3p1m3	-0.30	-0.07	-0.09	0.00	-0.02	-0.025	-0.015	0.01	0.00	0.00
W3p1m2	-0.36	-0.01	-0.07	0.00	0.00	-0.01	-0.04	-0.02	0.00	-0.02
W3p1m1	-0.34	-0.07	-0.06	0.00	-0.07	-0.09	-0.06	-0.04	0.00	-0.03
W3p1m0	-0.18	-0.03	-0.03	0.00	-0.04	-0.025	-0.015	0.01	0.00	0.00
W3p1p1	-0.22	-0.04	-0.07	0.00	0.00	-0.025	-0.015	0.01	0.00	0.00
W3p1p2	-0.17	-0.02	0.00	0.00	0.00	-0.025	-0.015	0.01	0.00	0.00
W4m3m0	-0.32	-0.02	-0.03	0.00	0.08	-0.06	0.00	0.01	0.00	-0.02
W4m3p1	-0.51	-0.16	-0.12	0.00	-0.04	-0.06	0.00	0.01	0.00	-0.02
W4m3p2	-0.31	-0.05	-0.05	0.00	0.06	-0.06	0.00	0.01	0.00	-0.02
W4m2m0	-0.19	0.18	0.20	0.00	0.29	-0.06	0.00	0.01	0.00	-0.02
W4m2p1	-0.35	-0.12	-0.01	0.00	0.02	-0.06	0.00	0.01	0.00	-0.02

pointing	stellar offsets					spectroscopic offsets				
	u^*	g'	r'	i'	z'	u^*	g'	r'	i'	z'
W4m1m2	-0.68	-0.06	0.02	0.00	0.15	-0.06	0.00	0.01	0.00	-0.02
W4m1m1	-0.50	-0.12	-0.09	0.00	0.06	-0.06	0.00	0.01	0.00	-0.02
W4m1m0	-0.28	-0.08	-0.10	0.00	-0.04	-0.06	0.00	0.01	0.00	-0.02
W4m1p1	-0.29	-0.12	-0.02	0.00	0.07	-0.06	0.00	0.01	0.00	-0.02
W4m0m2	-0.63	-0.15	-0.07	0.00	0.09	-0.06	-0.01	0.02	0.00	-0.04
W4m0m1	-0.60	-0.17	-0.14	0.00	0.04	-0.03	0.00	0.02	0.00	0.00
W4m0m0	-0.51	-0.05	0.03	0.00	0.03	-0.05	0.03	0.03	0.00	-0.02
W4m0p1	-0.33	-0.16	0.00	0.00	0.07	-0.06	0.00	0.01	0.00	-0.02
W4p1m2	-0.48	-0.14	-0.02	0.00	0.12	-0.06	0.00	0.00	0.00	-0.03
W4p1m1	-0.64	-0.17	-0.04	0.00	0.05	-0.10	-0.04	-0.02	0.00	-0.03
W4p1m0	-0.60	-0.10	-0.20	0.00	0.03	-0.03	-0.01	0.01	0.00	0.00
W4p1p1	-0.33	-0.07	-0.17	0.00	0.05	-0.06	0.00	0.01	0.00	-0.02
W4p2m2	-0.58	-0.12	-0.18	0.00	0.07	-0.09	-0.03	0.01	0.00	-0.04
W4p2m1	-0.62	-0.12	-0.17	0.00	0.06	-0.03	0.01	0.01	0.00	0.00
W4p2m0	-0.53	-0.06	-0.08	0.00	0.02	-0.06	0.04	0.04	0.00	-0.05

Acknowledgments / Danksagung

Vielen Dank an ...

Stella Seitz

für die Betreuung meiner Doktorarbeit über so viele Jahre, für die Unterstützung, die vielen Fachgespräche und vielfältigen Ideen, ohne die diese Arbeit nicht geworden wäre, was sie ist.

Ralf Bender

für die Zurverfügungstellung des Arbeitsplatzes, der Infrastruktur und für die Übernahme der Doktorvaterschaft.

Joe Mohr

für die Übernahme der Rolle des zweiten Gutachters und für die Unterstützung am Ende dieser Arbeit.

Mike Lerchster

für die freundschaftliche Unterstützung, die vielen Gespräche und nicht zuletzt für die Reduktion der Daten, die dieser Arbeit zugrunde liegen.

Meine Kollegen von der Sternwarte, Thomas Eichner, Natascha Greisel, Daniel Grün, Patrícia Figueró Spinelli, Jan Snigula und Armin Gabasch

für die Unterstützung und die vielen Gespräche.

Tadziu Hoffmann und Keith Butler

für ihre Hilfe und Unterstützung bei Computerproblemen.

Anna Monna, Arno Riffeser, Carsten Strübig, Chien-Hsiu 'Sherman' Lee, Christian Obermeier, Florian Lang, Jesús Zendejas, Johannes Koppenhöfer, Matthias Bierschenk, Mihael Kodric, Ralf Kosyra, Rebekka Grellmann, Yi-Hao Chen, Yulia Goranova, natürlich auch alle bereits genannten und viele mehr ...

für die freundschaftliche und kameradschaftliche Atmosphäre an der Sternwarte.

Peter Schneider, Thomas Erben, Tim Schrabback, Marco Hetterscheidt und Hendrik Hildebrandt vom AIfA in Bonn

für die Unterstützung und vielen Gespräche sowie der Bereitstellung und Einweisung in ihre wissenschaftliche Software (THELI-pipeline und KSB-Implementierung).

Meine Familie und insbesondere meine Eltern

die mich all die Jahre in meiner Arbeit unterstützt haben.

This work was supported by the the DFG priority programme 1177, the DFG Cluster of Excellence ‘Origin and Structure of the Universe’, the TRR33 ‘The Dark Universe’ and the Marie Curie research training network ‘DUEL’.